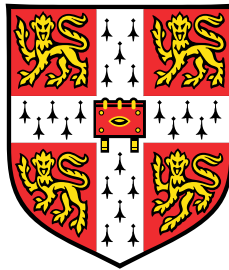


# Algorithmic generation of vascular network models for additive manufacturing



**Dulce Milagro Aguilar Garza**

Department of Engineering  
University of Cambridge

This dissertation is submitted for the degree of  
*Doctor of Philosophy*

Lucy Cavendish College

October 2020



## **Declaration**

I hereby declare that except where specific reference is made to the work of others, the contents of this dissertation are original and have not been submitted in whole or in part for consideration for any other degree or qualification in this, or any other university. This dissertation is my own work and contains nothing which is the outcome of work done in collaboration with others, except as specified in the text and Acknowledgements. This dissertation contains approximately 56,300 words including appendices, bibliography, footnotes, tables and equations and has 114 figures.

Dulce Milagro Aguilar Garza  
October 2020



## Abstract

Fabrication of functional vascularised three-dimensional tissue constructs has been a long-standing objective in the field of tissue engineering. Currently, the main limitation in this field is the inability to produce fully vascularised tissue with an internal mass transport system (vascular network) that can provide cells with nutrients and oxygen while removing waste, to imitate the functions of human living tissue. Achieving such a system would allow the development of large-scale tissue constructs and increase the potential for in vivo integration. There are different approaches to attempt vascularisation, which use a diversity of techniques. Among these, one of the most promising is additive manufacturing due to its versatility, reproducibility, and compatibility with suitable materials. With the aim of contributing towards the efforts in this field, the present work presents a method for the automatic generation of physiologically-based vascular network structures as solid 3D models suitable for additive manufacturing technologies. Considering the natural hierarchical branching vasculature as an ideal solution, an algorithm was developed to generate branching tree structures connected at the ends to form vascular networks. The implementation is based on previous work in the field of computational bio-simulation of arterial tree growth. It consists of a space-filling algorithm that connects all given points to a growing tree within a defined three-dimensional volume, while fulfilling constraints associated with the physiological laws of circulation. The networks are generated using a CAD environment and thus can be used in additive manufacturing processes. An investigation was carried out on the effect of three input parameters (namely volumetric flow rate, pressure difference across the tree, and number of terminal points) in order to find a suitable combination of parameters that would produce networks with diameters above the fabrication threshold.

In order to demonstrate feasibility and functionality of the networks fabricated using this proposed method, two network models were produced by 3D printing and subsequently used as a sacrificial structure to produce PDMS blocks with the hollow vascular networks embedded in it. Particle tracking was used to measure the flow velocity in the channels at two different inlet flow rates. Comparisons were made with theoretical values obtained from computational fluid dynamics simulations and show a good agreement between experiment

and theory. From the measurements of maximum velocity, it was observed that at a lower flow rate, the experimental values were closer to the theoretical values than at a higher flow rate. This might be due to the challenges that higher flow rates represent, such as less accurate particle tracking. Given the overall agreement, it is concluded that computational fluid dynamics simulations are a fast and effective way to analyse flow in vascular network models produced by the method here proposed.

I would like to dedicate this thesis to my beloved husband and to my parents,  
for without them I would not be who I am now.



## **Acknowledgements**

There are not enough words to express my gratitude to all the people who, in one way or another, professionally and personally, have helped me in the process of completing this work.

Firstly, I would like to thank my supervisor, Dr. Athina Markaki for her guidance throughout the whole research project. Her knowledge in the area and ideas were of great help during the development of my project. Without her support, encouragement and patience during the time I was unwell, I would not have been able to complete this research.

I would like to thank my colleagues of the MEMTI research group for providing a space for support and discussion. Particularly, I thank Dr. Alex W. Justin for his continuous support during my experimental work, Andrew Guy for his help with the development and improvement of the algorithm, and Agavi Stavropoulou-Tatla for her help with the initial microscope setup for particle tracking. I also thank Alex Casabuena for technical support and his help to obtain the necessary laboratory equipment.

My gratitude also goes to Dr. Ronan Daly and Dr. Etienne Rognin from the IfM for the guidance provided in the area of CFD simulations.

My research would not have been possible without the financial support from a partnership between the Mexican government institution CONACyT and the Cambridge TRUST, which supported me financially during most of my programme duration. In addition, I would like to thank the Cambridge Philosophical Society, the Cambridge TRUST and the Gilchrist Educational Trust for the additional funding they provided.

In a similar way, I thank the EPSRC Centre for Doctoral Training in Ultra Precision Engineering for funding my research project. I am also grateful to Professor Bill O' Neill for his encouragement to pursue this research.

Words cannot describe my gratitude towards my family. My parents, Ignacio and Juana Idalia, always provided me with the best education and gave me the invaluable gift of knowledge, and for this I will be eternally grateful. Without them and my brother, Ignacio (Jr.), and their continuous love, support and encouragement, I would not be the person I am today. I also thank my parents in law, Jesús and Marychuy, who I consider as my second parents and have always been supportive and understanding. All of them have, without a doubt, contributed to my personal development and I appreciate their constant help in all aspects of life (emotional, financial, health-related, to name a few). I also extend my gratitude to my dear friends who have made the hardest times bearable with their presence or words of encouragement.

Finally, I owe my deepest gratitude to my dear husband, Juan Antonio Rubio-Lara, who has been my greatest pillar of strength, comfort and advice on a personal and professional level. First, I thank him for his contribution to this work by helping with the particle tracking software development in LabVIEW, as well as for providing advice and motivated discussion of my work. I thank him also for his unconditional support and for sharing my happiness during the good times, and for his patience, love and encouragement during the hard times. I feel very lucky to have him as my life partner, as he is a continuous source of inspiration and this challenges me to become a better person and scientist.

# Table of contents

|   |            |
|---|------------|
| <b>List of figures</b>  | <b>xv</b>  |
| <b>List of tables</b>   | <b>xix</b> |
| <b>1 Introduction</b>   | <b>1</b>   |
| 1.1 Overview of vascularisation in tissue engineering . . . . . | 3          |
| 1.2 Research objectives . . . . .                               | 5          |
| 1.3 Outline of the dissertation . . . . .                       | 7          |
| <b>2 Vascular physiology: review</b>                            | <b>9</b>   |
| 2.1 Overview . . . . .  | 9          |
| 2.2 Vascular physiology . . . . .                               | 10         |
| 2.3 Physiological laws involved in blood circulation . . . . .  | 12         |
| 2.3.1 Poiseuille’s law and shear stress . . . . .               | 12         |
| 2.3.2 Murray’s law and arterial branching . . . . .             | 14         |
| 2.3.3 Optimisation principles . . . . .                         | 16         |
| 2.4 Considerations in the design of vascular networks . . . . . | 19         |
| 2.5 Conclusions . . . . .                                       | 20         |
| <b>3 Vascular tree modelling and fabrication: review</b>        | <b>23</b>  |
| 3.1 Overview . . . . .  | 23         |
| 3.2 Vascular tree modelling . . . . .                           | 24         |
| 3.3 Fabrication of vascular structures . . . . .                | 36         |
| 3.4 Discussion . . . . .  | 44         |
| 3.5 Conclusions . . . . .                                       | 47         |
| <b>4 Algorithmic vascular structure generation</b>              | <b>49</b>  |
| 4.1 Overview . . . . .  | 49         |
| 4.2 Algorithm Development . . . . .                             | 50         |

|          |  |            |
|----------|--|------------|
| 4.2.1    | Programming and modelling environment . . . . .                              | 50         |
| 4.2.2    | 3D volume delimitation and subdivision . . . . .                             | 51         |
| 4.2.3    | Fulfilment of physiological laws . . . . .                                   | 54         |
| 4.2.4    | Optimisation of bifurcation points . . . . .                                 | 61         |
| 4.2.5    | Connection of arterial tree and venous tree . . . . .                        | 64         |
| 4.2.6    | Detection and handling of collisions . . . . .                               | 66         |
| 4.2.7    | Algorithm sequence . . . . .   | 69         |
| 4.2.8    | Stages of tree growth . . . . .  | 72         |
| 4.2.9    | Examples of vascular structures . . . . .                                    | 73         |
| 4.3      | Analysis of algorithmically generated vascular structures . . . . .          | 73         |
| 4.3.1    | Effect of parameter change in algorithmically generated structures . . . . . | 75         |
| 4.3.2    | Effect of input parameter change in simplified planar network . . . . .      | 87         |
| 4.4      | Conclusions . . . . .  | 91         |
| <b>5</b> | <b>Flow in constructed vascular networks: Experimental work</b>              | <b>93</b>  |
| 5.1      | Overview of experimental flow analysis . . . . .                             | 93         |
| 5.2      | Experimental analysis of flow in vessel-like structures . . . . .            | 93         |
| 5.3      | Experimental analysis of flow in PDMS networks . . . . .                     | 97         |
| 5.3.1    | Experimental research goals . . . . .  | 98         |
| 5.3.2    | Materials and methods . . . . .  | 98         |
| 5.3.3    | Generation of vascular networks for experimental work . . . . .              | 100        |
| 5.3.4    | Fabrication of vascular network models . . . . .                             | 101        |
| 5.3.5    | Experimental setup for flow velocity measurements . . . . .                  | 107        |
| 5.3.6    | Measurement of flow velocity . . . . .                                       | 110        |
| 5.4      | Results and discussion . . . . .   | 112        |
| 5.4.1    | Comparison of theoretical and experimental data . . . . .                    | 119        |
| 5.5      | Conclusions . . . . .  | 124        |
| <b>6</b> | <b>Flow in vessels: Computational Fluid Dynamics analysis</b>                | <b>127</b> |
| 6.1      | Overview . . . . .   | 127        |
| 6.2      | Review of the use of CFD for studying flow in vessels . . . . .              | 128        |
| 6.3      | CFD analysis in vascular network models . . . . .                            | 133        |
| 6.3.1    | Setup . . . . .  | 133        |
| 6.4      | Results . . . . .  | 138        |
| 6.5      | Discussion . . . . .   | 149        |
| 6.6      | Conclusions . . . . .  | 160        |

|          |  |            |
|----------|--|------------|
| <b>7</b> | <b>Conclusions and Future Work</b>   | <b>163</b> |
| 7.1      | Conclusions . . . . .  | 163        |
| 7.1.1    | Algorithm development and implementation . . . . .   | 164        |
| 7.1.2    | Inaccuracies in the network fabrication . . . . .  | 165        |
| 7.1.3    | Experimental analysis of flow in fabricated network . . . . .  | 165        |
| 7.1.4    | Computational analysis of flow in fabricated network . . . . .   | 166        |
| 7.1.5    | Impact of the research in the field of tissue engineering . . . . .  | 167        |
| 7.2      | Future Work . . . . .  | 167        |
| 7.2.1    | Algorithm . . . . .  | 168        |
| 7.2.2    | Experimental analysis . . . . .  | 169        |
| 7.2.3    | CFD analysis . . . . .   | 170        |
|          | <b>References</b>  | <b>171</b> |
|          | <b>Appendix A Calculations for theoretical values of maximum velocity with original CAD model diameters and experimental diameters</b>   | <b>185</b> |
| A.1      | Calculations of theoretical max. velocity for model 01 . . . . .   | 186        |
| A.1.1    | Theoretical values of velocity with original CAD diameters . . . . .   | 186        |
| A.1.2    | Theoretical values of velocity with experimental diameters . . . . .   | 186        |
| A.2      | Calculations of theoretical max. velocity for model 02 . . . . .   | 187        |
| A.2.1    | Theoretical values of velocity with original CAD diameters . . . . .   | 187        |
| A.2.2    | Theoretical values of velocity with experimental diameters . . . . .   | 187        |
|          | <b>Appendix B Tables for estimation of pressure difference paths (inlet to outlet) based on experimental data (radius and flow rate)</b> | <b>189</b> |
| B.1      | Model 01 - 2mL/h . . . . .   | 190        |
| B.2      | Model 01 - 5mL/h . . . . .   | 191        |
| B.3      | Model 02 - 2mL/h . . . . .   | 192        |
| B.4      | Model 02 - 5mL/h . . . . .   | 193        |



# List of figures

|      |   |    |
|------|---|----|
| 1.1  | Organ demand chart from the US . . . . .          | 2  |
| 1.2  | Organ demand chart from the UK . . . . .          | 2  |
| 1.3  | Current vascularisation strategies . . . . .      | 3  |
| 1.4  | Lattice vs. Branching arrangement . . . . .       | 4  |
| 2.1  | Pressure drop in the circulatory system . . . . . | 11 |
| 2.2  | Schematic of Poiseuille's flow . . . . .          | 13 |
| 2.3  | Branching modes proposed by Zamir . . . . .       | 17 |
| 2.4  | Bifurcation measurement by Zamir . . . . .        | 18 |
| 3.1  | Schreiner's model . . . . .                       | 25 |
| 3.2  | Karch's models . . . . .                          | 28 |
| 3.3  | Kretowski's models . . . . .                      | 29 |
| 3.4  | Szczerba's models . . . . .                       | 30 |
| 3.5  | Georg's models . . . . .                          | 30 |
| 3.6  | Li's models . . . . .                             | 31 |
| 3.7  | Liu's model . . . . .                             | 31 |
| 3.8  | Hamarneh and Jassi's models . . . . .             | 32 |
| 3.9  | Schneider's model . . . . .                       | 33 |
| 3.10 | Kocinski's model . . . . .                        | 33 |
| 3.11 | Schwen and Preusser's models . . . . .            | 34 |
| 3.12 | Galarreta's model . . . . .                       | 34 |
| 3.13 | Linninger's model . . . . .                       | 35 |
| 3.14 | Guy's model . . . . .                             | 37 |
| 3.15 | Wu's networks . . . . .                           | 38 |
| 3.16 | Kolesky's networks . . . . .                      | 38 |
| 3.17 | Kolesky's network . . . . .                       | 39 |
| 3.18 | Huang's networks . . . . .                        | 39 |

|      |   |    |
|------|---|----|
| 3.19 | Miller's network . . . . .  | 40 |
| 3.20 | Bertassoni's networks . . . . .   | 40 |
| 3.21 | Heintz's networks . . . . .   | 41 |
| 3.22 | Wang's network . . . . .  | 42 |
| 3.23 | Morgan's network . . . . .  | 42 |
| 3.24 | Hinton's network . . . . .  | 43 |
| 3.25 | Justin's networks . . . . .   | 44 |
| 3.26 | Vessel Design for ArtiVasc Project . . . . .  | 45 |
| 3.27 | Guy's 3D printed vascular network . . . . .   | 46 |
|      |   |    |
| 4.1  | Example of single tree and arterio-venous network . . . . .   | 50 |
| 4.2  | Creation of a new project in Visual Basic . . . . .   | 52 |
| 4.3  | Representation of macro-cell . . . . .  | 52 |
| 4.4  | Depiction of 3D volume in the CAD interface . . . . .   | 53 |
| 4.5  | Schematic representation of the addition of a new terminal point for the three possible cases . . . . . | 55 |
| 4.6  | Schematic representation of the addition of a new branch . . . . .                                      | 55 |
| 4.7  | Schematic representation of flow rate updating when new point is added . . . . .                        | 57 |
| 4.8  | Algorithm to update the flow in the tree . . . . .  | 57 |
| 4.9  | Algorithm for reduced resistance update in the vascular structure . . . . .                             | 60 |
| 4.10 | Optimisation of bifurcation first step . . . . .  | 62 |
| 4.11 | Optimisation of bifurcation test point definition . . . . .   | 63 |
| 4.12 | Optimisation of bifurcation test point movement . . . . .   | 64 |
| 4.13 | Connection of arterial and venous trees . . . . .   | 65 |
| 4.14 | Connection point for arterial and venous trees . . . . .  | 65 |
| 4.15 | Example of collision in arterio-venous network . . . . .  | 67 |
| 4.16 | Shortest distance between two lines in a 3D space . . . . .   | 67 |
| 4.17 | Flow chart of main algorithm . . . . .  | 70 |
| 4.18 | Stages of tree growth . . . . .   | 74 |
| 4.19 | Vascular models created using the algorithm here presented. . . . .                                     | 75 |
| 4.20 | Test models for parameter effect analysis . . . . .   | 78 |
| 4.21 | Chart of average tree branch radius for original and test models . . . . .                              | 79 |
| 4.22 | Chart of average terminal branch radius for original and test models . . . . .                          | 80 |
| 4.23 | Chart branch $Q$ vs $r$ for models with different values of $\Delta P_{inlet-cell}$ . . . . .           | 82 |
| 4.24 | Chart branch $\Delta P$ vs $r$ for models with different values of $Q_{cell}$ . . . . .                 | 83 |
| 4.25 | Chart branch $Q$ vs $r$ for models with different values of $Q_{cell}$ . . . . .                        | 84 |
| 4.26 | Chart branch $\Delta P$ vs $r$ for models with different values of $\Delta P_{inlet-cell}$ . . . . .    | 85 |

---

|      |   |     |
|------|---|-----|
| 4.27 | Total tree volume of original and test models . . . . .   | 85  |
| 4.28 | Total computing time of original and test models . . . . .                                      | 86  |
| 4.29 | Simple models to inspect parameter effect in tree morphology . . . . .                          | 88  |
| 4.30 | Effect of parameter variation on planar networks with $N=5$ . . . . .                           | 89  |
| 4.31 | Effect of parameter variation on planar networks with $N=10$ . . . . .                          | 89  |
| 4.32 | Effect of parameter variation on planar networks with $N=15$ . . . . .                          | 90  |
| 4.33 | Effect of parameter variation on planar networks with $N=20$ . . . . .                          | 90  |
|      |   |     |
| 5.1  | 3D models of planar networks generated in Inventor® . . . . .                                   | 101 |
| 5.2  | 3D models of planar networks showing diameters . . . . .  | 102 |
| 5.3  | External dimensions of 3D networks . . . . .  | 102 |
| 5.4  | 3D printed network models in supporting frame . . . . .   | 103 |
| 5.5  | 3D printed network models in casting chambers . . . . .   | 104 |
| 5.6  | PDMS cast over network models . . . . .   | 104 |
| 5.7  | Cured PDMS network models . . . . .   | 105 |
| 5.8  | Finished PDMS experimental models . . . . .   | 106 |
| 5.9  | Assigned branch numbers . . . . .   | 106 |
| 5.10 | Chart design vs. measured diameters of experimental models . . . . .                            | 107 |
| 5.11 | Schematic of experimental setup . . . . .   | 108 |
| 5.12 | Zeiss microscope and experimental setup . . . . .   | 108 |
| 5.13 | Compound tiles image of M01 . . . . .   | 109 |
| 5.14 | Particle movement across channel . . . . .  | 111 |
| 5.15 | LabView interface of software for particle tracking . . . . .                                   | 113 |
| 5.16 | Experimental data M01 at 2 mL/h . . . . .   | 114 |
| 5.17 | Experimental data M01 at 5 mL/h . . . . .   | 115 |
| 5.18 | Experimental data M02 at 2 mL/h . . . . .   | 116 |
| 5.19 | Experimental data M02 at 5 mL/h . . . . .   | 117 |
| 5.20 | Comparison of experimental and theoretical data for max. velocity . . . . .                     | 121 |
| 5.21 | Representation in 3D of a straight and a tilted network in top and lateral views. 122           |     |
| 5.22 | Overlapping of straight and tilted views of networks from microscope per-<br>spective . . . . . | 123 |
| 5.23 | Displacement of particle in straight vs. tilted network, branches 07 and 12 .                   | 123 |
|      |   |     |
| 6.1  | Meshes for models 01 and 02 . . . . .   | 136 |
| 6.2  | Middle plane for velocity measurement CFD . . . . .   | 137 |
| 6.3  | CFD plots for velocity (midplane) for M01 and M02 at 2 and 5 mL/h . . . .                       | 139 |
| 6.4  | Velocity field at areas with greater velocity . . . . .   | 140 |

---

|      |  |     |
|------|--|-----|
| 6.5  | CFD plots for Velocity profiles for M01 branches at 2 and 5 mL/h . . . . .   | 141 |
| 6.6  | CFD plots for Velocity profiles for M02 branches at 2 and 5 mL/h . . . . .   | 142 |
| 6.7  | CFD plots for $\Delta P$ for M01 and M02 at 2 mL/h and 5 mL/h . . . . .      | 143 |
| 6.8  | Example of pressure path . . . . .   | 144 |
| 6.9  | CFD charts for shear stress in M01 at 2 and 5 mL/h . . . . .                 | 146 |
| 6.10 | CFD charts for shear stress in M02 at 2 and 5 mL/h . . . . .                 | 147 |
| 6.11 | Close-up of shear stress plot of model 01 at 5 mL/h . . . . .                | 149 |
| 6.12 | Comparison of CFD and experimental velocity profiles for M01 at 2 mL/h.      | 150 |
| 6.13 | Comparison of CFD and experimental velocity profiles for M01 at 5 mL/h .     | 151 |
| 6.14 | Comparison between experimental and CFD max. velocities . . . . .            | 153 |
| 6.15 | Velocity plot (midplane) for M01 at 20 mL/h . . . . .                        | 154 |
| 6.16 | Close-up of upper zero flow region for M01 at 20 mL/h . . . . .              | 155 |
| 6.17 | CFD plot for $\Delta P$ for M01 at 20 mL/h . . . . .                         | 156 |
| 6.18 | CFD chart for shear stress in M01 at 20 mL/h with PBS properties . . . . .   | 158 |
| 6.19 | CFD chart for shear stress in M01 at 20 mL/h with blood properties . . . . . | 158 |
| 6.20 | CFD chart for velocity in original M01 at 20 mL/h with blood properties . .  | 159 |
| 6.21 | CFD chart for shear stress in original M01 at 20 mL/h with blood properties  | 159 |
| 6.22 | CFD chart for pressure in original M01 at 20 mL/h with blood properties . .  | 160 |
| 7.1  | Depiction of reduced branching angle . . . . .                               | 168 |

# List of tables

|     |   |     |
|-----|---|-----|
| 3.1 | Summary of arterial tree growth algorithms . . . . .  | 26  |
| 4.1 | Input parameters for the algorithm . . . . .  | 69  |
| 4.2 | Input parameters for original and test models. . . . .                                      | 76  |
| 6.1 | Velocities for inlet boundary condition. . . . .  | 135 |
| 6.2 | Estimated values of pressure drop across experimental models in ‘pressure paths’. . . . .   | 144 |
| 6.3 | Experimental and CFD values of pressure drop across the networks. . . . .                   | 145 |
| 6.4 | Experimental and CFD values of shear stress in branch 13. . . . .                           | 148 |
| 6.5 | Experimental values of pressure drop across the models in all the ‘pressure paths’. . . . . | 156 |
| 6.6 | Experimental and CFD values of pressure drop across the networks. . . . .                   | 157 |



# Chapter 1

## Introduction

Shortage of organs for transplantation is one of the major challenges in global public health [1]. In the United States (US) 20 people die every day waiting for an organ transplant, and although the number of transplants increases slowly every year (reaching a record of 39,718 in 2019) there is still an important shortage of organs, as the number of patients on the waiting list is currently over 112,000 [2] [3]. Figure 1.1 shows the number of patients awaiting an organ, organ donors and organ transplants performed in the US every year in the past 29 years. In a similar way, Figure 1.2 shows transplant data in the United Kingdom (UK) for the past 10 years. It is evident in both cases that the number of people who require an organ transplant is significantly greater than the number of organs available from donors. In the UK in 2019, 400 people died waiting for a transplant and a further 777 were removed from the transplant list for being deemed ineligible, mainly due to deteriorating health [4].

Fabrication of artificially engineered tissue has the potential to increase organ availability through the generation of implantable organ tissue (parenchyma). In addition, engineering of artificial tissue would not only benefit the clinical approach, but is also promising for numerous applications such as providing alternatives towards the eradication or reduction of animal testing in the pharmaceutical and chemical industries [5]. Currently, the greatest limitation in the field of tissue engineering (TE) is the fabrication of vascularised three-dimensional (3D) thick tissue constructs. Without access to nutrients, cells cannot survive, as they develop a necrotic core [6]. Therefore, it is essential for tissue constructs to have an internal mass transport system (vascular network) to provide the cells with nutrients and oxygen, and remove waste, in order to imitate the functions of human living tissue. Adequate vascularisation would increase the potential for large-scale organ tissue survival and in vivo integration. However, achieving functional vascularised tissue remains a challenging task, which is why it is often considered “the Holy Grail” of tissue engineering [7].

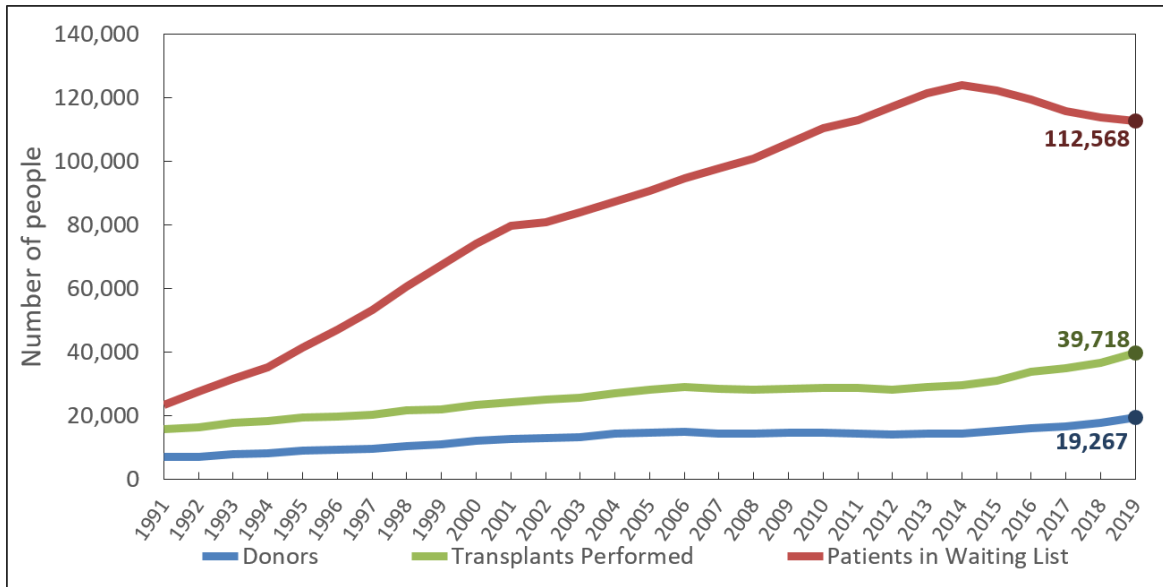


Fig. 1.1 Comparison between the number of donors (including living and deceased) and the transplants performed from them, versus the number of patients who are in waiting list, per annum in the United States for the past 29 years. Created with data from US Government Information on Organ Donation and Transplantation [2], originally retrieved from OPTN [3].

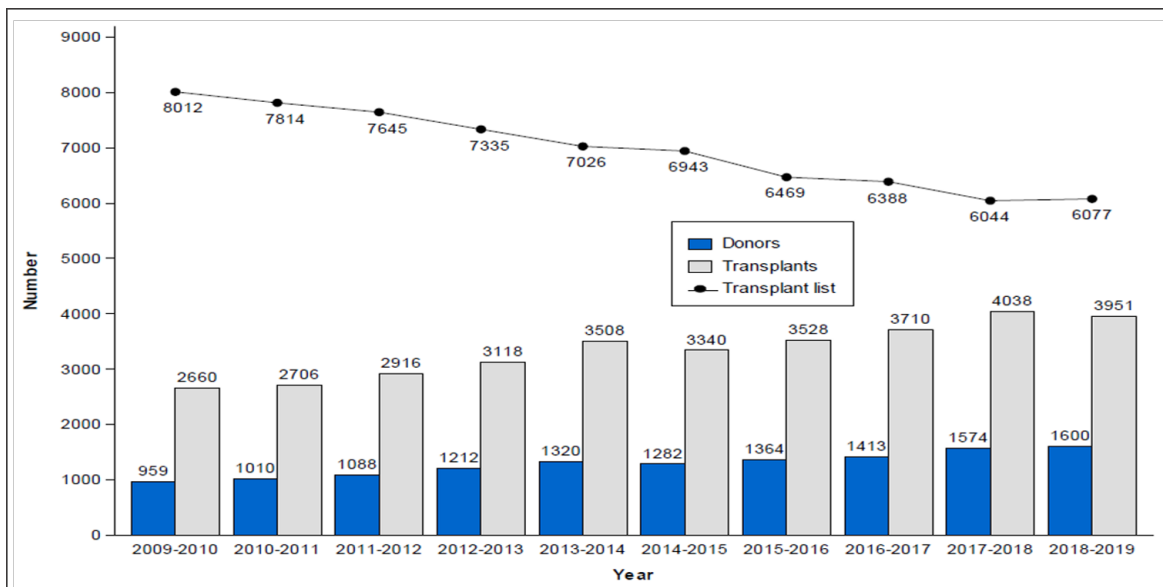


Fig. 1.2 Comparison between the number of donors, transplants performed and number of patients on the waiting list, per annum in the United Kingdom for the past 10 years. Image source: [4].

## 1.1 Overview of vascularisation in tissue engineering

There are different approaches to achieve vascularisation in tissue engineering, which can be categorised in three major categories [8]: i) cell-based strategies, ii) angiogenic factor-based strategies, and iii) scaffold-based strategies. Figure 1.3 shows a summary of the current approaches under their corresponding category. Cell-based and angiogenic factor-based strategies depend on the expansion of endothelial cells (ECs) to form vessel connections and are suitable for capillaries and micro-vascular network formation, whereas scaffold-based strategies rely on the use of artificially designed or acquired vascular network models and are more suitable for micro to meso scale vessel networks [9]. The present work aims to construct vascular networks in the micro-meso scale (representing small arteries), therefore, a scaffold-based strategy is used.

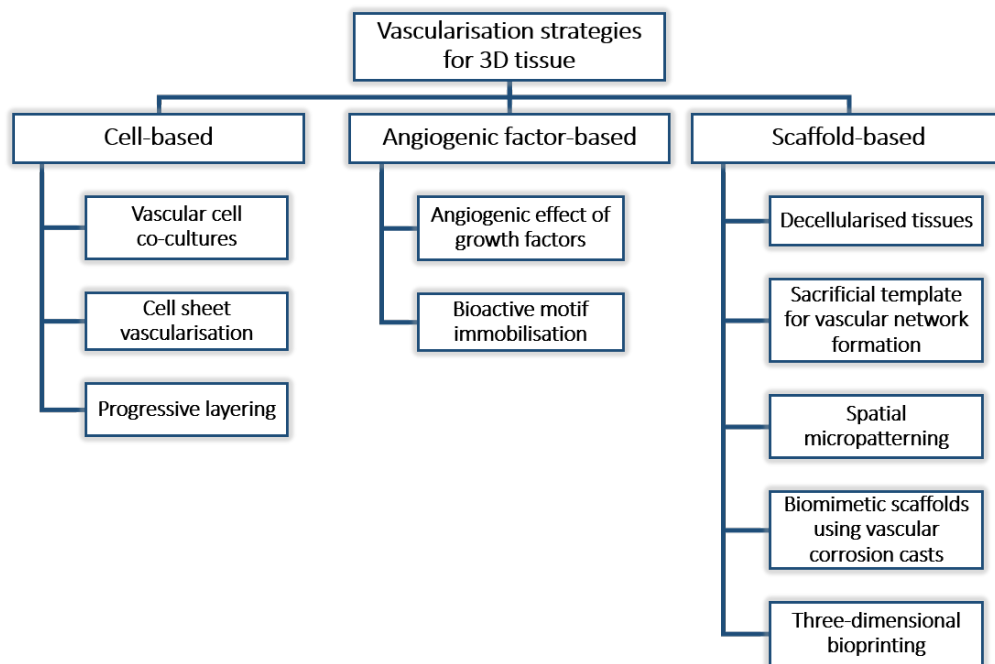


Fig. 1.3 Diagram showing the current vascularisation strategies for the development of 3D tissue. Adapted from [8].

Commonly, artificial scaffold-based approaches use micro-channels in a lattice arrangement (see Figure 1.4). These micro-channels are either single or multi-layered, to form scaffold structures or simple-design branching networks with a variety of fabrication techniques and materials [10]. Most of these network designs are not physiologically accurate, as there is no clear differentiation between two vascular tree structures (one for nutrient supply -arteries- and another for waste removal -veins-). In addition, the physiological

pressure and flow components of blood circulation are often ignored. It is essential to achieve physiologically relevant vascular structures based on the body's natural hierarchical vascular branching architecture, which consist of an interconnected network of an arterial tree and a venous tree.

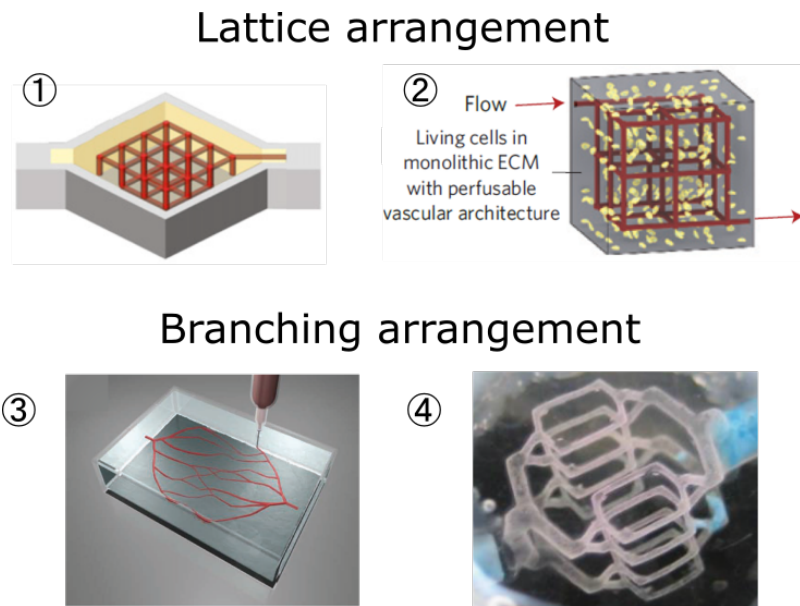


Fig. 1.4 Examples of approaches using a lattice arrangement and a branching arrangement. Images from: ① Network by Kolesky et al. [11]. ② Network by Miller et al. [6]. ③ Network by Wu et al. [12]. ④ Network by Justin et al. [13].

Regarding the fabrication of vascular networks for scaffold-based approaches, additive manufacturing (AM), commonly known as “3D printing”, is a reliable and reproducible method that has been widely used for this purpose [14] [15]. 3D printing-based techniques are used in a variety of ways, including the production of moulds, sacrificial templates or for the direct printing of the vascular structures. In order to generate the fabrication trajectories, a 3D model of the object to be printed is required.

There are two basic approaches for obtaining 3D models of vascular networks that are suitable for additive-manufacturing:

1. Depending on the organ or tissue to be engineered, one approach is to use a medical imaging technique, such as a computerised tomography (CT) scan of a patient's organ,

and following image processing a 3D model is obtained in a printing format (STL<sup>1</sup> file). Previous studies show the possibility of obtaining a 3D computer-aided design (CAD) model from the reconstruction of micro-CT data [16] [17]. However, the method used to obtain the data is corrosion cast, which is an *in vitro* (*ex vivo*) technique, and is unsuitable for patients. It is also possible to obtain CT data *in vivo* [18] [19]. Even though this technique shows promising results, it still requires the use of contrast agents. Currently, it is possible to visualise large arteries, but difficult to visualise smaller vascular channels such as capillaries.

2. The second approach is to manually design the network model using a commercial CAD software package (such as Autodesk® Inventor®, SolidWorks®, AutoCAD®, etc.) by building the trees on a branch-by-branch basis. Using this approach would only allow the design of simple networks that do not represent real hierarchical vascular architecture nor fulfil physiological laws [13] [20–22].

In the present work, an alternative approach is proposed and developed: the combination of algorithms for vascular tree simulations and CAD modelling in order to achieve the automatic generation of physiologically relevant vascular network models in a format suitable for additive manufacturing.

## 1.2 Research objectives

Considering the proposed approach, intended for the design and fabrication of large vascularised tissue constructs, the main research question of the present work can be formulated as:

---

Is it possible to design physiologically relevant vascular networks that fulfil the laws of circulation and can be fabricated by additive manufacturing?

---

To answer the question, it is necessary to consider the possible methods that are currently available for the creation of physiologically accurate vascular network models. Computational simulations allow very precise modelling of vascular structures. However, these

---

<sup>1</sup>STL is a file format widely used in CAD. It contains information about a 3D model's surface geometry. It was originally created for stereolithography software, and it is believed that the acronym STL is derived from this, although it is also referred to as "standard tessellation language".

models are typically built with a mathematical basis and the graphic visualization of the model is just a three dimensional visual representation of the computed data, and cannot be exported as a solid 3D model. In order to 3D print vascular structures, a file in “STL” format is required, which is created using a CAD software. There is a need for a method to generate vascular structures using a CAD software. Thus, the general aim of the project is to find an effective method of creating accurate blood vessel network structures as 3D solid models in a CAD environment for 3D printing.

While pursuing the general aim, the specific goals of the research project are:

- To understand the physiological principles involved in human blood vessel networks.
- Development of an algorithm for the generation of vascular network structures within a defined 3D space.
- Implementation of the algorithm in a computer programming environment that will allow to automatically run and execute commands in a CAD package to create the solid vascular model.
- To understand the effect of changing the input parameters in the algorithm on the vascular network architecture.
- To prove the feasibility of the proposed approach by fabricating vascular networks via 3D printing.
- To analyse the flow behaviour in the fabricated networks experimentally.
- To analyse the flow behaviour in the 3D network models by computational fluid dynamics analysis (CFD)
- To determine if the experimental flow analysis is in accordance with the CFD analysis and with the theoretical model used to design the networks.

The development of an algorithm for the construction of physiologically accurate vascular trees in a CAD environment is a complex task that requires the integration of three areas of knowledge: computer programming (creation of algorithm), biomedical science (vascular physiology) and engineering (CAD software). Because of this, some simplifications are needed regarding the physiological constraints, such as assuming Newtonian flow with constant viscosity and omitting certain realistic behavioural aspects of the blood networks (e.g. the pulsatility of blood flow).

## 1.3 Outline of the dissertation

The organisation of the thesis is as follows:

**Chapter 2** - An overview on vascular physiology, flow in vascular networks and the design principles used in the construction of vascular models, including assumptions to simplify the modelling of vascular networks.

**Chapter 3** - A review on the previous work on algorithms for the computational simulation of arterial trees, and a summary of the current techniques used in tissue engineering for attempting the production of vascularised tissue structures.

**Chapter 4** - Description of the algorithm developed for the proposed approach for the automatic generation of vascular network structures as 3D solid models in a CAD environment. The chapter includes an analysis of input parameter effect on the vascular tree morphology.

**Chapter 5** - Experimental flow analysis on simple planar networks fabricated by 3D printing, including brief overview of current techniques used for experimental flow analysis in fluidic channels. Fabrication, experimental setup, data processing and results are detailed.

**Chapter 6** - CFD analysis of flow in the 3D planar vascular network models including brief overview of recent work on CFD analysis in vasculature and fluidic channels. The main analysis is carried out using the experimental parameters as well as the theoretical values.

**Chapter 7** - Conclusions of the thesis including a summary, the main findings of the research, main challenges and future work.



# Chapter 2

## Vascular physiology: review

### 2.1 Overview

In Chapter 1 it has been stated that the aim of the present work is the construction of vascular networks which consider the human physiology in their design, with the purpose of using them for additive manufacturing in tissue engineering applications. In order to attempt to replicate the natural hierarchical branching structure of vasculature, it is important to understand the basic physiological principles involved in the circulatory system. This chapter presents a brief introduction to the physiology of vascular networks in the human body and the haemodynamics of blood circulation, including the physiological laws that should be considered when designing vascular network constructs.

Section 2.2 presents basic vascular network morphology and distribution data. Section 2.3 presents a summary of the physiological laws that are typically used to describe flow in vessels and arterial branching. Section 2.4 presents a list of recommended design rules for vascular networks.

Given the purpose of the present work, this brief review will additionally discuss the applicability of the physiological laws in vascular designs intended for additive manufacturing techniques.

## 2.2 Vascular physiology

The human circulatory system has a complex hierarchical network arrangement with multi-scale vasculature ranging from a few micrometers of diameter to a few centimetres [23]. In the macro-scale there is the aorta, with a diameter of approximately 2.5 cm, which is the main vessel that conveys blood to the circulatory system. Also in the macro-scale are the large arteries in a range of 1 to 4 mm in diameter, which distribute the blood to the organs. Small arteries range from 0.2 to 1 mm in diameter (meso-scale) and their function is to distribute the blood to all regions within the organs. As the small arteries branch, they become arterioles, ranging from 10 to 200  $\mu\text{m}$  in diameter (micro-scale) and their function, together with the small arteries, is to regulate the blood flow and pressure in the organs. Finally, as the arterioles branch they reduce their diameter until they become capillaries, which range from 6 to 10  $\mu\text{m}$ , and their function is the exchange of oxygen, carbon dioxide, nutrients and metabolic waste with the surrounding cells in the organ [24]. When pairs of capillaries join they form venules, which in turn will join to form larger venules (up to 0.2 mm in diameter), eventually becoming veins (from 0.2 to 5 mm in diameter). The vena cava, which transports the blood back to the right atrium of the heart, has a typical diameter of 3.5 cm.

The branching architecture has a vascular pattern specific to each organ in the body, but there are some rules that apply in a general way for the full circulatory system. The most important of these rules is that vessel networks must branch in a way that every small group of cells is supplied, at least, by one capillary [25]. Typical inter-capillary distances range from 50 to 300  $\mu\text{m}$ , which is a vital requirement for optimal metabolic exchanges [26], as the diffusion limit distance of oxygen is about 100–200  $\mu\text{m}$  [27].

Some vascular characteristics have been found to be organ specific. For example, in the liver, there is a pressure/flow autoregulatory mechanism in the hepatic artery, which allows the blood flow to remain constant through a vascular bed. However, this autoregulation is not found in the vascular bed of the portal vein [28]. It has also been stated in recent years that in different organs the micro-vasculature has different properties, for which it is considered an organotypic vasculature, particularly referring to the differentiation of endothelial cells (ECs) [29].

Arterial pressure is another important parameter to be accounted for in the design of vasculature. The average pressure drop in the human body is shown in Figure 2.1. In the aorta, the mean pressure is approximately 90 mm Hg. The largest pressure drop occurs at the smaller arteries and capillaries, where the pressure is approximately 25 mm Hg [24].

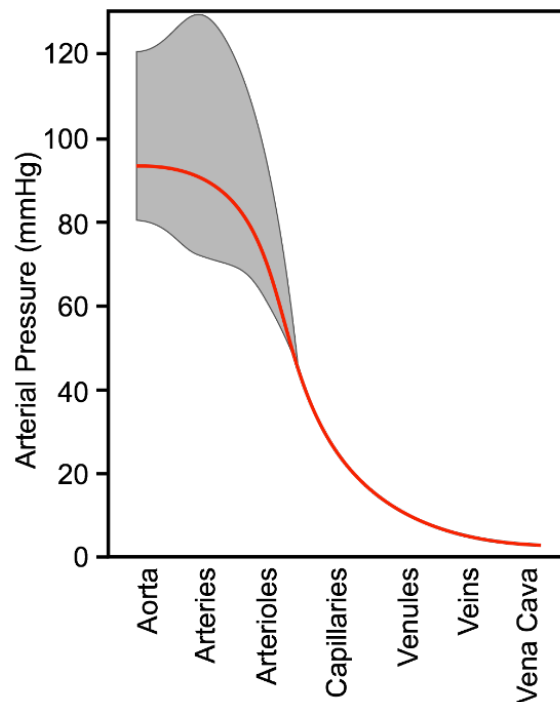


Fig. 2.1 Pressure drop across the circulatory system. The red curve indicates mean arterial pressure. The upper limit from the grey area represents systolic pressure, and the lower limit is the diastolic pressure. Image from Klabunde's book [24].

In the context of AM, it is not yet possible to achieve the fabrication of full organs or large biological constructs that fully reflect the complexity of the human vasculature with all its characteristics. One major challenge is the multi-scale distribution of the vascular system. In bio-printing, for example, a technique does not exist yet, that can allow the production of micrometer (capillaries) as well as centimetre (major vessels) size features within a reasonable time span to ensure survival of the printed cells in the structure. Depending on a combination of factors relative to the AM process, such as the desired materials and the resolution of the equipment, diverse results can be achieved in terms of vascular structure feature sizes. For example, inkjet printing is a versatile technique that allows printing meso-scale features, and depending on the resolution of the printer, also in the micro-scale. For the fabrication of capillary size micro-channels, multi-photon polymerization (MPP) and electrospinning have been proven useful [30].

## 2.3 Physiological laws involved in blood circulation

This section presents a brief summary of widely accepted physical laws used to describe the blood behaviour in the circulatory system and the assumptions required for their applicability in the circulation. The main laws discussed here are Poiseuille's law, Murray's law, and the optimality principles of arterial branching.

### 2.3.1 Poiseuille's law and shear stress

Interested in the study of flow in tubes of small diameters, J.L. Poiseuille [31] performed a series of experiments seeking to find a relationship linking the volumetric flow rate, the pressure difference, the tube length and the tube diameter, under steady flow conditions in a stiff tube. This work resulted in one of the most widely known laws to describe flow behaviour in pipes or cylindrical channels: Poiseuille's equation<sup>1</sup> or Poiseuille's law, which is mathematically expressed as:

$$Q = \frac{\pi D^4 \Delta P}{128 \mu L} \quad (2.1)$$

where  $Q$  is the volumetric flow rate,  $D$  is the diameter of the pipe,  $L$  is the length of the pipe segment over which the pressure drop  $\Delta P$  is measured, and  $\mu$  is the fluid kinetic viscosity. If the pressure difference  $\Delta P$  is expressed as the volumetric flow rate  $Q$  multiplied by the flow resistance  $R$ , then the resistance can be expressed as:

$$R = \frac{128 \mu L}{\pi D^4} \quad (2.2)$$

The vascular system is formed of branching arterial and venous trees, where each vessel section in between two bifurcations can be considered a small tube. Thus, in a simple approximation, blood flow in a single vessel can be compared to flow in a cylindrical pipe. Considering a steady laminar flow (non-turbulent) in a rigid pipe and assuming blood as a Newtonian fluid, Poiseuille's law can be used to model the flow [35] [36]. Figure 2.2 shows a schematic of Poiseuille's flow: in accordance with Equation 2.1,  $L$  is the length of the pipe and  $\Delta P$  is the pressure difference across the pipe, while  $D$  corresponds to the pipe diameter. The velocity profile is parabolic, and the maximum flow velocity is found at the central axis

---

<sup>1</sup>It is sometimes referred to as "Hagen-Poiseuille equation", as G.H.L. Hagen [32] published results similar to those obtained by Poiseuille, around the same time his work was published. Later, it was E. Hagenbach [33] who derived the most known form of the equation. For more on the history of Poiseuille's law, refer to [34].

of the pipe, with the flow being axisymmetric.

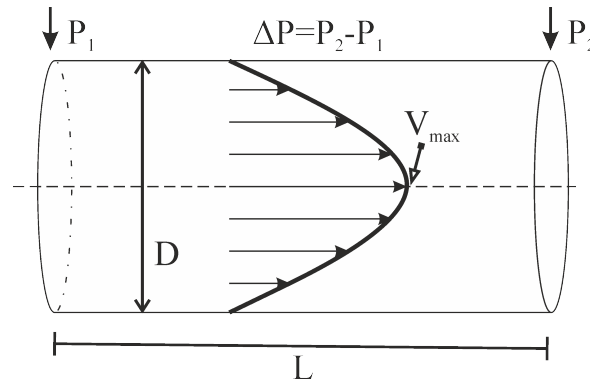


Fig. 2.2 Schematic of Poiseuille's flow in a rigid pipe with laminar steady flow.  $L$  = length of the pipe,  $D$  = diameter,  $\Delta P$  = pressure difference. The velocity profile is parabolic in shape and the maximum velocity is found at the central axis.

It is widely known that Poiseuille's equation governs the flow in Newtonian fluids, in which the viscosity is constant. Blood as a whole is a non-Newtonian fluid due to its multi-phase composition. Despite this, according to numerous studies, blood can be regarded as a Newtonian fluid in large vessels, where the scale of the microstructure (i.e. red blood cells, white blood cells and platelets) is much smaller than that of the flow. However, while most of the works on blood circulation agree that blood flow can be safely assumed Newtonian in most arteries [37], the specific diameter threshold to consider a vessel 'large' enough to assume Newtonian flow is different according to various authors. In his book, T.J. Pedley [38] suggested that flow in blood vessels of diameters larger than  $100 \mu\text{m}$  can be assumed Newtonian (which is roughly the size in which vessels cannot be observed without a microscope). However, in more recent studies, other authors use a vessel diameter threshold of  $200 \mu\text{m}$  [39], and even  $500 \mu\text{m}$  [40]. On the other hand, in vessels considered small (less than  $100 \mu\text{m}$  in diameter, which are typically arterioles, capillaries and venules), it is not possible to assume a Newtonian flow because of the size of the vessels compared to the haematocrit<sup>2</sup>. Thus, in the micro-circulation the blood viscosity dependence on the haematocrit is more significant than in larger vessels [41]. This is known as the Fåhræus-Lindqvist effect [42].

In addition to the flow rate, pressure and resistance, another parameter of interest in the study of flow in the vasculature is the shear stress at the vessel walls (WSS). Shear stress is a clinically relevant parameter that has been studied extensively [43] [44], as abnormal levels

<sup>2</sup>Haematocrit refers to the percentage of red blood cells present in the blood.

can be the cause for a diversity of negative effects in the circulation, such as atherosclerosis<sup>3</sup>, vascular remodelling and endothelial cell damage [46]. The shear stress in a Newtonian fluid is defined as the kinetic viscosity multiplied by the velocity gradient (or shear rate). Thus, using Poiseuille's law, the shear stress can be expressed as:

$$\tau = \frac{4\mu}{\pi r^3} Q \quad (2.3)$$

This indicates that the shear stress in the vessel walls is directly proportional to the volumetric flow rate and inversely proportional to the vessel diameter. This expression is relevant because the volumetric flow rate and the vessel radius can be clinically measured using non-invasive medical imaging techniques, such as magnetic resonance imaging (MRI) [47] and ultrasound [48] [49].

The shear stress and Poiseuille's equations can be implemented in the design of vascular networks in order to produce models that represent healthy vascular conditions. In addition, once the healthy 3D model from AM is achieved, it can be further modified in order to resemble pathological conditions, such as the formation of plaque by atherosclerosis. This would be useful to study and compare the changes in flow behaviour under normal and pathological circumstances, using either computational simulations of the 3D models, or physically studying the AM fabricated model.

### 2.3.2 Murray's law and arterial branching

In 1926, C.D. Murray published a series of work in which it was proposed to consider the application of the principle of minimum work to the operation of physiological systems, particularly to the vascular system [50–52]. This work resulted in Murray's law being considered one of the basic principles in the physiology of vascular networks, along with Poiseuille's law. Murray's work is based on the premise that the work involved in the operation of an arterial branch must be minimised. The total work consists of two terms: i) the work required by the flow of blood to overcome friction (expressed by the product of the pressure difference across the branch and the flow rate), and ii) the metabolic work to maintain the volume of blood inside the branch (expressed by the product of the blood volume and a constant representing the cost of blood). The equations for the calculations of work are based on

---

<sup>3</sup>Atherosclerosis is a condition in which the arteries become obstructed by plaque building up at the walls. Its development is believed to be directly correlated to local haemodynamics, and particularly to the wall shear stress [45].

Poiseuille's equation for flow in a cylindrical tube and assume steady state conditions.

Murray derived a series of equations regarding the branching angles of arteries, while assuming that the work of circulation is to be a minimum. As a result, the well-known statement of Murray's law to achieve geometric optimality in a branching system was determined: "*The sum of the cubes of the radii of the branches equals the cube of the radius of the main stem from which they arise.*" (from [52]), which is typically expressed as:

$$r_0^3 = r_1^3 + r_2^3 \quad (2.4)$$

Murray's law has been proven to be a fair approximation to the geometry of biological networks [53] [54]. In an extensive review of Murray's law, Sherman [55] compares studies by different authors on different arterial branching diameters. From this, it is concluded that their findings indicate agreement between the measurements and the predictions obtained by Murray's law. In addition, not only can Murray's law be related to branching in the vascular system, but also in other biological fluid transport systems, such as water transport in plants [56].

Murray's law has been comprehensively studied and is still extensively used in the design of vascular networks, for which AM techniques are considered convenient, since vessels and channels of circular cross-sectional shape can be easily achieved. However, complementary research work has been reported, where modified or generalised forms of the equation are proposed to overcome limitations mainly associated with network shape or those derived from the purpose of application. As an example, in the field of microfluidics it is not always possible to achieve such geometries, as the shapes are limited by the fabrication method. This typically involves planar construction (such as in photolithography or micro-machining), resulting in squared cross sections. Considering this, Emerson et al. [57] proposed a generalised Murray's law in which shear stress distribution in the network is used as a design rule. It is used in microfluidic structures that have symmetric branching and is applicable for channels with square, rectangular or trapezoidal cross sectional shapes. With a similar purpose, Stephenson et al. proposed their own generalised version of Murray's law that can be used for symmetric [58] and asymmetric [59] branching for channels of any given cross sectional shape, as it is based on the ratio of parent to daughter branch area.

Another generalisation of Murray's law was proposed by Zhou et al. [60] by considering the full tree structure as a whole, as opposed to defining the branching relationship at every single bifurcation. In this generalised law, they predict the correlation between a branch

diameter and the total length and volume of its corresponding subtree. In later research derived from this work, Kassab [61], extends the generalised law to include vascular tree morphology predictions for different organs and tissue. Another variation to Murray's law was proposed by Alarcon et al. [62] to include the effects of blood rheology, by including in the model complex parameters associated with the real behaviour of blood.

### 2.3.3 Optimisation principles

Following Murray's work, Zamir [63] published a series of work in which it is established that there are different optimality principles that dictate the branching angles of vessels. Zamir's optimality principles state that an arterial junction can be at an optimum state by different criteria:

1. When the total lumen surface of the arteries involved is minimum.
2. When the total lumen volume of the arteries involved is minimum.
3. When the power required for pumping blood through that junction is minimum.
4. When the total drag force acting on its lumen walls is minimum.

The principles of minimum surface and minimum volume predict that the optimum angles in the three modes depend only on the radii of the vessels. It must be noted that the principle of minimum blood volume had been previously proposed by Kamiya and Togawa [64], where the volume minimisation obeyed constraints for the pressure and flow rate at the origin and terminals. On the contrary, the principles of minimum power and minimum drag predict that they depend on the radii and on the flow in the vessels. However, it seems that all optimality principles give numerical results that suggest a parent-daughter branching relationship exponent of 3, in agreement with Murray's law [25].

According to Zamir, branching can only occur in three situations, which were called "branching modes". These situations are represented in Figure 2.3 and described below.

- Mode I: parent artery gives rise to a small branch and proceeds in its original course without change in direction.
- Mode II: parent artery undergoes a bifurcation at the junction, and its original course is discontinued at that point.

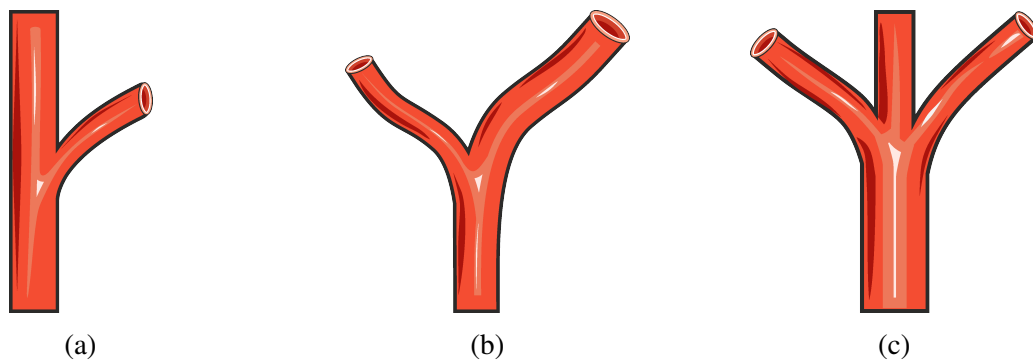


Fig. 2.3 Branching modes proposed by Zamir (adapted from [63]). (a) Mode I. (b) Mode II. (c) Mode III.

- Mode III: parent artery gives rise to two equal branches and also proceeds in its original course without a change in direction. This case is rare.

The geometry of a junction can be specified either by specifying the angles at which the centre lines meet, or by specifying the positions of the junction point and one end point of each vessel. The analysis of optimum branching geometry does not depend on the actual lengths of the vessels involved, but on the change in these lengths as a result of a change in branching angles.

In the cardiovascular system, the number of junctions is of the order of billions. The anatomy and function of particular tissues may influence the branching geometry of the smaller blood vessels serving these tissues. In [65], Zamir and Brown performed a series of measurements of arterial bifurcations from various parts of the cardiovascular network in the human body, and some from animals (rabbit and pig). As it can be observed in Figure 2.4, at each bifurcation, three diameter measurements were taken for each branch, and the central points of such measurements were joined (dashed line) in an attempt to create a centre line for the vessel. However, as the vessels presented a certain curvature, a tangential line to the curvature was drawn (solid line) and this was used as the centreline. The lines were then used to measure the branching angles. In the present work, the models are built following this convention, by considering the network base form as comprised of straight lines representing vessels, and the bifurcations consisting of the junction of the parent and daughter branches' centrelines.

Additional work by Zamir was published on studies of the relationship between vessel radius, flow and shear stress [66], arterial branching [67] [68], and the classification of arteries according to their function and zone (distributing and delivering vessels) [69]. Several

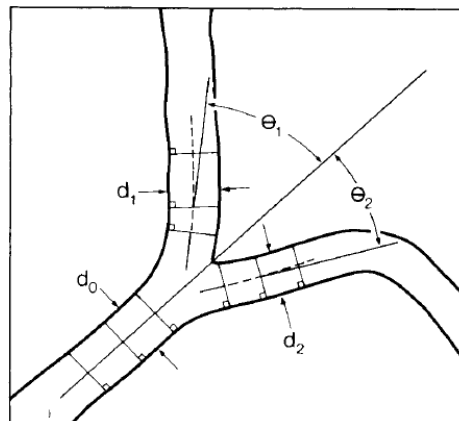


Fig. 2.4 Geometrical structure of arterial bifurcations, as measured by Zamir and Brown. Image source: [65]

other authors have studied or reviewed a diversity of optimisation principles involved in the vasculature [70], particularly in the branching angles [71–73] and for applications including fluidic network design [74–76].

Razavi et al. [72] investigated the effect of wall shear stress (WSS) distribution on the optimal design of vascular networks by establishing a relationship linking the branching angle to the ratio of WSS of parent to daughter vessels. A constant WSS in parent and daughter vessels was found to produce the minimum flow resistance and energy loss. A numerical simulation of the model showed that flow resistance is decreased at the optimal bifurcation angle. Khamassi et al. [73] investigated the correlation between WSS in a vascular bifurcation and two local parameters (asymmetry ratio and bifurcation angle). The models included rigid and elastic vessels for comparison. Among their findings, they established that for an optimal design, vessel elasticity has a major influence. For studies of rigid vessels the optimum geometry is a symmetrical bifurcation with the branching angle as small as possible. These studies are focused on the WSS to achieve geometrical optimisation on individual bifurcations. However, it must be noted that at different scales, the vascular system seems to have different optimisation principles associated with them and the use of a specific principle in the design of a vascular network will depend on the application and requirements of the system. In addition, the studies are carried out using single phase fluids. The use of multi-phase fluids (such as blood) is still a challenge and could help in understanding the cause of some pathological conditions such as platelet adhesion.

The study of flow in vascular networks can also benefit other areas of research such as fluidic network design, as channels are typically fabricated on a similar scale as the small

arteries and arterioles and an optimal branching design would improve their performance. In [74], different geometries of microchannels for cooling applications were analysed. Results indicated that smaller bifurcation angles are preferred in tree-shaped cooling networks, as larger angles cause an increased pressure drop across the network and deteriorate the flow field. In addition, the global distribution of the networks must also be considered, as different zones could have different cooling needs. This approach could be applied in the design of vascular systems, where different organs require different percentages of the total cardiac output, with the liver requiring the largest supply (25%) [77].

## 2.4 Considerations in the design of vascular networks

It has been stated previously in Chapter 1 that achieving vascularisation is a key challenge in tissue engineering. When designing a vascular construct it is essential that the requirements of every cell in the tissue are fulfilled by ensuring the proximity of a network vessel. For the adequate distribution of such vascular network, the use of design rules or principles that are in accordance with the physiological laws of circulation is necessary. Hoganson et al. [78] outlined a set of seven biomimetic principles to be established as the major guiding technical design considerations in the development of branching vascular networks for tissue engineering applications. These principles are based on the physiological laws studied above, and can be summarised as:

1. Defined relationship between parent and daughter diameters:  
From Murray's Law, the relationship  $r_0^3 = r_1^3 + r_2^3$  holds for symmetric and asymmetric relations. It was based on the principle of minimum work required to achieve flow through a network. There is uniform shear stress through the network.
2. Physiological branching angle:  
Bifurcation angle of vessels in the body is dictated by optimality principles. Bifurcation angles are a central design feature of natural blood vessels to achieve uniform flow at the site of bifurcations.
3. Biomimetic vessel length:  
Smaller diameter vessels have shorter lengths. Diameter-to-length relationship may minimise shear stress disturbances in the flow path.
4. 1:1 aspect ratio for all vascular channels:  
Width to height aspect ratio. In the case of rectangular microfluidic channels, 1:1

aspect ratio is desirable to achieve more uniform flow at the bifurcations, minimising flow disturbances.

5. Venous scaling:

The decrease in flow resistance is achieved by an increase in vascular diameter.

6. Uniform flow at bifurcations:

Bifurcations are principal sites for disturbances in the arterial system. Uniform flow must be achieved within a narrow range. This is a critical design criteria that must be met to minimise platelet activation.

7. Physiological shear stress:

Areas of high shear stress can induce platelet activation and adherence, which may lead to the formation of thrombus. Areas of low shear stress and flow velocity may also lead to the formation of thrombus. Uniform shear stress should be maintained within a narrow range throughout the vascular network.

Two parameters to consider in the design of vascular networks, although not listed by Hoganson et al. [78] as principles but equally important, are the pressure and flow distributions across the network. Equal flow and pressure values at all terminal outlets of a branching network are design constraints used by several authors when applying the principle of minimum blood volume for the optimisation of a network, to ensure a uniform blood supply for the tissue [79–85]. The use of these design principles is encouraged when designing a branching vascular network, although adjustments could be necessary to achieve the desired network architecture for a particular application.

## 2.5 Conclusions

This chapter has presented a summary of the physiological laws involved in the blood circulation, as understanding the basic principles is necessary for the design of functional vasculature. One key aspect to consider when designing artificial tissue constructs is the oxygen diffusion limit of the vessels and the inter-capillary distance in real vascular networks. In the absence of a proper vascular system that can deliver nutrients and oxygen to all the cells, necrotic regions may occur, leading to the eventual death of all cells in the tissue. Thus, any good design for a vascular network should ensure that both arterial and venous trees have branches that cover the entire volume of perfusion.

In the present work, Poiseuille's law is used, for which the following assumptions are fundamental [46]: i) laminar, steady flow (not pulsatile) in which the velocity at the wall is zero (no slip condition); ii) blood is assumed a Newtonian fluid, in which the viscosity is constant; iii) each vessel is regarded as a straight stiff tube of uniform radius. Poiseuille's law indicates that the radius is the most effective parameter that controls the blood flow. For a given pressure drop, a change of 1% in vessel radius will produce a 4% change in blood flow and vice versa. Thus, an effective way of controlling blood pressure is by altering a vessel's radius.

Shear stress is an important parameter in the study of blood flow. Abnormal levels can lead to the development of pathologies (e.g. atherosclerosis), thus it is clinically relevant. Using AM, 3D model comparisons can be carried out between healthy and pathological conditions of the vasculature.

Although the studied optimisation approaches are widely accepted and used for the design of vascular networks, they certainly have some limitations. For instance, Murray's law can only be applied to branching systems under laminar flow conditions. Therefore, only in vessels within an acceptable diameter range<sup>4</sup>, laminar flow could be assumed and therefore could be accurately modelled using Murray's law. In addition, it was noted that the majority of the research work on the design and computer simulation of vascular networks is based on the principle of minimum blood volume. Using this principle is convenient because, from a perspective of cost optimisation, the metabolic cost of blood as a substance is high and must be minimised [64]. However, there is little work using other optimality principles (e.g. minimum lumen surface, minimum power, minimum wall shear stress). This could be a potential area to explore, by creating vascular models using different optimisation principles and comparing their performance using computer simulations.

In order to achieve optimisation of a vascular network, vessel branching architecture is critical. A brief review on research work in this area has been presented, where the focus was the study of the effect of WSS on vascular branching. While understanding the behaviour at single bifurcations is crucial, it is also important to study branching in the vasculature either as a whole or organ-specific branching architecture.

Most of the work studied here focuses mainly on the geometric aspect of optimisation of vascular networks. However, there is a need for more realistic models that take into account

---

<sup>4</sup>According to Sayed and Shirani [72], Murray's law seems appropriate in vessels of size between 50  $\mu\text{m}$  and 500  $\mu\text{m}$

other physiological phenomena. For example, it could include the effect of vasculogenesis and angiogenesis (i.e. vascular system growth), which could potentially be dictated by the needs of the tissue. Similarly, the spatial distribution of vessels is another key to produce a realistic vascular model. As noted by Zamir [69] when observing the branching vessels in the heart, there are vessels with a distributing function which convey blood to the periphery of myocardial zones, and inside these zones there are vessels with the actual function of delivering blood to the tissue. The observed branching architecture is different for these two types of vessels, as the delivering vessels have a more profuse branching and are shorter. This could indicate that there is an optimal combination of distributing and delivering vessels for every organ to ensure its supply.

The applicability of the physiological laws in vascular designs for AM has been discussed. From the perspective of a multi-scale hierarchical vasculature, and considering that the physiological laws (i.e. Murray's law and Poiseuille's law assuming Newtonian flow) can be used in channels of approximately the size of large vessels ( $>200\ \mu\text{m}$ ), a versatile AM technique that allows the fabrication of models with feature sizes in the order of hundreds of micrometers to a few millimetres should be considered, such as inkjet printing.

Physiological factors are extensively used in the computational simulation of arterial tree growth. Having completed this brief review as a basis, the study of algorithms for the development of vascular networks was carried out and is presented in the next chapter.

# Chapter 3

## Vascular tree modelling and fabrication: review

### 3.1 Overview

Chapter 2 presented a brief introduction to the physiology of vascular networks and the haemodynamics of blood circulation, which serve as a basis for the design of vascular networks. These design principles for vascular physiology are extensively used in the computational simulation of arterial trees, which has the aim of simulating realistic vascular structures for a variety of purposes. Section 3.2 will present a diversity of algorithms from different authors for the simulation of arterial trees. These algorithms can potentially be used for 3D modelling of vascular networks.

On the other hand, there has been extensive research in the field of tissue engineering regarding vascularisation, with the aim of artificially engineering fully vascularised tissue constructs. Section 3.3 will present a brief summary of the current techniques used in tissue engineering for attempting the production of vascularised tissue structures.

Considering that the current fabrication methods for vascularisation typically involve additive manufacturing, it would be advantageous to use algorithmically generated vascular network models that can be exported for use in AM, as a novel vascularisation approach. Thus, in Section 3.4 it is discussed how 3D models can be used in AM technologies to solve some of the main challenges from the current vascularisation techniques.

## 3.2 Vascular tree modelling algorithms

The aim of the present work is to construct vascular network structures in a suitable environment that would allow to export into an STL format for use in additive manufacturing techniques. In order to automatically construct the structures with an iterative method, the development of an algorithm is essential. In the past decades extensive research has been done on the computational bio-simulation of arterial tree growth. Different vascular models have been proposed, which can be categorised according to purpose, organ of interest, physiological relevance, optimisation principle it serves, or method of construction.

Although there is a diversity of models, the focus of the present review is on algorithms that produce three-dimensional vascular structures with a realistic architecture that is intended to mimic the natural hierarchical branching vasculature in the human body. Despite the fact that the models have different methods and input variables, the vast majority of them use the approach of physiological law fulfilment and minimisation of a cost function (which in most cases is the intra-vascular blood volume) as design constraints. In this section, a brief description of the most relevant algorithms that have been developed over the past 25 years is presented.

Table 3.1 shows a summary of the main features of the algorithms described in this section. In the table, the column titled "Method" represents the approach for the development of the algorithm. "Optimality criteria" shows the parameter that the algorithm seeks to minimise in accordance with an optimality principle. "Network/Tree" is to define if the method produces single vascular trees or a full vascular network with two interconnected trees. "Construction environment" shows the development software or tools used to program the algorithm and/or to produce the visual representation of the models. The column titled "Assumptions" describes the main physiological constraints used in the algorithm. Finally, "Applications" describes the main purpose for which the algorithm was developed.

Overall, one of the most commonly accepted methods for the simulation of vascular trees is Constrained Constructive Optimisation (CCO). It is the first algorithm in the table and was developed by Schreiner [86]. CCO is a method to simulate the generation of arterial tree models by connecting a given number of points within the area of interest to the tree by successively adding branches, while obeying a set of constraints that represent physiological characteristics, such as a) equal pressure and flow values at all the terminal points; and b) a bifurcation rule that sets the relationship between the radii of each branch and its daughter branches. The model uses Poiseuille's law of flow [31], which assumes a laminar flow in

incompressible Newtonian fluids. A further optimisation method was developed by Schreiner and Buxbaum [87] to optimise the tree geometrically and topologically, both achieved by minimising a target function: total blood volume. The result is a binary branching tree that extends within a specified circular area (Figure 3.1).

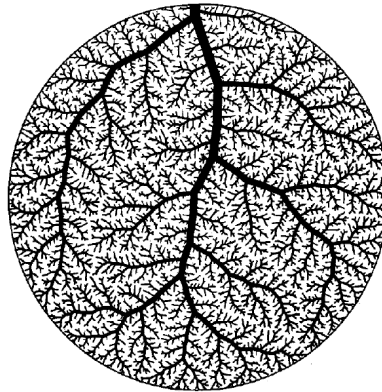


Fig. 3.1 Schreiner's arterial tree model with 4000 terminal points. Source:[87]

Based on Schreiner's work, Karch [88] extended the CCO method to three dimensions to cover a spherical volume rather than a circular area, and included terminal flow variability in the model. As in Schreiner's model, Karch's CCO method is based on a set of assumptions. These include: (i) steady state laminar flow, (ii) blood as homogeneous Newtonian fluid, (iii) a set of physiological constraints regarding pressures and flows, and (iv) a bifurcation law to define the relationship between parent and daughter branches. The models are visually represented using image-based direct volume rendering, as seen in Figure 3.2(a). Later, based on the same principle, a variation of the method was implemented for the staged growth of arterial tree models [79]. In this new model, the growth is restricted by domains in the volume given by a time-dependent probability density function, allowing the positioning of the main branches of the tree as convenient (see Figure 3.2(b)). The model uses simple shapes as rectangles, triangles and circles to define the areas and volumes to perfuse, therefore, anatomical shapes such as organs are not modelled.

Table 3.1 Summary of arterial tree growth algorithms

| Ref.                   | Method  | Optimality criteria       | Network/ Tree                            | Construction environment     | Assumptions   | Applications   |
|------------------------|---|---------------------------|--|------------------------------|---|--|
| [86], [87], [88], [79] | CCO/<br>Staged<br>growth                                | Minimum<br>volume         | Single<br>tree                           | Image-based<br>rendering     | - Laminar flow<br>- Omits resistance due to branching<br>- Blood as Newtonian fluid ( $\mu = \text{constant}$ ) | To produce realistic models of arterial trees for sub-endocardium, sub-epicardium.                   |
| [80], [81], [89], [90] | Iterative<br>growth<br>by needs<br>of growing<br>tissue | Minimum<br>volume         | Network                                  | C++                          | - Blood as Newtonian fluid<br>- Flow conservation<br>- Equal terminal flow and pressure                         | To simulate development and pathology of vascular systems in abdominal organs.                       |
| [91]                   | RWA<br>(growth<br>by oxygen<br>demand)                  | Not<br>specified          | Single<br>trees/<br>Capillary<br>network | C++                          | - Vessels as straight elastic pipes<br>- Fåhræus-Lindqvist effect   | To obtain realistic models of vasculature for surgical simulations.                                  |
| [92]                   | GCO   | Minimum<br>volume         | Single<br>tree                           | MeVisLab                     | - Laminar flow<br>- Blood as Newtonian fluid<br>- Omits effect of bifurcation and vessel curvature              | To obtain better vascular models for surgery planning and to assess vascular image analysis methods. |
| [93], [94]             | Algorithms<br>for<br>macro/<br>micro<br>vessels         | Minimal<br>energy<br>loss | Single<br>tree                           | Swept<br>Volume<br>Modelling | - Blood as Newtonian fluid<br>-Laminar flow<br>- Murray's law   | Modelling vascular trees for use in computer-aided TE and surgical planning.                         |
| [95]                   | Improved<br>L-<br>systems                               | Minimum<br>volume         | Single<br>tree                           | Not specified                | - Flow conservation<br>- Murray's law<br>- Branching angles rule  | Generation of realistic blood vessels for surgery simulators.  |

|            |                                       |  |                          |   |   |  |
|------------|---------------------------------------|--|--------------------------|---|---|--|
| [82], [83] | CCO<br>volume de-<br>mand)            | Minimum<br>volume<br>(oxygen<br>de-<br>mand) | Single<br>tree           | MIP                                       | - Flow conservation<br>- Equal terminal flow and pressure<br>- Murray's law<br>- Blood as Newtonian fluid | To validate vasculature segmentation algorithms.   |
| [96], [97] | Iterative tree construction algorithm | Minimum building material                    | Single tree              | Not specified                             | - Vessels as rigid cylindrical tubes<br>- Tissue assumed homogeneous<br>- Laminar flow                    | Validation of segmentation and reconstruction of arterial trees, and understanding of normal and pathologic vasculature. |
| [98]       | Karch's algorithm                     | Minimum volume                               | Single tree              | 3D visualization by raster images and MIP | - Laminar flow<br>- Omits resistance due to branching<br>- Blood as Newtonian fluid                       | Demonstrate relationships between physical parameters of blood vessels and numerical parameters.                         |
| [84], [99] | Improved CCO                          | Minimum intra-vascular volume                | Independent trees        | Not specified                             | - Equal terminal flow<br>- Laminar flow<br>- Fåhræus-Lindqvist effect                                     | To extend measured vascular networks by more details than imaging data.  |
| [100]      | L-systems                             | Not specified                                | Single tree              | MIP                                       | - Stochastic and parametric rules for L-systems   | To validate vessel segmentation techniques.  |
| [85]       | CCO + Delunay triangulation           | Minimum volume                               | Network with capillaries | Not specified                             | - Equal terminal flow.<br>- constraints to avoid overlap  | For the simulation of cerebral multi-scale vascular trees.   |
| [101]      | ACCO                                  | Minimum volume                               | Network                  | C#  | - Laminar flow<br>- Omits resistance due to branching<br>- Blood as Newtonian fluid                       | For 3D printing of vascular networks in tissue engineering.  |

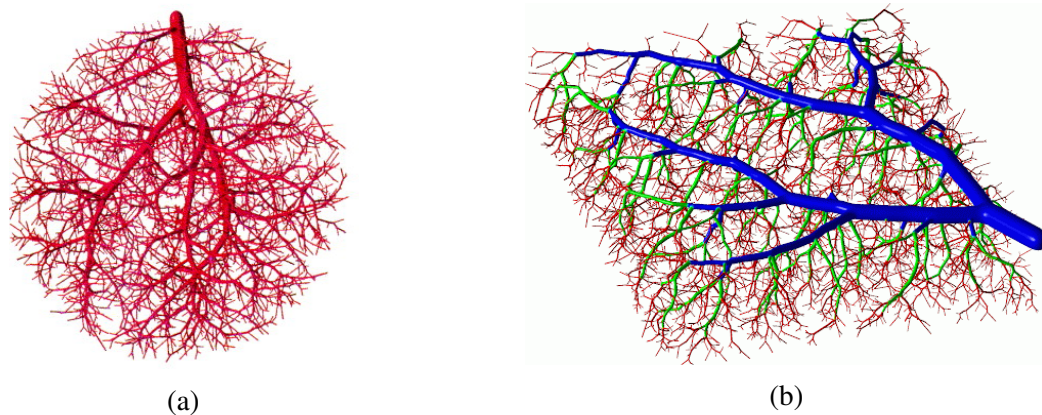


Fig. 3.2 Karch's models by CCO. (a) Tree with 4000 terminals by CCO (Image source: [88]). (b) Tree with 6000 terminals by CCO and staged growth (Image source: [79]).

Bezy-Wendling and Bruno [80] developed a three-dimensional dynamic vascular tree model which grows in response to the needs of the surrounding tissue, within a defined 3D volume which simulates an organ shape. The model growth depends on a set of physiological constraints related to the pressure and flow in the tree and the law of matter preservation, as well as anatomical constraints that define the shape of the tree as it grows. The optimality criterion that is fulfilled is minimisation of total blood volume in the tree. Later, in [102], changes were introduced in the model to simulate structural and geometrical variations in the tree by simulating diverse changes such as cell density, cell properties (in the simulated cells) and blood flow. By changing these properties, the model allows the simulation of pathological conditions such as hyper-vascularisation (tumour).

Continuing Bezy-Wendling and Rolland's work, Kretowski et al.[81] developed an algorithm for fast updating of the vascular trees, which replaced the original method. The fast updating method avoids repeating operations at all the nodes in the sub-trees during the tree growth process by storing the relevant coefficient values at the root nodes of the sub-trees, and after the tree is finished, the stored information is processed at once. The concept of a "macro-cell" is introduced, representing a small cluster of capillaries, and has specific properties to that small volume of tissue. Later, Kretowski et al. [89] presented the modelling of two vascular trees connected at the macro-cell level, to simulate a complete vascular network. The model finds the optimal geometry of the network by creating candidate vessels from each tree for the connection of each macro-cell. The candidate vessel that provides the minimum volume and that is not in collision with the opposite tree is selected as a permanent vessel. A collision resolution method is proposed, which involves switching to the next pair of candidate vessels with the smallest volume until no collision is found, or elimination of

the macro-cell if no suitable configuration was found. The model was used to simulate the growth of liver vascular trees for medical image analysis applications. In [90] the model was used to simulate a kidney vascular network (arterial and venous trees) and hepatic vascular network constituted by three trees (hepatic artery, hepatic vein, portal vein) in normal and pathological conditions (see Figure 3.3).

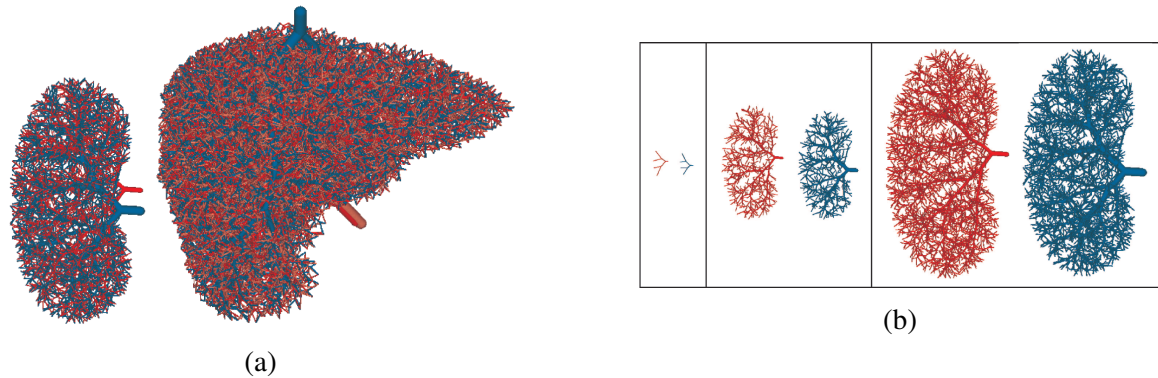


Fig. 3.3 Kretowski's models. (a) Full vascular network structures of kidney and liver. (b) Growth process of arterial and venous trees of kidney, shown separately. (Images source: [90]).

Szczerba and Székely [91] proposed an algorithm for the simulation of vascular growth that is mainly comprised of two parts: the creation of a preliminary capillary bed in the simulated tissue, and the growth of vessels in accordance with physiological and haemodynamic rules. The model, which is based on the random walk algorithm (RWA), considers biophysical operations such as oxygen demand of tissue, flow and pressure in vessels (given by Poiseuille's law), vessel wall tension, shear stress and oxygen transport. Examples of the structures generated with the code are shown in Figure 3.4. The model was created for surgical simulation purposes.

Georg et al. [92] developed a model for the construction of macroscopic vascular structures with a global optimisation method, based on CCO, which they call Global Constructive Optimisation (GCO). The model uses direct optimisation of a fully grown tree, as opposed to simulating tree growth. Optimality criteria and physiological constraints are established, such as Poiseuille's law of flow and the principle of minimum intravascular volume. A cost function is defined, that minimises the volume. The algorithm consists of a local optimisation loop for the minimisation of the cost function and fulfilment of constraints, and an outer loop that achieves global optimisation. The GCO method iterates using the data of previously generated sub-optimal trees to optimise the new tree, until an optimal result is achieved. The

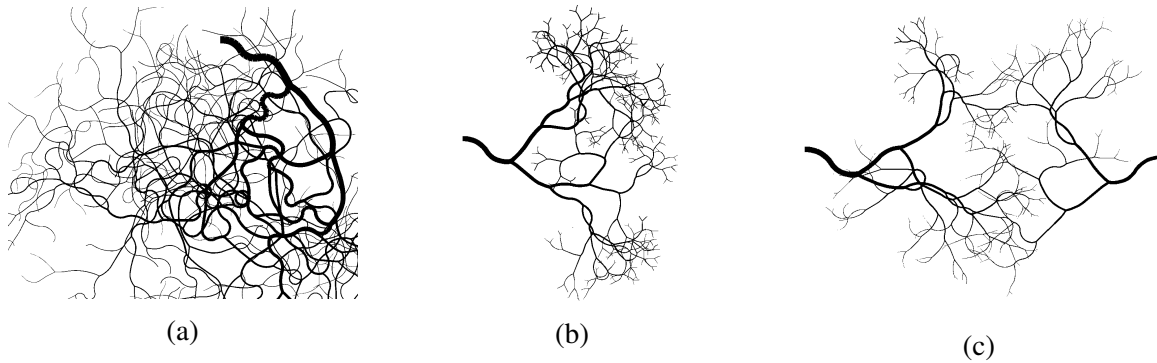


Fig. 3.4 Examples of structures generated with Szczerba's code. (Image source: [91]).

model presents single trees, but it considers the possibility of creating a vascular network by creating two trees which are defined by the same set of input nodes, however, the challenges of doing this (collisions between the trees and the inconsistency on pressure drops) are not addressed in the model. The nodes of the tree are provided by the user, and can be obtained from medical imaging sources. Figure 3.5 shows vascular tree models grown by GCO in a liver-shaped volume.

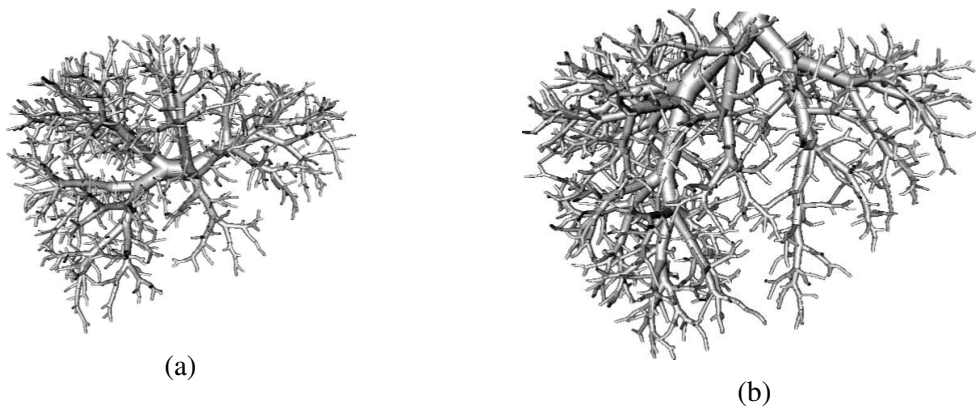


Fig. 3.5 Models generated with Georg's approach within a liver-shaped volume. The differences between the models are the initial root points and terminal points position. (a) Tree simulating a portal vein. (b) Tree simulating a hepatic vein. (Images source: [92]).

Li et al.[93] [94] developed an algorithm for the feature-based modelling of vascular trees for application in computer-aided tissue engineering. The approach creates two versions of the vascular model: a macro-scale model that consists of coarse approximate morphology of the structure which can be based on medical images, and a micro-scale model that is based on the macro-scale model and has a detailed structure geometry and physiological properties. The micro-scale model is constrained by physiological principles such as Poiseuille's law

of flow and Murray's law. For the representation of micro-scale models with the swept volume method, Non-uniform rational basis spline (NURBS) curves are used for the 3D CAD representation of the model. Figure 3.6 shows a swept volume model for a tree with 70 terminal nodes.

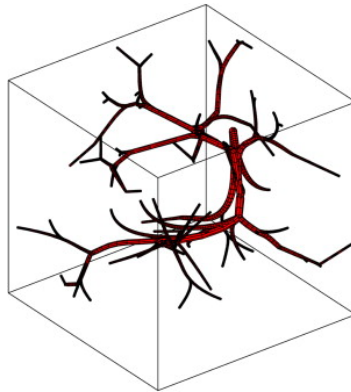


Fig. 3.6 Li's model of vascular tree with swept volumes. The tree has 70 terminal nodes ("leaves") (Images source: [93]).

Liu et al.[95] proposed a model based on L-systems (originated from Lindenmayer's work [103]). The model considers some physiological constraints such as flow conservation, equal shear stress between blood and vessel walls (which implies a bifurcation exponent of 3, or Murray's law of bifurcation), ratio of the length of parent-daughter branches and rules for branching angles. Figure 3.7 shows a simulated model for the human renal artery using stochastic parameter L-systems.

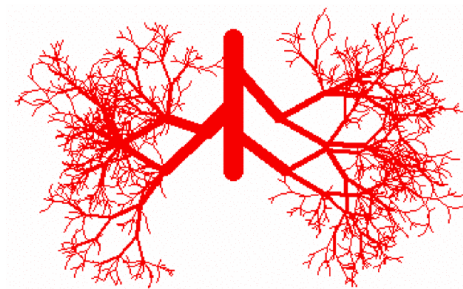


Fig. 3.7 Liu's model of human renal artery. (Images source: [95]).

Hamarneh and Jassi [82] [83] developed an open source software package (VascuSynth) for the generation of volumetric images of vascular tree structures. The algorithm is based on Karch's CCO approach [88], explained previously. It consists of the iterative growth

of a tree by connecting new terminal points, within a given volume. The model considers physiological constraints including flow conservation, the bifurcations rule with a variable exponent and equal terminal flow and pressure. The target function is proportional to the volume of the tree, therefore, minimisation of the volume is sought. The algorithm simulates tree growth given by an oxygen demand map for the available points in the volume. Figure 3.8 shows an example of vascular tree constructed with VascuSynth using rigid branches and the same tree with curved non-rigid branches. The tree models are used mainly for the validation of medical image analysis and segmentation.

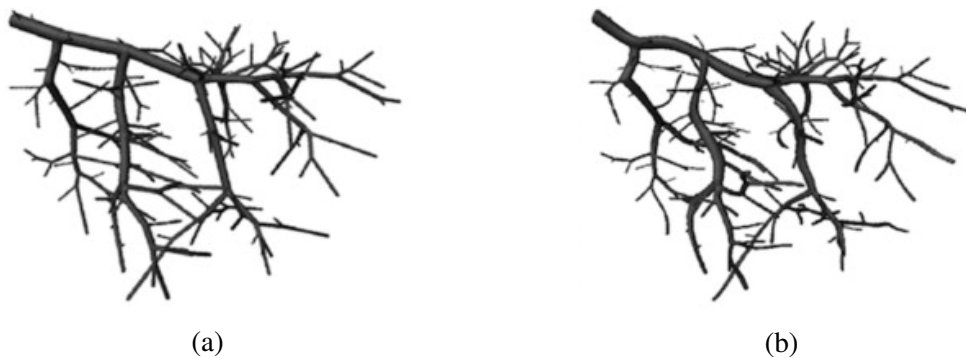


Fig. 3.8 Models generated with VascuSynth. (a) Vascular tree with rigid branches. (b) Vascular tree with curved vasculature using B-splines. (Images source: [82]).

Schneider et al. [96] [97] developed a model for the simulation of multi-scale arterial tree growth, including capillaries. In contrast with the previous methods, this model does not consider the haemodynamic rules of blood flow as constraints and is purely based on structural properties and physiological principles related to angiogenesis (formation of new vessels). The model assumes rigid cylindrical tubes for the vessels and binary branching with Murray's law of bifurcations. The simulation of growth within the tissue is given by simulating oxygen demand and angiogenesis factors (vascular endothelial growth factor, or VEGF). It is, therefore, possible to simulate pathological conditions such as hyper-vascularisation and increased demand of oxygen. Figure 3.9 shows a simulation of an arterial tree model using this approach.

Kociński et al. [98] created a model based on Karch's approach [88] for the simulation of vascular tree structures for image texture analysis purposes. The model fulfils the haemodynamic rules of blood flow and the main constraints of the algorithm are: the flow conservation principle, Poiseuille's law of flow and Murray's law of bifurcations. The tree vessels are represented by straight cylinders. The input parameters were varied in order to observe the

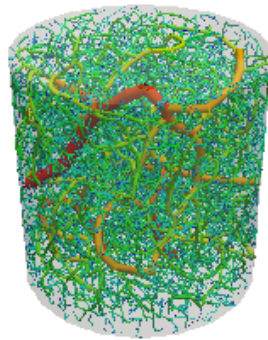


Fig. 3.9 Simulated model in cylindric volume under uniform metabolic conditions. Image source: [96].

effect in the image texture features. Viscosity was found to be one of the main parameters that substantially affects the vessel images. Figure 3.10 shows a simulated arterial tree with this approach.

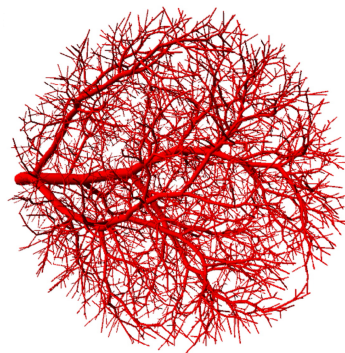


Fig. 3.10 Simulation of arterial tree in spherical volume with 4000 terminal points and nominal parameter values. Image source: [98].

Schwen and Preusser [84] present an improvement to the CCO method by calibrating the model using measured vascular network data from CT imaging. The model fulfils the physiological constraints associated with CCO and obeys the principle of minimum intravascular volume. The model considers Fåhræus-Lindqvist effect, in which constant viscosity is assumed for vessels  $>150 \mu\text{m}$ , and below this value viscosity is changing. The bifurcation nodes are optimised using a gradient descent method (a first-order optimisation algorithm to find the minimum of a function by taking steps proportional to the negative of the gradient of the function). The tree is generated within a defined 3D volume in accordance to the shape of the measured organ, in this case, the liver. Figure 3.11(a) shows a liver portal vein model using this approach. Later, Schwen et al. [99] extended the approach to

the modelling of rodent livers. Figure 3.11(b) shows the model of a mouse liver with two vascular trees representing the portal vein and hepatic vein (there is no connection at the end points). In both cases, the models were generated using base trees generated from their respective CT scan data sets.

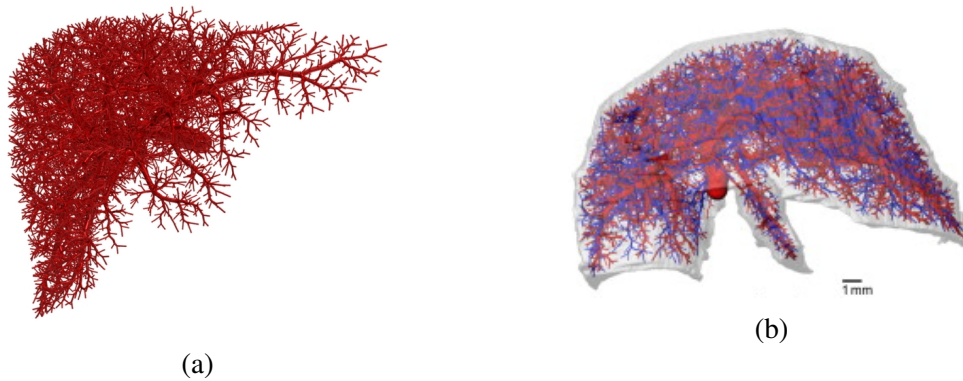


Fig. 3.11 Models generated with Schwen's approach. (a) Human liver vascular tree (portal vein) with 10,000 terminal nodes. Image source: [84]. (b) Mouse liver vascular trees (portal vein and hepatic vein) with 6,281 terminal nodes. Image source: [99].

Galarreta-Valverde et al. [100] proposed a method for the construction of synthetic vascular trees for the validation of segmentation algorithms. The proposed method is an extension to the traditional L-systems by adding stochastic and parametric rules to the model. This approach is similar to the work of Liu et al.[95], but the simulated model is extended to 3D with spatial constraints. It does not consider physiological constraints of blood circulation. When the tree node points are defined by L-systems, the tree skeleton is created using a modified version of Bresenham's line-drawing algorithm. B-Spline interpolation function are used to avoid sharp angles in the tree. Figure 3.12 shows a vascular model generated with this approach, within a simulated liver volume.

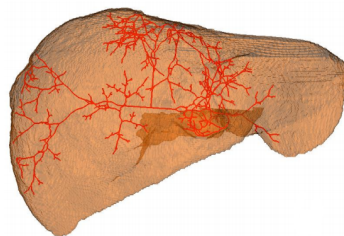


Fig. 3.12 Synthetic vessel structure generated with L-systems in a liver-shaped volume. Image source: [100].

Linninger et al. [85] proposed a model for the simulation of cerebral multi-scale vascular trees, particularly the microcirculation. 3D imaging techniques were used to generate a reconstruction of the pial arteries (intracranial vessels located on the surface of the brain). Using the reconstructed arterial trees as a backbone, penetrating arteries and arterioles are modelled using a vasculature growth algorithm based on CCO and is governed by the principle of minimum volume and the physiological constraints of blood flow. Under this approach, optimisation of the tree volume represents a 'non-linear constrained optimisation problem' (in which the objective function is non-linear and/or has non-linear constraints) and is given by the geometric optimisation of the bifurcation points. As segments are added to the tree, repeated solutions to the optimisation problem are required. For this purpose, non-linear constrained optimisation algorithms previously developed in their research group were used. For the creation of capillary beds, a method was implemented by dividing the volume with a mesh by Delaunay triangulation and using the corresponding Voronoi mesh (dual of the Delaunay mesh) to define the capillary segments as the edges of the Voronoi mesh. Figure 3.13 shows a subsection of the secondary cortex with multi-scale vasculature.

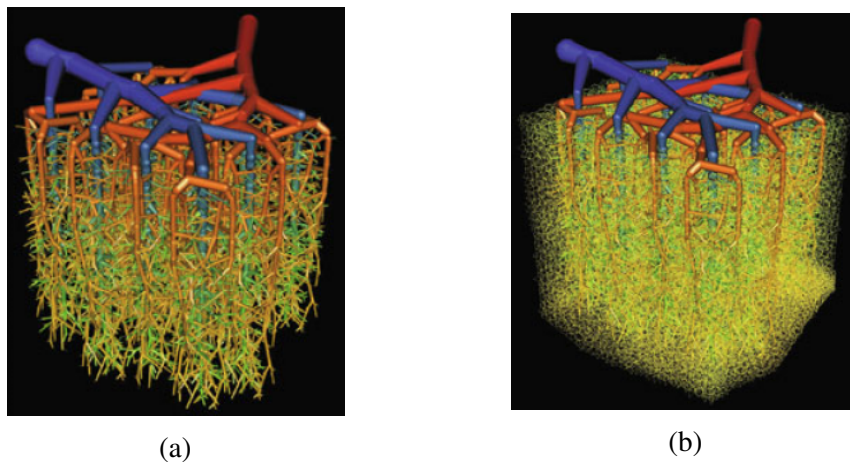


Fig. 3.13 Simulation of subsection of the cerebral secondary cortex with Linninger's approach. (a) Without capillary bed. (b) With capillary bed. (Images source: [85])

The final algorithm in Table 3.1 was developed within the Materials Engineering & Material-Tissue Interactions (MEMTI) research group as an extension to the algorithmic method here proposed. Guy et al. [101] propose an improved algorithm which has been denominated "Accelerated Constrained Constructive Optimisation" (ACCO) and is intended for the construction of vascular networks with the aim of maximising the volume of useful tissue (minimisation of network volume). The method is divided in three main stages of network development: 1) construction, 2) optimisation, and 3) collision resolution. Construction is the

process of adding new branches to the network by creating a new bifurcation to connect the new point. In order to select the best branch candidate for the new bifurcation, a new method is proposed, called "counted" selection process, where the tree is analysed in a downstream manner discarding groups of branches that are considered less suitable according to a set of rules. Optimisation is the process of finding the optimal position for each bifurcation node in terms of the minimisation of tree volume. There are 3 types of optimisation: i) accelerated incremental optimization, for optimising individual bifurcation nodes of a new branch, it is stated that the total volume downstream of a given branch can be expressed as a function of its effective length, therefore, allowing a faster calculation of the optimal bifurcation position; ii) batch optimisation, which is used in models with a large number of nodes (where the effect of moving a single bifurcation node is negligible), is a method that calculates an approximation to the gradient descent method (which is the simplest method of minimisation, but is computationally expensive to use for each bifurcation) and results in a faster calculation; and iii) initial bifurcation position, which is a method that calculates the optimal position of a bifurcation node upon its creation, based on a weighted arithmetic mean that uses the flow rate of the branches involved. Finally, collision resolution is a method to address the problem of colliding branches of opposite trees. It consists of three potential courses of action: i) inserting a transient node in the colliding branch and moving it to create a small deviation, ii) moving a bifurcation or transient node, or iii) removing a terminal branch where necessary. Collision resolution is based on the assumption that the branches are small relative to the volumes they serve. Therefore if a collision is detected, it can most likely be resolved by making small perturbations around the contact site, normal to the plane created by the intersecting branches. With this algorithm, it is possible to model complex arterio-venous structures with a large number of terminal points with a very efficient computing time (i.e. for trees of sizes where previous authors have reported days of computing, ACCO allows to construct in minutes). In addition, multiple interconnected vascular trees can be constructed within the given volume. Example of the vascular structures generated with ACCO are shown in Figure 3.14.

### 3.3 Fabrication of vascular structures

In the past decades, there has been extensive research in the field of Tissue Engineering regarding vascularisation, where the main aim is the creation of artificially engineered fully vascularised tissue constructs. There is particular focus on techniques involving bioprinter technologies [104] [105], especially for the bio-fabrication of vascularised tissue [10] [106–

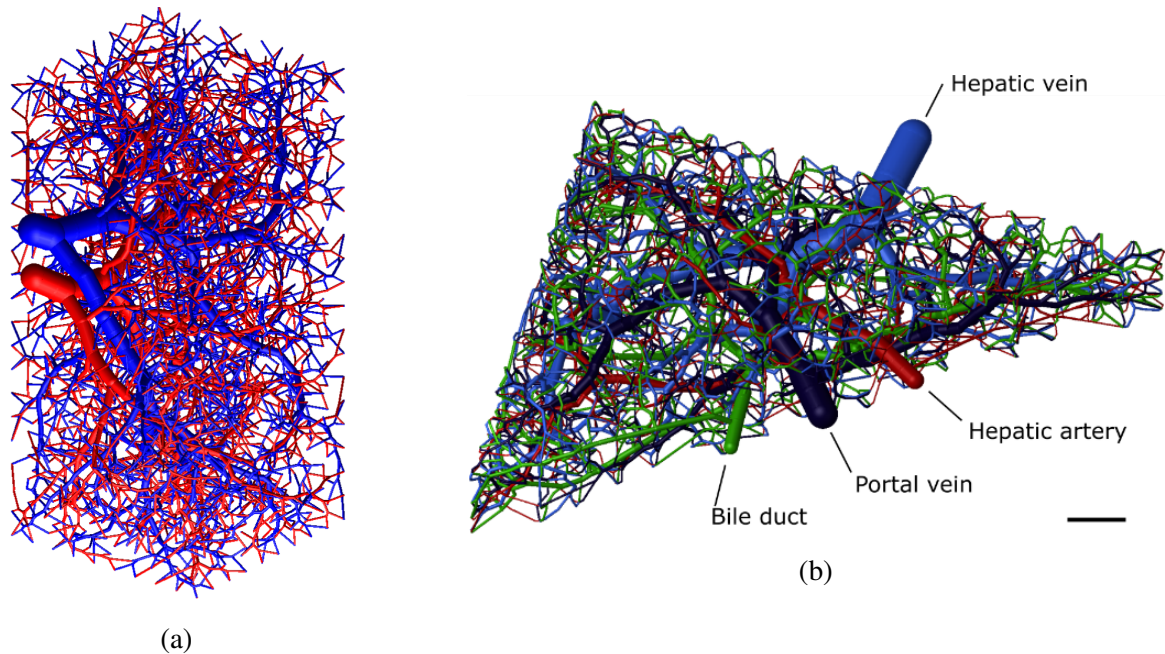


Fig. 3.14 Arterio-venous networks generated by ACCO. (a) Spacing between terminals is 5 mm, with 2000 terminals (1.95 seconds to produce). (b) 4-tree network with liver-like dimensions, 750 terminals spaced by 10 mm (1.22 seconds to produce). (Images source: [101])

108]. This section presents a brief review of the current techniques used for attempting the production of vascularised tissue or vascular networks embedded in relevant biologic materials.

From the Lewis research group in Harvard, there have been some relevant attempts at vascularised tissues. Wu et al. [12] presented a method for achieving omni-directional printing of vascular networks by using a direct ink writing technique that prints sacrificial ink filaments within a gel volume. This is depicted in Figure 3.15. The advantage of this method is the freedom of movement in the given 3D space, which enables the creation of complex vascular network structures inside the gel. However, after printing the ink, the structure requires chemical cross-linking, which means it is not possible to seed cells in the gel material from the beginning.

Kolesky et al. [109] presented a multi-material printing approach that allows the bio-printing of tissue that includes perfusable vasculature, two different types of cells and an Extra Cellular Matrix (ECM) by using different types of inks. To print the vasculature in different sizes, they modify the ink filament printing parameters such as pressure, speed

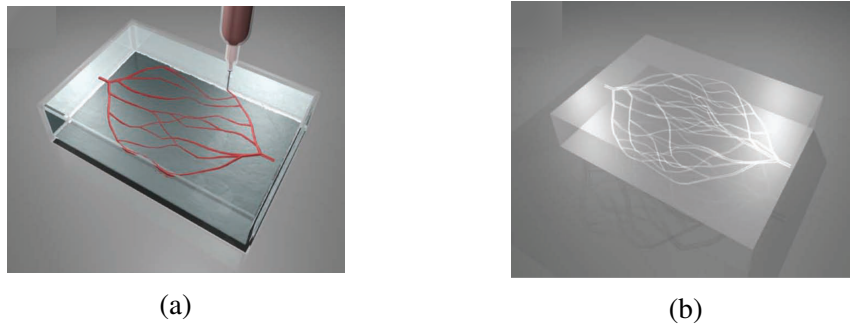


Fig. 3.15 Schematics of Wu's direct ink writing method for vascular networks. (a) Depiction of printing of sacrificial ink filaments into gel volume. (b) Finished model with embedded network after flushing of sacrificial ink. (Images source: [12])

or nozzle height. They present two models that have an embedded vascular network: one in 2D and one in 3D, and they are shown in Figure 3.16. The 2D vascular network design has a hierarchical branching structure, but the design is very simple and not physiologically relevant. The 3D network is comprised of sets of tubular channels of uniform diameter printed in layers and alternating the direction of printing. While the 2D and 3D structures might be functional, their shapes do not resemble physiological vasculature, and therefore are not ideal solutions. Later, in [11] Kolesky et al. extended their work by improving the process and the composition of the inks involved. With this approach, the creation of thick vascularised tissue constructs ( $\geq 1$  cm) is possible, ensuring as well cell viability over the span of several weeks. However, the vascular structure design, shown in Figure 3.17 is still formed by tubular channels and overall does not represent a physiological structure.

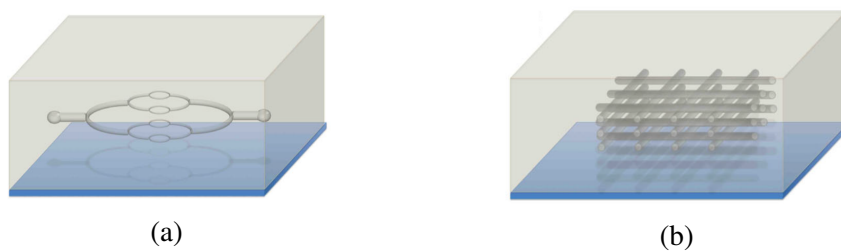


Fig. 3.16 Schematics of Kolesky's approach for vascular networks by sacrificial ink printing. (a) 2D network design. (b) 3D network design. (Images source: [109])

Huang et al. [110] achieved embedding of vascular-like tree structures in plastic materials by applying a high electric charge that vaporises and fractures the material into tree shapes. Although the tree structures look realistic in architecture (see Figure 3.18), this method is not reproducible due to the nature of the process. In addition, the end points of the trees are not

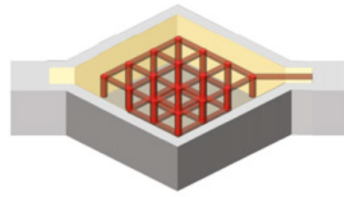


Fig. 3.17 Schematic of vascular network design from Kolesky's improved process. Image source: [11].

necessarily all connected to a branch of the opposite tree, therefore many dead ends occur, which is not desirable. The main limitation of this technique is the range of materials on which it can be successfully performed (i.e. it could not be applied for biological materials), and the lack of control over the shape and size of the tree branches.

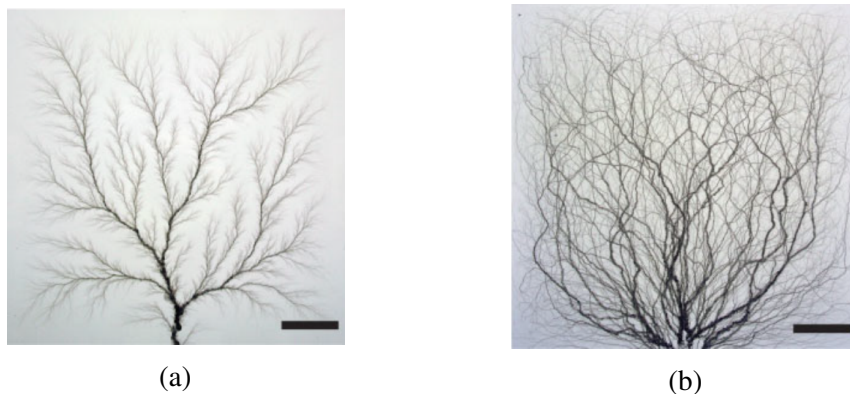


Fig. 3.18 Tree-shaped networks formed by Huang's method with two different techniques. (a) Tree generated by ground contact method, where a grounded electrode is in contact with the substrate surface. (b) Spontaneous discharge method, where a small defect is created on the substrate surface to act as a nucleation site for spontaneous energy release. (Images source: [110])

Miller et al. [6] proposed a method in which a carbohydrate glass sacrificial template is printed and used to produce tissue constructs with an embedded fluidic network. The template, which represents the vasculature of the tissue, is formed by interconnected vertical and horizontal cylindrical channels in a scaffold shape. The fabrication process is shown in Figure 3.19. The use of carbohydrate glass as a sacrificial material makes this process compatible with different cell types and extra cellular matrices. However it could be considered potentially negative for the cells due to cytotoxicity from the dissolution of the carbohydrate glass, and it requires a coating layer of poly (d-lactide-co-glycolide) (PDLGA) before casting

the ECM to avoid osmotic damage in the cells. In addition, the shape of the network is not representative of native tissue vasculature.

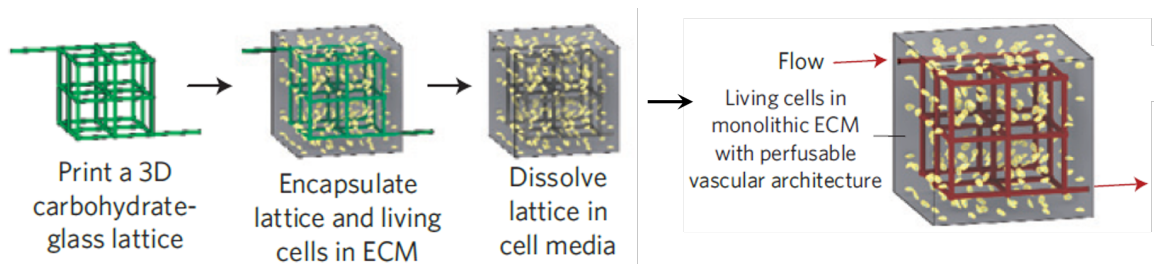


Fig. 3.19 Schematic of Miller's method for obtaining perfusable vascularised tissue. Image source: [6].

From the Khademhosseini group at the UCLA, Bertassoni et al. [111] reported a bio-printing approach using agarose as a template material for the fabrication of vascularised hydrogel constructs. Agarose fibers are printed in a predefined 3D architecture to form a network structure, simultaneously controlling the material dispensing speed and the motion of the X-Y-Z stages of the printer. Figure 3.20 shows two models printed with agarose fibres. A hydrogel is then cast over the printed agarose models, surrounding it completely. The hydrogel is photo polymerised using UV light and after this the agarose fibres can be easily removed by aspiration with vacuum or manually pulling them. The result is a hydrogel structure with an embedded network. While the process seems to have compatibility with diverse hydrogels and to be innocuous to cells, there are disadvantages. The fact that it is necessary to remove the solidified agarose fibres one by one probably means that the production of complex branching vascular structures is not possible. Also, the 3D network that is presented is in the shape of a lattice or scaffold, which is not in accordance with real vascular structures.

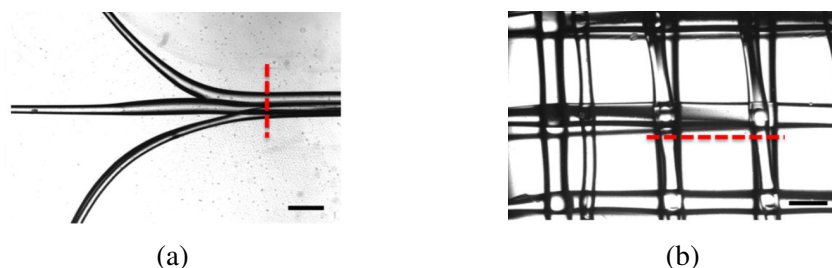


Fig. 3.20 Example of bio-printed agarose fibre networks created with Bertassoni's method. (a) Planar bifurcating design. (b) 3D lattice design. (Images source: [111])

Heintz [20] developed a novel method for the fabrication of microfluidic networks embedded in poly(ethylene glycol) diacrylate (PEGDA) hydrogels. The method combines a laser-based hydrogel degradation process with image-guide laser control and it can create complex 3D structures. Localised degradation in the hydrogels is achieved using a femtosecond pulsed laser focused through a water immersion objective. The degraded geometries are created by guiding the position of the laser within a region of interest given by a virtual mask. Such regions of interest can be created from complex 3D models generated by CAD software, as shown in Figure 3.21. This seems like a promising approach for the fabrication of micro-vasculature in engineered tissue given the high resolution of the process. However, for meso-scale vasculature it could require a much larger fabrication time. In addition, this is one of the processes where the seeding of cells needs to be done after the vasculature creation.

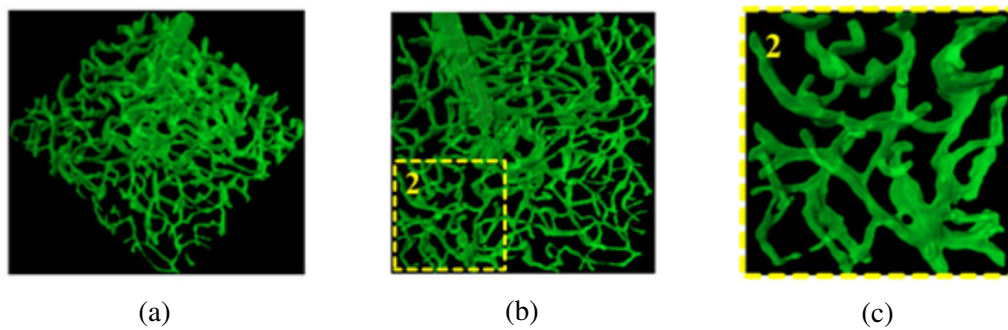


Fig. 3.21 Heintz's network model by femtosecond laser-based hydrogel degradation. (a) Biomimetic microfluidic network in a PEGDA hydrogel, with vasculature produced from a stack of cerebral cortex images. (b) Same model showing an inset. (c) Inset from (b). (Images source: [20])

Wang et al. [112] proposed a method for creating vascular networks in hydrogels by using a sodium alginate lattice as a sacrificial template. The template is fabricated using a patterned PDMS mould created by photo-lithography. After the sodium alginate solution is injected in the mould it is chemically cross-linked for stability. The alginate template is then encapsulated by a hydrogel and is later dissolved by injecting ethylene diamine tetra-acetic acid (EDTA). Figure 3.22 shows an alginate template and its corresponding network after dissolving the alginate. It is also reported that it is possible to stack multiple alginate template layers to form a multi-layer network. A disadvantage of this method is that the network shape is only planar and does not seem to be applicable for the creation of thicker 3D interconnected structures. Also, as with most of the methods, the seeding of cells in the model is done after the hydrogel is cross-linked.

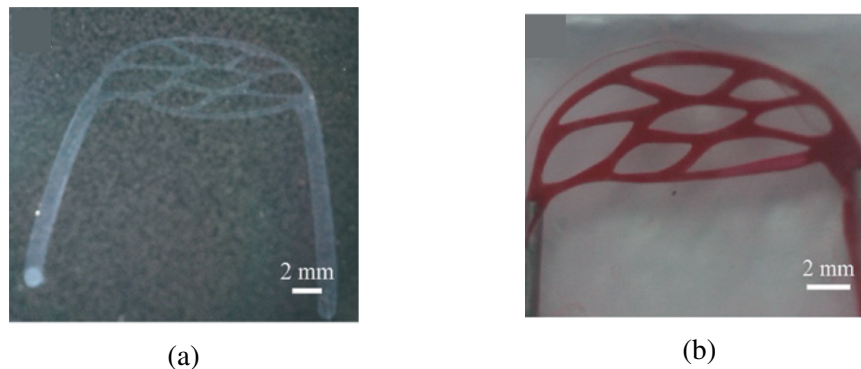


Fig. 3.22 Example of printed networks created with Wang's method. (a) Sodium alginate template. (b) Microfluidic network in gelatin hydrogel. (Images source: [112])

Morgan et al. [21] developed a protocol for the formation of 3D cell cultures which include perfusable endothelialised micro-vessels embedded in a hydrogel (type I collagen). A schematic illustration of the network is shown in Figure 3.23. For the fabrication of the vascular network a 3D model is created in a CAD software and used to fabricate a photo-lithographic plate (mask) as the first step in the micro-fabrication process. The main limitation of this approach is that the network can only be a planar representation with a simple 2D geometry, and that the channels produced by this method are limited to a rectangular cross section.

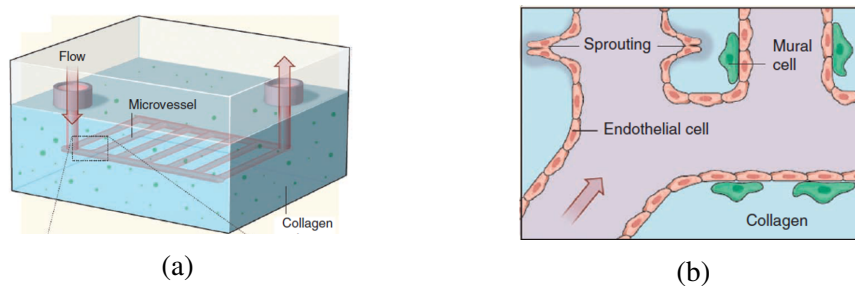


Fig. 3.23 Microfluidic networks created with Morgan's method. (a) Schematic of a microfluidic network in a cell-laden collagen construct. The network is coated with endothelial cells. (b) Inset of (a) showing angiogenic sprouting from the channel. (Images source: [21])

Hinton et al. [22] presented a 3D bioprinting technique, which they denominate "free-form reversible embedding of suspended hydrogels" (FRESH), for the creation of complex 3D structures by embedding a printed hydrogel ink into a gelatin hydrogel bath as a temporary support. A variety of hydrogel inks can be used in this technique, including alginate, fibrin, collagen and Matrigel. Bioprinting of CAD models is reported, including a section of the

right coronary artery vascular tree, which was printed in alginate as a hollow structure with a wall thickness of less than 1 mm and is shown in Figure 3.24. This seems like a promising technique for the fabrication of biological structures, however, construction of hydrogel structures with functional embedded networks to supply the full volume has not been demonstrated. In addition, the vessel diameters were in the order of millimetres, which limits its application to the larger vessels in the circulatory system, unless the technique is refined to obtain a higher resolution.

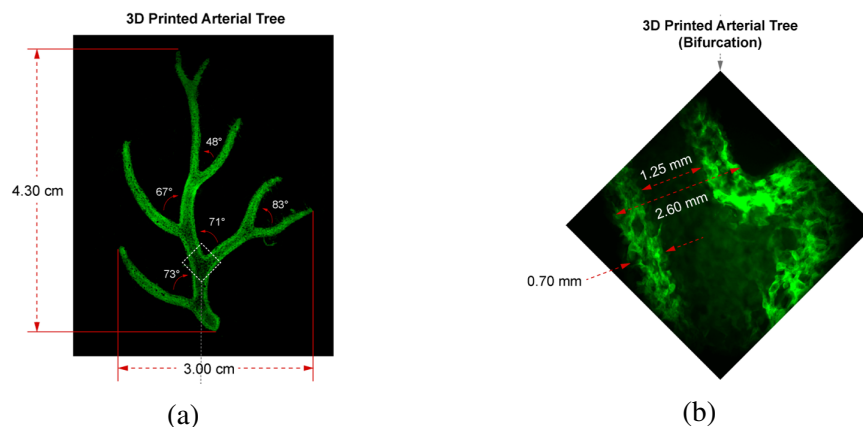


Fig. 3.24 Model of right coronary artery created by Hinton's technique. (a) Model printed in alginate with fluorescence. (b) Inset of (a) showing the internal wall at a bifurcation. (Images source: [22])

Justin et al. [13] developed a method for the production of a three-dimensional perfusable vascular network structure within a hydrogel. The 3D model of the network is fabricated by 3D printing using a thermoplastic material. The printed network model is embedded in a cast alginate gel inside a special chamber and subsequently the thermoplastic is dissolved, leaving the network shape embedded inside. The network is filled with gelatin to produce a solid temporary template and the alginate gel is removed. An ECM hydrogel is cast in the chamber to surround the gelatin model and the gelatin is later flushed out, leaving a fully perfusable network within the hydrogel. Figure 3.25 shows the model and the network embedded inside the alginate. This fabrication method is highly convenient, as it ensures the reproducibility of the models and it can be produced using different materials according to the intended application. One disadvantage in this approach is that the 3D model that was used was generated manually in a CAD software package and does not consider physiological flow constraints in its design. The main limitation of this method is the resolution of the 3D printer that can be used to print the required thermoplastic material, which currently is about 250  $\mu\text{m}$ .

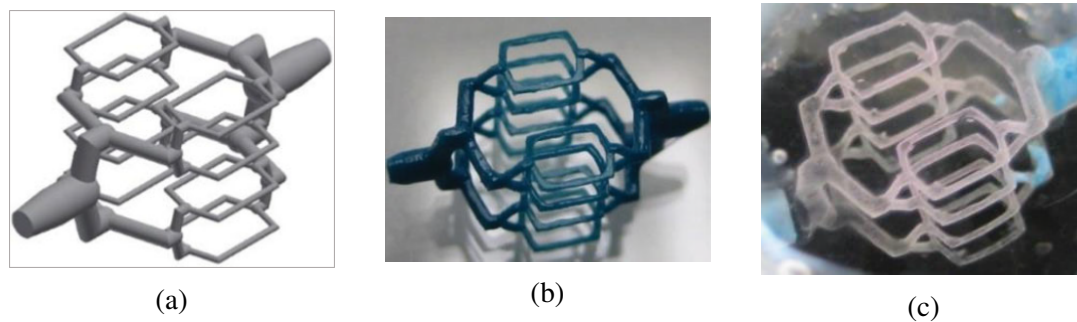


Fig. 3.25 Justin's network model by 3D printing of sacrificial thermoplastic model. (a) 3D model design of network for 3D printing. (b) 3D printed model in a thermoplastic material. (c) Embedded network in alginate gel. (Images source: [13])

### 3.4 Discussion

3D printing is one of the most investigated solid free-form fabrication techniques in tissue engineering, particularly in the production of scaffolds [14]. The majority of the current vascularisation approaches that produce relevant models (including those presented in Section 3.3) involve the use of a 3D printing-based technique either for the production of moulds, sacrificial template models, or for the direct printing (or bioprinting) of the structures. 3D printing is a versatile additive manufacturing technique that allows free-form fabrication of models in a three-dimensional space in a variety of materials, while ensuring high repeatability and reproducibility of the printed models. The advances in 3D bioprinting technologies show models with different feature sizes ranging from 1  $\mu\text{m}$  (which can be fabricated by emerging bioprinting technologies such as digital light processing (DLP) and multi-photon laser scanning) to 1 mm (using extrusion or laser based techniques) depending on the printed materials and the application for which they are intended [113]. It has been extensively used in the field of tissue engineering as it has a large range of applications, which include producing bulk structures (such as moulds and sacrificial pieces) and even functional structures such as cell-laden tissue scaffolds.

The vast majority of these models, however, focus on the functionality of the network and do not exhibit any physiological characteristics. The complex architecture of real vascular networks and the physiological principles that accompany them are typically disregarded (such as a multi-scale hierarchical branching distribution that obeys an optimality principle and blood flow circulation, as explained in Chapter 2).

On the other hand, regarding the vascular network models produced algorithmically described in Section 3.2, it is evident that most of the models are used for validation of segmentation techniques or surgery planning and simulation, however, none of them are used as the base for the fabrication of vascular structures in tissue engineering (with the exception of the algorithm developed by Guy et al. [101], which is an extension to the work here presented). Considering the advantages of potentially using physiologically relevant networks in vascularisation approaches, the present research proposes the use of algorithmically generated three-dimensional models of vascular structures, which can be exported as CAD models, for 3D printing-based processes.

In [30], automated generation for simple planar vascular designs has been developed for the ArtiVasc 3D Project, where the user introduces a few parameters and the models are produced accordingly by inkjet printing and stereolithography, and later combined with other techniques (multi-photon polymerisation and electrospinning) to produce vessels of smaller sizes in an attempt to create fully vascularised skin patches. The design of the artificial vascular vessels focuses on the bifurcation junctions, particularly in two key factors in the design (maximum junction curvature and bifurcation volume) [114]. They present a parametric map for the achievement of an optimal model. However, the manually generated design of the vascular model is planar and symmetrical, as seen in Figure 3.26.

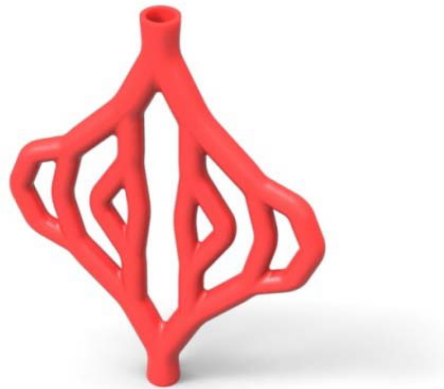


Fig. 3.26 Example of vessel design for ArtiVasc Project, by automatic generation. Image source:[30]

Apart from this method that uses a simple manually created network and the work of Guy et al. [101] (who successfully printed a 3D vascular network, shown in Figure 3.27), to the best of the author's knowledge there is no other previous approach in the field of

tissue vascularisation that combines the use of complex algorithmically generated vascular structures with 3D printing techniques for further use in tissue engineering applications.

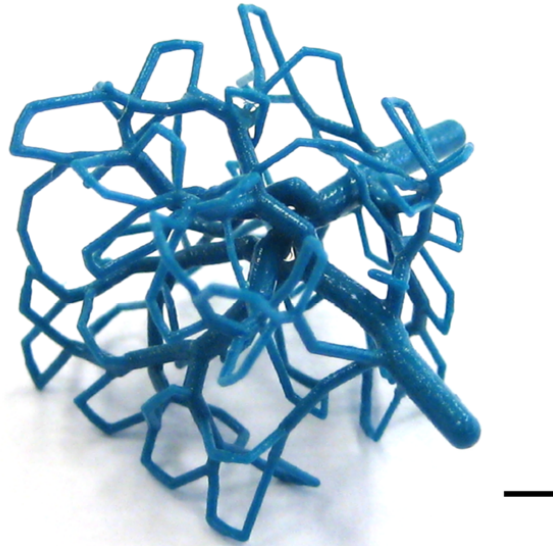


Fig. 3.27 Example of a successfully 3D printed model of a multi-level vascular network in a cubic volume with a minimum feature size of  $250\ \mu\text{m}$  (the smallest resolution of the current generation of printers), by Guy et al. Scale bar = 2.5 mm. Image source:[101]

From the fabrication approaches reviewed in Section 3.3, some of them have disadvantages in their processes. For example, there are approaches where the hydrogel is photo-polymerised and the cells need to be seeded in a subsequent step, causing a poor uniformity in the distribution within the ECM [6] [12] [20] [111] [112]. Therefore, a method where the cells are added in the hydrogel without the need of cross-linking is preferred. Also, in some approaches the use of certain materials as sacrificial templates (such as carbohydrate glass [6], and Pluronic F127 [11] [12] [109]), or harsh agents to dissolve the templates, may cause damage to the cells in the hydrogel as they have been reported to have a degree of toxicity [111] [115]. Thus, a method where the cells are not in direct contact with the initial sacrificial template is preferred. In some of the techniques, it is possible to use a 3D model that was previously created with a CAD software package [13] [20–22]. For these models it would be beneficial to use a physiologically relevant 3D model of the vascular network instead of a simple manually designed network.

The present work intends to combine the use of algorithmic vascular structure generation with a suitable fabrication method that allows the use of a 3D model as the vascular design. Considering all this, the approach of Justin et al. [13] seems appropriate given that the cells are already contained in the hydrogel when it is cast in the chamber and does not require

additional cross-linking. As this is the last step in the process, the cells are never in contact with the sacrificial template, as there are a series of intermediate casts of other biocompatible materials (alginate, gelatin).

## 3.5 Conclusions

This chapter presented two brief reviews; the first is about algorithms for the simulation of arterial trees, and the second about fabrication approaches for vascularised tissue constructs. The present work intends to link these topics by applying the benefits of algorithmically generated vascular structures into one of the most established fabrication methods: 3D printing.

Numerous algorithms have been developed over the past decades for the bio-simulation of arterial tree construction. The algorithms consider the physiological constraints associated with blood flow and the hierarchical branching vasculature in the human body. Constrained constructive optimization (CCO) is a widely accepted method for the generation of vascular trees. In order to build a physiologically relevant arterial tree, an optimality criterion must be fulfilled. The principle of minimum intra-vascular volume is extensively used to ensure an optimal build.

In the field of tissue engineering there has been considerable research regarding vascularisation. The most common approaches use 3D printing-based techniques. There is a diversity of methods to produce vascular structures within hydrogels. However, it seems that none of the approaches consider the complexity of real vascular networks in their design. As a result, the fabricated structures may be lacking physiological relevance.

The present work aims to integrate the algorithmic construction of vascular networks with the fabrication of networks by 3D printing technologies used in vascularisation approaches in order to achieve physiologically relevant functional vascularised tissue constructs. The model here proposed is based on CCO, particularly on Karch's approach [88], as it has been proved a reliable method and is extensively used for arterial tree simulations. The algorithm development is presented in Chapter 4. The fabrication for the algorithmically generated 3D models is based on the work of Justin et al. [13] as it is considered the most compatible of the studied methods.



# Chapter 4

## Algorithmic vascular structure generation

### 4.1 Overview

The literature review in Chapter 3 provided an overview of the algorithms used for the computational simulation of vascular structures. Regardless of the approach, all algorithms follow a set of constraints for the achievement of physiologically relevant structures. The use of these constraints allows the fulfilment of the physiological principles of blood flow and circulation such as flow conservation, Pouseuille's law of flow, Murray's law for bifurcations, equal terminal flow and equal terminal pressure.

In accordance with the project aim, an algorithm for the construction of vascular structures has been developed. The proposed algorithm is a modified version of the studied algorithms, keeping the essential physiological constraints and adapting it to the research needs. In essence, the algorithm follows the general approach of [88] and has a similar implementation as that of VascoSynth [82]. The concept of a "macro-cell" introduced by Kretowski and Bezy-Wendling [81] is used in the present work. A macro-cell is the fundamental unit of the model and is a simplified representation of a group of capillaries within a small cubic region where the exchange of nutrients and waste occurs. This will be explained further in Section 4.2. It must be noted that in this chapter pressure is expressed in millimetres of mercury (mm Hg), as this is the standard unit for the measurement of blood pressure. Flow rate is expressed in millilitres per minute (mL/min) or millilitres per hour (mL/h), in accordance with physiology textbooks. The remaining parameters are expressed in S.I. units.

The algorithm creates an arterio-venous network that fulfils the physiological principles of arterial flow and branching. The algorithmic arterio-venous network development process begins with the delimitation of a three-dimensional volume shape where the network will

be created. The volume is then divided in cubical sub-units (macro-cells) and each of them is represented by their centre point. Starting points for two trees –arterial and venous– are defined in the desired position. These points represent the inlet and outlet of the network. The tree formation starts from both initial points and follows a space-filling approach in which new branches are added iteratively and independently for each tree until all the macro-cell centre points within the volume are connected to both trees. With the addition of each new branch an optimisation for its bifurcation position is performed, in accordance with the principle of minimum blood volume. After the tree data has been computed (i.e. branches' starting and end points coordinates, corresponding radii, flow rates and pressures), the resulting tree structures are created in a CAD environment (Autodesk® Inventor®) where the branches are represented with cylindrical extrusions. Examples of a single vascular tree and an arterio-venous network created with the proposed algorithm are shown in Figure 4.1.

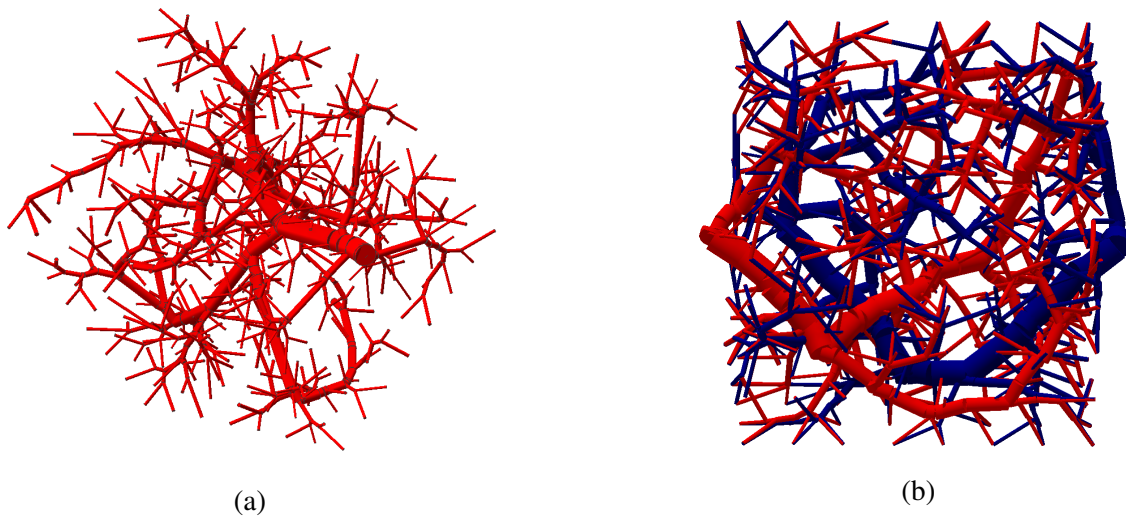


Fig. 4.1 (a) A single arterial tree. (b) An arterio-venous network generated using the algorithm developed here.

## 4.2 Algorithm Development

### 4.2.1 Programming and modelling environment

Given the experimental purpose of the vascular networks, it is of great importance that the outcome of the algorithmic tree construction is a 3D solid model that can be exported into STL format for use with additive manufacturing equipment. Therefore, the use of a CAD

software is essential. Autodesk® Inventor® Professional 2018 (64-Bit Edition) is a versatile CAD software package and is used in the present work to build the 3D solid models of the vascular structures. Its flexibility allows the development of specialised applications by means of the Software Development Kit (SDK) included in the standard installation with a student licence. With the SDK it is possible to create user interfaces using a programming language, in this case Visual Basic (VB), and link them to the Autodesk® Inventor® interface, allowing the automation of repetitive and time-consuming operations by means of the Application Programming Interface (API). The algorithm developed in the present work is designed to iteratively add branches to a tree given branch-specific parameters such as starting point, end point and radius. Thus, it is convenient to automate the task by using Inventor® API.

The programming platform used in the present work is Microsoft Visual Studio Community 2015© with an academic licence, where Microsoft Visual Basic 2015 (VB) was selected as the preferred programming language given its compatibility with Inventor® API. To develop the programming code for the algorithm, a new project was created in VB by selecting the template "Windows Forms Application", as shown in Figure 4.2. In order to use the Inventor® API in the new project in VB, a reference to the API's Dynamic-Link Library (DLL) was added. This was achieved by loading the "Autodesk.Inventor.Interop.dll" file as a reference in the new project, which is located within Autodesk® Inventor® Professional 2018 SDK folder (C:\...\Autodesk\Inventor2018\SDK\UserTools\CopyDesign\Bin). After adding this reference, all the commands from Inventor were available in the VB project. In the same manner, a second reference was created for Microsoft Excel "Microsoft.Office.Interop.Excel.dll" to allow saving and importing numerical data in the code.

### 4.2.2 3D volume delimitation and subdivision

The first step in the algorithm sequence is the delimitation of a three-dimensional volume where the arterio-venous network will be created. For practical purposes the present work is limited to the use of cubic or cuboidal volumes, although the process can be extrapolated to produce the networks into volumes of different shapes, including organ-specific shapes obtained from CT scans or other medical imaging means. Following the approach and nomenclature of [81], the 3D volume is then subdivided into cubical sub-units called "macro-cells", which are distributed uniformly within the 3D volume and represent a small cluster of capillaries (or capillary beds) that will ensure the perfusion within that region. The capillary bed representation is depicted in Figure 4.3.

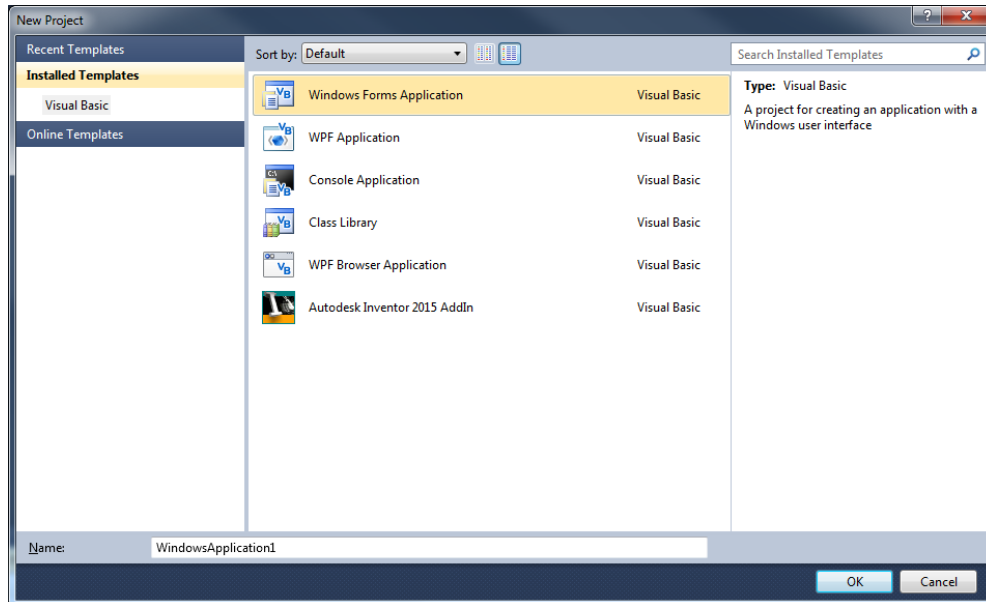


Fig. 4.2 Creation of a new project in Visual Basic.

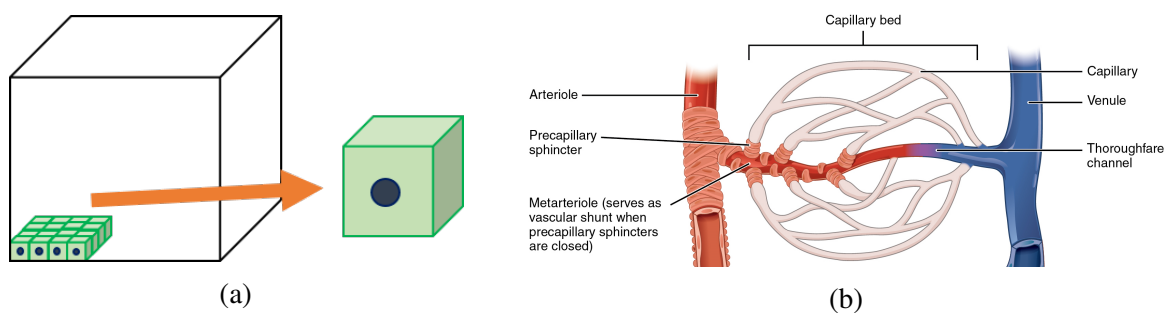


Fig. 4.3 (a) Subdivision of the main 3D volume into sub-units called "macro-cells". (b) Bed of capillaries in the human body, that every macro-cell represent. The connection between arterial-venous trees represents a thoroughfare channel. Image source for (b): [116].

Each macro-cell is represented by their centre point. The aim is that all the points are connected to a terminal branch of the arterial tree and to a terminal branch of the venous tree, forming a connection between both trees. As the trees are connected by their terminal branches, they constitute a network and it ensures the flow from inlet (arterial tree's starting point) to outlet (venous tree starting point). In the present work, the volume of the macro-cell and the desired number of macro-cells per side of the cube are user-defined parameters. Considering, as an example, a cubic 3D volume with 6 macro-cells per side, each macro-cell has a volume of  $0.125 \text{ mm}^3$  (0.5 mm each edge of the macro-cell), which means that the main cubic shape has an edge length of 3 cm and a total volume of  $27 \text{ cm}^3$ . The total number of macro-cell centre points (also referred to as "terminal points" in the present work) inside the volume is  $N = 6 \times 6 \times 6 = 216$ . In order to delimit the 3D volume in the algorithm, appropriate XYZ coordinates for the cube's vertices are first assigned, according to the user-defined macro-cell volume and number of units per side, and stored in an array. In a similar manner, XYZ coordinates for the macro-cells' centre points are assigned and stored in an array. The position of every point is accessible by the array index. With this data, the graphic depiction is performed in Inventor® using lines and points in a sketch, as shown in Figure 4.4.

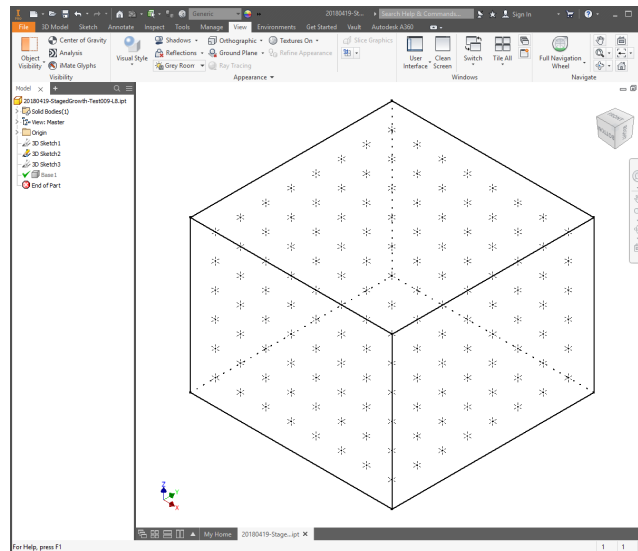


Fig. 4.4 Depiction of 3D volume in Inventor®'s interface. The macro-cells' centre points are drawn inside the main volume.

### 4.2.3 Fulfilment of physiological laws

The process of generating each tree starts when a single point is randomly selected from the array of macro-cell centre points. A "branch" or "vessel" is then created from the predefined starting point (also called root point) of each tree to the selected random point. The new branch is assigned a representative number, starting and end points, as well as the corresponding values of volumetric flow rate ( $Q$ ) and reduced resistance ( $R^*$ , explained below in detail), that will be used later to calculate the corresponding radius ( $r$ ) of the vessel according to its length ( $L$ ) and the given values for input pressure ( $P_{in}$ ) and terminal pressure ( $P_{term}$ ).

When a new random point is selected, there are three possible situations: i) Case 1: the first terminal point, ii) Case 2: the second terminal point and iii) Case 3: the third and all subsequent terminal points. These cases and their respective sequence of steps for the addition of a new point are depicted in Figure 4.5. The approach of the proposed algorithm is to look for the branch that is closest to the new point (excluding case 1, where there are not any existing branches yet). This is achieved by calculating the distance between every existing branch (at their middle point) and the new point. The branch that has the shortest distance is selected and a new bifurcation occurs.

The initial point for a bifurcation is at the middle point of the selected vessel. The selected vessel is then called "parent" vessel, and its length is reduced to half by setting its new end point to where its middle point had originally been. Two new vessels are then created: one from the bifurcation point (which is now the new end point of the parent branch) towards the parent's original end point, and the other vessel from the bifurcation point towards the point that needs to be connected to the tree. This process is depicted in Figure 4.6. The model here presented is restricted to binary trees (each parent branch at a bifurcation can only have two daughter<sup>1</sup> branches). This is due to the fact that in the human body the optimal arrangement consists of bifurcating trees, while trifurcations are very rare [63].

As previously mentioned, for every new branch added to the tree there are branch-specific attributes that are calculated and assigned, such as: branch number, start and end point coordinates, flow rate and reduced resistance (which is a simplified expression of the resistance and will be explained later). Adding a new branch implies a change in the flow and reduced resistance values of the existing branches, so the tree must be updated accordingly. The flow and reduced resistance of every branch of the tree are re-calculated and the corresponding arrays are updated to be in consistency with the newly added branch.

<sup>1</sup>Daughters of the same parent branch are referred to as 'siblings'.

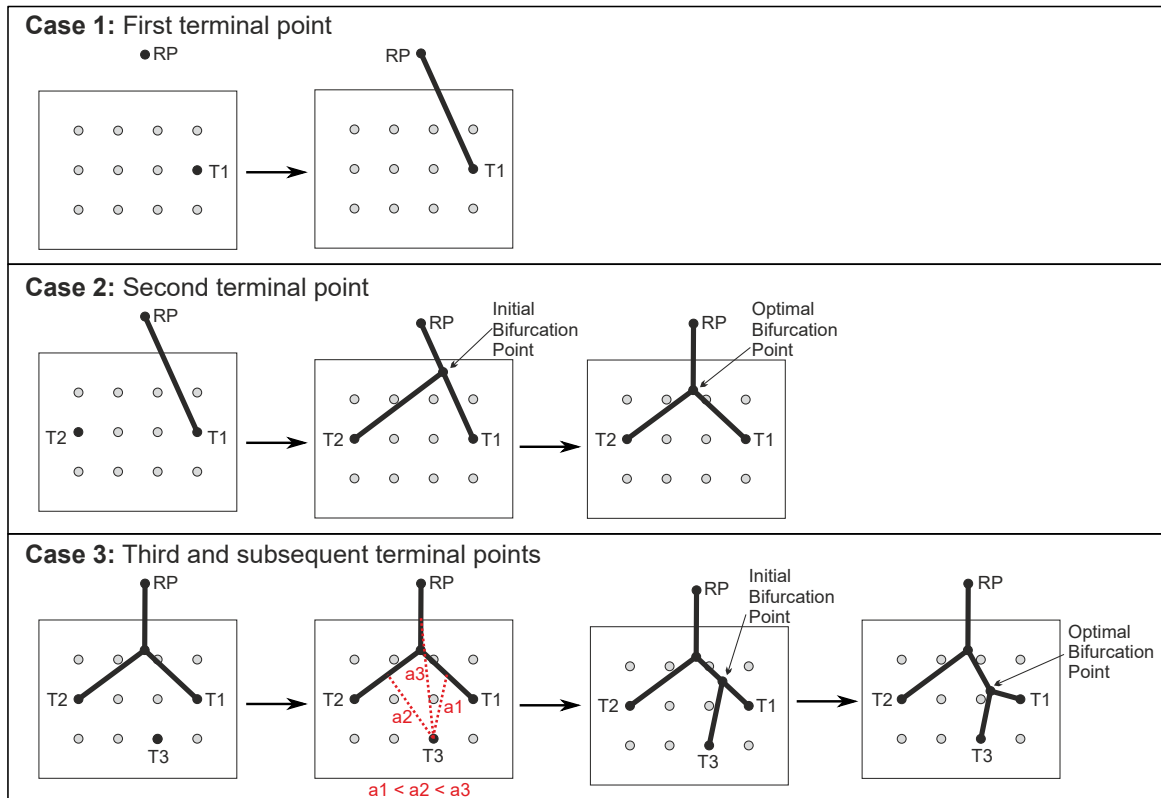


Fig. 4.5 Schematic representation of the addition of a new terminal point for the three possible cases. RP: root point, T1: terminal point 1, T2: terminal point 2, T3: terminal point 3,  $a1$ : distance from T3 to the middle point of T1,  $a2$ : distance from T3 to the middle point of T2,  $a3$ : distance from T3 to the middle point of P. In case 3, the shortest distance among  $a1$ ,  $a2$  and  $a3$  is selected and the corresponding branch is chosen for the new bifurcation.

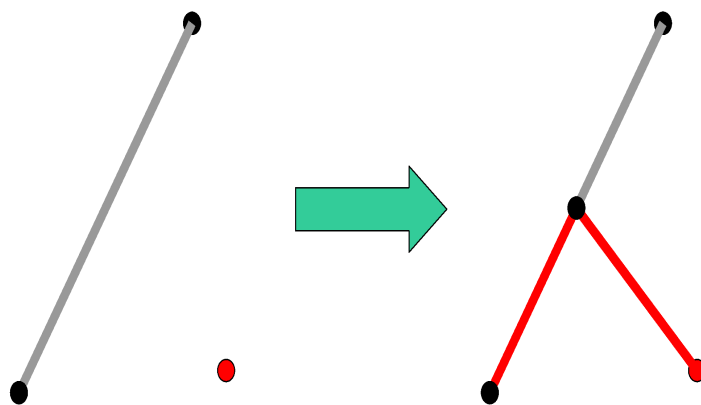


Fig. 4.6 Schematic representation of the addition of a new branch to the tree. The branch closest to the new point is reduced in length to its middle point, which is now the bifurcation point. Two new branches (shown in red) are grown from the bifurcation point: one to the original end point of the parent branch, and the other to the new point.

As stated in Chapter 2, the present work is based on assumptions that simplify the constraints for an approximate physiological representation of vascular networks. The tree branches (or vessels) are assumed rigid pipes with laminar steady state flow and the fluid is considered incompressible and Newtonian. Therefore, Poiseuille's law is applied. Regarding the flow rate, for every terminal vessel (vessels connecting to a point) the value of terminal flow rate  $Q_{term}$  is assigned. It is a constant value that is calculated by dividing the inlet flow of the tree  $Q_{in}$  (a user-defined value) by the total number of terminal points or cells in the volume. Following the laws of flow conservation, the flow in every parent branch must be equal to the sum of the flow rates in its daughter branches, as indicated by Equation 4.1

$$Q_p = Q_1 + Q_2 \quad (4.1)$$

Thus, the flow rate in every branch of the whole tree is updated as indicated previously, starting from the terminal branches and going up to the root. Figure 4.7 presents a schematic of the addition of a new branch and explains how the flow rate is updated accordingly. For this update, an algorithm was implemented and its sequence is shown in Figure 4.8.

For the reduced resistance, the approach of [88] was followed and will be detailed here. According to this method, depending on whether the new branch is a terminal branch or a parent branch, the reduced resistance is calculated differently. By Poiseuille's law, it is known that the pressure difference and hydrodynamic resistance in a vessel segment are expressed as:

$$\Delta P = RQ \quad (4.2)$$

$$R = \frac{8\mu L}{\pi r^4} \quad (4.3)$$

$$\Delta P = \frac{8\mu LQ}{\pi r^4} \quad (4.4)$$

where  $\Delta P$  is the pressure difference from inlet to outlet of the vessel,  $R$  is the hydrodynamic resistance,  $\mu$  is the blood viscosity (considered constant for simplicity) and  $L$  is the length of the vessel. Factorizing  $Rr^4$  is convenient because it can be assumed that the resulting equation (which is called reduced resistance) does not depend on the radius, as shown:

$$R^* = Rr^4 = \frac{8\mu L}{\pi} \quad (4.5)$$

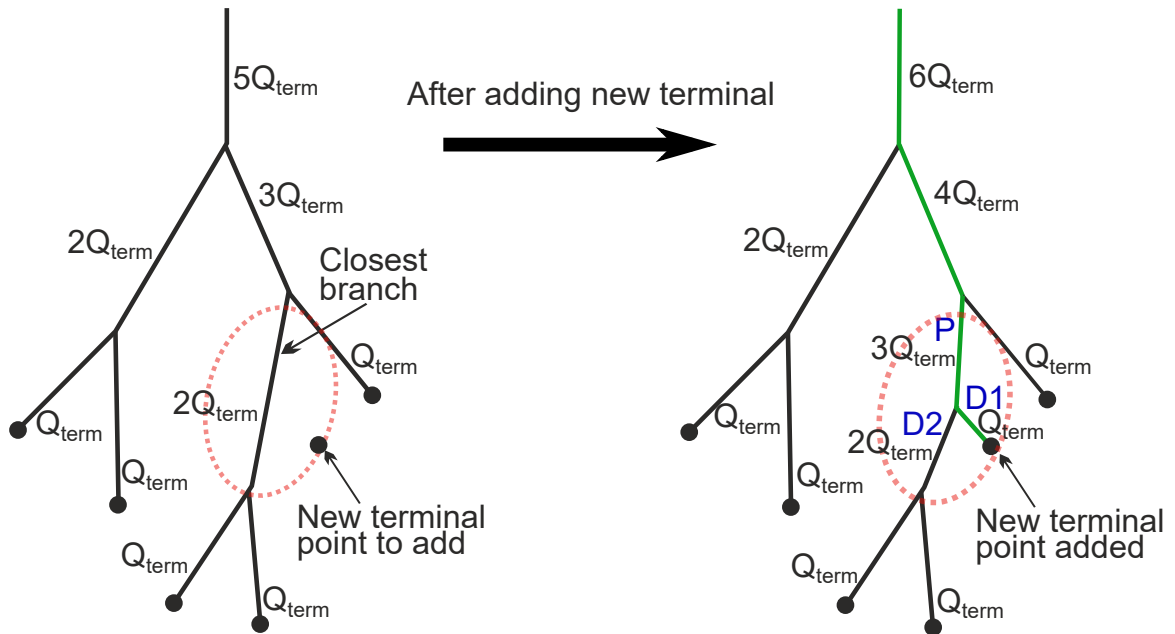


Fig. 4.7 Schematic representation of flow rate updating when new terminal point is added. The selected branch (closest to the new terminal point) becomes a bifurcation with a parent (P) and two daughter branches (D1 and D2). For D1, which is connected to the new point,  $Q_{term}$  value is assigned. For D2, which is connected to a previously existing part of the tree, the flow rate value  $Q$  of the original branch is inherited. For the parent branch P, the new flow rate is calculated using Equation 4.1. The flow rates of the branches affected by this change (highlighted in green) are updated accordingly using the flow updating algorithm.

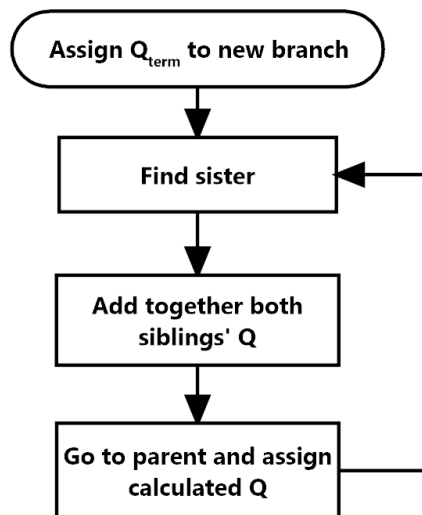


Fig. 4.8 Algorithm to update the flow in the tree.

Then, the reduced resistance (also referred to as  $RRes$  or  $R^*$ ) for each daughter branch is:

$$R_1^* = R_1 r_1^4 \quad (4.6)$$

$$R_2^* = R_2 r_2^4 \quad (4.7)$$

Following these principles, for a terminal branch, the reduced resistance is simply calculated as in Equation 4.5:

$$R_{term}^* = \frac{8\mu L}{\pi} \quad (4.8)$$

However, for a parent branch, the calculation of the reduced resistance is more complex, as it involves the ratio of the radius of daughter branch 1 to the radius of daughter branch 2, as well as the ratio of each of the daughters to the parent branch, and includes the corresponding reduced resistance of the daughters. Therefore, the reduced resistance for a parent branch can be calculated as [88]:

$$R_p^* = \frac{8\mu L_p}{\pi} + \left[ \frac{F_1^4}{R_1^*} + \frac{F_2^4}{R_2^*} \right]^{-1} \quad (4.9)$$

where  $\mu$  is the blood viscosity,  $L_p$  is the length of the parent vessel,  $F_1$  and  $F_2$  are the fractions of the radii of the daughters over the radius of the parent, and  $R_1^*$  and  $R_2^*$  are the corresponding reduced resistance values of the daughters.

$$F_1 = \frac{r_1}{r_p} \quad (4.10)$$

$$F_2 = \frac{r_2}{r_p} \quad (4.11)$$

The radii are unknown, but it is known that Murray's law must be fulfilled, therefore:

$$r_p^\gamma = r_1^\gamma + r_2^\gamma \quad (4.12)$$

Then, dividing by  $r_1^\gamma$  and  $r_2^\gamma$  respectively, the fractions can now be expressed as:

$$F_1 = \left[ 1 + \left( \frac{r_1}{r_2} \right)^{-\gamma} \right]^{\frac{-1}{\gamma}} \quad (4.13)$$

$$F_2 = \left[ 1 + \left( \frac{r_1}{r_2} \right)^\gamma \right]^{\frac{-1}{\gamma}} \quad (4.14)$$

The ratio  $r_1/r_2$  is now required. By equating the pressure differences  $\Delta P_1$  and  $\Delta P_2$ , equation 4.17 is obtained:

$$\Delta P_1 = R_1 Q_1 \quad (4.15)$$

$$\Delta P_2 = R_2 Q_2 \quad (4.16)$$

$$\frac{Q_1}{Q_2} = \frac{R_2}{R_1} \quad (4.17)$$

Then, by substituting  $R$  from the  $R^*$  factorization in the previous equation, it can be expressed as:

$$\frac{Q_1}{Q_2} = \frac{R_2^*/r_2^4}{R_1^*/r_1^4} \quad (4.18)$$

which leads to the ratio:

$$\frac{r_1}{r_2} = \left( \frac{R_1^* Q_1}{R_2^* Q_2} \right)^{\frac{1}{4}} \quad (4.19)$$

By substituting this equivalence in Equations 4.13 and 4.14, it can be noticed that the reduced resistance of the parent branch can be calculated only in terms of viscosity, length, flow and the reduced resistance of the daughters, but is independent of the radius of any of the branches. The reduced resistance is then updated for each branch of the tree as described. The algorithm that was created and programmed to update the reduced resistance of every tree branch is graphically represented in Figure 4.9.

After the flow and reduced resistance have been updated for every branch of the current tree structure, the radii of every branch must be calculated in accordance with the physiological laws. The first radius to be calculated is that of the root branch. Applying the reduced resistance factorization in Equation 4.5 to the root branch, we have:

$$R_{root}^* = R_{root} r_{root}^4 \quad (4.20)$$

Then, the radius would be:

$$r_{root} = \left( \frac{R_{root}^*}{R_{root}} \right)^{\frac{1}{4}} \quad (4.21)$$

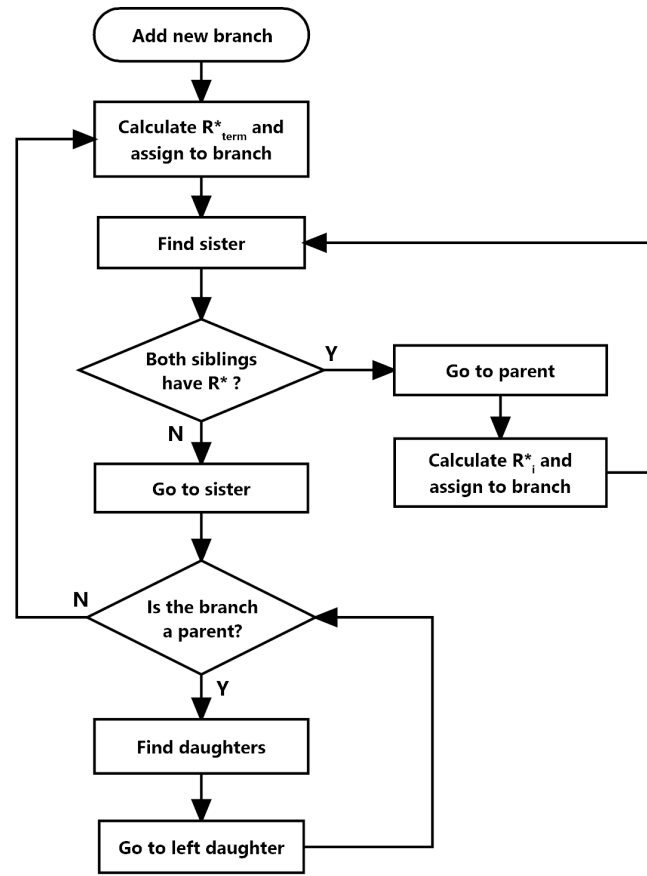


Fig. 4.9 Algorithm for reduced resistance update in the vascular structure.

where  $R_{root}^*$  is the reduced resistance of the whole tree. Considering this, and taking Equation 4.2, we can express  $R_{root}$  as:

$$R_{root} = \frac{P_{in} - P_{term}}{Q_{in}} \quad (4.22)$$

The root radius can then be calculated as:

$$r_{root} = \left( \frac{Q_{in} R_{root}^*}{P_{in} - P_{term}} \right)^{\frac{1}{4}} \quad (4.23)$$

After the root radius has been calculated, the radii of the daughter branches of the root can be calculated in the following way. First, the ratio  $r_1/r_2$  is calculated as previously explained, with Equation 4.19. By having this ratio, the values of  $F_1$  and  $F_2$  mentioned earlier can be calculated using Equations 4.13 and 4.14. Now that  $F_1$  and  $F_2$  are known, as well as the radius of the parent branch (which is, in this case, the root radius), then  $r_1$  and  $r_2$  can be

easily calculated as:

$$r_1 = r_p F_1 \quad (4.24)$$

$$r_2 = r_p F_2 \quad (4.25)$$

Then, for each of the daughter branches, the procedure is repeated to find the radii of the sub-daughters, and the process is repeated until all the branches of the tree have their radii calculated and saved in the corresponding array. For every new point connected to the tree, the whole process described above (updating flow and reduced resistance of the tree branch by branch and calculating the branches' radii) is repeated until all the remaining points are connected to the tree. This constitutes the main loop cycle of the VB code.

#### 4.2.4 Optimisation of bifurcation points

As mentioned in Chapter 3, different approaches have been studied in the literature regarding the construction of vascular trees according to optimality principles, where a certain quantifiable characteristic is to be minimised [63] [80]. The optimality criterion used in the present work is minimisation of blood volume in order to maximise the amount of useful tissue. This criterion is widely accepted for the development of arterial tree growth algorithms [88] [80] [89].

As explained in the previous section and depicted in Figure 4.6, when a new macro-cell is to be connected to the tree, a bifurcation is created at the middle point of the closest branch and a new branch is added to connect the new point. If the minimum volume of the tree structure is to be considered, then each bifurcation point must be moved to an optimal location. For this purpose, different positions for the new bifurcation are tested in a sequential manner, generating the corresponding volumes for every tree configuration produced. The volumes obtained with the test points are stored and compared, and the bifurcation test position that produces a structure with the smallest volume will be chosen as the optimal position.

When a new bifurcation is created the optimal position coordinates are found using the following steps:

1. The flow and pressure data for each branch of the tree is updated, and from these values, the radii of the branches are calculated. The volume of the structure is then

calculated as the sum of the volumes of all branches in the model and stored for further comparison.

2. A plane is formed by three points (see Figure 4.10): The start point of the parent vessel (P0), the end point of daughter vessel 1 (P1), and the end point of daughter vessel 2 (P2). This is the plane where the bifurcation point will be moving (two-dimensional movement), as moving it outside of the plane will result in longer lengths and therefore greater volumes. The three points (P0, P1 and P2) will represent the vertices of a triangle that will be used as a reference.
3. The position of the centre point of the reference triangle is found as the intersection of the three medians of the triangle (lines connecting each vertex of the triangle with the midpoint of the opposite side), and the bifurcation point is moved there as a starting point for the testing, as shown in the second schematic in Figure 4.10.

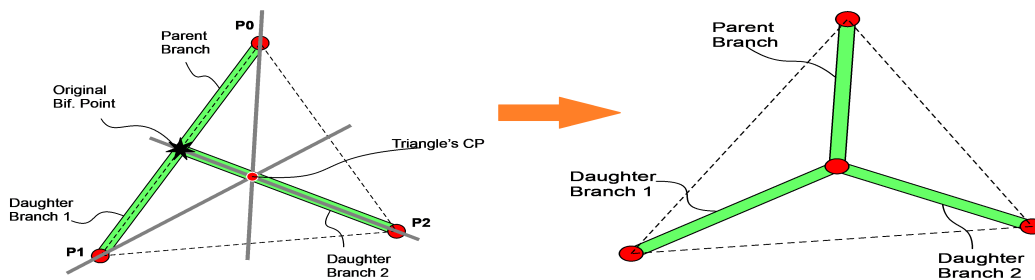


Fig. 4.10 Movement of original bifurcation point to triangle's centre point (CP).

4. The whole tree structure's flow, resistance and radii are then recalculated in order to account for this change of position, and the new tree volume is calculated and stored. For most cases, the volume at this point is smaller than that generated with the bifurcation point at the original position, because the length of the daughter vessel 2 is significantly reduced.
5. Taking as base the centre point of the triangle, four "test points" are created around it within the plane, by modifying the central point's coordinates by  $+\Delta X$ ,  $-\Delta X$ ,  $+\Delta Y$  and  $-\Delta Y$ , as shown in Figure 4.11. In order to find the 3D coordinates of the test points, a series of translations and rotations are performed on the triangle points (P0, P1, P2 and centre point) in order to align them to the XY plane from the original coordinate system in the 3D space. The four test points are created on the XY plane, each being equidistant (by  $\Delta$ ) to the centre point of the triangle and parallel to the X and Y axes, respectively. The newly added test points are then rotated and translated

back to the original triangle position and thus, the 3D coordinates of the four test points are obtained. The value of  $\Delta$  is calculated by multiplying the length of the smallest side of the reference triangle by a user-defined fraction, also referred to in the present work as "bifurcation optimisation variable". This approach was taken in order to make a consistent optimisation of the tree structure by focusing on the current bifurcation and avoid having a set value which may result in having very coarse or small movements for some bifurcations.

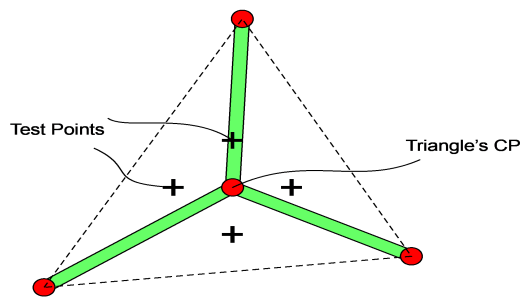


Fig. 4.11 Depiction of test points where the bifurcation point will be moved.

6. The whole tree structure's flow, resistance, radii are recalculated and the volume found for every test point, as depicted in Figure 4.12. The point that produces the smallest volume of the structure is selected as the new centre point.
7. From the new centre point, four new test points are created around it and the process (steps from 5 to 7) is repeated until all the test points produce a volume larger than the centre point. When this happens, it means that the optimal bifurcation point is the one currently defined as centre point.

This optimisation process follows a 'local-minimum' approach, in which the optimal point is found by starting at a central location and following the path to the closest minimum. When the optimum bifurcation point is found, its coordinates are stored and the point is fixed as part of the geometry of the tree. For every new macro-cell connected, only the new bifurcation will be moved. Thus, after all the cells have been connected to the tree, the coordinates of all the bifurcation points will be known.

Originally, the optimisation approach was programmed using Inventor® features (a new set of points, lines, and planes were created every time the bifurcation point was moved). However, this caused a long computing time due to the high amount of computing resources required while processing data between Inventor® and Visual Basic® and because of the large number of elements that remained in Inventor®'s objects list.

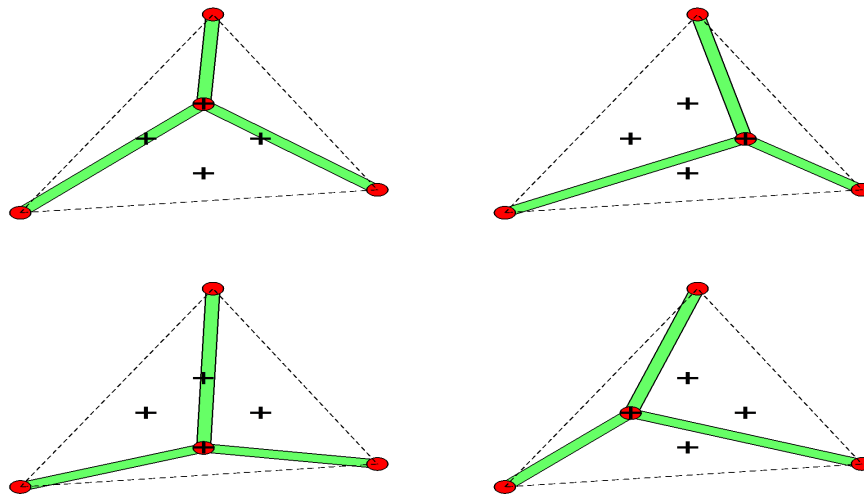


Fig. 4.12 Movement of bifurcation point to every test point.

A faster method was implemented by substituting the operations performed in Inventor® by customised functions in the code, with which the coordinates of the test points are mathematically calculated in the VB code, therefore, saving resources from Inventor®. This method corresponds to the optimisation steps described above. In addition, a new class was created in the code for all the 3D points used to avoid processing them in Inventor®, which resulted in a further computing time reduction. The original code took approximately 16 hours to produce a network of 216 macro-cells, considering the network's skeleton and data (branches coordinates, flow, pressures, radii). After the improvements, the code can produce the same structure in approximately 35 minutes.

#### 4.2.5 Connection of arterial tree and venous tree

As mentioned in Section 4.2.2 in order to generate a perfusable vascular network, two individual vascular trees (an arterial tree and a venous tree) must be connected at the macro-cell central points, also referred to as "terminals" or "terminal points" (see Figure 4.13).

Following the approach of Bezy-Wendling and Bruno [80], and Kretowski et al. [89], the present work presents the generation of two connecting trees by alternating the generation of the branches for every new random point from one tree to the other. This means that a branch is created first from the arterial tree and immediately after another branch is created from the venous tree to the same point. This is visually represented in Figure 4.14.

After the selection of the new random point to be connected, the process of connection, flow and reduced resistance update, radius update and optimisation of bifurcation point are

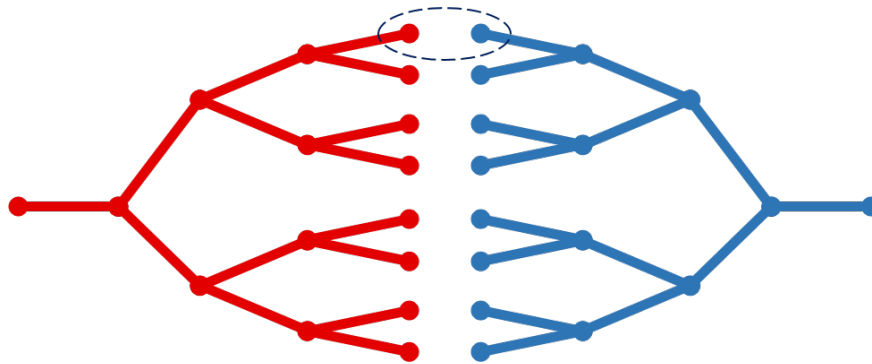


Fig. 4.13 A vascular network consists of two trees connected at the macro-cell level. Image adapted from original in [89].

all performed for the arterial tree and subsequently for the venous tree. Given that both trees have different starting point coordinates, their structures are different.

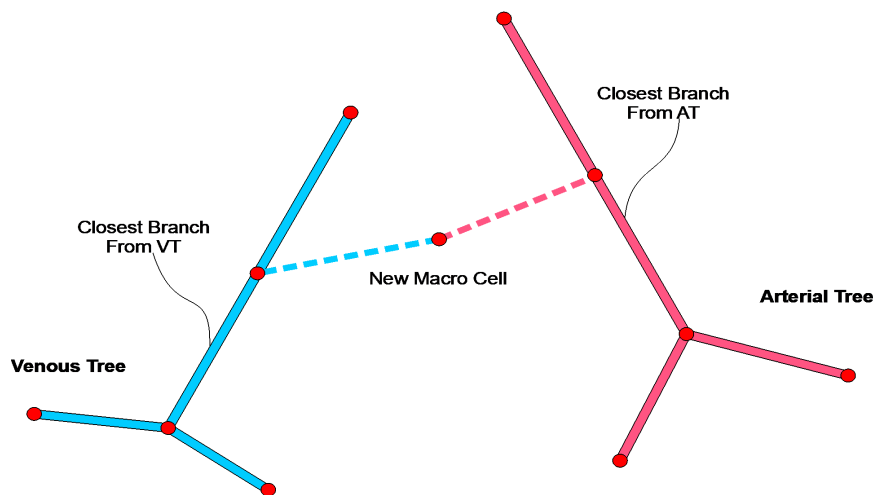


Fig. 4.14 Depiction of new point being connected to arterial tree (AT) and venous tree (VT).

This stage of the development presented the greatest challenges. Given that the same method is used to generate both tree structures independently, some problems arise due to the fact that they share the same 3D volume. The most notorious problem is the collision between both branching structures. This will be discussed in Section 4.2.6.

Another problem, less noticeable as the number of cells increase, but nevertheless present, is the difference in the radius of the connecting terminals from one tree with respect to the other tree. This is expected given that both trees are built with the same method, under the same conditions and sharing the same set of points, but having different starting points. Thus, although the arterial tree and venous tree are built while fulfilling the physiological

laws, they grow independently of each other. This means that, in order to reach every new desired cell, both trees will grow a branch with the same physiological restrictions, but their lengths will be different (as they have different starting coordinates), which will result in them having different radii. This is a problem because for practical purposes, the radii of each pair of arterio-venous connecting branches must ideally be equal to allow flow in the network without additional pressure losses.

To address this issue, a solution was developed by creating a function that adjusts the radii of the venous terminal branches to equal the radii of their corresponding arterial terminal branches. Then, based on their new terminal radii, the radii of the branches of the whole venous tree are recalculated backwards (from the terminal branches going up to the root) following Murray's law. However, doing this will inevitably modify the volume of the venous tree, which was originally optimised for minimum volume. The function that adjusts the radii of the venous tree branches can be disabled, should the real minimum-volume morphology of the venous tree be necessary.

#### 4.2.6 Detection and handling of collisions

Given that the arterial and venous trees grow in an independent way, they are susceptible to collide with each other, as shown in Figure 4.15. Following the approach used by Kretowski et al. [89], the detection of colliding branches was based on the calculation of the shortest distance between two lines in a three dimensional space.

The equations for the calculations of the shortest distance between two lines in a three-dimensional space were obtained from the Paul Bourke website [117] and his approach is explained as follows. Considering two lines (see Figure 4.16) defined by two points (line "a" from  $P1 - P2$  and line "b" from  $P3 - P4$ ), a point on line "a", which will be called  $Pa$  has the Equation 4.26 and in a similar way, a point on line "b", which will be called  $Pb$  has the Equation 4.27.

$$Pa = P1 + mu_a(P2 - P1) \quad (4.26)$$

$$Pb = P3 + mu_b(P4 - P3) \quad (4.27)$$

To find the shortest line segment between lines A and B the length of the line segment joining the two lines must be minimised:

$$||Pa - Pb||^2 \quad (4.28)$$

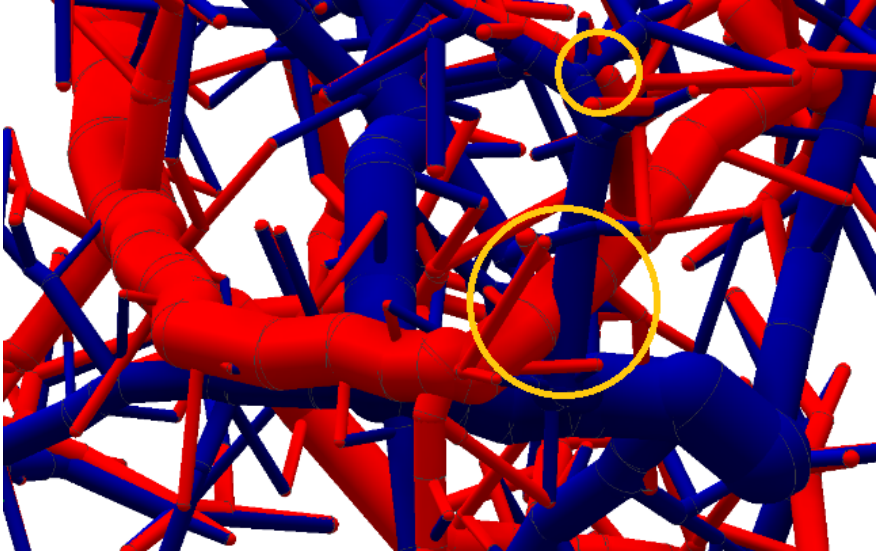


Fig. 4.15 Visible collisions in the Arterio-Venous Network.

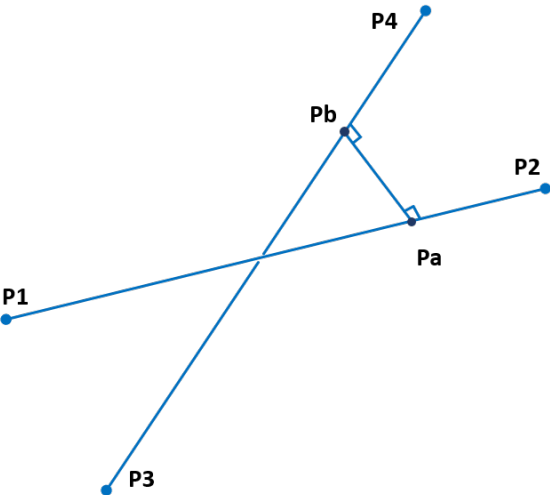


Fig. 4.16 Shortest distance between two lines in a three-dimensional space. Adapted from original image in [117].

Substituting the equations of the points  $Pa$  and  $Pb$  gives:

$$\|P1 - P3 + mu_a(P2 - P1) - mu_b(P4 - P3)\|^2 \quad (4.29)$$

Equation 4.29 can be expanded out in the XYZ components of points  $P1$ ,  $P2$ ,  $P3$  and  $P4$ . At the minimum, the derivative with respect to  $mu_a$  and  $mu_b$  must be zero. Then, these two equations can be solved for  $mu_a$  and  $mu_b$ , and the intersection points are found by substituting the values of  $mu$  into the original equations of the points  $Pa$  and  $Pb$ .

Based on this approach, Thomas Ludewig [118] developed an open source code for the calculation of the shortest distance between two lines in Visual Basic, which is available on P. Bourke's website [117]. Ludewig's VB code was used as a base for the function that detects the collisions in the present work. The approach employed here was that when a new branch is added to the arterial tree (which is represented by a line segment), it is checked against all the existing branches of the venous tree (also, line segments) by calculating the shortest distance between two line segments. If the sum of the radii of the two branches being compared is greater than the shortest distance between them, it means they are colliding. An exception is made for the matching terminal branches, which are joined at one of their extremes, and therefore, their shortest distance is zero. In this case, the collision is neglected.

The detection method is effective, however, as it requires the iterative comparison between every new branch in the tree and every branch of the opposite tree, it can represent a significant amount of computing time. The number of iterations needed just for this purpose might be expressed as:  $\sum_{(k=2)}^N 3(2k - 1)$ , where  $N$  is the total number of points in the 3D space. The multiplying factor of 3 represents the new branch, its sister and its parent branch (which were modified by moving the bifurcation point in search for the optimal configuration). The  $2k - 1$  represents the number of branches that currently exist in the opposite tree, where  $k$  is the current number of terminals.

After detecting a collision while the tree grows, the problem must be handled to avoid it. This is an issue that remains unsolved in the proposed algorithm at the present time. Different approaches could be taken, such as:

- Moving the bifurcation point of the colliding venous branch until it is free of collision.
- Moving the bifurcation point of both colliding arterial and venous branches until they are free of collision.

Table 4.1 Input parameters for the algorithm

| Variable      | Parameter name/description                   | Units           |
|---------------|--|-----------------|
| Volume        | Total volume of the 3D space                 | cm <sup>3</sup> |
| CellVol       | Volume of the sub-units that form the volume | cm <sup>3</sup> |
| $Q_{cell}$    | Flow rate at each macro-cell                 | mL/min          |
| $P_{in}$      | Arterial input pressure                      | mm Hg           |
| $P_{cell}$    | Pressure at each macro-cell                  | mm Hg           |
| Viscosity     | Blood viscosity                              | Pa.s            |
| Murray        | Murray's law coefficient (Std: 3)            | –               |
| aPointInitial | Initial point for Arterial tree              | XYZ coord       |
| vPointInitial | Initial point for Venous tree                | XYZ coord       |
| FractDist     | bifurcation optimisation variable (>0 to 1)  | –               |

- Skipping the current random macro-cell and selecting the next one, until no collision is detected.

### 4.2.7 Algorithm sequence

In this section, the main steps of the network-building algorithm, shown in Figure 4.17, are explained.

- 1 - Input Variables** The algorithm starts by setting the input parameters which are defined by the user, and are shown in Table 4.1.
- 2 - Create new Inventor® Part** A command is sent to open Autodesk® Inventor® (if it is not already open) and a new Inventor® Part file is created.
- 3 - Initialization of 3D volume** Based on the input parameters, the dimensions of the 3D cube are calculated and its edges are drawn as lines in a 3D Sketch. The interior volume of the cube is filled with  $N$  equidistant points, where  $N$  is also calculated from the input data. See Figure 4.4.
- 4 - Order of selection of points** Each point in the 3D volume is assigned a number from 1 to  $N$ . A random point is selected out of the  $N$  possible points and its number is stored in an array-list. Another random point is selected (excluding the number selected previously) and added to the list. The process is repeated until all the points have been stored in the array-list, sorted in a random order. This list will indicate the order in which the points will be reached by the arterial and venous trees.

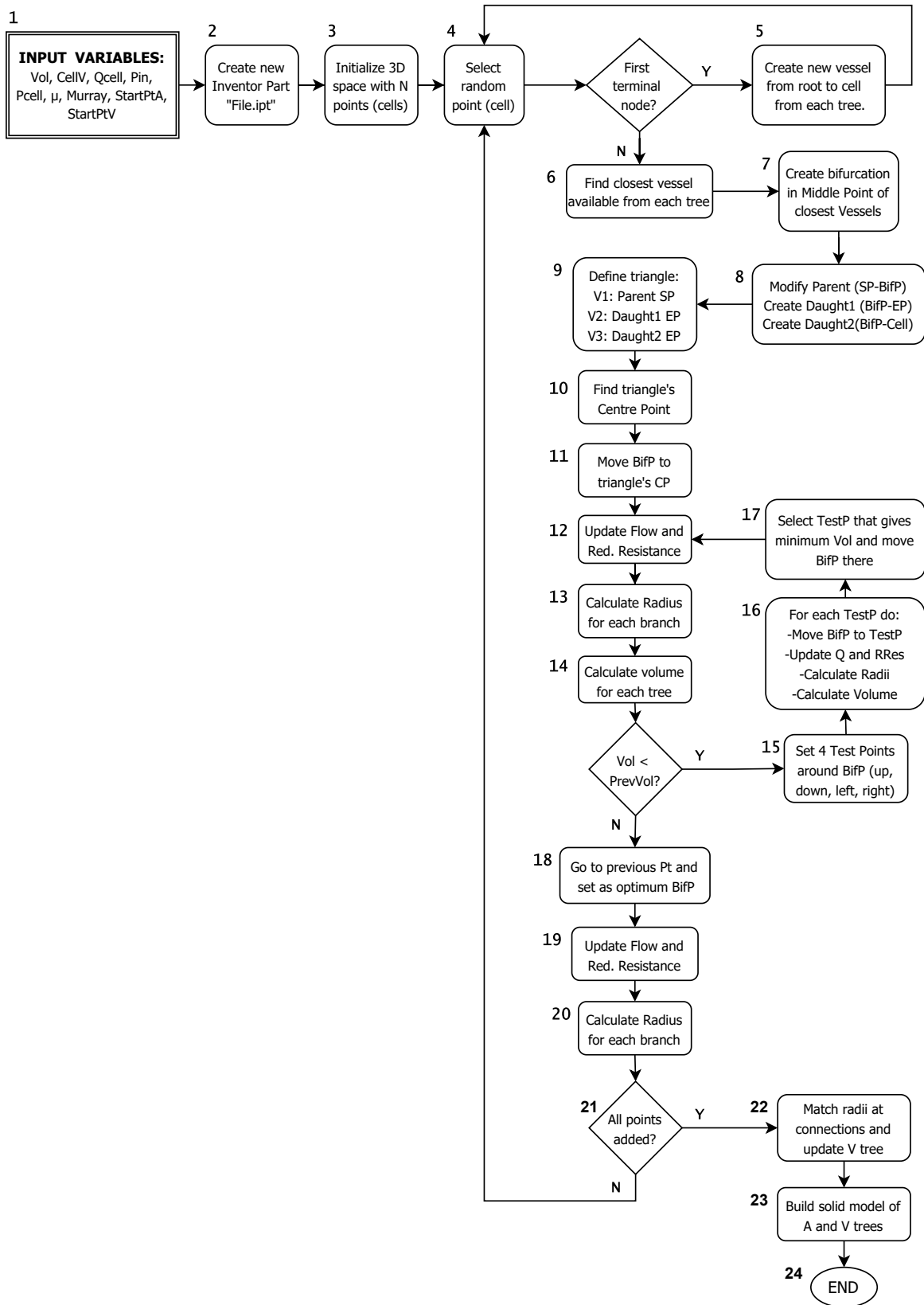


Fig. 4.17 Flow diagram of main steps in the algorithm.

- 5 - Creation of first tree branch** The creation of the first branch is treated as a special case, as no bifurcations are needed. A single line is created from the point previously set as root (typically lying on one of the faces of the cube), to the first randomly selected point. The corresponding input parameters (flow at the cell, pressure at the root and pressure at the cell) are assigned to the branch, kept and handled as arrays in the code, and used to calculate the radius. The branch is assigned a number, in this case, No. 1. At this stage, the branch is depicted in Figure 4.18(a). The same process is executed for the venous tree.
- 6 - Finding the closest branch** The next random point is selected according to the list. A new branch must grow from the existing tree structure towards the new point. To achieve this, the distance from the new point to every existing branch (at the middle point) is calculated, and the existing branch that has the shortest distance is selected. The same process is executed for the venous tree.
- 7, 8 - Creating a bifurcation** The selected branch (closest to the new point) is divided in two branches at the middle point. The upper part of the branch keeps its previously assigned branch number, and represents the 'parent'. The lower part of the branch is assigned the next consecutive branch number and represents 'daughter 1'. A new branch is created from the middle point, to the new point. It is assigned the next consecutive branch number and represents 'daughter 2'. The new corresponding values of the parameters are assigned to each branch in the new bifurcation (flow, input and output pressure). See Figure 4.10. The same process is executed for the venous tree.
- 9 to 17 - Optimization of bifurcation point** The bifurcation location must be optimized to ensure the minimum blood volume. The bifurcation point is moved to the central point of the triangle formed by the vertices: 1) Start point of parent branch, 2) End point of daughter 1 branch, and 3) End point of daughter 2 branch. Using the flow and pressure data of each branch, and their new lengths due to the relocation of the bifurcation, the radius of each branch is calculated. From the radii data, the volume of the tree is calculated in this configuration and stored. Four test points are created around the central point in the same plane as the triangle, and the bifurcation point is moved to each of the points. See Figure 4.12. For each of the four cases, the flow, pressure and radii data is updated and the volume of the tree is calculated. The test point that produces the minimum volume is set as the new central point. The testing process is repeated until the minimum volume is found, which means that the bifurcation is at the optimal position. The same process is executed for the venous tree.

- 18 to 20 - After finding optimal bifurcation point** The radii of all the branches in the tree are recalculated once again, in the optimal configuration for the bifurcation. The update starts at the root and advances toward the terminal branches. The next random point in the list is then selected and the cycle is reiterated. The same process is executed for the venous tree.
- 21 - Adding all the points to the tree** The cycle of adding branches to the tree while maintaining the optimal configuration continues until all the points in the 3D volume have been reached, following the previously set random order. The same process is executed for the venous tree.
- 22 - Matching radii of venous tree** After both trees have been constructed in their individual optimal configuration, the radii of the branches that connect the trees must be equal. Each pair of matching terminals is identified and the radius of the venous branch is forced to match the corresponding arterial radius. When all the venous terminal branches have been assigned the new radii, the radii of the rest of the branches are recalculated up to the root branch, following Murray's law.
- 23 - Construction of solid model** From the stored tree data arrays that contain the basic information of each branch in the tree (flow, input pressure, output pressure, radius, start and end point coordinates), each branch is modelled as a cylinder in Inventor®. Two parallel work planes are created: one at the starting point and one at the end point of the branch. On the first work plane, a circle is created with the corresponding branch radius and the circular profile is extruded toward the second work plane. At the end of each cylinder, that is, at the second work plane, a sphere feature is revolved to act as a joint at the bifurcations. The arterial tree is represented by red cylinders, while the venous tree is represented by blue cylinders.
- 24 - END** When the algorithm finishes its execution, the solid arterio-venous network model file in Inventor® is saved, and the building data of the trees is stored and saved in an Excel® file.

#### 4.2.8 Stages of tree growth

As mentioned previously, the structure of each tree is given by the order of selection of the macro-cell points. Because of this, the first few selected points will define the location and shape of the main branches of the tree. To visualise the iterative construction of the models, a single tree is shown in figure 4.18 at different stages of growth, for a 3D space that has

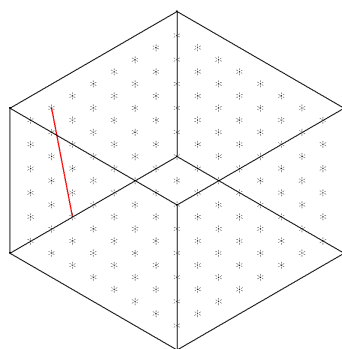
an arrangement of  $8 \times 8 \times 6$  cells, with a total macro-cell number of 384 and a volume of  $48 \text{ cm}^3$ . In (a) the first point was randomly selected and the first tree branch was created. In (b) the second point was selected and the first bifurcation was created to connect the point to the initial branch. In (c) the third randomly selected point is chosen and a new bifurcation is created (from the closest branch) to connect the new point to the tree. In (d), (e), (f) and (g) the tree is shown after connecting the first 10, 50, 100 and 250 selected points, respectively. In (h) the full tree is shown after all 384 points have been connected.

### 4.2.9 Examples of vascular structures

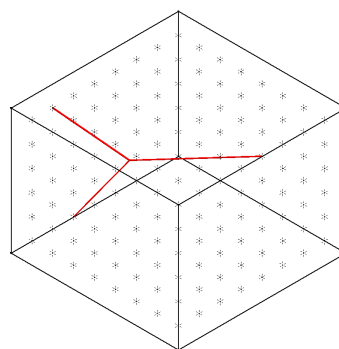
Using the presented algorithm the user can modify the main construction parameters, which are the physiological constraints (flow rate, pressure difference, viscosity, etc.), but it is also possible to change other parameters such as the shape of the three-dimensional volume, the number of macro-cells contained and their arrangement within the space, the size of the macro-cell, the root branch starting point and whether or not a second tree will be constructed (to form a network). Figure 4.19 shows a variety of models that have been constructed using the algorithm. They are presented merely to show the different structures that can be achieved.

## 4.3 Analysis of algorithmically generated vascular structures

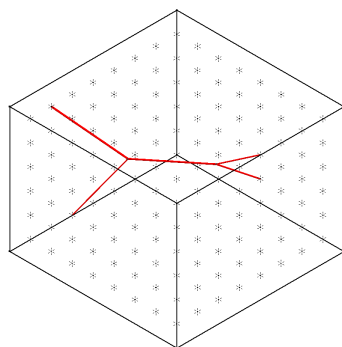
To demonstrate the capability of the proposed algorithm for the intended purpose (for tissue engineering constructs using additive manufacturing methods), experimental fabrication of the model is required. Depending on the type and building material, 3D printers have different resolutions, which will dictate the smallest feature size to achieve an accurate 3D printed structure. The algorithm can produce a wide range of models, depending on the input parameters. In order to find a model suitable for printing, analysing the effect of parameter change on the model branching architecture is essential. Section 4.3.1 will present a brief analysis of nine vascular trees (single trees, to allow for a better visual inspection of the branches) with different input data. After understanding the effect of parameter change and deciding on the basic network branching shape (a planar network), a short analysis is presented in Section 4.3.2 with the aim of finding the set of parameters (namely pressure difference, inlet flow rate and number of terminals in the model) that will produce a model above the required printing threshold.



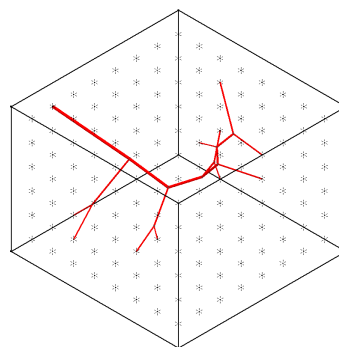
(a) 1 macro-cell connected



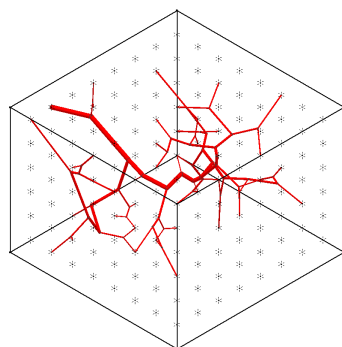
(b) 2 macro-cells connected



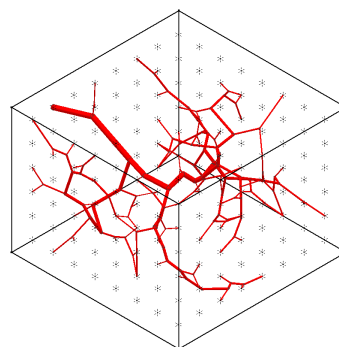
(c) 3 macro-cells connected



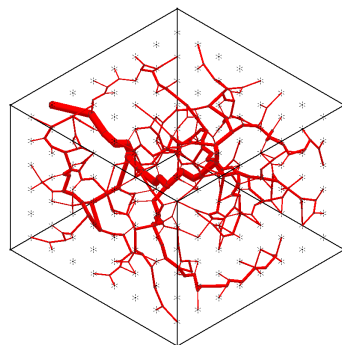
(d) 10 macro-cells connected



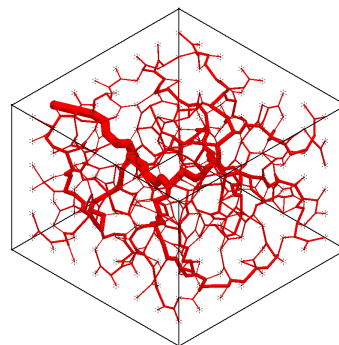
(e) 50 macro-cells connected



(f) 100 macro-cells connected



(g) 250 macro-cells connected



(h) 384 macro-cells connected

Fig. 4.18 Arterial tree at different stages of growth. The image shows increasing number of macro-cells connected to the tree, from a single branch in Figure 4.18(a) to a full tree in Figure 4.18(h).

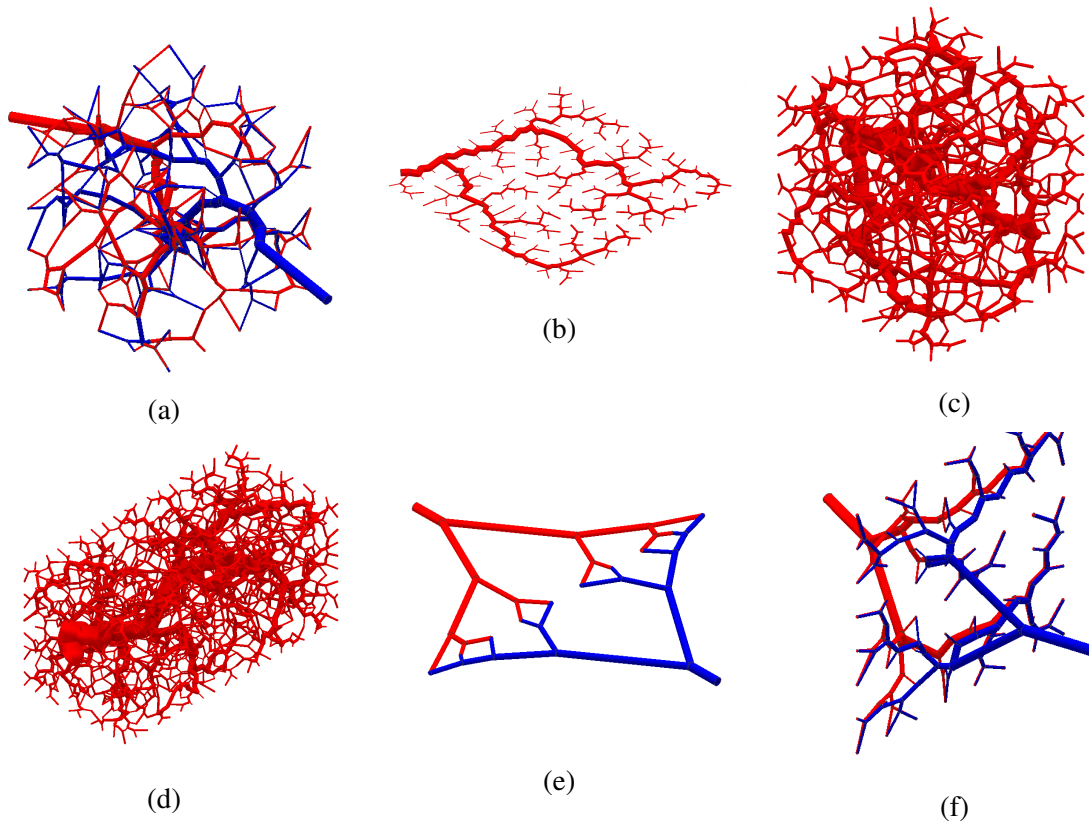


Fig. 4.19 Different vascular models that have been created using the algorithm here presented. (a) Vascular network with 125 macro-cell points. (b) Planar vascular tree with 256 macro-cell points. (c) Vascular tree with 1000 macro-cell points. (d) Vascular tree with 2000 macro-cell points. (e) Planar vascular network with 10 macro-cell points arranged in a line. (f) Vascular network with 64 macro-cell points arranged in a plane.

### 4.3.1 Effect of parameter change in algorithmically generated structures

The change in structures driven by parameter variations is studied in this section with a set of 9 models and their analysis. The setup for the construction of the models will be explained first. As stated in 4.2.2, a macro-cell is a sub-unit of the main volume that represents a cluster of cells and capillaries. By connecting the macro-cell to the arterio-venous network, perfusion of the internal macro-cell region is ensured. Following the approach of Kretowski et al. [81], in the present work the simulated volume of the macro-cell is set to  $0.125 \text{ cm}^3$

(0.5 cm per edge). For all vascular trees in this section the simulated three-dimensional cubical space has 6 macro-cells per side (3 cm), thus, having a total volume of  $27 \text{ cm}^3$ . Each tree has 216 macro-cells (number of terminal points  $N$ ) in total, which means there are  $(2 \times N) - 1 = 431$  branches per tree.

A model was first created with a specific set of input parameters and is referred to as "original model". The order of selection of the macro-cell points from the original model was saved and used to produce the subsequent models (referred to as "test models"), to allow all the trees to have the same branching structure for a consistent comparison. With the purpose of observing the effects of each input parameter individually in the vascular tree morphology, in each of the test models only one input parameter value was modified, either an increase or a decrease of the original value, while the rest of the parameters remained the same as in the original model. The input parameters of the original model and test models are shown in Table 4.2.

Table 4.2 Input parameters for original and test models.

| Model  | $Q_{\text{cell}}$<br>[mL/h] | $\Delta P_{\text{inlet-term}}$<br>[mm Hg] | $\mu$<br>[Pa.s]    | Bif. opt.<br>variable |
|--|-----------------------------|---|--------------------|-----------------------|
| Original model   | 4                           | 95 → 90                                   | $4 \times 10^{-3}$ | 0.2                   |
| Test model 01 - Decreased $Q_{\text{cell}}$              | 2                           | 95 → 90                                   | $4 \times 10^{-3}$ | 0.2                   |
| Test model 02 - Increased $Q_{\text{cell}}$              | 6                           | 95 → 90                                   | $4 \times 10^{-3}$ | 0.2                   |
| Test model 03 - Decreased $\Delta P_{\text{inlet-cell}}$ | 4                           | 95 → 93                                   | $4 \times 10^{-3}$ | 0.2                   |
| Test model 04 - Increased $\Delta P_{\text{inlet-cell}}$ | 4                           | 95 → 80                                   | $4 \times 10^{-3}$ | 0.2                   |
| Test model 05 - Decreased $\mu$                          | 4                           | 95 → 90                                   | $4 \times 10^{-4}$ | 0.2                   |
| Test model 06 - Increased $\mu$                          | 4                           | 95 → 90                                   | $4 \times 10^{-2}$ | 0.2                   |
| Test model 07 - Dec bif. opt. const.                     | 4                           | 95 → 90                                   | $4 \times 10^{-3}$ | 0.05                  |
| Test model 08 - Inc bif. opt. const.                     | 4                           | 95 → 90                                   | $4 \times 10^{-3}$ | 0.4                   |

From the table,  $Q_{\text{cell}}$  is the volumetric flow rate at the macro-cell level,  $\Delta P_{\text{inlet-cell}}$  is the pressure difference between the inlet and macro-cell points (or terminal points) and  $\mu$  is the fluid viscosity. The values of these parameters were intended as an approximation to physiological values, calculated from [23]. The bifurcation optimisation variable is a fraction that defines the length of the test distance for the optimisation of bifurcations, as explained in Section 4.2.4.

The original model and the test models were built in Inventor® as solid three-dimensional models and are shown in Figure 4.20. Upon visual inspection, it is evident that the radii of

the branches vary, with test model 05 (low viscosity) having the thinnest branches and test model 06 (high viscosity) having the thickest. Most of the models have the same branching structure and positioning, with the exception of test model 07 (low bifurcation optimisation variable value) and test model 08 (high bifurcation optimisation variable value). As explained in 4.2.4, the bifurcation optimisation variable is a fraction of the smallest side of the triangle formed by the external points of the parent and daughter branches of the current bifurcation. It defines the resolution of the optimisation (the length that the bifurcation point will move in the plane). Thus, although all of the models follow the same iterative order of selection of points it is expected that by changing the constant in test models 07 and 08, most of the original bifurcation points were modified. It can be observed that in test models 07 in Figure 4.20(h) and 08 in Figure 4.20(i) the main branches of the trees have a different structure than the rest of the models. The bifurcation optimisation variable is a parameter that aids in the tree structure formation, but does not have a direct relationship with  $Q$  or  $\Delta P$ .

The data that defines a vascular tree morphology are the branching structure (tree skeleton, which is represented by an array of three dimensional coordinates of each branch's start and end points) and the branches' radii. The models are in accordance with Poiseuille's law of flow and Murray's law of bifurcations. Thus, if the input values are the viscosity, flow rate, and the pressure difference from inlet to terminal points, this means that the variables that change when a tree is constructed are the lengths and radii of the tree branches. If the order of selection of points is the same for all the models, this means that the tree skeleton is the same for all of them. Thus, for the original model and test models 01 to 06 the only variable that can change, given any variation in input parameters, is the branches' radii. The aim of this section is to determine in which ways the parameter variations affect the radii (i.e. whether the change is linear, non-linear, with abrupt or small changes, distribution and dispersion of the radii, etc.) with the purpose of evaluating the viability for fabrication and experimental flow analysis.

Figure 4.21 presents a chart of all the models and their average branch radius. The error bars indicate the range of radii in the models, where the upper bar shows the largest radius (root branch) and the lower bar represents the smallest radius (which corresponds to one of the terminal branches of the tree). It is evident that the maximum changes in the range of the branches' radii are shown in the models with a change of viscosity  $\mu$  (models 05 and 06). With respect to the original model, the model with a lower viscosity shows a smaller average branch radius and a smaller range of branch radii, while the model with a larger viscosity shows the opposite behaviour: a larger average branch radius and the largest range of branch

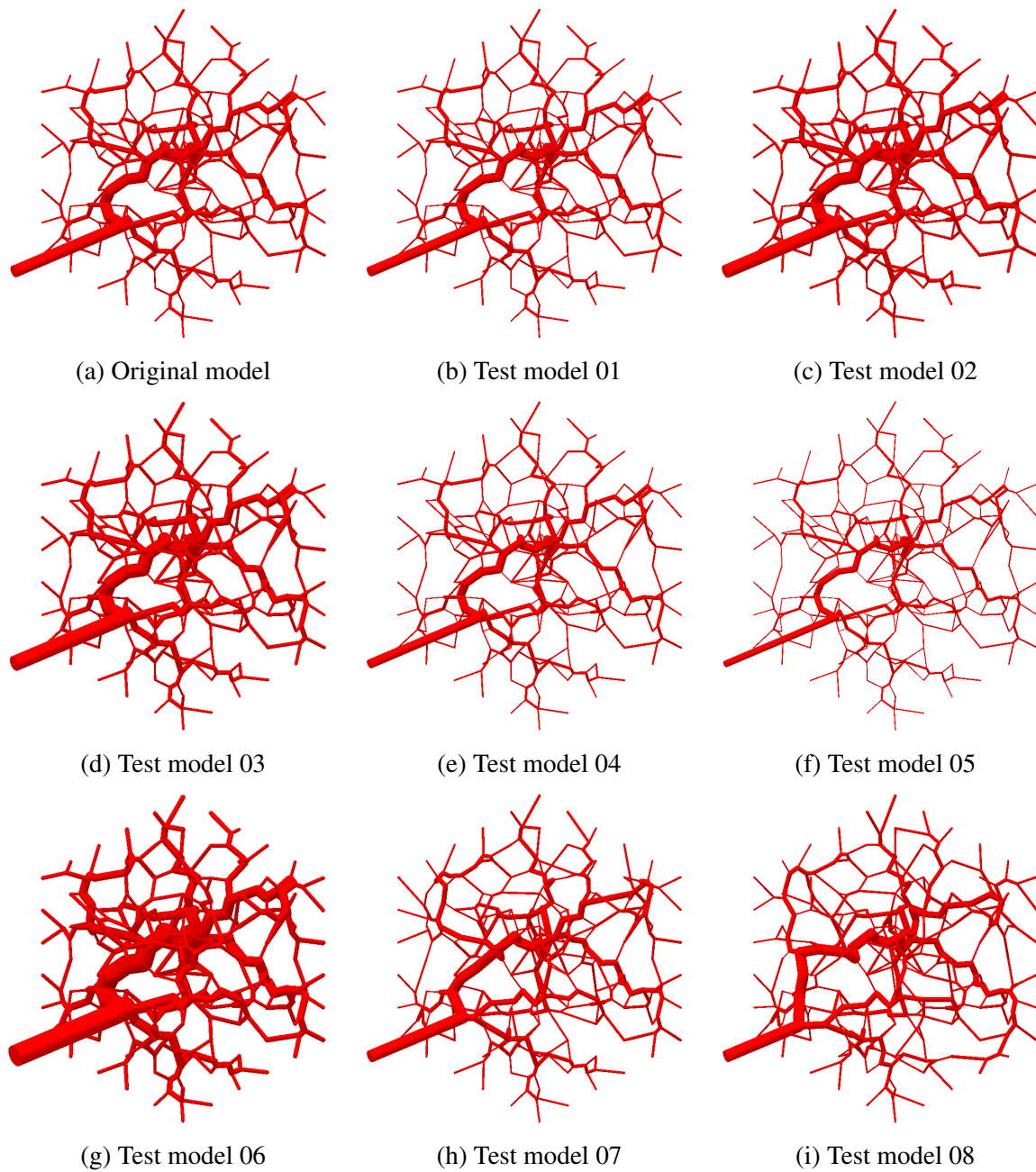


Fig. 4.20 Test models for parameter effect analysis.

radii of all the test models. The models with increased and decreased value of the bifurcation optimisation variable (07 and 08) have no apparent difference from the original model. Apart from models 07 and 08, it can be observed that the models with increased and decreased  $Q_{cell}$  (01 and 02) have a very small variation from the original model. This could be useful for experimental work, as it would allow some variation of the flow rate without significantly affecting the results (i.e. having the structure of the original model but experimentally using a smaller value of  $Q_{cell}$ ).

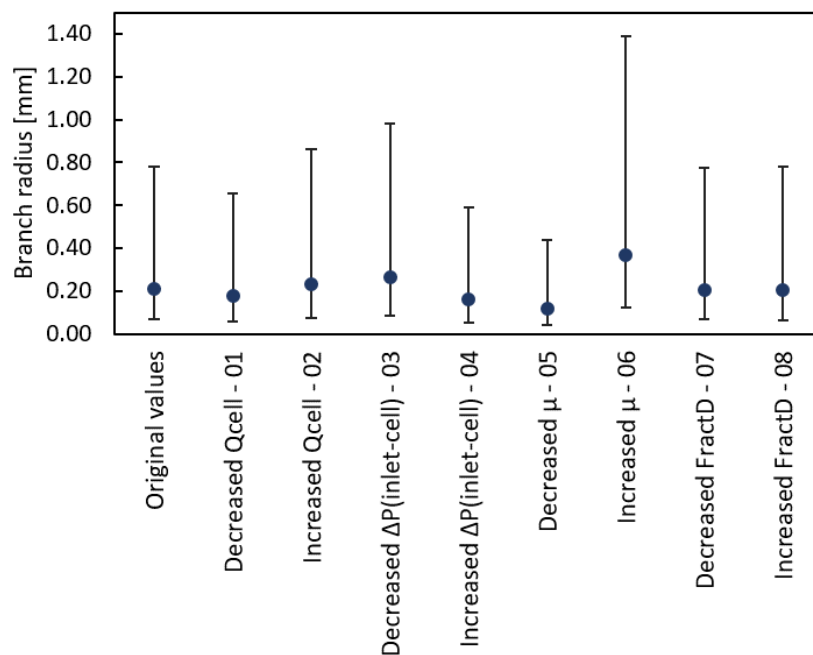


Fig. 4.21 Average tree branch radius of original model and test models. The upper error bars show the largest branch radius in the tree (root branch), and the lower error bars indicate the radius of the smallest branch (terminal).

Figure 4.22 shows a chart of the average terminal branch radius of the models. The error bars in this chart indicate the standard deviation of the terminal branch radii. For example, from Figures 4.21 and 4.22, the original model presents a root radius of 780  $\mu\text{m}$ , an average branch radius of 208  $\mu\text{m}$  (considering all tree branches in the model), and most of the terminal branches fall approximately between 100  $\mu\text{m}$  and 150  $\mu\text{m}$ , with the average terminal radius being 125  $\mu\text{m}$ . The largest changes in average terminal radius and their standard deviation are found on the models with modified viscosity (models 05 and 06). It is observed that in Figure 4.21 the average branch radius of the original model is similar to both models with different bifurcation optimisation variable (models 07 and 08), as well as their

root branch radius and smallest terminal branch radius. However, Figure 4.22 shows that the average terminal radii of these models are both larger than the original model, as well as their standard deviation. It would be expected that the model with decreased bifurcation optimisation variable (07) had a smaller distribution range of the terminal radii given that the resolution for the optimisation process is higher, but it is observed that its range of terminal radii is greater than the original model. This could indicate that the benefits of a higher optimisation resolution might be lost if the value is not optimal, as in this case. Therefore, this parameter could have a crucial impact for a better physiological representation of the tree structures.

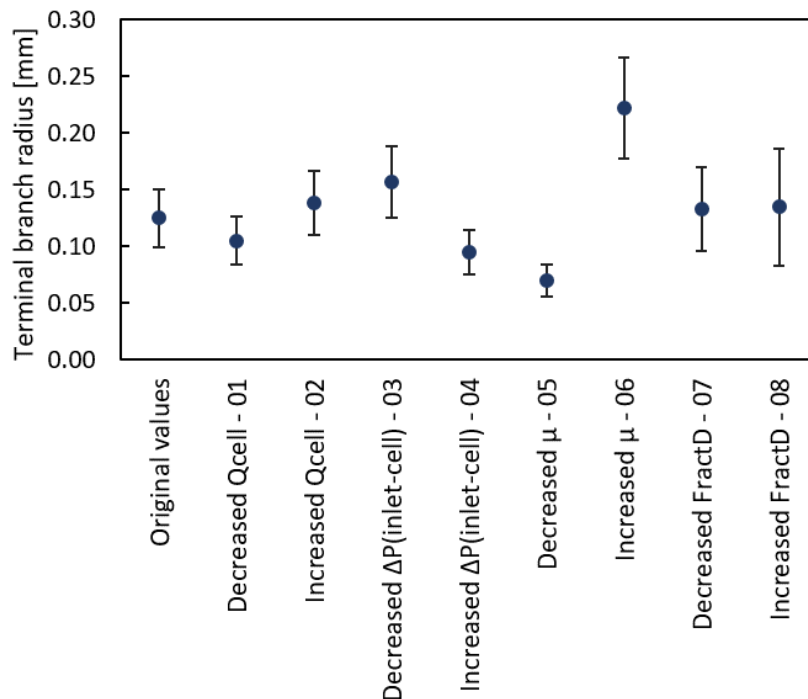


Fig. 4.22 Average terminal branch radius of original model and test models. The error bars indicate the standard deviation of the terminal branches on each model.

In Figures 4.23 to 4.26, the individual branches of the model were sorted by their radius in increasing order, and the corresponding value of flow rate  $Q$  or pressure difference  $\Delta P$  are plotted in the charts, as these are the main variables of interest in the analysis. For each chart, the profile shape is the same for the models being compared but the range of radii across which it is extended varies. Viscosity was modified only for the purpose of observing the difference in radii with different values, but for experimental models in chapters ahead this

parameter will be constant and in accordance with the fluid in use.

Figure 4.23 shows the flow rate  $Q$  corresponding to each branch radius, for different  $\Delta P_{inlet-cell}$  values (original model, and test models 03 and 04). All the terminals have a fixed  $Q_{cell}$  value and this is the same for the three models, which means that they will have the same  $Q_{inlet} = 864$  mL/h at their root branch. However, due to the change in  $\Delta P_{inlet-cell}$ , the radii of the models differ. For example, in test model 04 (with  $\Delta P_{inlet-cell} = 15$  mm Hg) the maximum  $Q$  is achieved at the root branch (inlet) which has a radius of  $592 \mu\text{m}$ . The same  $Q_{inlet}$  value is achieved at the roots of the other two models, but at their respective root radii of  $780 \mu\text{m}$  for the original model (with  $\Delta P_{inlet-cell} = 5$  mm Hg) and  $980 \mu\text{m}$  for test model 03 (with  $\Delta P_{inlet-cell} = 2$  mm Hg). Thus, for an increase in  $\Delta P_{inlet-cell}$  at a constant branch  $Q$ , the branch radii tend to decrease. Although it may seem from the chart that the decrease in radii is linear, it is important to notice that the increments of the pressure difference are not at constant intervals. When increasing  $\Delta P_{inlet-cell}$  from 2 to 5 mm Hg (increment of 3 mm Hg), the root radius decreases by  $200 \mu\text{m}$ , but when increasing  $\Delta P_{inlet-cell}$  from 5 to 15 mm Hg (increment of 10 mm Hg), the root radius only decreases by  $188 \mu\text{m}$ . For the experimental models the main restriction is regarding the resolution of the 3D printer used to fabricate the models, so all the diameters in the model should be greater than  $250 \mu\text{m}$ . It is observed in the chart that from the three models, model 03 has almost all of its branches greater than  $125 \mu\text{m}$ , so it indicates that using a low value of  $\Delta P_{inlet-cell}$  will produce structures that are suitable for printing.

In a similar manner, Figure 4.24 shows the values of  $\Delta P$  of each branch according to its radius, and it is evaluated for three different values of flow rate at the cell  $Q_{cell}$ . In this case, the pressure difference is preserved across the models, but the radii varies due to a change in  $Q_{cell}$ . For example, in test model 01 (with  $Q_{cell} = 2$  mL/h), the pressure difference at the root branch (which has a radius of  $650 \mu\text{m}$ ) is  $0.84$  mm Hg. In the other two models the root branch has the same value, but at their respective radii ( $780 \mu\text{m}$  for the original model with  $Q_{cell} = 4$  mL/h and  $862 \mu\text{m}$  for test model 02 with  $Q_{cell} = 6$  mL/h). Thus, for an increase in  $Q_{cell}$ , and at a constant branch  $\Delta P$ , the branch radii increase. It is also observed that in this case, even though the increase in  $Q_{cell}$  is linear (with increments of 2 mL/h), the chart shows that the profiles do not have the same separation among them. If we observe the data points that represent the root branches in the models (the largest radius from each data set) it is clear that the red square is closer to the blue dot than the green triangle, which indicates the non-linearity of the change. However, the chart shows that most of the points of the data sets fall on the same region, which indicates that the change  $Q_{cell}$  might not be

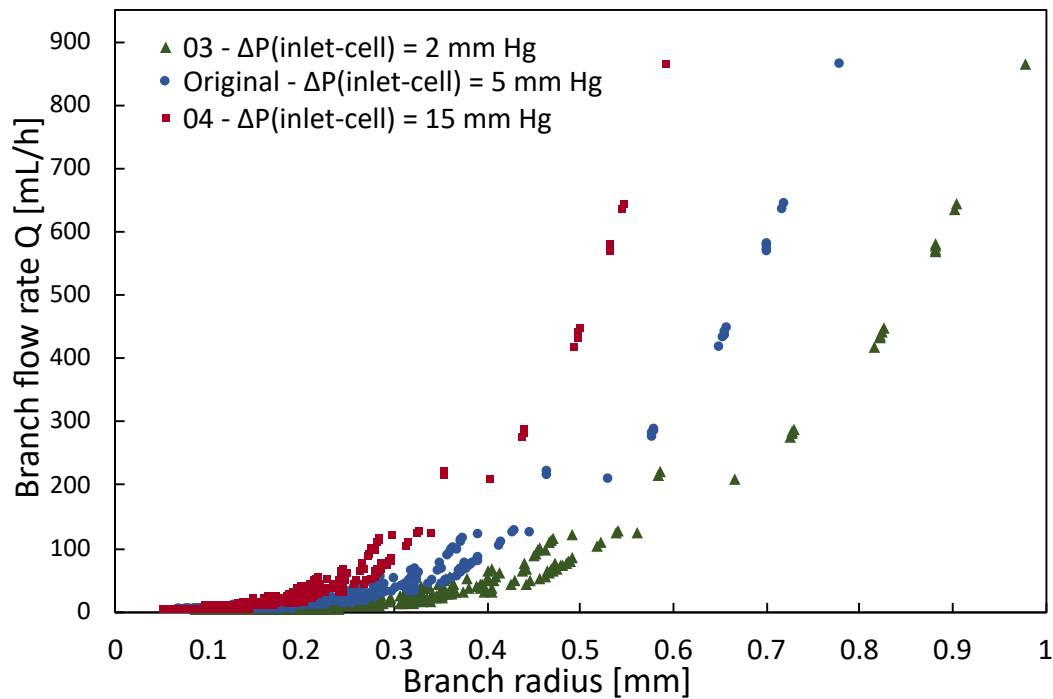


Fig. 4.23 Branch flow rate  $Q$  vs radius  $r$  for models with different values of  $\Delta P_{\text{inlet-cell}}$ . Original model  $\Delta P_{\text{inlet-cell}} = 5 \text{ mm Hg}$ , Decreased  $\Delta P_{\text{inlet-cell}}$  (test model 03) = 2 mm Hg, Increased  $\Delta P$  (test model 04) = 15 mm Hg.

significant. Knowing this would be useful for experimental purposes, as it could possibly be the safest parameter to alter without significantly compromising the closeness to an optimal physiological geometry. Although initially from the chart it would be implied that having a higher flow rate would produce structures where all the branch radii are greater than 125  $\mu\text{m}$ , in practice a very high flow rate might not be ideal for the experimental work. If the flow rate is set too high, it would be physically impossible to use conventional experimental methods to study the flow behaviour, such as particle image velocimetry. Therefore, it would be better to choose lower flow rates, as long as the structures are above the printing limit.

Figure 4.25 shows a chart of the branch flow rate  $Q$  for each branch radius, evaluated for three different values of flow rate at the cell  $Q_{\text{cell}}$  (model 01 with  $Q_{\text{cell}} = 2 \text{ mL/h}$ , original model with  $Q_{\text{cell}} = 4 \text{ mL/h}$  and model 02 with  $Q_{\text{cell}} = 6 \text{ mL/h}$ ). The purpose of this chart is to show the effect of a change in  $Q_{\text{cell}}$  in the general  $Q$  profile of the tree. For an increase in  $Q_{\text{cell}}$ , there is an increase in the radii of the model, and obviously an increase in the  $Q_{\text{inlet}}$  at the root branch. For model 01 the root branch has a radius of 660  $\mu\text{m}$  and a  $Q_{\text{inlet}}$  of 432 mL/h; for the original model the root branch has a radius of 780  $\mu\text{m}$  and a  $Q_{\text{inlet}}$  of 864 mL/h; for model 02 the root branch has a radius of 860  $\mu\text{m}$  and a  $Q_{\text{inlet}}$  of 1296 mL/h.

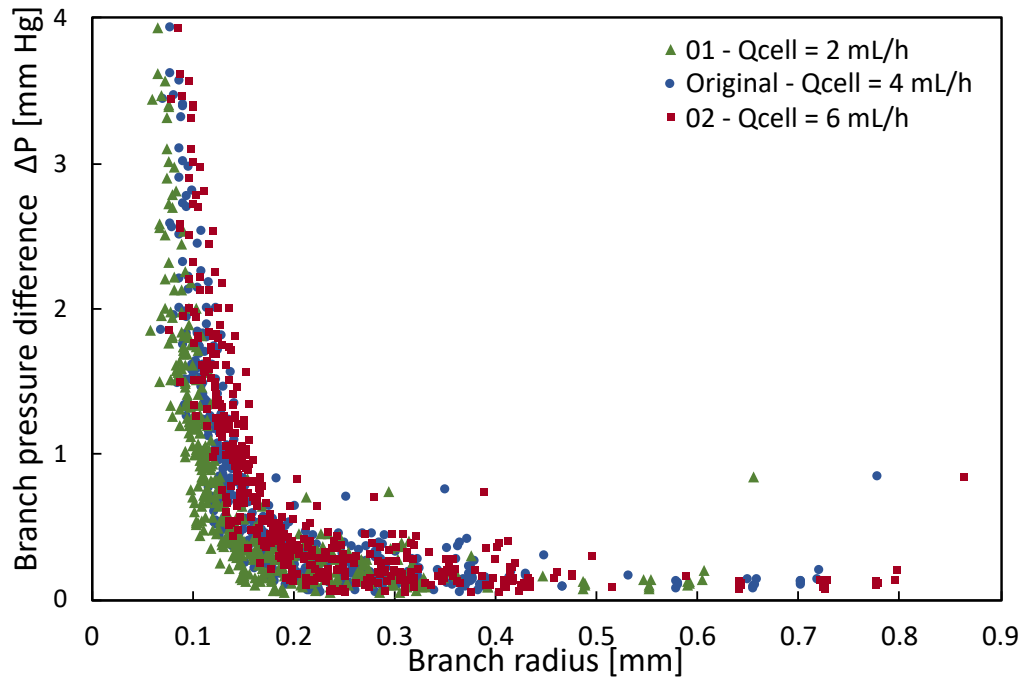


Fig. 4.24 Branch pressure difference  $\Delta P$  vs radius  $r$  for models with different values of  $Q_{cell}$ . Original model  $Q_{cell} = 4$  mL/h, Decreased  $Q_{cell}$  (test model 01) = 2 mL/h, Increased  $Q_{cell}$  (test model 02) = 6 mL/h.

This shows that the change is close to being linear, as there is approximately the same increment in both branch radii and branch flow rate  $Q$  from model 01 to original model, and from original model to model 02. In this chart it is also evident that the distribution of the data points is very similar among the three models, which is in accordance with the observations from the chart in Figure 4.24.

Similarly, Figure 4.26 shows a chart of the pressure difference  $\Delta P$  for each branch according to its radius, evaluated for different values of total pressure difference from inlet to cell  $\Delta P_{inlet-cell}$  (model 03 with  $\Delta P_{inlet-cell} = 2$  mm Hg, original model with  $\Delta P_{inlet-cell} = 5$  mm Hg and model 04 with  $\Delta P_{inlet-cell} = 15$  mm Hg). It is observed that for an increase in  $\Delta P_{inlet-cell}$  there is a decrease in the radii of the model and an overall increase in the  $\Delta P$  of each individual branch in the tree. As with the chart in Figure 4.23, the increments of  $\Delta P_{inlet-cell}$  are not linear (from 2 to 5 mm Hg and from 5 to 15 mm Hg). It is observed that the distribution of data points for the model with increased  $\Delta P_{inlet-cell}$  (red squares) has the greatest number of branches with radius smaller than 125  $\mu\text{m}$ . Thus, the same conclusion is obtained from both charts: a model with a lower value of  $\Delta P_{inlet-cell}$  is preferred.

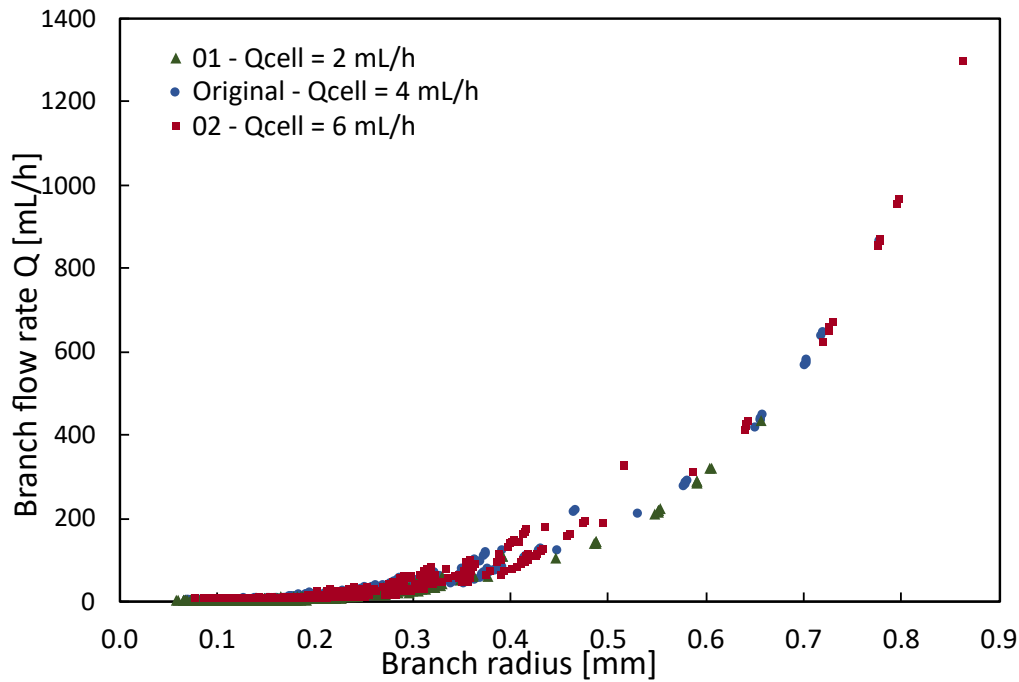


Fig. 4.25 Branch flow rate  $Q$  vs radius for models with different values of  $Q_{cell}$ . Original model  $Q_{cell} = 4$  mL/h, Decreased  $Q_{cell}$  (test model 01) = 2 mL/h, Increased  $Q_{cell}$  (test model 02) = 6 mL/h.

The total tree volume of each model is shown in Figure 4.27. The volume was calculated by adding the volumes of each individual branch in the tree, as their radii and lengths are known. It is evident that viscosity is the variable that produces the greatest change in volume, followed by  $\Delta P$ . It is observed that the models with different bifurcation optimisation variable values (models 07 and 08 with values of 0.05 and 0.4, respectively) have very similar volumes ( $204.7 \text{ mm}^3$  for model 07 and  $208.7 \text{ mm}^3$  for model 08) and also very similar to the original model, which may indicate that the volume of the models is preserved despite having a slightly different tree structure. From the previous charts, it was determined that a decreased value of  $\Delta P_{inlet-cell}$  would be considered advantageous. However, it must be taken into account that it produced the second largest volume from the models, and that the aim of the algorithm is to minimise it. In a similar way, it was discussed that it would be ideal to have a small value of  $Q_{cell}$  due to visualization of flow under the microscope. Although a reduced  $Q_{cell}$  produces a smaller volume, it also means that the radii in the structure are smaller and possibly not suitable for fabrication. Therefore, a balance must be achieved where optimal values of  $\Delta P_{inlet-cell}$  and  $Q_{cell}$  are found.

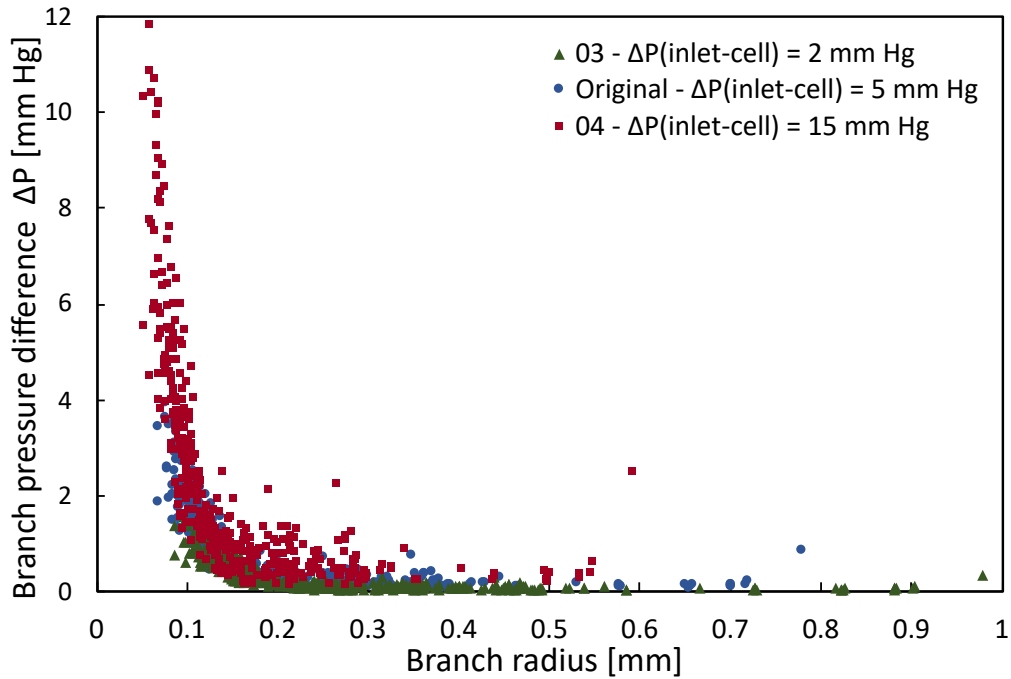


Fig. 4.26 Branch pressure difference  $\Delta P$  vs radius  $r$  for models with different values of  $\Delta P_{\text{inlet-cell}}$ . Original model  $\Delta P_{\text{inlet-cell}} = 5$  mm Hg, Decreased  $\Delta P_{\text{inlet-cell}}$  (test model 03) = 2 mm Hg, Increased  $\Delta P_{\text{inlet-cell}}$  (test model 04) = 15 mm Hg.

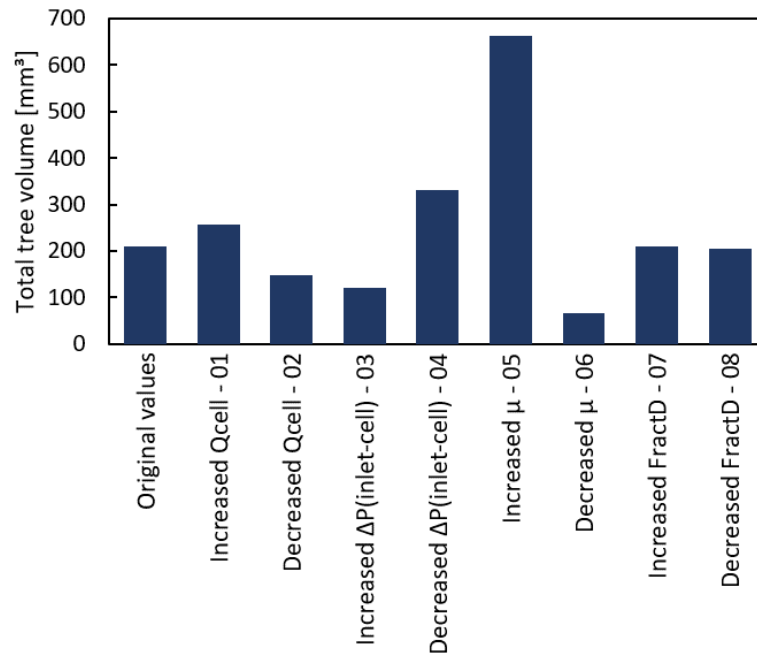


Fig. 4.27 Total tree volume of original and test models. It was calculated as the sum of individual volumes of the trees' branches.

Figure 4.28 shows the total computing time (in minutes) of each model. To obtain the computing time, a time stamp was created for each model at the beginning and at the end of its construction process. As expected, the model that took the longest computing time was test model 07, with a bifurcation optimisation variable of 0.05. By decreasing the distance of the movement of test points for the optimal bifurcation point, it is obvious that the process will consume more time. What is unexpected is that despite the notorious difference in computing time, both models 07 and 08 have a very similar volume (as seen above in Figure 4.27), which indicates that it might be unnecessary to use a small constant in order to produce a structure with a minimised volume, as it could only lead to a greater computing time while maintaining a similar volume as a structure produced with a larger constant.

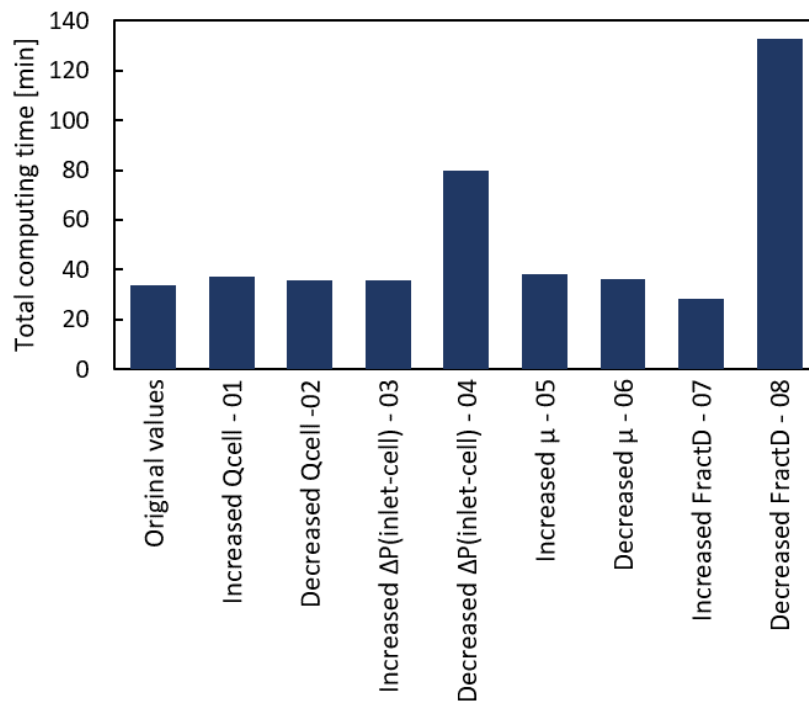


Fig. 4.28 Total computing time of original and test models. It is calculated by registering the time at the beginning and end of the tree construction process.

The change in bifurcation optimisation variable value appears to have no effect on the tree volume. However, considering that the smaller the value is, it needs more computing time, it has been decided that the best value would be that of the original model as it produces a structure with a smaller range of terminal branches' radii, as shown in Figure 4.22 and discussed previously.

### 4.3.2 Effect of input parameter change in simplified planar network

In the previous section, a set of models was built by changing one parameter at a time, in order to study the effect of each input parameter in the vascular tree structures. For experimental purposes, however, it is not possible to use such tree structures mainly for two reasons: a vascular network requires two trees and it would be a very complex structure with many collisions among their branches, and there is the limitation regarding the size of the vessels, as the minimum feature size that can be fabricated with the available 3D printing technology is 250  $\mu\text{m}$ . For this motive, a set of 48 models with a simplified planar structure were created. The models were simplified by defining a single line of macro-cells in the centre of the 3D volume in order to produce a planar network structure. Although the networks seem too simple, they are a good representation of the algorithm's behaviour and will allow for a better inspection of each individual branch under the microscope, contrary to inspecting branches with the complex morphology of a cubic-bound network with multiple macro-cells per side.

Similar to the previous section, the parameter values that were selected were based on physiological data, calculated from [23] and taking into consideration the main observations from the charts in Figures 4.21 to 4.28. The parameters are:

- Pressure difference (inlet to macro-cell):

$$\Delta P_{inlet-cell} = 1, 2, 3 \text{ mm Hg}$$

- Volumetric flow rate (at inlet):

$$Q_{cell} = 1, 2, 3, 4 \text{ mL/h - for each value of } \Delta P$$

- Number of macro-cells in the model:

$$N = 5, 10, 15, 20 - \text{for each value of } \Delta P \text{ and } Q_{in}$$

With these parameters, there are four main sets of models, which correspond to the number of macro-cells in the model. Thus, there is a set of models with 5 cells, a set with 10 cells, a set with 15 cells and a set with 20 cells. Each set has 3 subsets, one for each value of  $\Delta P_{inlet-cell}$ . And in turn, each of these subsets has a model with each of the test values of  $Q_{in}$ . Then, there are 48 models in total.

Each subset of models given by the number of macro-cells was arranged to have the same tree branching shape (by assigning the same order of selection of points for all the models in the set) in order to be able to compare the structures by the variation in radii only. Otherwise, the model branches would have also varied in length and position, making it impossible to compare the structures to each other. The branching shape of each set of vascular networks

for a given  $N$  are shown in Figure 4.29. In other words, all the 12 models in the set of  $N = 5$  cells have the same branching structure shown in (a), all the 12 models in the set of  $N = 10$  cells have the same branching structure shown in (b), and similarly for the sets of  $N = 15$  and  $N = 20$ . Thus, the radii is the only attribute that will change in the models.

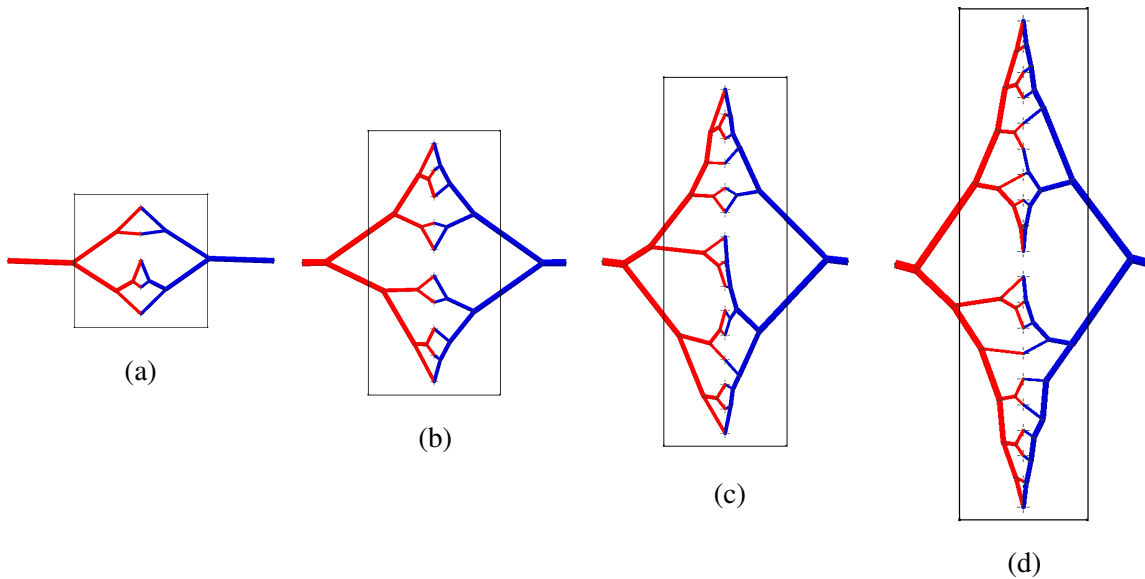
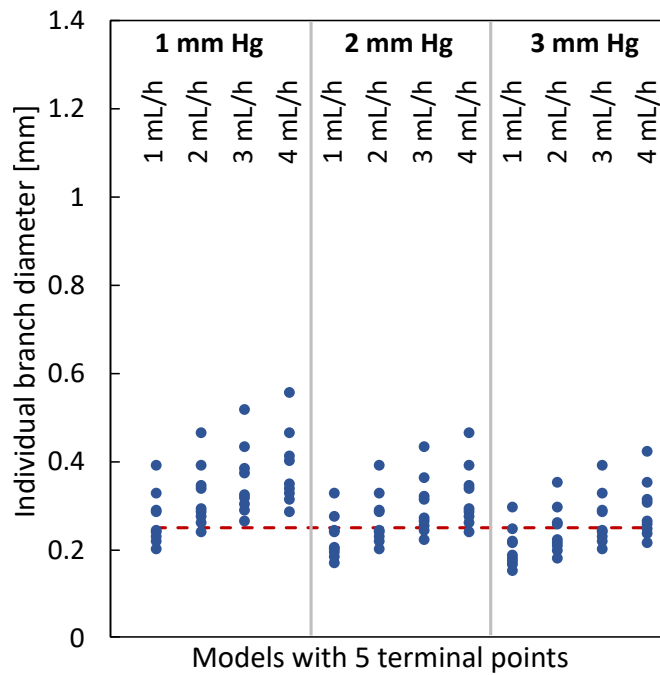
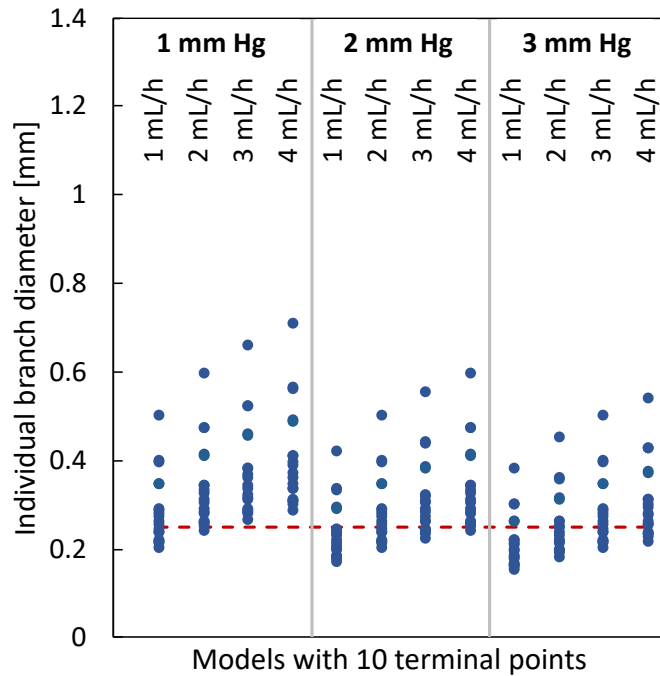


Fig. 4.29 Shape of network structures with (a)  $N = 5$ . (b)  $N = 10$ . (c)  $N = 15$ . (d)  $N = 20$ .

The comparison of radii between the 48 models evaluated is shown in Figures 4.30 to 4.33. Each set of models is shown in a different chart, and the subsets are denoted by vertical grey lines. Each vertical line of blue points in the chart represents a model's arterial tree (only the arterial tree in each network was studied for a consistent comparison). Each point marks the value for the diameter of a branch in the tree, with the point at the top representing the root branch diameter, and the point at the bottom representing the smallest terminal branch in the model. The dotted red line across models represents the limitation in size for the additive manufacturing process that is currently used for the physical fabrication of the models (3D printing). This means that only models with all of their points above the red line ( $250 \mu\text{m}$ ) are candidates for 3D printing.

It can be observed that as the volumetric flow rate  $Q_{cell}$  increases, so does the diameter of the branches and their dispersion (by dispersion, the intended meaning is the range from the radius of the root branch to the radius of the smallest terminal branch). On the contrary, increasing the pressure difference  $\Delta P$  decreases the diameters and the dispersion. Increasing the number of macro-cells  $N$  obviously increases the number of branches in the models,

Fig. 4.30 Effect of parameter variation on planar networks with  $N=5$ .Fig. 4.31 Effect of parameter variation on planar networks with  $N=10$ .

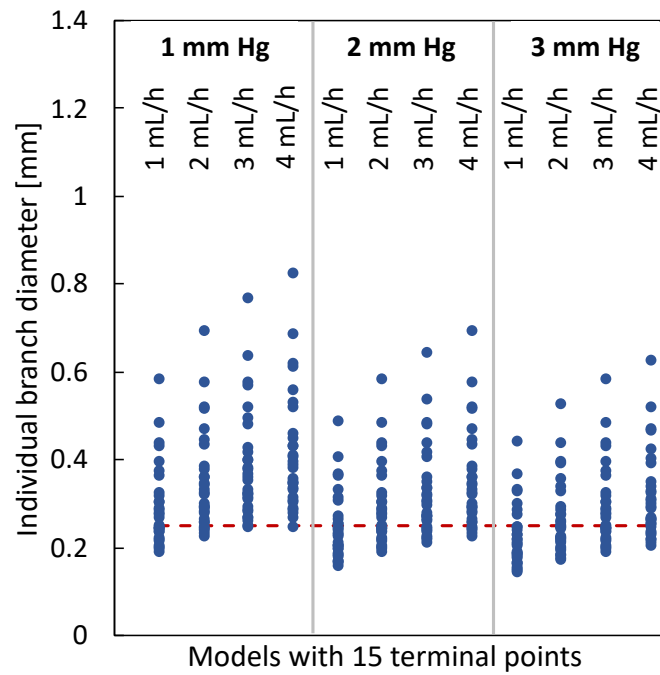


Fig. 4.32 Effect of parameter variation on planar networks with  $N=15$ .

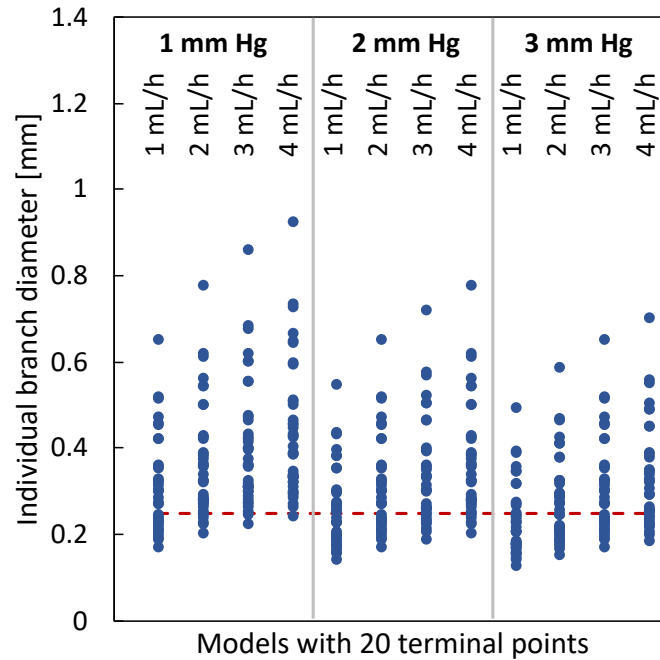


Fig. 4.33 Effect of parameter variation on planar networks with  $N=20$ .

overall increasing the size range of the branches. None of the models with 20 cells or 15 cells fulfil the condition of having all the branches' diameters above the printing threshold, therefore these were discarded for experimental purposes. From the remaining models with 5 and 10 cells, the ones above the threshold were selected as potential experimental models.

## 4.4 Conclusions

In this chapter, a description of the algorithm developed for the automatic construction of three-dimensional vascular structures was presented and described in detail, including the fulfilment of physiological laws, optimisation of bifurcation points, arterio-venous connections and detection of collisions. A set of models in a cubical shape with 216 cells was created and analysed to observe the effect of changing input parameters on the tree structure. From this, it was observed that:

- For an increase in  $\Delta P_{inlet-cell}$  at a constant  $Q$ , the branch radii decrease (see Figure 4.23).
- For an increase in  $Q_{cell}$ , and at a constant branch  $\Delta P$ , the branch radii increase (see Figure 4.24).
- For an increase in  $Q_{cell}$ , there is an increase in the radii of the model, and an increase in the  $Q_{inlet}$  at the root branch (see Figure 4.25).
- For an increase in  $\Delta P_{inlet-cell}$  there is a decrease in the radii of the model and an overall increase in the  $\Delta P$  of each individual branch in the tree (see Figure 4.26).
- Although a reduced  $Q_{cell}$  produces a smaller volume, it also means that the radii in the structure are smaller and possibly not suitable for fabrication. Thus, an optimal balance must be achieved between the values of  $\Delta P_{inlet-cell}$  and  $Q_{cell}$ .
- A model with a large number of cells would imply a large dispersion where some of the branch radii would be below the 3D printing threshold. In addition, a large cubical-shaped network would be physically impossible to analyse under a microscope.
- Ideally, the flow rate  $Q_{cell}$  must be low enough to allow experimental flow analysis with fluorescent beads.

- Variations in  $Q_{cell}$  produce a small change in the structures. Thus, given the similarities, it indicates the possibility to experimentally use a lower  $Q_{cell}$  in a structure created with a higher  $Q_{cell}$  value without significantly affecting the experimental results.
- The bifurcation optimisation variable value will be set to the original value for experimental work, as it showed no significant difference in the radii of the tree structures (compared to the original model) and it had a much larger computing time when set to the smallest value.

Based on these findings and their implications for experimental work, a simplified set of models (planar networks) was created to show the input parameter effects on potential experimental models. The radii behaviour in these models is in accordance with the first set of models. The criteria for the eligibility of a network as suitable for 3D printing was based mainly on two factors: i) the smallest branch diameter being above the printing threshold of 250  $\mu\text{m}$ , and ii) the least potentially problematic areas for 3D printing, such as sharp angles, overlapping branches or insufficient spacing between branches near the connecting terminals. From Figure 4.29, it is clear that the models with 15 and 20 terminals have many of such problematic regions due to their branching shape, particularly at the upper and lower extremes. As a result, all the models with 15 and 20 terminals were discarded. From the models with 5 and 10 terminal points, only four models were considered potentially suitable based on their minimum diameter being above the 3D printing threshold. These models are:

- $N = 5, \Delta P_{inlet-cell} = 1 \text{ mm Hg}, Q_{cell} = 3$
- $N = 5, \Delta P_{inlet-cell} = 1 \text{ mm Hg}, Q_{cell} = 4$
- $N = 10, \Delta P_{inlet-cell} = 1 \text{ mm Hg}, Q_{cell} = 3$
- $N = 10, \Delta P_{inlet-cell} = 1 \text{ mm Hg}, Q_{cell} = 4$

These parameters are therefore considered in the construction of a model for experimental purposes. The next chapter will present the experimental work carried out for the analysis of flow in the channels of a vascular network model created with the proposed approach.

# Chapter 5

## Flow in constructed vascular networks: Experimental work

### 5.1 Overview of experimental flow analysis

Chapter 4 presented the proposed method for the creation of 3D vascular network models by means of an algorithm. In order to validate the practical application of the vascular models, experimental analysis of flow through the networks is required. This chapter will present an experimental approach to flow analysis in two algorithmically designed vascular networks fabricated in PDMS. Section 5.2 presents a brief review on techniques used for experimental flow measurements in vessels or fluidic/micro-fluidic channels.

The biggest challenge of the experimental work was that the measurement of flow velocity under high flow rates was not possible due to technical limitations. This represented a problem because the original design parameters involved a high value of flow rate, which could not be recreated experimentally. However, an alternative solution was implemented. This will be explained further in Section 5.3.5, which details the experimental setup used in the present work. Section 5.4 presents the results obtained, which show that the experimental measurements approximate the theoretical calculations.

### 5.2 Experimental analysis of flow in vessel-like structures

Different techniques have been reported over the years for the measurement of flow in micro-vasculature and micro-channels, particularly with application in microfluidics. Among these techniques are: double-slit photometric, video microscopy and image analysis, laser

Doppler anemometer, and particle-measuring methods [119]. Depending on the scale of the flow and the application, some methods are more suitable than others. For example, in some cases it is convenient to measure the differential pressure between inlet and outlet of a channel network [120] [121]. This section presents an overview of the main techniques used for the analysis of flow in vessel-like structures and in fluidic and micro-fluidic channels under experimental conditions. A brief critical analysis is presented for each technique in relation to its suitability for the experimental work performed in this chapter.

Particle image velocimetry (PIV), a method developed by Ludwig Prandtl [122] [123], is considered the most commonly used technique for the measurement of flow [124]. It combines the use of a light source and a camera to capture consecutive images of particles suspended in a fluid as they move across a channel. PIV had issues since its conception as it required manual analysis and measurement of the images. However, with the development of modern technology such as high-speed cameras, and with computer calculations being faster, it is a technique easy to implement on a microfluidic device. Furthermore, the same sample can be used for measuring the flow previous to or during an experiment. It has its drawbacks, for example the solvent requires to be clear for the microscope to be able to discern the particle. Similarly, the substrate of the microfluidic system must be clear. Blood, as a carrying solvent, would be translucent but not clear where particles would be difficult to track, but not impossible. In fact, the use of PIV for measurement of flow in micro-scale channels has been extensively reported, for numerous applications which include measurement of blood flow rates in microfluidic channels [125] [126].

Another technique that would solve the issue of a microfluidic device with non-clear solution or substrate is thermal mass flow sensing. This technique is extensively used for low flow rate measurements, particularly in microfluidics and medical applications [127] [128]. The principle behind thermal mass flow sensors is that a sensing element is surrounded by a fluid and subjected to heat. As the flow past the element increases, the heat dissipation increases. Because of the need for the built-in sensing element, measurement at an arbitrary point is not possible, which would prevent its use for determining flow rates in individual micro-channels of a network. In addition, the sensors are typically expensive.

The most basic approach to measure flow rate is the gravimetric method, which consists of weighing the volume of liquid accumulated over a known time frame, and dividing the total measured weight by the amount of time. It is widely used as a standard method and in some cases for calibration of flowmeters. Richter et al. [129] fabricated microchannels by

micro-machining, varying in width from 28 to 182  $\mu\text{m}$ . For flow rates higher than 0.1  $\mu\text{L}/\text{min}$  they used the gravimetric method, while for flow rates below this value they developed an optical method where a measuring micro-channel with a meniscus is placed after the test channel and the flow velocity at the meniscus is determined using a microscope. However, this technique would require having an opening on each branch (branch cut) to be able to provide the velocity for the whole network, leading to the destruction of the microfluidic device or to the fabrication of multiple samples. Therefore, the sample could not be used after the velocity measurement or would be a different one.

Alvarado et al. [130] developed a micro-scale flowmeter based on electrical capacitance measurement, which is intended for applications of low flow conditions (Reynolds number  $<50$ ). With a similar approach, Arjmandi et al. [131] developed a micro-flow sensor based on the electrical impedance measurement between two electrodes placed on the channel walls. This technique is feasible for using blood as solvent but requires further fabrication steps for each branch (electrodes on the walls) and the “cast method” would not be feasible with this technique.

To overcome the requirement of a clear solvent in PIV, Kim et al. [126] used confocal laser scanning microscopy (CLSM) micro-PIV for the study of blood flow in a micro-channel. The study demonstrates the use of blood cells as the tracing particles, as opposed to most studies of this kind, which use fluorescent particles. The images were acquired at a rate of 30 fps. The micro-channel had a round profile of 100  $\mu\text{m}$  diameter and was fabricated in borosilicate glass. A syringe pump was used to feed the flow. The flow rate is not mentioned, but the reported maximum velocity was of about 200  $\mu\text{m}/\text{s}$ , with a parabolic velocity profile. This technique, however, might not allow substrates with autofluorescence like PDMS to detect the particles. To solve this, an appropriate laser setup might be required or substrate treatment like adding carbon particles to the PDMS.

Leslie et al. [132] proposed a method called ‘multiplexed fluidic resistance measurement’ for micro-channel characterisation by using visible-wavelength dyes (as molecular markers) and a spectrophotometer to measure the flow resistance in different channels simultaneously. This technique would only be useful for independent channels (not interconnected networks), as it is necessary to use different ink dyes for every desired measurement. In addition, it limits the materials that can be used with the spectrometer.

Campagnolo et al. [133] developed a sensor that measures flow velocity in micrometer-scale channels (320  $\mu\text{m}$  of diameter) by 'optical feedback interferometry' (OFI) [134], a technique that uses a laser source as light transmitter as well as detector of the back-scattered light after it hits a moving particle in the fluid. This sensor enables the reconstruction of the velocity profile of flow in the channel. This technique is used in-situ and shows potential but requires a complicated setup and would not be feasible for the present experimental work because of the constrained size of the sensor.

Stern et al. [135] developed a method for flow analysis in microfluidic devices which uses Doppler laser velocimetry (DLV) to measure the Doppler shift of a sequence of bubbles flowing constantly within a microfluidic channel. The Doppler shift is linearly proportional to the flow rate, thus, it can be used to measure it. The channels in the microfluidic device range from 30 to 100  $\mu\text{m}$  and flow rates of approximately 2 mm/s were measured with a reported resolution of 0.08 mm/s. Although it offers a good resolution, this method requires the use of two different liquids that do not mix and have contrasting refraction indices.

Lee et al. [124] proposed a flow rate measuring technique using near infrared (NIR) absorption. With this method, the flow rate is calculated from the temperature difference between the room temperature and the in-situ temperature measurement at the channel obtained by NIR absorption, as the temperature difference varies at different flow rates. The measured flow rates vary from 1 to 100 mL/h in a tube of 3 mm of diameter. This technique requires precise temperature control and a setup for the NIR spectroscopy, which would complicate the measurement of multiple branches.

In the present work, it is necessary to analyse flow in PDMS networks formed by cylindrical channels of diameters varying between 250 and 550  $\mu\text{m}$ , for which the flow is considered Newtonian. The networks are planar and comprised of bifurcating channels, which means that one of the main requirements is that every channel must be measured. Another requirement is that the technique should allow to obtain measurements of velocity profiles. The method should be non-invasive, as it is intended to preserve the PDMS network models for future use. Considering all of this, PIV seems like the most suitable technique for the required experimental measurements.

Regarding the Newtonian flow measurement, Sousa et al. [136] report an analysis of flow patterns for two types of fluids: Newtonian (de-ionised water) and non-Newtonian (aqueous solution of polyacrylamide) in PDMS microchannels. The planar channels have a

rectangular cross section of  $100\ \mu\text{m}$  by  $105\ \mu\text{m}$  and have a bifurcating angle of  $45^\circ$  between the daughter segments. The fluids were seeded with fluorescent particles, which were tracked using a fluorescence microscope with a charge-coupled device (CCD) camera. The results showed that at this scale, for this channel architecture with upstream flow, the behaviour was different for the Newtonian and non-Newtonian fluids, as the non-Newtonian presented some recirculation in the channels.

Regarding velocity profiles and parameter extraction, Pitts and Fenech [137] reported a protocol to obtain micro-PIV measurements of blood flow in PDMS micro-channels, where parameters of interest can be derived, such as shear rate, velocity profile and flow rate. The channels have a rectangular cross section with  $140\ \mu\text{m}$  by  $40\ \mu\text{m}$ . The commercial package Davis (from LaVision) was used to perform the micro-PIV analysis.

Boutin et al. [138] used PIV to study the distribution of flow in a multi-channel fluidic network fabricated in PMMA. The channels of  $5\ \text{mm}$  of width and the particles had an average diameter of  $5\ \mu\text{m}$ . The light source was a laser (Nd-Yag) and the images were captured by a CCD camera.

Overall, PIV is a technique that allows the use of Newtonian fluids, can obtain velocity profiles, and can be used in multi-branched networks.

### **5.3 Experimental analysis of flow in PDMS networks**

Having reviewed some of the most common techniques for experimental flow measurement, it was decided that the experimental flow analysis would be carried out using particle tracking velocimetry (PTV), a process similar to PIV, but where individual particles are traced in order to find the velocity of a fluid. PTV seems to be the most suitable technique for the project, considering size of the network, fabrication material, fluid and particles. This section describes the full experimental process of the present work, including the generation of the 3D network models, the fabrication of the physical experimental models in PDMS, the experimental setup and measurement of flow velocity in the network.

### 5.3.1 Experimental research goals

The main aim of the experimental analysis in this section is to observe the flow behaviour in the PDMS model channels (using PTV) and to determine whether the values of flow velocity are consistent with calculated theoretical values. A secondary aim is to observe how much the diameters of the channels in the fabricated PDMS model deviate from the diameters of the original CAD model.

### 5.3.2 Materials and methods

In this subsection, a summary of materials and methods for the experimental analysis of flow in PDMS networks is provided. In the following sections, every step of the process is explained in more detail.

**Algorithmically-generated planar vascular networks:** Two simplified planar network models were produced for the characterisation of flow (see Figure 5.1, generated with the algorithm presented in [101]). The models are considered representative of the attributes and branching morphology of a complex 3D network. The minimum feature size in the models is 250  $\mu\text{m}$ , considering the limitations of the 3D printing equipment. The key design parameters are: 5 terminal points,  $Q_{term} = 4 \text{ mL/h}$ , dynamic viscosity  $\mu = 0.004 \text{ Pa} \cdot \text{s}$ , and a pressure difference inlet-terminals  $\Delta P_{inlet-term} = 1 \text{ mm Hg}$  for Model 01, 2 mm Hg for Model 02. The algorithm uses Autodesk® Inventor® for the 3D construction of the model.

**PDMS casting of vascular template:** The resulting models were converted to STL file format and fabricated using a Solidscape® S350. This printer used Solidscape® Midas™ castable material (model) and Solidscape® Melt (supporting material). The support material was dissolved in a selective solvent bath (Solidscape® BioAct VSO) in the oven at 65 °C for 4 hours. The models (see Figure 5.4) were stored in fresh solvent at room temperature, until use. Custom-made cylindrical PDMS chambers of 20 mm diameter and 10 mm of depth were used to produce the hollow network models. The chambers had two axially aligned holes on opposite sides for inlet and outlet, in which two pieces of flexible silicone tubing of 1 mm internal diameter were inserted to hold the models in place (see Figure 5.5). A solution of PDMS was prepared using the DOWSIL™ 184 Silicone Elastomer Kit. 18 mL of elastomer was mixed with 1.8 mL of catalyst, and the solution was centrifuged for 5 minutes at 4000g. The PDMS solution was cast inside the chambers to fully cover the network models. For degasification, the sample was placed in a vacuum

chamber (CENCO HYVAC PUMP) and subjected to a few cycles of increasing/releasing the vacuum (up to 29 in Hg). The PDMS was cured in the oven at 60 °C overnight (see Figure 5.7). The Midas™ material was liquefied in the PDMS by placing the sample in a bath of nearly boiling distilled water for 5 minutes, and it was flushed out of the network using a syringe. Acetone was injected into the network to eliminate any residue of the model material. The finished PDMS model with the embedded vascular network is shown in Figure 5.8. Branch diameters were measured using a Zeiss microscope (Axio Observer Z1/7).

**Flow velocity measurements:** Particle Tracking Velocimetry (PTV) was used to measure the flow velocities in the middle plane of the channels under steady flow conditions. Phosphate buffered saline (PBS) with 1 µm red fluorescent beads (FluoSpheres™ Polystyrene Microspheres) was fed into the PDMS network using a syringe pump (Graseby 3200). A concentration of 10,000 beads/mL was used. Each end of the PDMS network was connected to a 2 mm diameter tube via luer lock interfaces. At the inlet, a 65 mm long tube was connected to a 20 mL syringe mounted to the pump, to supply the working fluid into the PDMS network. The outlet of the PDMS worked as the drain reservoir. A 55 cm long tube was connected to a Petri dish through a drilled hole on its wall. A small hydrophilic membrane was attached to the tubing outlet to avoid drop formation. Images were acquired using a Zeiss Microscope (Axio Observer Z1/7), equipped with an ORCA-Flash4.0 Scientific CMOS camera (Hamamatsu C11440, 2048 x 2048 pixels). The experimental setup was on a vibration-isolation air table. Images were analysed using a custom LabView-based script. The acquired raw images in the jpeg format were post-processed using ImageJ by splitting every image in its red, blue and green channels (RGB), eliminating the blue and green, and converting the remaining red channel images to greyscale (8-bit image). The software analysed a sequence of images taken at a frame rate of 30 fps and calculated the distance that individual beads moved from one frame to the next (see Figure 5.14). For every branch in the PDMS network, three sets of 300 consecutive images were obtained at two different flow rates (2 and 5 mL/h), giving a total of 900 images for each branch per flow rate value. Charts for the velocity profile of flow in every channel of the network were obtained by plotting the obtained velocity for each bead (see Figures 5.16 to 5.19).

**Comparison of experimental flow velocity measurements and theoretical calculations:** Experimental branch maximum velocities were obtained from the velocity profile charts. For every branch, two theoretical maximum velocity values were calculated: one using the original diameter from the CAD model, and another using the experimental model diameter. Theoretical maximum velocities were calculated as twice the mean velocity (Equa-

tion 5.1), which was obtained using the branch flow rate divided by the cross-sectional area (Equation 5.2). The cross-sectional area was calculated using the corresponding radius (i.e. CAD model radius and PDMS model measured radius). Given the flow conservation law and equal flow at the terminal branches, the inlet flow rate was divided among the number of terminal branches of each tree (five). Thus, for the experiments with  $Q_{inlet} = 2$  mL/h, the flow rate of the terminal branches was 0.4 mL/h, and for the experiments with  $Q_{inlet} = 5$  mL/h, the flow rate of the terminal branches was 1 mL/h. The flow rates for the intermediate branches were calculated according to the law of flow conservation by adding the flow rate of the daughter branches for every parent branch (see Chapter 3, Equation 4.1). Tables with all the calculated branch values are included in Appendix A.

### 5.3.3 Generation of vascular networks for experimental work

For the purpose of studying the flow behaviour in the channels of the physiologically constrained model, a simplified planar version of the vascular model was used for experimental work due to the difficulty to process, visualize and obtain measurements from a multi-level network. The model, however simple, is considered to be a representative sample of the attributes and branching morphology of a multiple-plane full network.

It must be noted that the algorithm used to produce the experimental models is not the same as that presented in Chapter 4, but the previously mentioned improved version developed in the same research group by Guy et al. [101] (see Section 3.2) in order to overcome the limitations of the original algorithm (e.g. collisions between arterial and venous tree branches). Although the improved algorithm is intended to generate more complex 3D vascular models, it can also produce planar models. In fact, the planar models produced by the original algorithm and the improved algorithm are very similar, as there is no need to compensate for collisions. The decision to use the improved version lies in the fact that any future research involving the algorithmic generation of vascular structures will be carried out using this improved algorithm. Therefore, with the aim of being able to compare the data obtained in the present work with any related future work, using the new algorithm is preferred to ensure consistency.

Based on the findings of Chapter 4, Section 4.3.2, two planar network models were generated for experimental work (model 01 and model 02), using a minimum feature size of 250  $\mu\text{m}$  and with the following design parameters:

- Number of terminals: 5
- $Q_{term} = 4$  mL/h (which means  $Q_{inlet} = 20$  mL/h)
- $\mu = 0.004$  Pa · s
- $\Delta P_{inlet-term} = 1$  mm Hg for Model 01, 2 mm Hg for Model 02

The resulting structures after its automatic generation in Inventor® are shown in Figure 5.1. The red branches represent the arterial tree and the blue branches represent the venous tree. The middle points (connections between arterial and venous trees) are the terminal points for both trees. As expected, because of the difference in the  $\Delta P_{inlet-terminals}$  values, model 01 has slightly larger branch diameters than model 02. The diameters of every branch in both models are shown in Figure 5.2. As it can be observed, the smallest diameter is found in model 02 (249  $\mu\text{m}$ ) and is at the limit of the printing threshold. Figure 5.3 shows the total length and width of the networks and the spacing distance between terminal points, which are the same in both models.

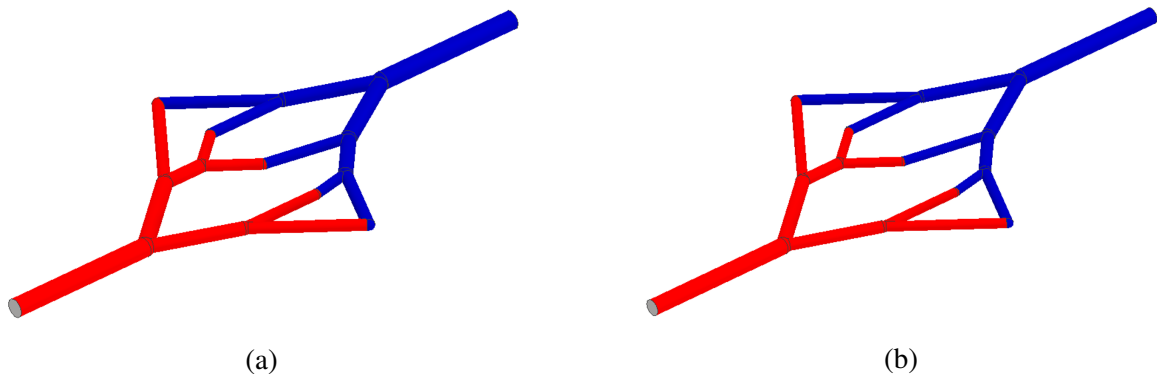


Fig. 5.1 3D models of planar networks generated in Inventor®. (a) Model 01. (b) Model 02. The models vary slightly in diameters due to the difference in  $\Delta P_{inlet-terminals}$ .

### 5.3.4 Fabrication of vascular network models

Models 01 and 02 were exported as solid models in Autodesk® Inventor®. A supporting frame was modelled around the network to facilitate manipulation of the model after printing. The models were converted to STL format and 3D printed in a Solidscape® S350. This printer uses Solidscape® Midas™ castable material for the network structure and Solidscape® Melt, a dissolvable supporting material. The minimum practical printable feature size is of approximately 250  $\mu\text{m}$ .

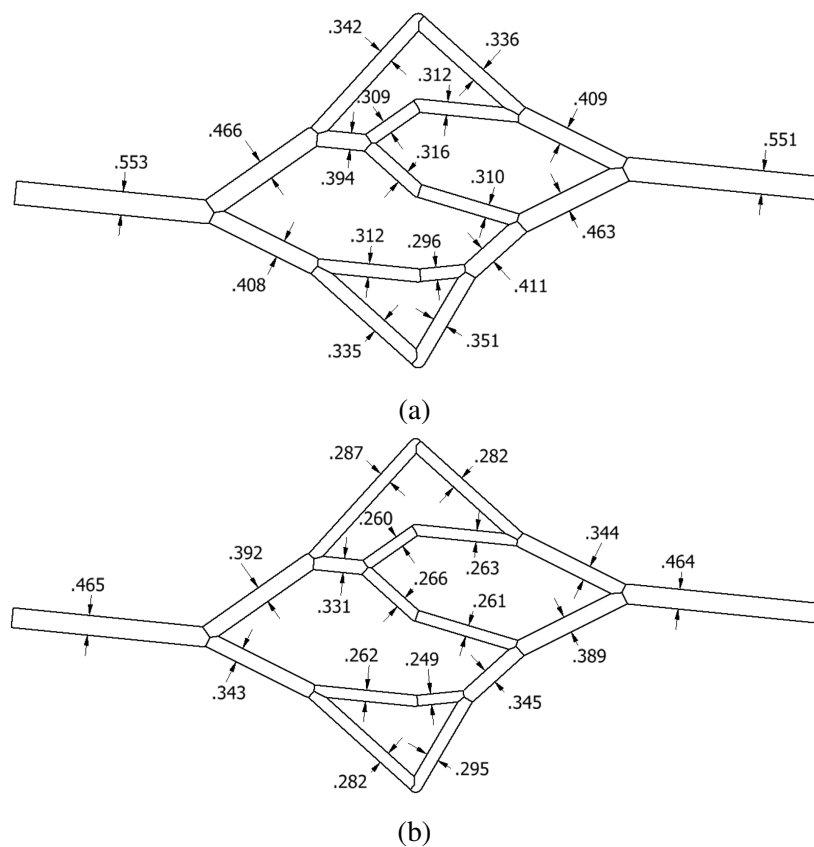


Fig. 5.2 Drawings of top view of the models showing the diameter dimensions of each branch for (a) Model 01, and (b) Model 02. Dimensions are in mm.

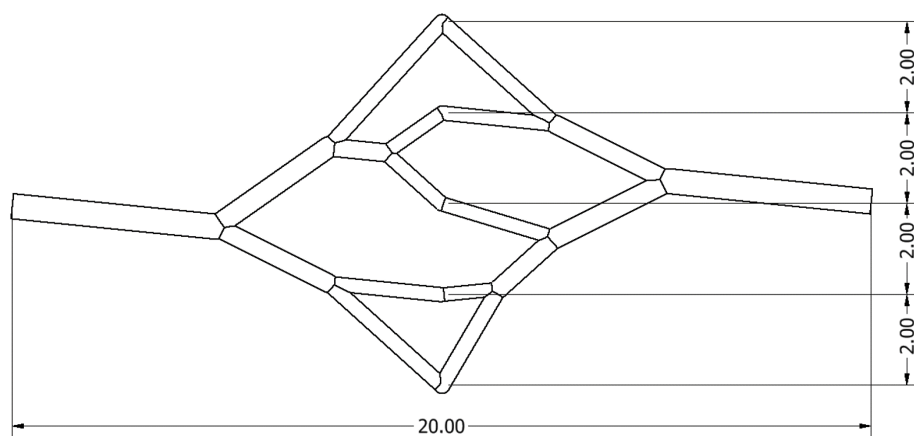


Fig. 5.3 External dimensions of 3D networks. Dimensions are in mm.

The resulting printed structure is a wax block encapsulating the network structure. The support wax was dissolved in a bath of a selective solvent (Solidscap BioAct VSO) inside a temperature controlled atmosphere (oven at 65 °C) for 4 hours. The network model after

dissolving the wax is shown in Figure 5.4 in its supporting frame. The printed models are very fragile and need to be handled with care. The models were stored in fresh solvent at room temperature, until use.

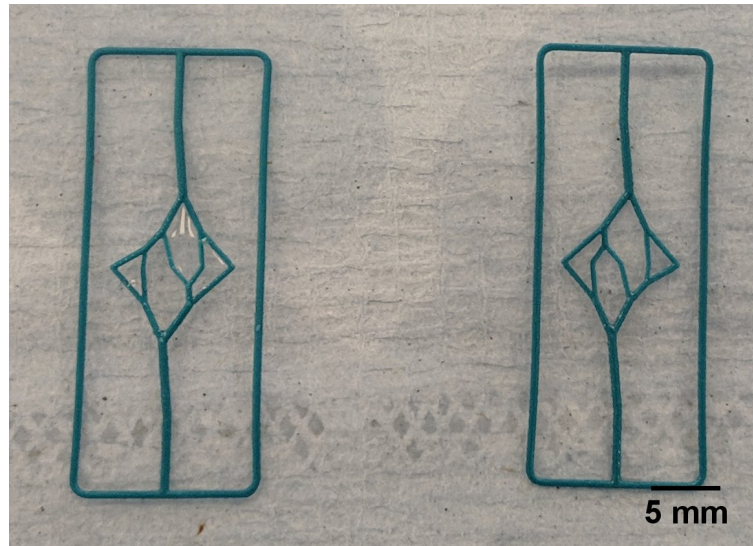


Fig. 5.4 3D printed network models in supporting frame, after removing the wax around them.

Cylindrical PDMS chambers of 20 mm diameter and 10 mm of depth were used to produce the vascularised structure. A fabrication protocol similar to that described by Justin et al. [13] was used. The chambers had two holes on opposite sides (for inlet and outlet). Each network model was cut off from the supporting frame and the extremes were trimmed for a better fit in the chamber. Two pieces of flexible silicone tubing of 1 mm internal diameter (from VWR) were fitted inside the holes to hold the model in place inside the chamber. Using tweezers, the models were carefully placed in the silicone tubing, as shown in Figure 5.5.

A solution of PDMS for casting was prepared using the DOWSIL™ 184 Silicone Elastomer Kit. 18 mL of elastomer was mixed with 1.8 mL of catalyst, and the solution was centrifuged for 5 minutes at 4000g. The PDMS solution was cast inside the chambers to fully cover the network models. A large number of bubbles of different sizes were formed in the PDMS during the casting process, especially in the surface areas of the chamber and model, as can be seen in Figure 5.6.

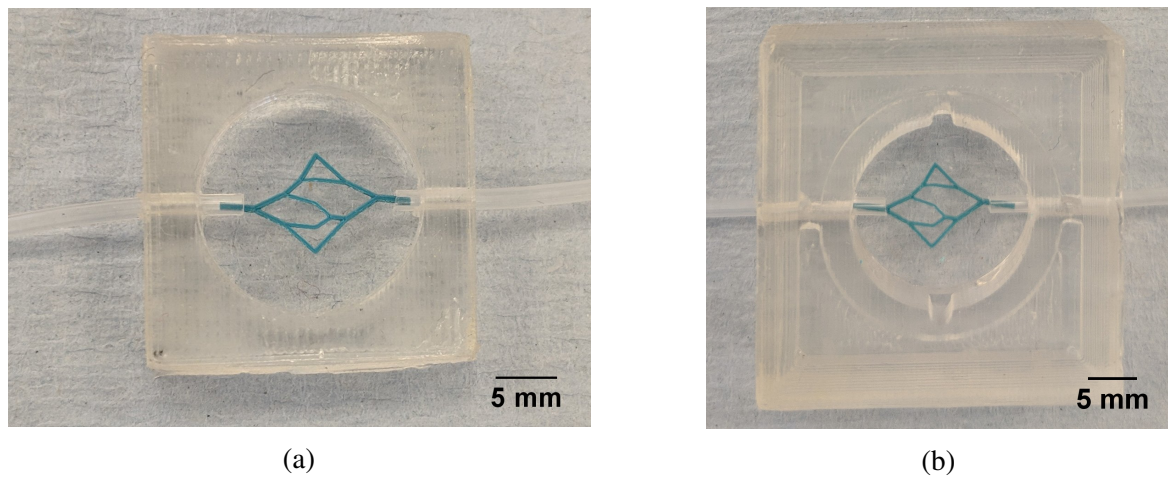


Fig. 5.5 3D printed network models in PDMS casting chambers. (a) Model 01. (b) Model 02. The external dimensions of the chamber for model 02 were larger than those of the chamber of model 01, but the chamber size is the same for both models (diameter of 20 mm and depth of 10 mm).

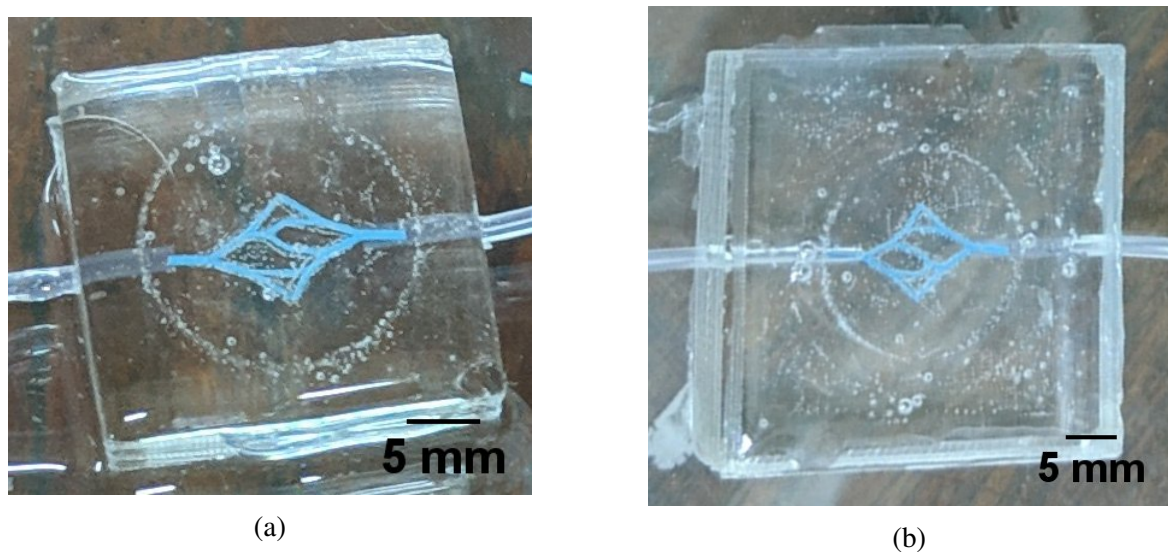


Fig. 5.6 PDMS solution cast over network models in casting chambers. A large number of bubbles are formed in the casting process. (a) Model 01. (b) Model 02.

To solve this, the samples were placed in a vacuum chamber (CENCO HYVAC PUMP) and were subjected to a few cycles of increasing the vacuum to 29 in Hg (inches of mercury, the measurement unit of the pump) and releasing the vacuum in order to allow the bubbles to rise to the surface and disperse. Once the samples were bubble-free, they were placed in the oven at 60 °C and left overnight to cure the PDMS. The cured models are shown in Figure 5.7. During the vacuum process the network model 02 suffered a significant tilting

from the original position (parallel to the surface of the cast PDMS). The movement of the network might have been caused either by the rising bubbles, or by the cast PDMS trying to fill the space in the tubing around the root branches due to the vacuum. Model 01 appears to be horizontally aligned.

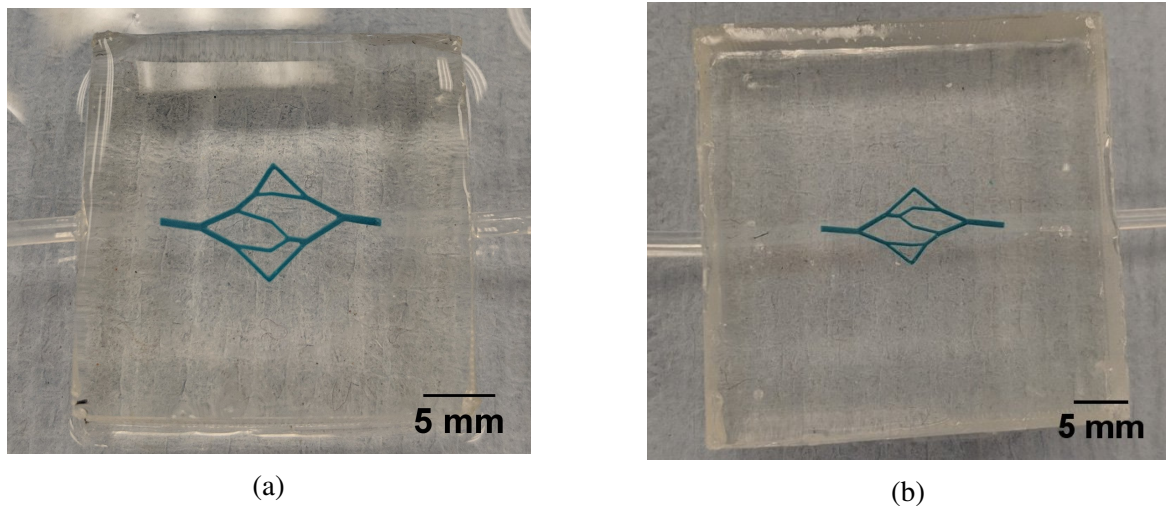


Fig. 5.7 After curing the models, the cast PDMS is clear and bubble-free. (a) Model 01. (b) Model 02.

Finally, the Midas™ material was removed from the PDMS by placing the chambers in a bath of hot distilled water (nearly boiling). After 5 minutes, the model material had liquefied and it was gently flushed out of the networks using a syringe. Acetone was then injected into the network to eliminate any residue of the model material. Figure 5.8 shows the finished PDMS models (after cleaning) with their respective embedded vascular networks.

To facilitate comparison between models in the experimental process, every branch in the network structures was assigned a number, starting from the inlet branch and ending in the outlet branch. The assigned numbers are shown in Figure 5.9. As it can be observed in 5.8, the network models lost their original root branches (except for a segment of branch 01 in model 01) and they are replaced by the shape of the tubing used to support the networks in the chamber during the PDMS casting process.

In order to find out if the networks dimensions were in accordance with the 3D models, all branches of each model (from the arterial tree) were measured using a Zeiss microscope (Axio Observer Z1/7). A comparison chart between the design and measured diameters is presented in Figure 5.10. In this figure, six measurements of each branch diameter were

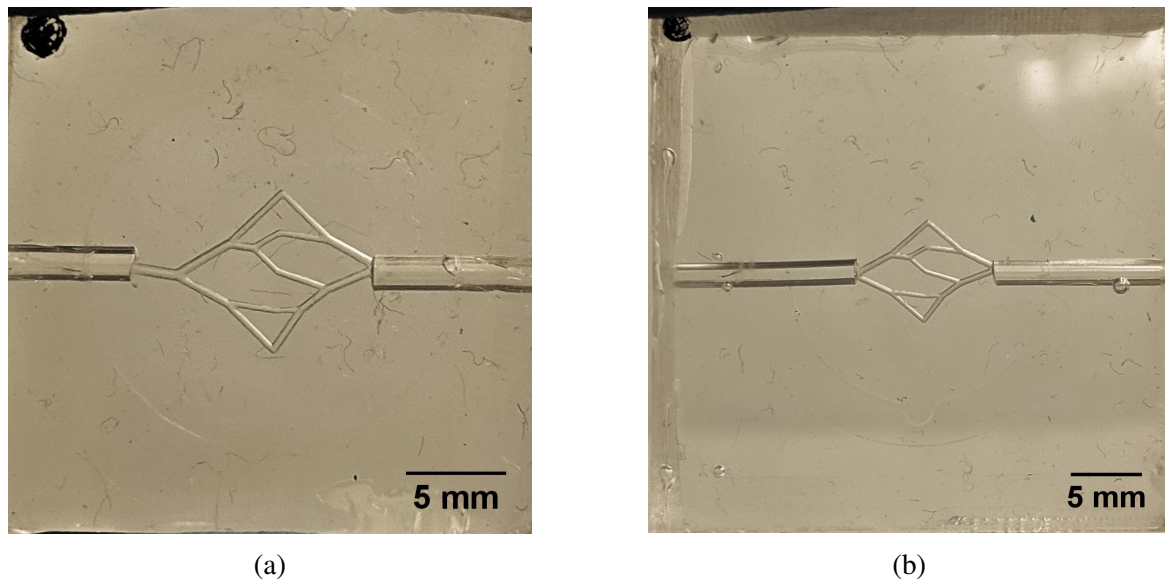


Fig. 5.8 Finished PDMS experimental models with embedded planar networks. (a) Model 01. (b) Model 02.

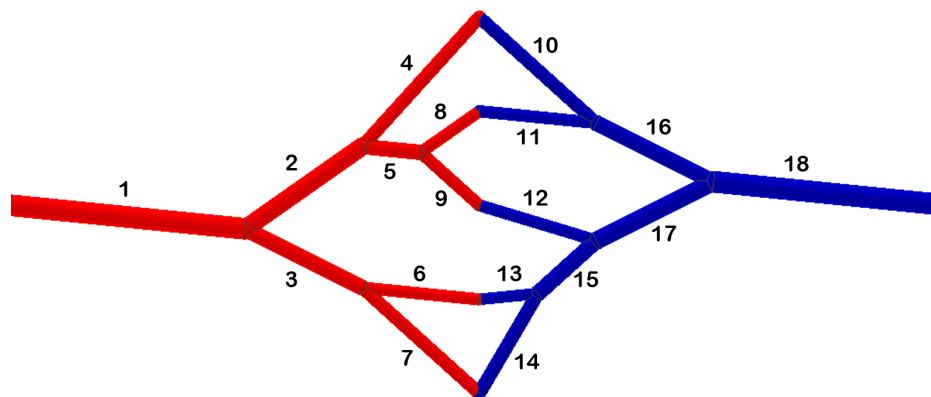


Fig. 5.9 Assigned branch numbers for comparison in experimental analysis. Models 01 and 02 have the same branching structure, therefore the numbering applies for both of them. The red tree represents the arterial tree, while blue tree represents the venous tree.

taken and averaged. However, the standard deviations from the measured diameters are very small (2-5  $\mu\text{m}$ ) and the symbols are larger. It is evident that the models vary slightly from the design values, especially for model 02. The variation might be a combination of factors such as the accuracy of the 3D printer, the network fabrication process (which involved PDMS casting around the model and subsequent flushing of the model material) and the manual measurement of the channels diameters in the microscope.

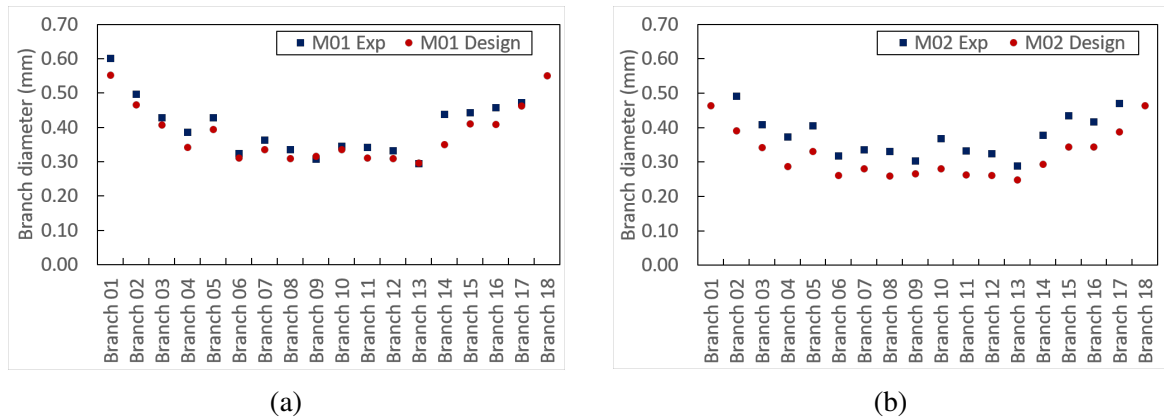


Fig. 5.10 Chart comparing measured diameters in both experimental models, against their corresponding design values. Branch diameters based on the CAD design are shown in Figure 5.2. (a) Model 01. (b) Model 02. Error bars in the experimental models are not visible behind the symbols.

### 5.3.5 Experimental setup for flow velocity measurements

The purpose of the experimental work is to determine the flow velocity in the fabricated vascular channels and comparing it to calculated theoretical values.

A Graseby 3200 syringe pump was used to provide constant flow rates. The main experimental setup is comprised of the following elements: a 20 mL syringe (mounted on the syringe pump) is connected to a 50 cm long tubing segment (2 mm diameter), which is connected on the other end to the inlet side of the first pressure sensor (1.7 mm diameter). From the outlet side of the sensor a shorter tubing segment of 15 cm is connected (2 mm diameter), and on the other end a luer lock interface is connected to allow attachment to the inlet of the PDMS network, which has a diameter of 1 mm. On the outlet side of the network the same arrangement is done: a luer lock interface that attaches the outlet to a 15 cm long tubing segment (2 mm diameter), and on the other end is connected to the inlet side of the second pressure sensor. From the outlet side of the sensor a 40 cm long tubing segment is connected, and the other end is placed through a hole on the wall of a Petri dish for fluid collection. A small hydrophilic membrane is attached to the tubing outlet to avoid drop formation and act as a guide for the fluid to the base of the Petri dish. The Petri dish is placed on a tower of 1 cm tiles for added height to aid with the pressure measurements. A schematic of the setup is shown in Figure 5.11.

Figure 5.12(a) shows the physical arrangement of the network on the microscope stage, including the tubing, Petri dish, pressure sensors and an electronic circuit for the sensor

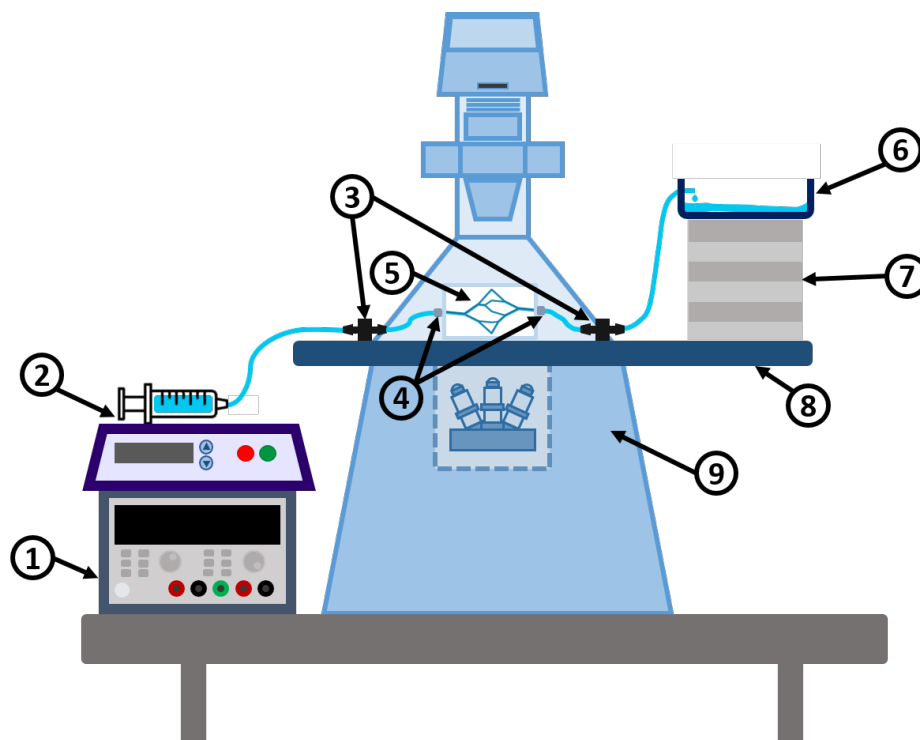
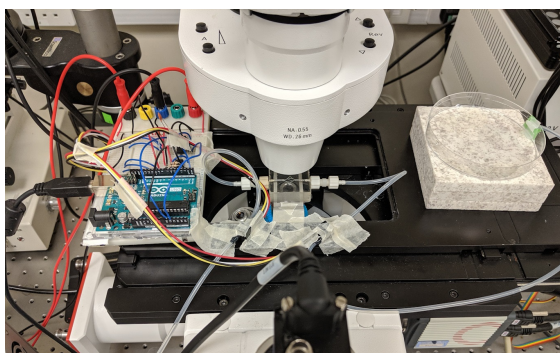
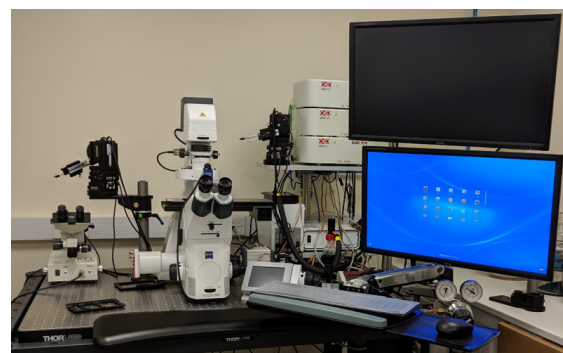


Fig. 5.11 Schematic of experimental setup. ① Power Supply. ② Syringe Pump. ③ Pressure sensors. ④ Luer-lock interfaces. ⑤ Planar network in PDMS. ⑥ Petri dish for collection of fluid from outlet. ⑦ Tiles for added height. ⑧ Microscope moving stage. ⑨ Inverted microscope structure (Zeiss Axio Observer Z1).

operation. The microscope as well as all the necessary equipment (i.e. syringe pump) are located on an air table, which prevents the measurements from being affected by vibrations.



(a)



(b)

Fig. 5.12 (a) Experimental setup of the network on the microscope stage. (b) Zeiss microscope (Axio Observer Z1/7) used in experimental measurement of flow velocity.

Pressure sensors are included in the setup, as they were originally intended to measure the pressure difference across the network. The use of pressure sensors with microfluidic devices has been reported in the literature to obtain pressure drops in the systems [120] [121]. Several attempts were made to work with the sensors, but the obtained measurements were unstable and unreliable mainly caused by the sensor's noise and lack of sensitivity, among other factors (e.g. syringe pump mechanism, syringe total volume, the remaining liquid volume in the syringe, the height of the output with respect to the sensors, the positioning of the sensors, droplet formation and use of an air table vs a normal lab bench). As a result, it was decided to focus only on the flow velocity measurements.

Images were acquired using a Zeiss Microscope (Axio Observer Z1/7), shown in Figure 5.12(b), equipped with a Hamamatsu C11440 (ORCA-Flash4.0 LT+ Digital CMOS camera), which has a frame rate of 30 fps at full resolution (2048 x 2048 pixels). A fluorescent light source (HXP 120 V) and a 63 HE Red fluorescence filter were used. Individual branch images were taken with a 10X objective. Figure 5.13 shows a compound image formed by tiles taken individually with a 5X objective using the red fluorescent light. The model shown is M01.

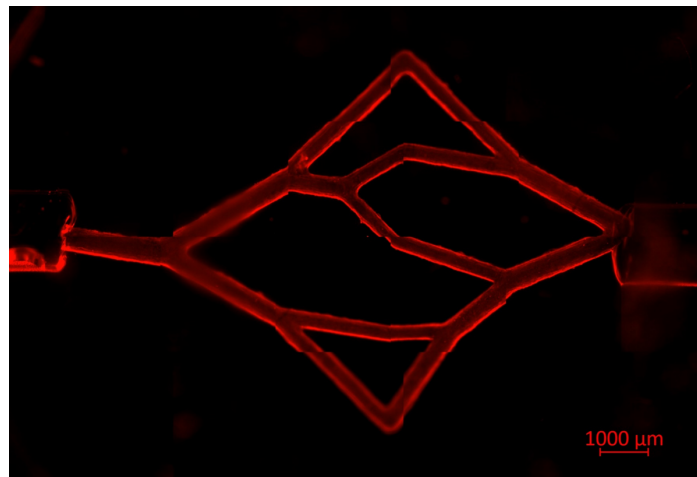


Fig. 5.13 Compound tiles image of model 01 using a 5X objective for each tile.

Originally, the intended flow rate for experimental measurements was 20 mL/h, as this was the flow rate used for the design of the network. However, a technical problem arose; the microscope camera used could not image the beads clearly at flow rates higher than 5 mL/h as even the smallest possible exposure time was still larger than the time it took the particle to cross the imaging area (i.e. the image showed the beads as long lines across the channels).

As a result, the experimental flow rate was set to two arbitrary values: 5 mL/h and 2 mL/h.

Even though the network models were designed considering the properties of blood, for practical purposes the use of human blood was not possible due to safety reasons. For convenience, phosphate-buffered saline solution (PBS) was used as the experimental fluid. A solution was prepared using PBS (Dulbecco PBS - D8537 from SIGMA) and fluorescent beads (FluoSpheres™ Polystyrene Microspheres, 1.0  $\mu\text{m}$ , red fluorescent). Based on existing data for PIV analysis [137], it was estimated that the number of beads needed per second for a good particle tracking analysis would be between 10-15. Considering this, and the fact that the maximum flow rate to test experimentally is 5 mL/h, an estimated concentration of 10,000 beads/mL was calculated (as 5 mL/h equals 50,000 beads/h or 13.9 beads/sec). This concentration is used in the experimental work.

### 5.3.6 Measurement of flow velocity

The aim of the experiments is to find out if the values of the flow velocity in the channels are consistent with the theoretical values. Poiseuille's law (see Chapter 2, Section 2.3) indicates that the highest flow velocity is found at the centre of the tube (assuming a Newtonian fluid and laminar flow). Thus, this is the expected location of the highest velocity for experimental measurements in the channels. Considering this, the focus of the microscope was set on the middle plane of each channel. This was carried out by aiming for a clear focus at the edges of the channels. In this way, the particles that are moving in the middle plane are well focused, including those that have the highest velocity. However, it must be considered that the networks were fabricated in a manual process and their final position in the PDMS is not perfectly aligned horizontally with respect to the surface. In fact, model 02 presents a significant tilting, which further complicated its measurements. Thus, in some cases the microscope focus plane may only partially correspond to that of the middle plane of the channel. This led to a poor focus for some of the particles of interest for some of their displacement across the channel. In the same manner, some of the particles from upper or lower planes -which are not of interest- can be unintentionally focused (i.e. a particle that is travelling near the wall at the bottom part of the channel, but appears to be on the central axis).

For every branch in each model, three sets of 300 consecutive images were obtained at two different flow rates (2 mL/h and 5 mL/h), giving a total of 900 images for each branch per flow rate value. The aim was to track single particles across the frames and calculate their displacement. Figure 5.14 shows an example of a particle moving across 8 consecutive

images. Although the particles are round with a diameter of 1  $\mu\text{m}$ , in the images they are captured as lines due to the movement of the particle during the exposure time.

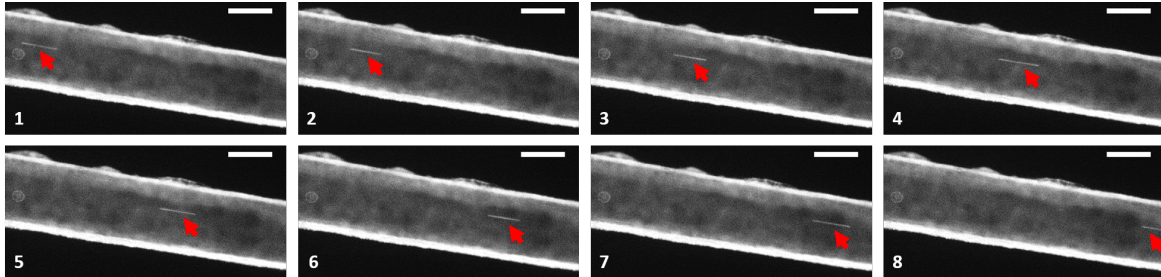


Fig. 5.14 Sequence of consecutive images taken to measure the distance traveled by the particle (pointed by red arrows) across frames. The images correspond to branch 6 at an inlet flow rate of 5 mL/h, and were acquired with a frame rate of 30 fps. The scale bar in all images is 200  $\mu\text{m}$ .

The image sets obtained from the Zeiss microscope were exported as “.jpeg” files using the software ZEN 2.5 (blue edition) from Zeiss, and were subsequently processed using ImageJ by splitting every image in its Red, Blue and Green channels (RGB), eliminating the Blue and Green, and converting the remaining Red channel images to greyscale (8-bit image). This process was carried out in order to increase contrast of the images and facilitate the detection of particles moving within the channels.

To speed up the task of calculating the displacement (and avoid doing it manually) the image sets were analysed using a LabView-based software developed by Dr. Juan Rubio (postdoctoral researcher in David Kent’s group at the University of York). The software was specifically implemented to analyse the data sets obtained in the present work. Overall, the software analyses a sequence of images and calculates the distance that a particle moved from one frame to the next, based on a known distance given in pixels (i.e. the scale bar in any of the images, as all of them are of the same magnification). The software’s logic was implemented based on the needs of the research data and it comprises some pre-existing LabView VIs (virtual instrument file format, which can be considered as functions/sub-functions) from particle detection and object tracking examples in LabView’s documentation.

The main steps to use the software are the following: first, the set of images (greyscale 8-bit, as described previously) is imported in the software’s graphic user interface. The brightness and contrast must be adjusted in order to improve the edge detection of the vessels. The background is then removed from all the images, by subtracting an averaged image to

remove all the static objects (i.e. vessel walls, static particles stuck to the walls, and in general all elements that are not moving particles). An example of this is shown in Figure 5.15(a). Then, the image is rotated to align the branch to an horizontal position (as every branch is at a different bifurcating angle), using the edge detection function (Figure 5.15(b)). This is done in order to facilitate the distance measurement by having only horizontally moving particles. Next, the area of interest for the analysis is selected as a rectangle (Figure 5.15(c)). Finally, the test is run and the displacement of every particle detected in the selected region is saved. The average displacement of each particle is calculated, across the number of images where it was fully visible, and is used to calculate the velocity of the particle based on two known variables: i) displacement distance (in pixels), and ii) time (displayed as image frame number). The calculated velocity (in pixels/frame) for each particle is then plotted as a line, allowing to visualise the velocity profile (see Figure 5.15(d)).

After the data was acquired, it was then processed in LabView to obtain the velocity plots in m/s, as it was originally captured in pixels/frame. For this, the equivalence of pixels in micrometers is calculated (from the scale bar on the microscope images,  $100\ \mu\text{m} = 154\ \text{pixels}$ ). The time between picture frames was calculated as well (the pictures were taken at full resolution -2048 x 2048 pixels- for which the Hamamatsu C11440 camera has a frame rate of 30 fps). With these conversions, the velocity was obtained in m/s. The data was plotted using the commercial package Origin. The resulting plots are shown and discussed in Section 5.4.

## 5.4 Results and discussion

This section presents the results obtained by the experimental measurement of flow velocity in the channels of the PDMS vascular network models. The image analysis carried out using the LabView program produced a series of plots for the velocity of every detected particle in the image sequences. The plots for every branch in models M01 and M02, each measured with inlet flow rate values of  $Q_{inlet} = 2\ \text{mL/h}$  and  $Q_{inlet} = 5\ \text{mL/h}$ , are shown in Figures 5.16 to 5.19. As it is observed, the plots provide a good estimation of the velocity profiles for each branch.

In the charts, each data point represents the average of a number of measurements for the velocity of a given particle travelling across the channel. Each particle has a unique number of measurements depending on the number of frames where it was detected. The

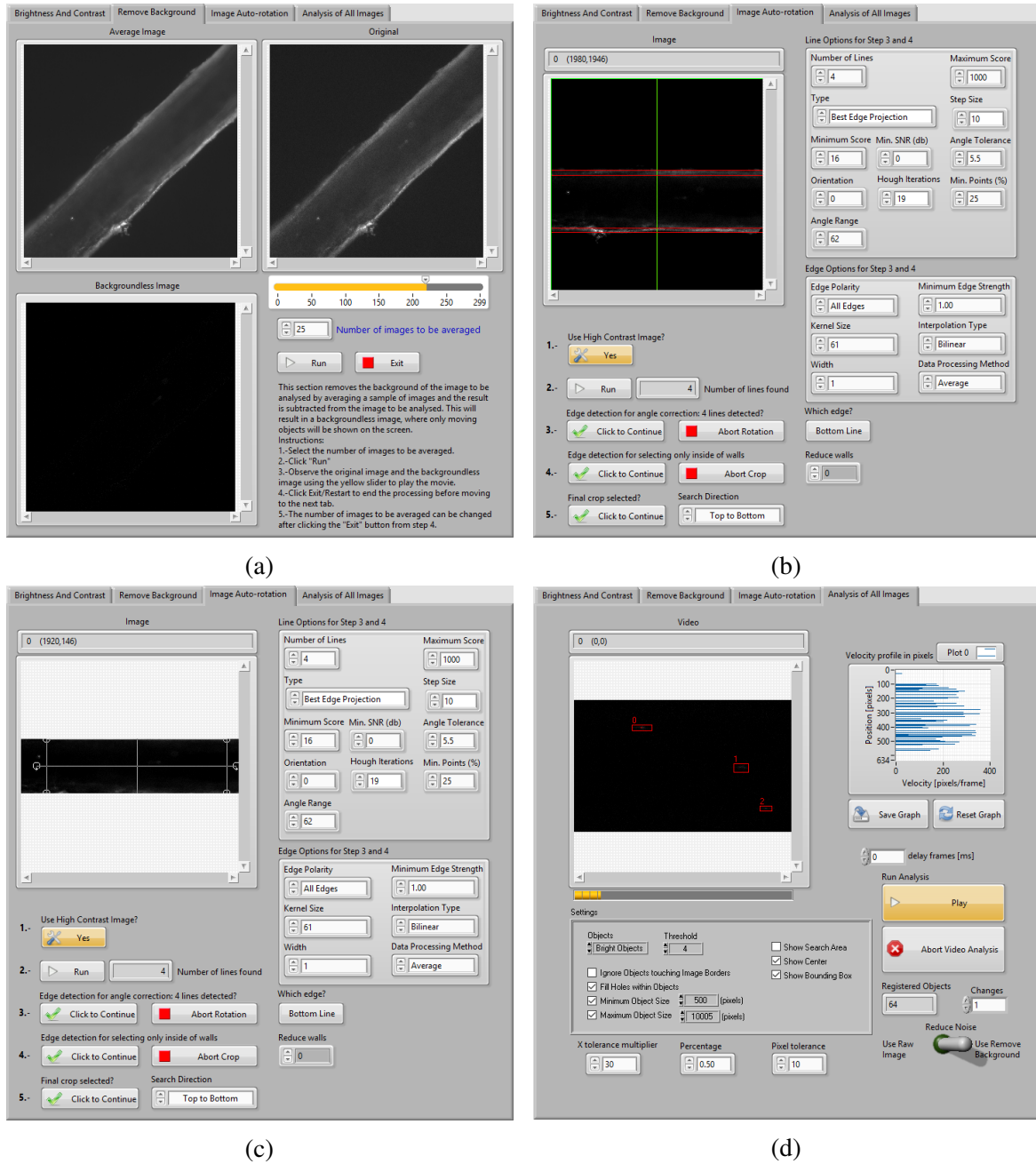


Fig. 5.15 LabView interface of software developed for particle displacement analysis. (a) Background removing step. (b) Rotated image into horizontal position. (c) Selection of area of interest for analysis. (d) Detected particles shown in red rectangles and cumulative chart of currently analysed particles.

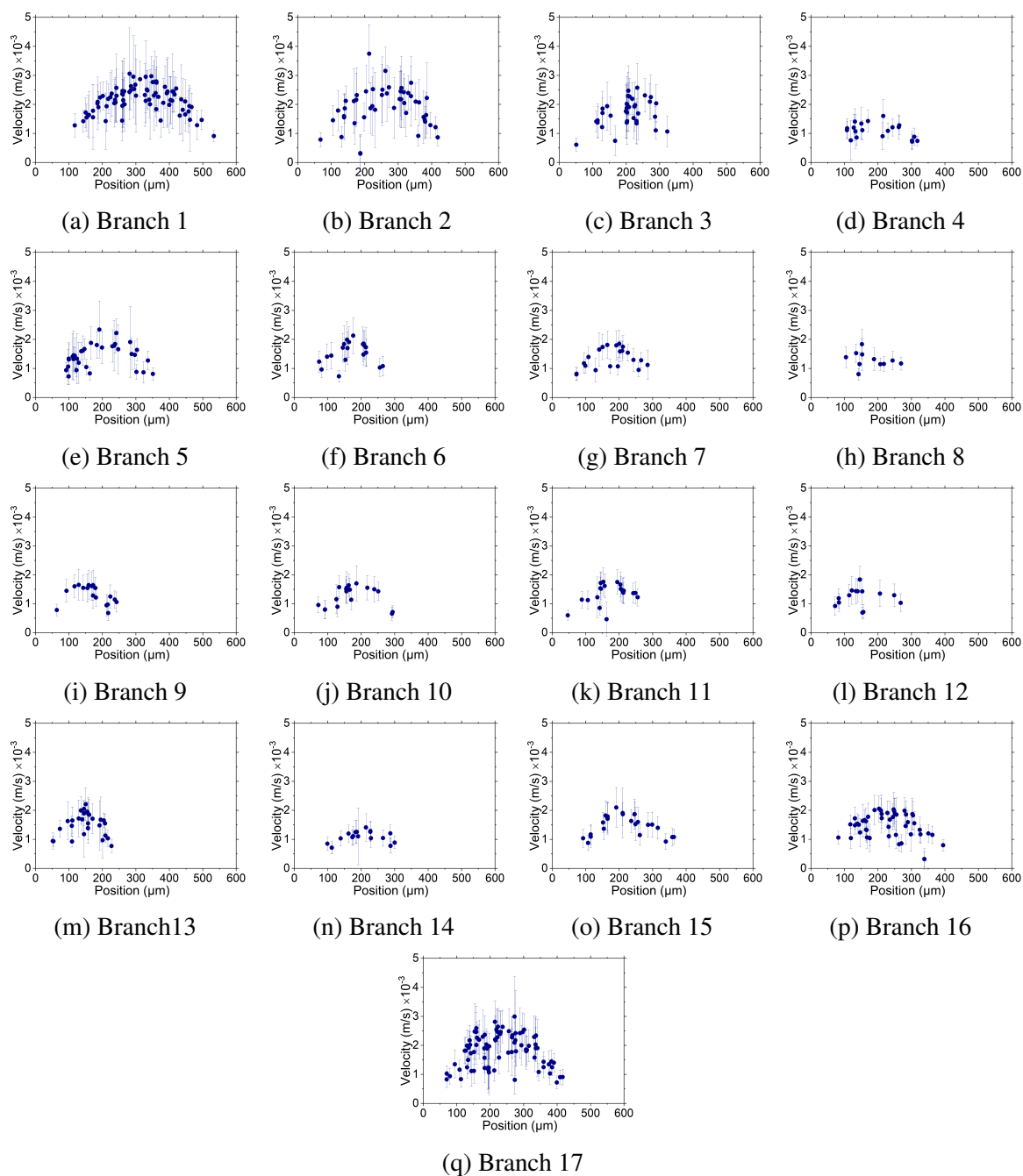


Fig. 5.16 Experimental data from model 01 at an inlet flow rate  $Q_{inlet} = 2$  mL/h. Each data point in the plot represents the measured velocity of a traced particle. The error bars represent the standard deviation of the velocity measurements for that particle. The x-axis represents the diameter of the channel (in  $\mu\text{m}$ ). The y-axis is the average velocity of the particle in units of mm/s (or  $1 \times 10^{-3}$  m/s).

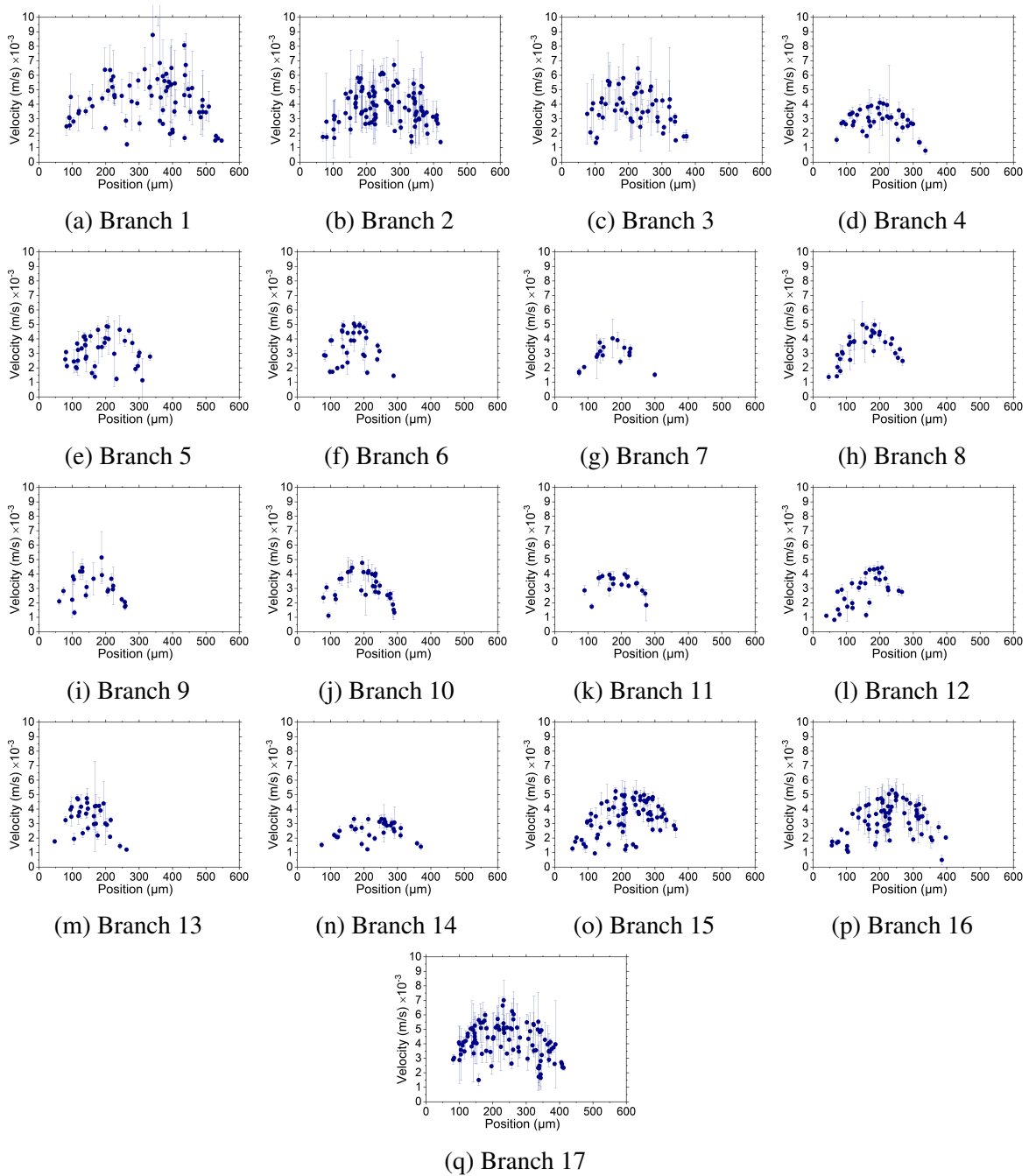


Fig. 5.17 Experimental data from model 01 at an inlet flow rate  $Q_{inlet} = 5$  mL/h. Each data point in the plot represents the measured velocity of a traced particle. The error bars represent the standard deviation of the velocity measurements for that particle. The x-axis represents the diameter of the channel (in  $\mu\text{m}$ ). The y-axis is the average velocity of the particle in units of mm/s (or  $1 \times 10^{-3}$  m/s).

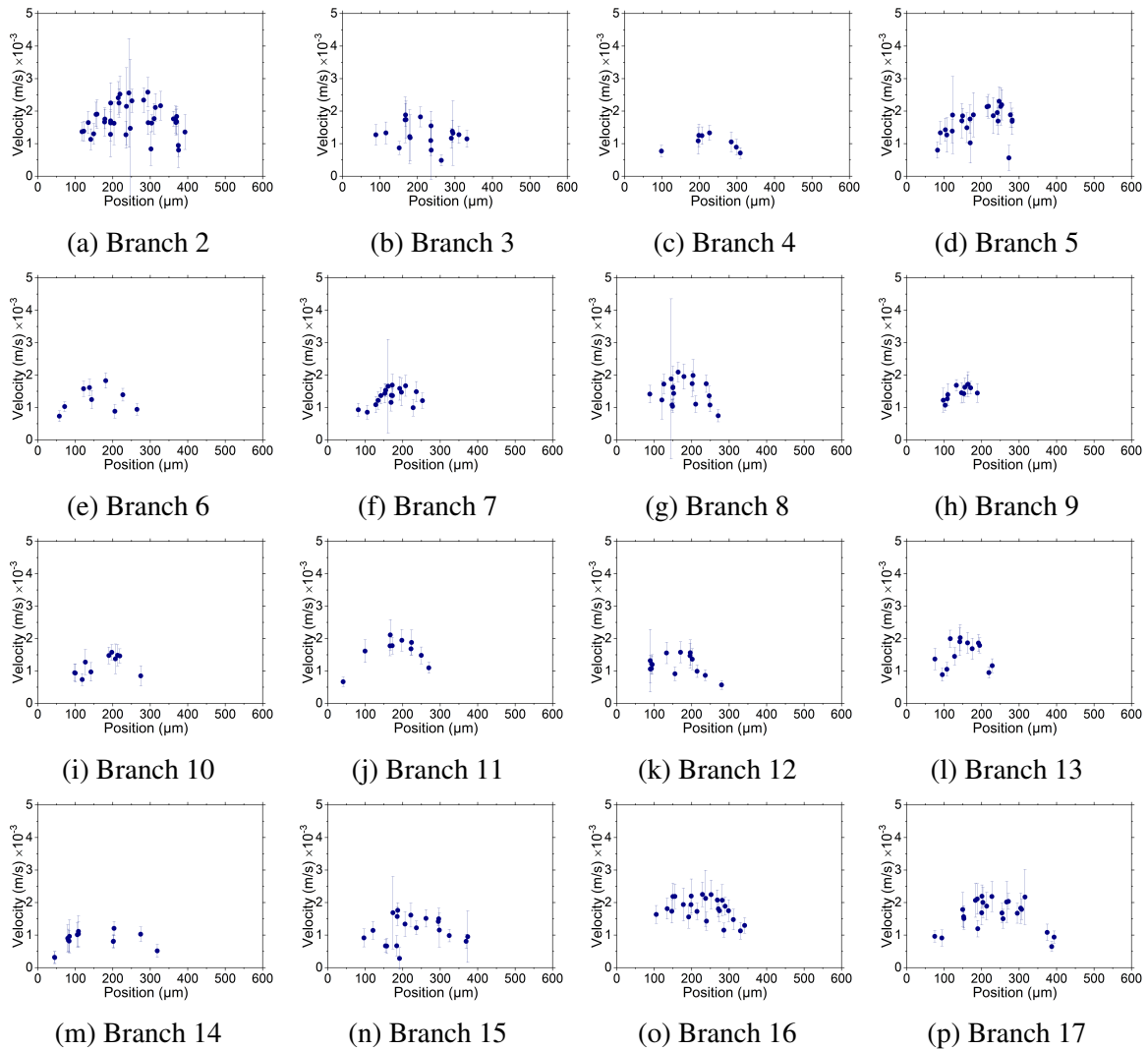


Fig. 5.18 Experimental data from model 02 at an inlet flow rate  $Q_{inlet} = 2$  mL/h. Each data point in the plot represents the measured velocity of a traced particle. The error bars represent the standard deviation of the velocity measurements for that particle. The x-axis represents the diameter of the channel (in  $\mu\text{m}$ ). The y-axis is the average velocity of the particle in units of mm/s (or  $1 \times 10^{-3}$  m/s).

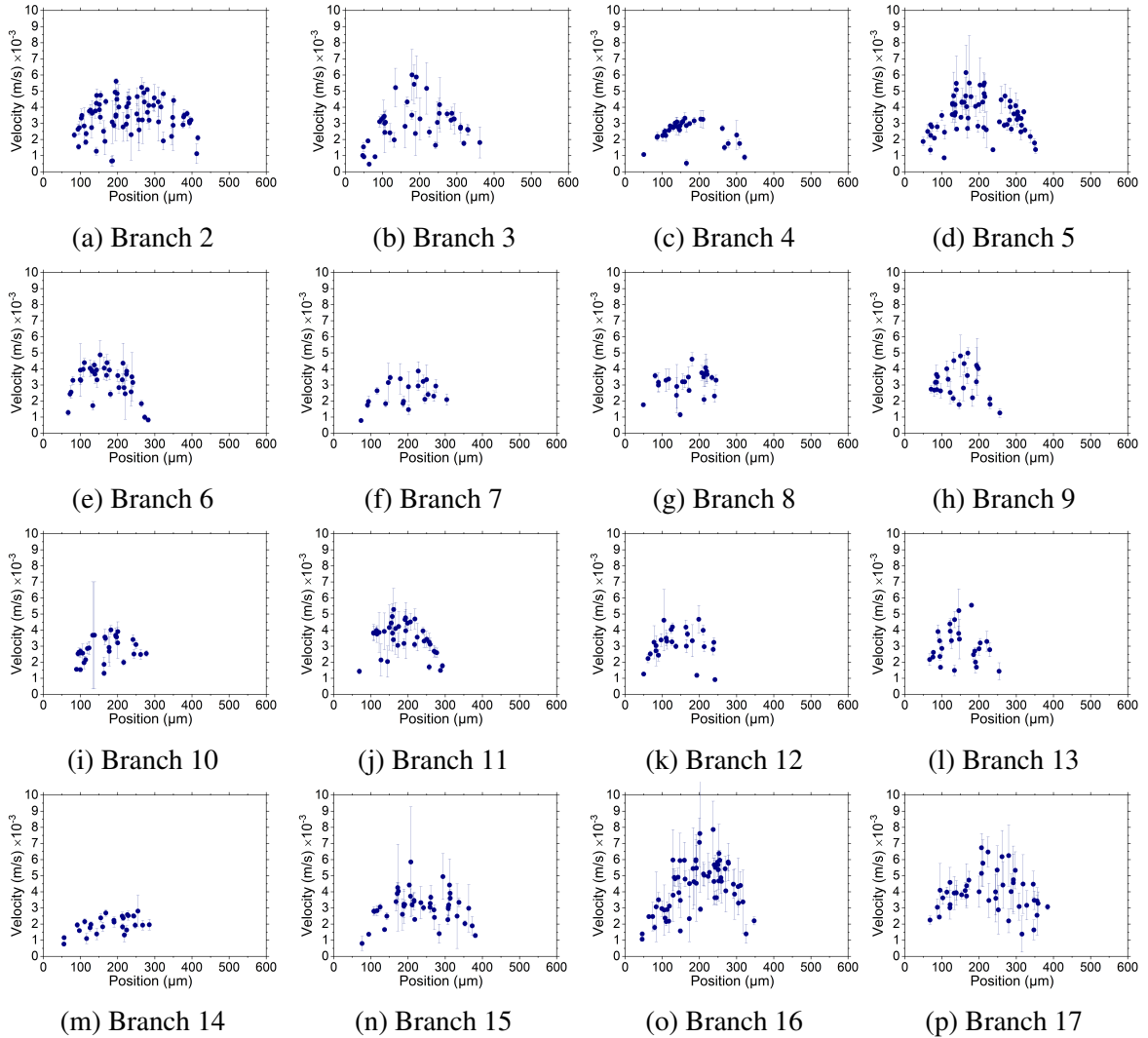


Fig. 5.19 Experimental data from model 02 at an inlet flow rate  $Q_{inlet} = 5$  mL/h. Each data point in the plot represents the measured velocity of a traced particle. The error bars represent the standard deviation of the velocity measurements for that particle. The x-axis represents the diameter of the channel (in  $\mu\text{m}$ ). The y-axis is the average velocity of the particle in units of mm/s (or  $1 \times 10^{-3}$  m/s).

error bars shown in the charts represent the standard deviation of the velocity measurements corresponding to the given particle. A large standard deviation means that the movement of the particle was not constant across frames. This happened in some branches where it was noted that the particles seemed to move faster in the central portion of the channel, and slower near the entrance or exit (depending on the branch being from the arterial or venous tree). In the branches with a shorter standard deviation, this means that the particle kept a more constant velocity across frames. It can also be noticed that in the charts for the higher flow rate (5 mL/h), the standard deviations are shorter than in the slower flow rate (2 mL/h). This can be explained by the fact that at a higher velocity there were fewer measurements for a given particle travelling across the scanning area (e.g. for the slow flow rate, more than 10 measurements were taken for each particle because it was traced across more than 10 frames, while for the high flow rate, particles were only visible in about 3-4 frames, thus only 3-4 measurements were available).

One obvious thing to observe is that the amount of particles detected in each branch is different (the number of data points in the plots). For the inlet branch (in case of model 01) or the branches closest to the inlets and outlets, the number of particles is higher, while the branches in the middle of the network (connections of arterial tree and venous tree, which correspond to branches no. 4 and 6-14) the number of particles detected is lower. This is a rough indicator of the distribution of flow in the channels. It is observed that overall, the plots of model 02 (Figures 5.18 and 5.19) have a smaller number of particles detected than those of model 01 (Figures 5.16 and 5.17). This happened mostly due to the complications in measurements given by the significantly tilted position of the model. As explained in the previous section, in these cases only partial regions of the channels were focused in the images, causing that only in these regions the particles were detected by the software.

In the particular case of branch 08 in model 01 at 2 mL/h (Figure 5.16(h)), the data was not acquired correctly while taking and saving the measured images (possibly due to a software error related to the lack of available RAM memory in the microscope computer). As a result, instead of recording three sets of 300 images (900 in total), only 545 images were acquired. In addition to missing some data, it is also the branch with the lowest number of detected particles, among all the plots in Figure 5.16.

In the charts, the shape of the profile (formed by the magnitude of the velocities of the particles detected) is parabolic, as expected from fluids that obey Poiseuille's law. The closest a particle is to the centre, the highest the velocity. However, it can be observed that some

of the measurements seem to be below the expected value from the parabolic shape (e.g. Figure 5.16(g) has two measurements close to the middle of the channel (position  $200\mu\text{m}$ ), but it is not as high as the surrounding particles). These ‘shorter’ measurements are in reality particles that were on a different depth, and probably not as focused as those in the main plane, but the software detected them nevertheless.

### 5.4.1 Comparison of theoretical and experimental data

In order to analyse the measured values resulting from the particle tracking velocimetry analysis and prove the functionality of the networks, a comparison with the expected (theoretical) values is necessary. This section presents a brief comparative analysis of experimental vs. theoretical branch maximum velocity.

For the analysis, the experimental branch maximum velocities were obtained from the velocity charts by selecting the highest velocity measurement from each chart (figures 5.16 to 5.19). For a thorough comparison, two theoretical branch maximum velocity values were calculated: one using the original diameters from the CAD model, and another using the experimental model diameters. These theoretical maximum velocities were calculated for every branch as twice the mean velocity (Equation 5.1), which was obtained using the branch flow rate and cross-sectional area (Equation 5.2).

$$v_{max} = 2v_{mean} \quad (5.1)$$

$$v_{mean} = \frac{Q}{A} \quad (5.2)$$

The cross-sectional area of the branches was calculated using the corresponding radius (i.e. one value was obtained using the original CAD model radius and another using the experimental model measured diameter). The branch flow rates were calculated in the following manner: Given the flow conservation law and equal flow at the terminal branches used in the model design, the inlet flow rate was divided among the number of terminal branches of each tree (five terminal branches). Thus, for the experiments with  $Q_{inlet} = 2 \text{ mL/h}$ , the flow rate of the terminal branches was  $0.4 \text{ mL/h}$ , and for the experiments with  $Q_{inlet} = 5 \text{ mL/h}$ , the flow rate of the terminal branches was  $1 \text{ mL/h}$ . The flow rates for the intermediate branches were calculated according to the law of flow conservation by adding the flow rate of the daughter branches for every parent branch (see Chapter 3, Equation 4.1). Tables with all the calculated branch values are included in Appendix A.

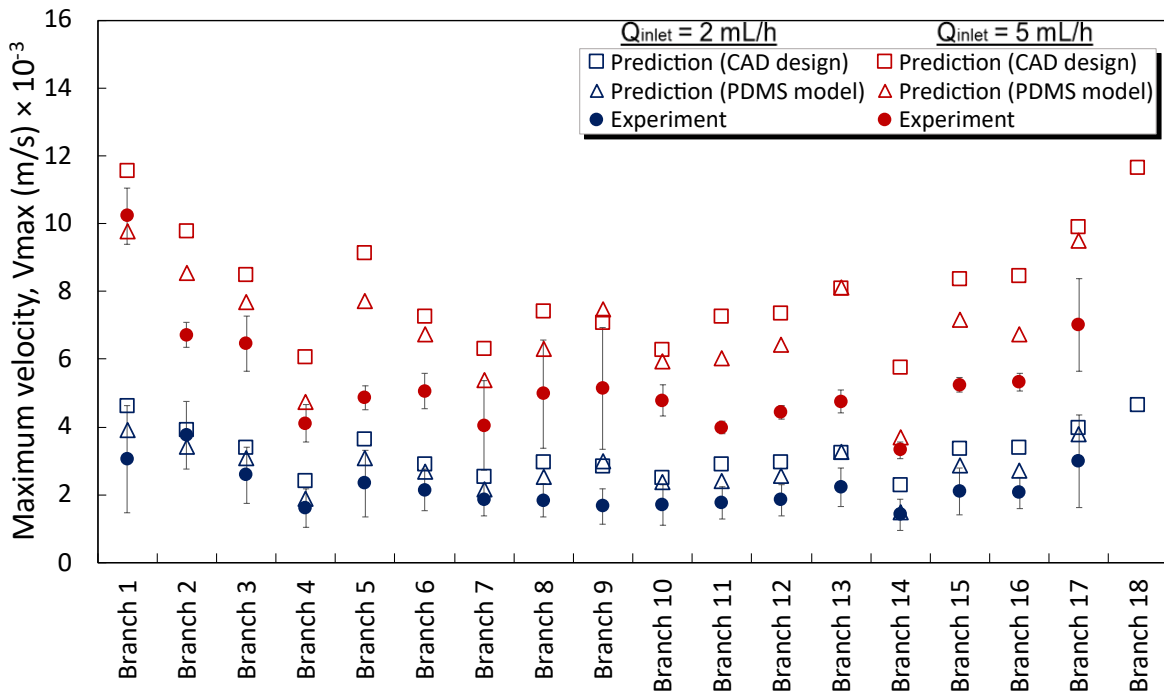
Having obtained the experimental and theoretical values of the maximum branch velocities, comparative charts were created and are shown in Figure 5.20. One chart was made for each model: (a) for M01 and (b) for M02. For each, the theoretical and experimental values are plotted for both experimental inlet flow rates ( $Q_{inlet} = 2$  mL/h and  $Q_{inlet} = 5$  mL/h). It must be noted that for M01 the experimental value for branch 18 is not available, as there is no branch 18. In a similar way, M02 lacks the experimental values for branches 01 and 18 (see Figure 5.8). In these cases only the theoretical values are plotted.

The charts show two theoretical values of the maximum velocity, calculated as explained earlier. One value was calculated using the original CAD models for each case (represented by squared symbols), while the second value used the corresponding diameter measurements from the PDMS models (represented by triangles). Considering this, the latter are a better estimation of the expected values from the experimentally acquired data (represented by filled circles). For the experimental data, the particle that was recorded having the maximum velocity from each chart was used, including its corresponding standard deviation.

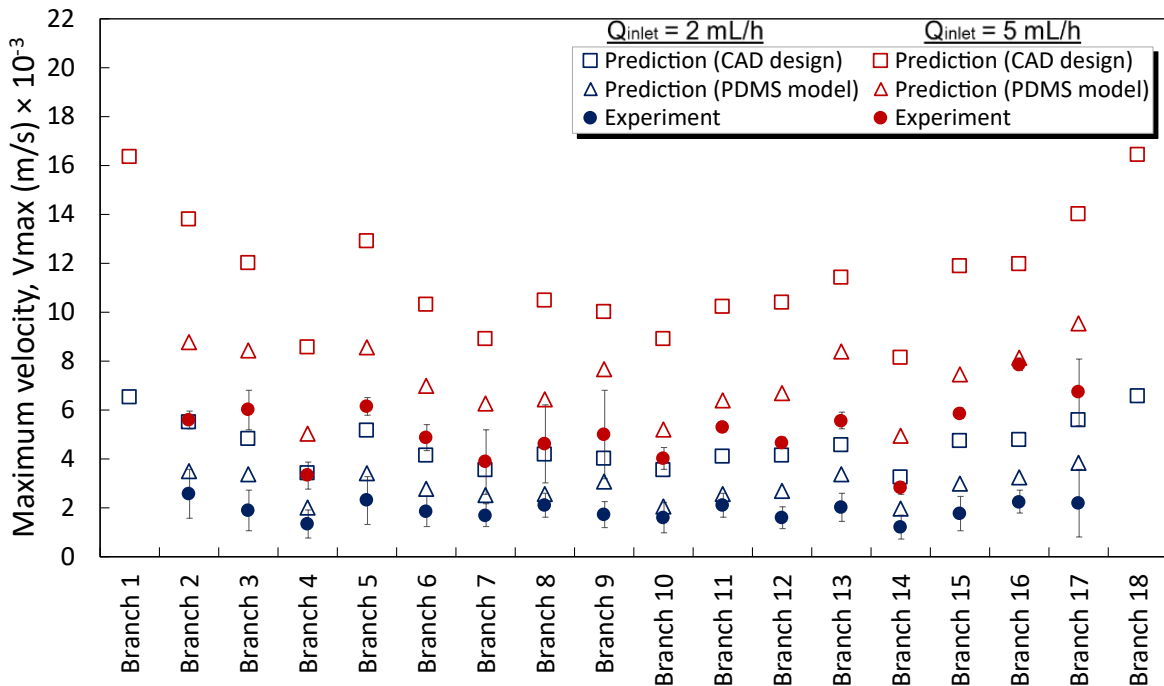
As it can be observed from the charts, for both models the experimental values (filled circles) are lower than the theoretical values in most of the branches. There are three main reasons to explain this. The first reason is related to the acquisition of experimental data: the values obtained experimentally are considered an approximation of the true velocity values in the physical models. This is because the likelihood of having obtained the true maximum values for every tree branch is small, due to the low probability of having recorded a particle exactly at the central axis of every channel in both models, for both flow rate values. This situation particularly affected the values with a flow rate of 5 mL/h, as tracking becomes more difficult with increased particle velocity. The second reason is related to the fabrication of the PDMS models. As the PDMS models have slightly larger diameters than the original CAD models (see Figure 5.10), the velocity would also be expected to be slightly lower. The third reason is that in some cases, particularly in the shortest branches, the scanning area for particle tracing included the complete length of the channel. This means that the measurements included the velocity of particles that were within the hydrodynamic entrance region<sup>1</sup> of the channel. Considering this, some of the particle measurements could have included velocities of the under-developed flow, which resulted in a lower average velocity.

---

<sup>1</sup>In Poiseuille flow, the hydrodynamic entrance region is the length starting from the entrance of a pipe until the flow becomes fully developed in the characteristic parabolic shape.



(a)



(b)

Fig. 5.20 Comparison of experimental and theoretical data for maximum velocity in all branches of the models. Blue symbols represent the models with  $Q_{inlet} = 2 \text{ mL/h}$ , while red symbols represent  $Q_{inlet} = 5 \text{ mL/h}$ . Squares represent theoretical values with the 3D model original dimensions; circles represent experimental values, and triangles represent theoretical values with the experimental model dimensions. (a) Model 01. (b) Model 02.

From the charts, it is obvious that for model 01 (Figure 5.20(a)) the difference between experimental and theoretical values is smaller than that shown in model 02 (Figure 5.20(b)). One possible explanation for this is that, given the severe tilting of model 02, the obtained particle displacements could be actually projections of the real displacement values. To explain the effect of tilting of network model 02, Figure 5.21 shows a 3D representation of a straight network and a tilted network, both contained in a box for 3D space visualisation. The table shows the top and side views of the models. The top view corresponds to the perspective of the microscope camera in all experimental image acquisition. Figure 5.22 shows an overlapping of the top views of both straight and tilted networks to show that model M02 appears smaller due to the tilting. It can be observed that the branches that are closer to the central axis (i.e. an imaginary axis that passes through the inlet and outlet center points) are less affected by the tilting (such as branch 12), while the branches further from the centre appear shorter (branch 07).

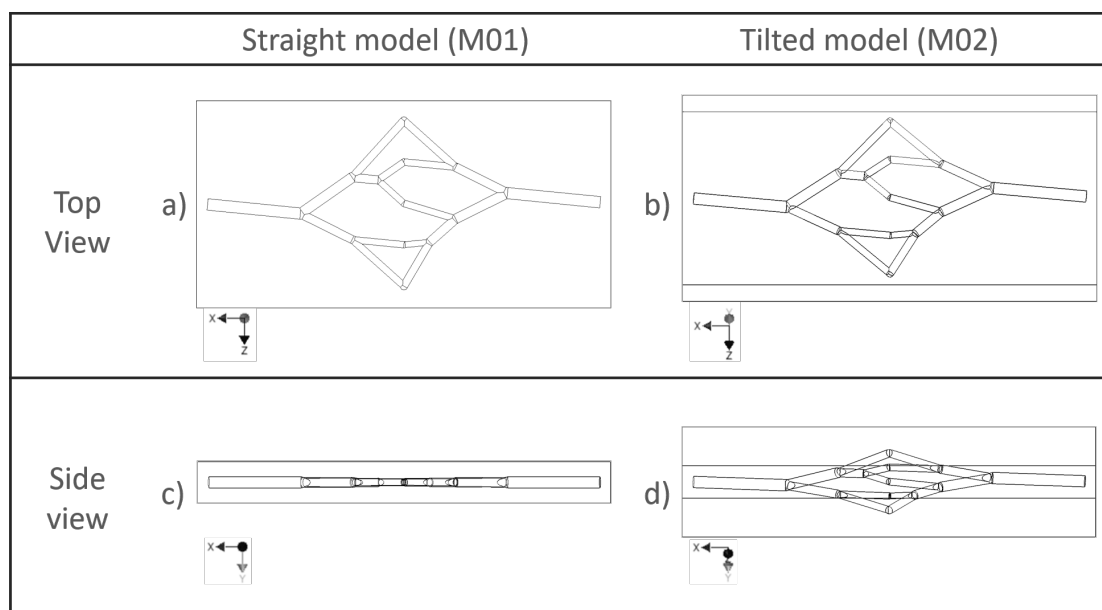


Fig. 5.21 Representation in 3D of a straight and a tilted network in top and side views.

The software for particle detection aligns the branches in a horizontal position and measures the displacement of particles between frames, as explained in Section 5.3.6. As some branches in the tilted model appear shorter, this means that the measured displacement of the particle will be smaller, compared to the displacement measured on a straight model. This is depicted in Figure 5.23. A smaller displacement results in a lower velocity, which would explain the greater difference between experimental and theoretical values in model

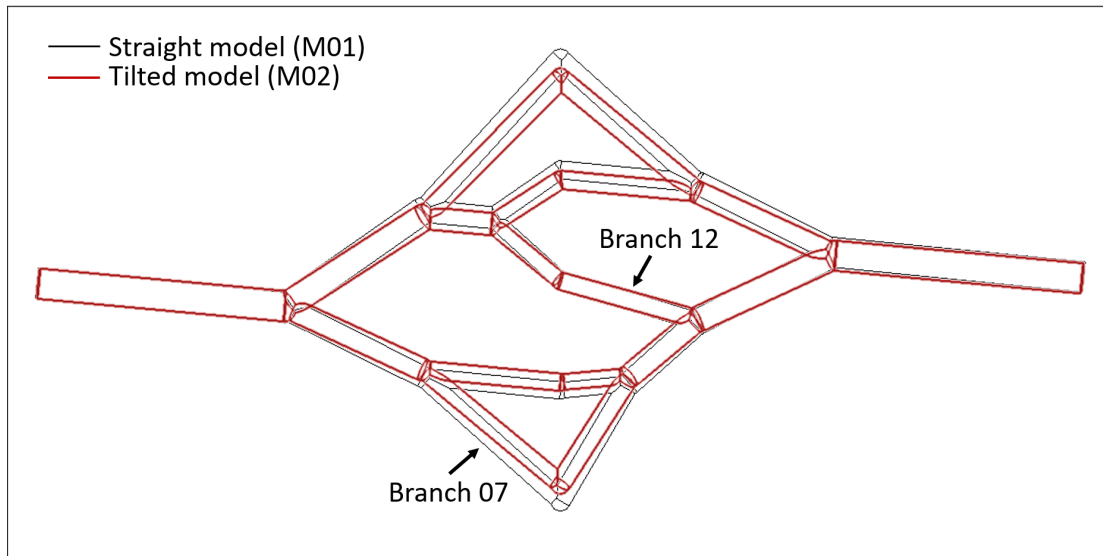


Fig. 5.22 Overlapping of straight and tilted views of networks from microscope camera perspective. Branches close to the central axis are less affected by tilting (e.g. branch 12), as opposed to branches further from the centre, which appear shorter (e.g. branch 07).

02, particularly in the outer branches such as 07, 14 and 16.

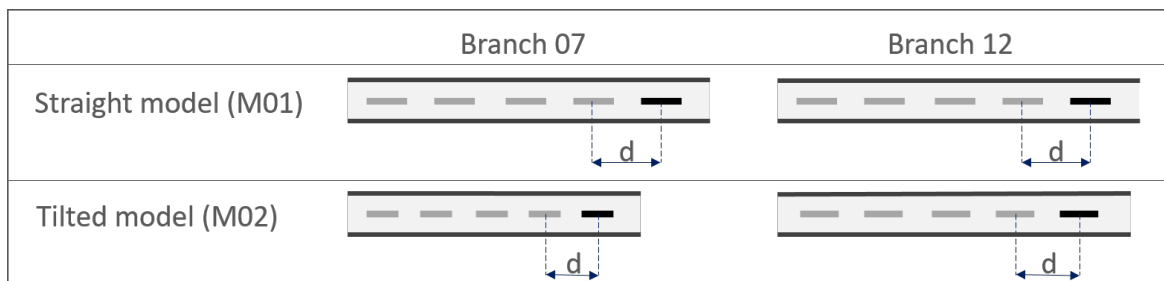


Fig. 5.23 Displacement of particle in straight vs. in tilted network for branches 07 and 12.

From the maximum velocity comparison charts it is also noticeable that for both models M01 and M02, the experiments with  $Q_{inlet} = 2 \text{ mL/h}$  (blue symbols) show a smaller difference between experimental and theoretical values than the experiments with  $Q_{inlet} = 5 \text{ mL/h}$  (red symbols). The reason for this is that at higher flow rates, the tracking of particles becomes harder and less accurate. As the particles travel faster across a given branch, the number of images where the particle is present are reduced. Therefore there are less images from which the displacement can be averaged, thus making it error-prone. In model 01 the acquired images are clear enough to measure the particles. However, in model 02 the tilting affected

the focus of the branches, causing that in most branches only a section of the branch was clear. This affected the number of particle displacement measurements that were taken, and explains why the number of measurements seem smaller for M02 than for M01 in the raw data charts (Figures 5.16 to 5.19).

## 5.5 Conclusions

In order to validate the practical application of the vascular networks, an experimental approach to the measurement of flow velocity was presented in this chapter. The present work uses PTV, an approach similar to PIV, using a fluorescence microscope with a CMOS camera to capture consecutive images of a particle-seeded fluid flowing through channels, and subsequently using the images to calculate the displacement of the particles. The only difference between the method here presented, and the traditional PIV approach is that the latter typically uses specialised PIV software with complex tools and correlation parameters, while the present work uses a custom-made software programmed in LabView to process the obtained images. With the LabView software, it is possible to calculate the variable of interest: maximum flow velocity in the channels.

The experimental models were generated with dimensions and geometry based on the findings of Chapter 4 (Section 4.3.2). Two models were fabricated in PDMS with different design values of pressure difference across the networks, for comparison. Model 01 appears to be aligned horizontally, but model 02 suffered from a significant tilting during the fabrication process. The tilting complicated the measurement process, as the microscope could not be focused on the entire length of the channels, which resulted in lower velocity values for model 02 due to measuring the projected velocities and not the real ones.

From the consecutive image sets obtained from the microscope, measurements of flow velocity were achieved for every branch in models 01 and 02, at two experimental flow rate values ( $Q_{inlet} = 2$  mL/h and  $Q_{inlet} = 5$  mL/h). The plots for particle velocity (Figures 5.16 to 5.19) provide a good estimation of the velocity profile for each channel as it shows parabolic shapes, as expected from fluids that obey Poiseuille's law.

Regarding the model fabrication, Figure 5.10 showed that there is some variation between the original design diameters and the fabricated models' diameters. In the case of model 01

the difference is subtle, but model 2 presents a variation of approximately 20%.

The particle imaging method here implemented produces a good approximation to the velocity profile. However, in order to make it more reliable, a larger amount of pictures are needed to allow more particles to be tracked and have a better probability of obtaining the fastest particle at the central axis. However, this could be technically impractical. During the experimental measurements, the maximum number of images taken per branch, per flow rate was 900. The files generated by the microscope for each set of 900 images used approximately 7 GB of disk space. Considering that 72 sets were necessary (18 branches, 2 flow rates, 2 models), the space necessary was approximately 0.5 TB.

The differences between experimental and theoretical values for the maximum velocity (5.20) are larger in the experiments with flow rate  $Q_{inlet} = 5$  mL/h than in those with  $Q_{inlet} = 2$  mL/h. This happens because at higher flow rates, the imaging becomes more challenging as the particles move faster. The limited exposure time of the camera results in the particles appearing as straight lines in the captured images. In addition, the length of the straight lines might vary from one frame to the next, making the average measurement more prone to errors.

As mentioned at the beginning of the chapter, using a physiological flow rate was not feasible due to technical limitations, which was the greatest challenge of the experimental work. Originally, the experimental inlet flow rate value was intended as 20 mL/h for a direct comparison with the design parameter (which was this same value). However, the microscope camera used in the measurements could not image the fluorescent particles, as the exposure time was larger than the time it took the particles to travel the imaging distance. A microscope with a high speed camera could have solved this problem. Because of this, it was decided to use two arbitrary values (2 and 5 mL/h), at which the images showed clear particles for tracking.

Considering that the original flow rate value could not be tested experimentally, an alternative would be to use another method to calculate it. Computational fluid dynamic (CFD) analysis is a well documented technique that could be used to obtain these results. The next chapter will present a CFD-based analysis of the same models used in this chapter (M01 and M02).



# Chapter 6

## Flow in vessels: Computational Fluid Dynamics analysis

### 6.1 Overview

Chapter 5 presented an experimental approach to flow analysis in two planar vascular network models. In order to validate the experimental work, a further flow analysis is necessary using a reliable numerical analysis tool such as a CFD software package. This chapter presents a CFD analysis approach to simulate flow in the 3D models of experimental vascular networks. During the experimental work, measurements of velocity using a physiologically relevant inlet flow rate were not possible due to the technical limitations of the equipment (as explained in 5.3.5). Thus, the CFD analysis was performed using the low flow rate of the experimental models.

Section 6.2 presents a brief review on the use of CFD tools for the simulation of flow in vessels or micro-channels. Section 6.3 comprehends a CFD analysis of 3D models of the networks with modified diameters to be in accordance with the measurements from the experimentally fabricated networks. Setup for the CFD simulations is detailed. Section 6.4 presents the resulting plots and charts from the CFD analysis. Section 6.5 includes discussion on the results, as well as a comparison between experimental and CFD data of the main parameter of interest: the velocity. An additional simulation of model 01 at the original design flow rate (20 mL/h) is presented.

Overall, the aim of the chapter is to validate the experimental data by comparing it to simulations from a reliable CFD software package (COMSOL Multiphysics). One important

fact to note is that in the literature, Pascals is the preferred unit for pressure and pressure difference. To be in accordance, this chapter will use Pascals to measure pressure, and the equivalent value in mm Hg is also provided when appropriate.

## 6.2 Review of the use of CFD for studying flow in vessels

Numerical methods can be used to solve engineering problems that are represented by differential equations, including fluid flow in channels. These methods are the core of what is known as computational fluid dynamics (CFD) and can produce accurate results if the parameters and boundary conditions are set as close as possible to the physical model.

There are three classic methods in to find the numerical solution of differential equations: finite difference method (FDM), finite volume method (FVM) and finite element method (FEM) [139]. The three methods have one aspect in common: the need to discretise the domain of interest (i.e. a 3D model) into a number of elements. This step is crucial in all finite analysis methods, as a poorly discretised domain can produce inexact solutions. FDM is the oldest approach and uses approximation of differentials (typically based on Taylor series approximations) [140]. Its main advantage is the fact that it produces the most accurate results, but its greatest disadvantage is that it requires the elements to form a structured grid which is typically formed by squares (in 2D) or cubical elements (in 3D), thus, limiting the shape of the geometries where it can be used efficiently. As opposed to the differential approach used in FDM, an integral approach is used in FVM and FEM. In FVM the main analysis unit is a cell, whereas in FEM it is an element. Both integral methods are flexible with regards to the geometry of the domain of interest, allowing complex shapes to be modelled. FVM is based on conservation laws and its main advantage is that it ensures that for every cell (volume of control) the equation is integrated and the flux on a given cell boundary is equal to the opposing flux in the next cell [141]. FEM is based on integral approximations of the solution at each element in the domain. By a large margin, FEM is the most commonly used approach in numerical analysis, and the most flexible, which allows a large number of numerical problems to be solved. It was originally a tool developed to solve problems in solid-state mechanics, but since its development in the 1960's it has become the most robust method available and is widely used in all areas of physics and engineering, including CFD [142], as opposed to FVM which is typically used for CFD only. The advantage of using a FEM-based solver is the possibility to combine multiple physics equations (to represent multiple physics phenomena) in a single problem.

In addition to the finite analysis methods (FDM, FVM and FEM) there is a method that emerged 20 years ago but only recently became attractive for flow analysis. It is called the lattice Boltzmann method (LBM) and it is used largely for CFD analysis in applications involving modelling of biological phenomena [143], although its use has also been reported in other areas such as for the analysis of thermal airflow in data centre facilities [141]. LBM is a special discretisation of the simplified Boltzmann equation (see [144]) used to describe transport phenomena at the mesoscale level. Fluid is modelled as the transport of fictitious particles using a probability function to describe the distribution of particles at a given velocity [145]. Among the advantages of LBM over the continuum methods are its relatively simple implementation, capability for parallelisation and handling of microscopic interactions [146]. The main limitations of LBM are the incompatibility with flows of high Mach numbers <sup>1</sup> (in aerodynamics) and the lack of a consistent thermo-hydrodynamic scheme [147].

Commercial packages for numerical analysis are available and many authors have reported its use for the simulation of flow in biological structures. Some of the packages most commonly used for this purpose include: COMSOL [148][149], ANSYS (Fluent [150][151] and CFX [152]), OpenFOAM [153], and others [154]. Most of the available CFD commercial software packages use FVM-based solvers (i.e. ANSYS Fluent, Flow-3D, SOLIDWORKS FloWorks). On the other hand, one of the most well-established and widely used numerical analysis packages (COMSOL Multiphysics) uses a FEM-based approach. There is debate in the engineering community regarding which approach is better, with the general consent being that FEM has a wider number of applications and its level of complexity is higher, but ultimately agreeing that it depends on the application to decide which approach is the most suitable.

Despite their differences, FEM, FVM and LBM have been used in CFD to understand flow through channels in vascular tissue engineering and microfluidics. There have been different simulation approaches which have shown results similar to real physiological values, demonstrating that modelling using CFD could be used as an alternative powerful tool, to measure real life physiological parameters.

Some approaches use medical imaging techniques (i.e. MRI, CT scan) for vascular structures, particularly in the aorta and carotid bifurcation models. Köhler et al. [155], and Marshall et al. [156] report similar comparisons between in-vivo MRI analysis for the

---

<sup>1</sup>The Mach number represents the ratio of the velocity of an object moving through a fluid, to the velocity of sound in the fluid. Mach < 1 indicate subsonic flow; Mach > 1 indicate supersonic flow.

quantification of blood flow in a carotid bifurcation, and CFD analysis of the same carotid model obtained from the MRI data. The simulations were performed based on the Navier-Stokes equations (assuming rigid walls) with the CFD package CFX4 from AEA Technology, which is based on FVM. Their results showed that the wall shear stress predicted by the CFD analysis is qualitatively in accordance with the MRI derived measurements. In a later work, Marshall [157] demonstrated that it is possible to use CFD-based MRI simulations to predict the MRI flow behaviour in the same carotid model. Large-scale trees have also been modelled based on these types of imaging. Grinberg et al. [154] report the development of a CFD code called 'NEKTAR', which is used for large-scale simulations of flow in models of the aorta and a cranial arterial tree reconstructed from MR and CT images. This shows that CFD of large physiological systems can be achieved with these methods and not only of basic elements like bifurcations.

In addition, models of full organ vasculature have also been reported. Simoncini et al. [158] developed a method for the CFD simulation of flow (containing microspheres) in patient-specific hepatic arterial trees. The model was obtained by cone-beam CT angiography and converted into a 3D model for CFD analysis using ANSYS Fluent. The radius of the vessels in the trees range from approximately 0.49 mm to 3.6 mm. Data for the boundary conditions of the model (i.e. blood inlet velocity) was obtained experimentally from the patients using a phase-contrast MR. Their results showed that the flow is coherent with literature values for the larger arteries, but for the smaller there is little information to compare.

Besides simulations using models obtained from imaging techniques, there are also approaches that use computer-generated vascular trees. Jurczuk et al. [153] developed a CFD-based MR flow imaging simulator for complex vascular structures generated with an algorithm (see Table 3.1 in Chapter 3). This approach uses the lattice Boltzmann method (LBM) to model the flow, as opposed to the conventional CFD approach that uses the Navier-Stokes equations, as it is intended for complex models with many elements and it has been reported that its performance is approximately like the Navier-Stokes method [145]. The LBM simulation was compared to a model solved by numerical Navier-Stokes equation (using OpenFOAM) and the results report no significant difference observed in the flow behaviour.

Apart from the CFD simulations on biologically derived models, there are also extensive reports of CFD analysis for microfluidic networks. Boutin et al. [138] presented a study of flow distribution in a micro-fluidic network using experimental (PIV) and computational

methods (CFD) under the same conditions. The network had 15 parallel channels with constant squared cross-section of  $2 \text{ mm} \times 2 \text{ mm}$ . ANSYS FLUENT was used for the CFD simulations. The analysis showed that for low flow conditions (inlet flow rate =  $0.18 \text{ L/min}$ ) the CFD results are in strong agreement with the experimental PIV measurements, while for higher flow rates ( $1.8 \text{ L/min}$ ) the general tendency for both the CFD and PIV is in accordance, but discrepancies were found in some of the channels, which may indicate that the model does not accurately represent the physical model. However it is believed that this difference might be caused by difficulties in the simulation due to turbulence in the flow. The shape of the network is also something to consider. Sharp corners or edges might be troublesome areas for CFD solvers, so the simulations might not describe the physical models accurately. Low et al. [159] studied the flow within various microfluidic network designs for dielectrophoresis applications. Their original proposed design was a network with squared bifurcating channels. However, after CFD analysis it was noticed that at the corners of the channels the flow was zero (which was not ideal for the application as it could cause collection of cells in these zones). A new design was proposed using rounded corners, which improved the velocity profiles in the model. Therefore, this indicates that models without sharp corners have a better chance of congruence between experimental and CFD results.

CFD simulations are also a tool used to investigate physiologically relevant parameters (e.g. flow velocity, wall shear stress, bifurcating angles) as they can be used as an aid in model design for fabrication. Han et al. [149][160] presented a CFD analysis of flow in different arterial branching angles to investigate the change in velocity profiles and wall shear stresses. The models had one branch (parent) of  $5 \text{ mm}$  of diameter and two branches (daughters) of  $3.87 \text{ mm}$  of diameter, and the tested branching angles were  $45^\circ$ ,  $85^\circ$  and  $125^\circ$ , each with sharp and smoothed junctions. The CFD simulations are carried out in COMSOL Multiphysics using the Navier-Stokes equations, assuming incompressible Newtonian flow, steady state flow, and no-slip conditions at the wall. Results showed that a smaller branching angle with smoothed edges is preferred for a lower wall shear stress and to avoid recirculation. Chaichana et al. [152] performed CFD simulations to study the effect of variations in the bifurcating angle of the left coronary artery. The models included some derived from CT angiography images, and others were artificially modelled as simple bifurcating structures based on anatomical data. ANSYS CFX was used for the simulations, based on the Navier-Stokes equations, under realistic physiological conditions including pulsatile flow. Their results indicate that there is a correlation between wide angles and a disturbed flow pattern, lowering the wall shear stress (which may be a cause for atherosclerosis). Therefore, bifurcating angles play an important role to represent vascular physiology in healthy and

pathological conditions, to achieve adequate values of shear stress. Considering this, and the fact that in the widely used Poiseuille flow model the angles are not included, Yang et al. [151] proposed a modified Poiseuille's law equation, where a coefficient to represent the angles is added.

Noticeably, other physiologically relevant factors to consider are the pulsatility of blood flow, the presence of particles (red blood cells, white blood cells and platelets) and the non-Newtonian behaviour of blood. There are reports of CFD studies that consider these factors. Liu et al. [150] used CFD simulations to compare the effect of Newtonian and non-Newtonian steady and pulsatile blood flow on the distribution of low density lipo-proteins (LDLs) in a model of the human aorta obtained by MRI. The flow simulation for the Newtonian fluid conditions was performed using the Navier-Stokes equations, while for the non-Newtonian conditions, the Carreau fluid model is used<sup>2</sup>. For both cases, the numerical analysis was carried out using the commercial package ANSYS Fluent. Their findings indicate that for non-Newtonian flow behaviour there is little effect on the concentration of LDLs or oxygen transport in comparison with the Newtonian fluid behaviour. Similar findings were found with steady and pulsatile flow. The only places where a difference was found were in regions where there was a flow disturbance. This indicates that for many anatomically relevant simulations, both a steady flow and a Newtonian model can be used to represent the human counterpart. In fact, a more precise model would include the presence of cells in the simulated flow. Bagchi et al. [40] report using the immersed boundary method for the simulation of blood flow in vessels ranging from 20-300  $\mu\text{m}$  including deformable red blood cells (RBCs) in the model. The simulation uses a non-Newtonian flow and considers the Fåhræus-Lindqvist effect (change of viscosity dependent of vessel size). The simulation of additional physiological representations are reported by Choudhari and Panse [162], where they model the main arterial tree in the human arm, considering the flexibility of arteries and a pulsatile flow.

Another aspect of interest is the simulation of oxygen diffusion from a vascular network to the surrounding tissue. In regard to this, Ball et al. [148] used CFD simulations to analyse the flow, particularly oxygen diffusion, from a porous macro-vascular network structure through alginate constructs in a perfusion bio-reactor chamber. COMSOL Multiphysics was used to model the diffusion throughout the perfusion system. The CFD simulations were in accordance with the experimental work, predicting cell viability at steady state flow.

---

<sup>2</sup>A Carreau fluid is a type of generalised Newtonian fluid in which viscosity is dependent on the shear rate. This model was first proposed by Pierre Carreau (see [161]).

Overall, the scope of the present work is to analyse flow behaviour in simple planar networks of cylindrical channels, with a small number of bifurcations and branches. The diameters of the channels are between 250 and 600  $\mu\text{m}$  (approximately the size of small arteries in the circulatory system), and Newtonian flow is assumed. Either FVM or FEM based approaches could be suitable for the simulations, given the simple design. However, among the available numeric solvers, the use of COMSOL Multiphysics was deemed advantageous due to the wide range of physics models that can be simulated simultaneously, which could not be achieved using the CFD specific FVM-based methods. For example, considering all the physiological features that were simulated separately by the authors mentioned above (e.g. concentration of molecules in blood, presence of cells, flexibility of arteries, pulsatility of blood flow and oxygen diffusion), COMSOL Multiphysics seems appropriate to use given the possibility to simulate all of them together. These features could be added in future work either for the models presented here or more complex structures. Thus, COMSOL Multiphysics is used for all the CFD simulations.

## 6.3 CFD analysis in vascular network models

Having discussed the advantages of using CFD tools in diverse vascular models and microfluidic channels, this section presents a CFD approach to flow simulation and analysis in the vascular network models used for experimental work in the previous chapter. The aim of the CFD analysis is to further validate the results obtained experimentally by comparing them with those obtained by simulations. In addition, the CFD simulations could provide data about other parameters to further improve the designed model.

### 6.3.1 Setup

In this section, the CFD analysis setup in COMSOL is detailed including a sequence of steps to run the simulations. The aim of the chapter is to observe how the CFD simulation results differ from the values measured by experimental means. In order to have a consistent comparison between the experimental and simulated models, the original 3D designs were modified to match the shape and diameters of the fabricated models measured with the microscope software. CFD model 01 is based on the measurements of experimental model 01, and CFD model 02 is based on experimental model 02. As explained in Chapter 5, due to fabrication, the experimental models lost segments of the root branches from the original

designs (inlet and outlet). These changes are reflected in the CFD models.

The simulations were performed on a personal computer equipped with Intel® Core™ i7-6700 CPU @ 3.4 GHz, 4 Cores, 8 Logical Processors, 32 GB of RAM and NVIDIA GeForce GTX 1060 6GB graphics card. COMSOL Multiphysics 5.4 is used for all simulations. Computational time of the simulations varied as a function of the parameters (particularly the mesh element size), but most of the models took approximately 6 minutes to compute. The main procedure for the CFD analysis in COMSOL consists of simulating flow in the vascular network by applying the same values of inlet flow rate as that of the experimental work (2 and 5 mL/h). All the simulations were performed using the following sequence:

1) Export model in IGS format in Inventor.

The modified models were exported as initial graphics exchange specification format (IGES), which is a neutral file format used to transfer 2D and 3D models between different CAD systems.

2) Import IGS format in COMSOL using the CAD import module.

The 'Model Wizard' was used, selecting a 3D space dimension with a laminar flow study (stationary). In the Geometry tab the Import option was used and the location of the IGES file was specified. The standard import parameters were used except the import tolerance, which was set to  $1 \times 10^{-6}$ , as the main length unit in COMSOL are meters (m) and the models are in the range of micrometers ( $\mu\text{m}$ ).

3) Define materials, parameters and boundary conditions for CFD analysis.

Under the Materials tab, a new blank material was created. For the experimental work, PBS was used, therefore, in order to simulate under the same conditions, the properties of PBS were assigned to the new material. According to the technical specifications of the PBS (Dulbecco PBS - D8537 from SIGMA), the density is 1.00-1.01 g/mL, so an average value of 1.005 g/mL was used. The density units in COMSOL are  $\text{kg/m}^3$ , thus, the value was set to  $1005 \text{ kg/m}^3$ . The dynamic viscosity value was not available from the technical information, so it was approximated to 0.00105 Pa·s based on the values from other brands of PBS. Under the Laminar Flow tab, in the Fluid Properties sub-section, the fluid properties must be set to 'From material'. The initial values sub-section was left with the default parameters. Then, two boundaries were created under the Laminar Flow tab: one for the Inlet, and one for the Outlet. For the Inlet, the surface of the model that represents the inlet is assigned. The boundary condition is Velocity, and it is set to the corresponding velocity value, as shown in

Table 6.1 Velocities for inlet boundary condition.

|     |                              | $V_{mean}$                         |
|-----|------------------------------|------------------------------------|
| M01 | $Q_{inlet} = 2 \text{ mL/h}$ | $1.943 \times 10^{-3} \text{ m/s}$ |
|     | $Q_{inlet} = 5 \text{ mL/h}$ | $4.856 \times 10^{-3} \text{ m/s}$ |
| M02 | $Q_{inlet} = 2 \text{ mL/h}$ | $2.258 \times 10^{-3} \text{ m/s}$ |
|     | $Q_{inlet} = 5 \text{ mL/h}$ | $5.646 \times 10^{-3} \text{ m/s}$ |

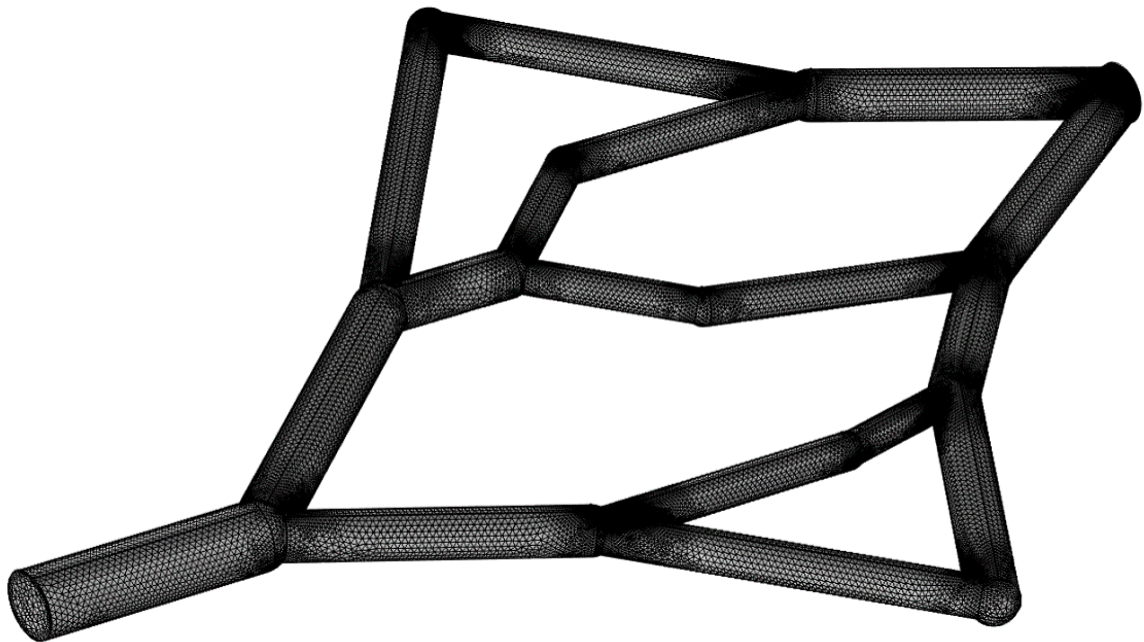
Table 6.1. The inlet velocities were calculated by dividing the inlet flow rate by the area of the root branch (which is the definition of the mean velocity in a channel, with Poiseuille's flow). For the Outlet, the surface of the model representing the fluid outlet is assigned. The boundary condition is Pressure, and it is set to 0 Pa for all cases. Finally, in the Wall sub-section, the boundary selection must be assigned to all the surfaces in the model, except the ones set as inlet and outlet. The boundary condition is set to 'No slip'.

#### 4) Create mesh for 3D model.

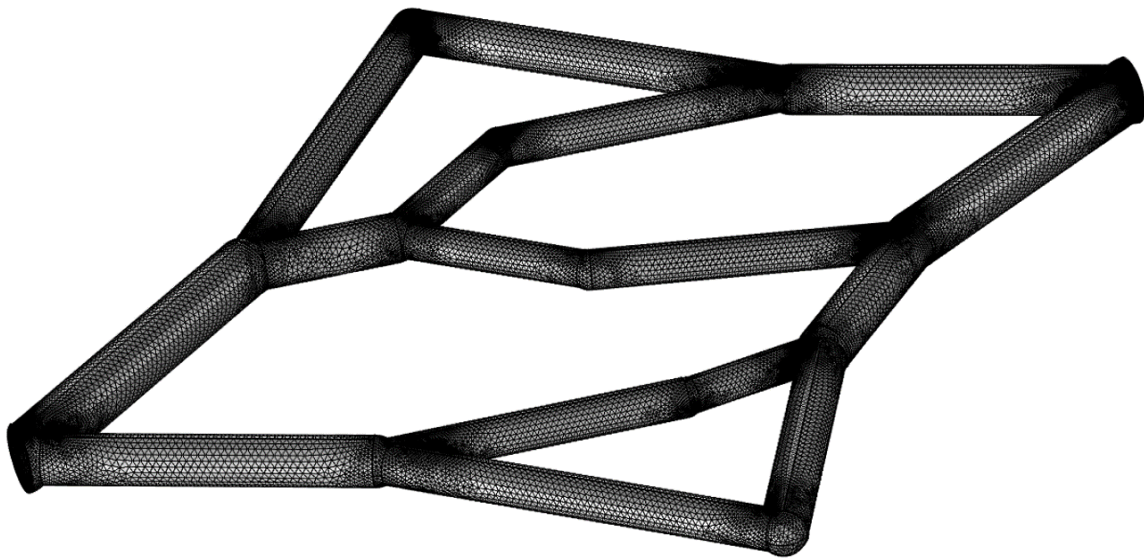
The mesh was built with the following parameters: in the Mesh section, a Physics controlled mesh was selected. As a general rule in finite element analysis (FEA), models with a fine mesh produce more accurate results than models with a coarse mesh [163]. However, a fine mesh will always require a longer computing time than a coarse mesh. As a result, finding the optimal element size in a mesh is required to ensure accuracy while saving computing time. In the present research the models present a simple branching geometry consisting of cylindrical branches and spherical junctions. The cylinders and spheres have diameters in the range of hundreds of microns, therefore a relatively fine mesh is preferred. In the mesh section in COMSOL the available mesh element size options are: extremely coarse, extra coarse, coarser, coarse, normal, fine, finer, extra fine and extremely fine. Considering the performance of the computing equipment and after trying different element sizes, it was deemed that the 'finer' element size was the most appropriate, as it produces a quality mesh while maintaining the total computing time in the order of minutes. Thus, for all simulations the mesh element size was set to 'finer'. The computing time for mesh generation was similar for all models and was around 1 minute. For model 01 the generated mesh had 1,604,919 elements (tetrahedra, pyramids, prisms) regardless of the specified boundary conditions, while for model 02 the mesh had 1,647,010 elements. Both meshes are shown in Figure 6.1. The meshing statistics data from COMSOL for the models is included in Appendix B.

#### 5) Run simulation and visualise results.

Under the tab Study the simulation is solved using the 'Compute' function. The simulation



(a)



(b)

Fig. 6.1 Meshes generated in COMSOL for both models. (a) Model 01. (b) Model 02. Note that the models reflect the changes in shape of the experimental PDMS models (i.e. diameters and lack of inlet/outlets).

time was similar for all models (approximately 6 minutes). After the simulation is completed, the results can be observed in a variety of manners. Groups of 3D, 2D and 1D plots can be created, depending on the variables of interest. For the current study, the flow velocity was analysed as well as pressure difference and wall shear stress. Several plots were created for these variables and after careful examination the following plots were considered to be the most suitable for each case:

- Velocity: 2D surface plot, using the middle plane of the model.

Given the cylindrical shape of the channels, the highest velocity is found at the centre. Thus, a cut plane was created at the middle section across the model as shown in Figure 6.2. A surface plot was created in this plane to show the velocity magnitude. In addition, for each branch a 1D plot was created using a line perpendicular to the channel to have a better visualisation of the corresponding velocity profiles.

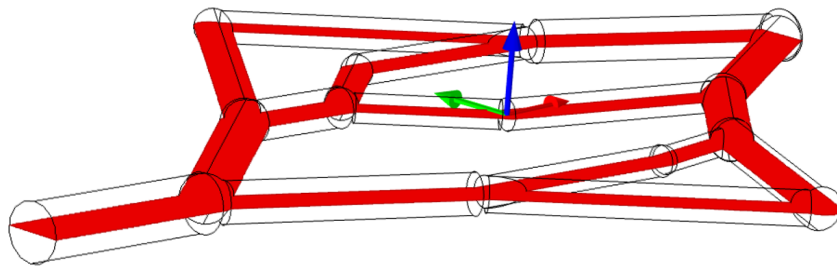


Fig. 6.2 Middle plane used for velocity measurement in CFD results.

- Pressure difference: 3D surface plot using the whole model.

In any branch of the model, the pressure changes along the axis of the branch. For this measurement, a 3D plot was generated where the contour of the model shows the corresponding pressure values. It could also have been represented by a 2D surface plot on the middle plane (as the values are exactly the same) but a 3D plot was preferred for better visualisation.

- Shear stress: 2D surface plot (using the midplane).

In order to visualise the distribution of shear stress at the wall of all branches, a 2D surface plot was used at the middle plane of the model, in a similar way as the velocity.

## 6.4 Results

This section presents the results obtained by CFD analysis of network models designed based on the dimensions of the fabricated networks for the experimental work (presented in Chapter 5). For an easier comparison, the network branches in this section follow the same numbering arrangement as in the previous chapter (see Figure 5.9), omitting the missing branches (branch 18 in model 01, and branches 01 and 18 in model 02).

The first variable of interest is the flow velocity. Given the cylindrical shape of the channels in the network, the midplane was used to observe the velocity distribution. Figure 6.3 shows velocity plots for CFD models 01 and 02 for the same values of inlet flow rate used in the experimental work (2 and 5 mL/h). As expected in a cylindrical channel with Poiseuille flow, the highest velocity is found at the central part of the channel. It can be observed that at some bifurcation areas there is an increase in flow velocity prior to the bifurcation, particularly noticeable in the zone where branch 3 bifurcates into branches 6 and 7, and the zone where branches 10 and 11 merge into branch 16. Figure 6.4 shows close up images of these areas with a velocity field plot, which indicates that there is no re-circulation or abnormal flow behaviour at the zones. In [151], Yang et al. observed a similar behaviour, where the increase in velocity was larger as the bifurcation angle became wider. At the upper and lower arterio-venous connection points of the networks the dark blue regions indicate zero flow. This is probably due to the sharp angle at which the channels are connected.

Velocity profile plots were generated for every branch by creating a 1D linear plot perpendicular to each channel and plotting the velocity across the line. The resulting plots were grouped by arterial and venous tree branches for a better visualisation, where the arterial tree comprises branches 1 to 9 (or 2 to 9 for model 02) and the venous tree, branches 10 to 17. The plots are shown in Figures 6.5 and 6.6. As expected, the velocity profiles present a parabolic shape as dictated by Poiseuille's law for laminar, Newtonian flow.

The second variable of interest is the pressure difference across the network. The plots obtained by CFD simulation are shown in Figure 6.7. In COMSOL the default unit for pressure is Pascals, thus it is used in this section. Originally, the models were created with a pressure difference of 1 and 2 mm Hg from inlet to terminal points, which means a total network pressure drop of 2 and 4 mm Hg (267 and 533 Pascals), respectively, for an inlet flow rate of 20 mL/h for models 01 and 02. In this case, however, given that the experimental work used the values of 2 and 5 mL/h as an alternative to 20 mL/h (because of technical limitations for flow measurement), in the CFD simulations the same values were used, and

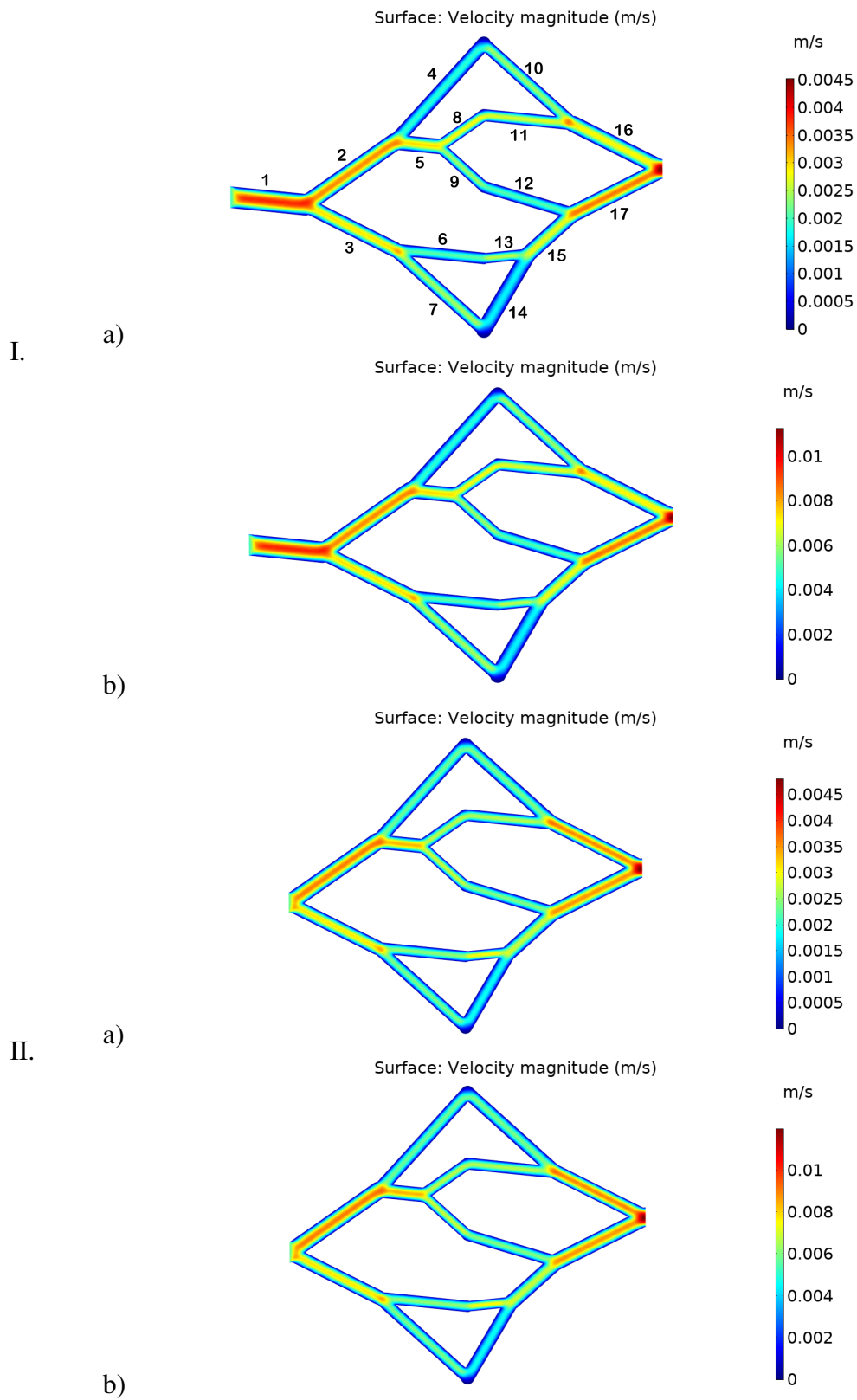


Fig. 6.3 Velocity plots (at the midplane) obtained by CFD analysis. (I.) Model 01. (II.) Model 02. (a)  $Q_{inlet} = 2$  mL/h, and (b)  $Q_{inlet} = 5$  mL/h.)

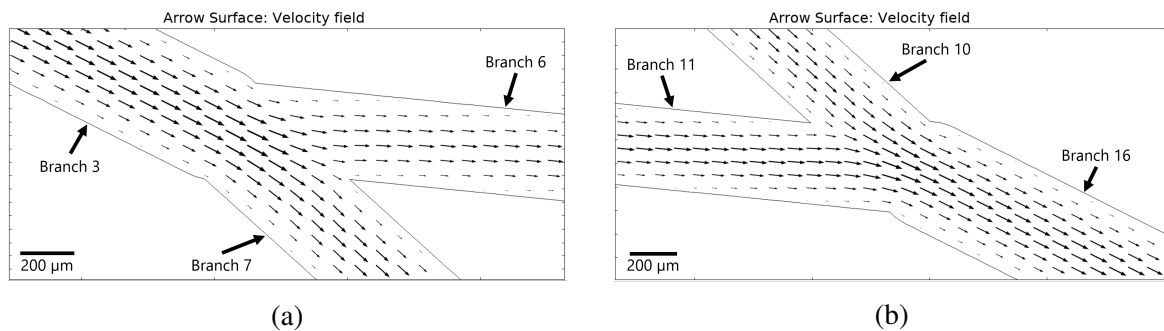


Fig. 6.4 Velocity field plot with close up at zones where the velocity is greater. (a) Junction where branch 3 bifurcates. (b) Junction where branches 10 and 11 merge.

therefore the expected pressure drop using these flow rate values is much lower. Given the lack of experimentally obtained pressure data, estimated values of the pressure drop across the networks were calculated using the Poiseuille's flow equation (see Equation 4.4) with the corresponding experimentally obtained values: measured radii, experimental  $Q$  obtained from the flow velocity measurement and PBS viscosity. The only values that were kept the same as the design values are the branch lengths, as it was not physically possible to measure full branches with the current microscope objective setup due to the dimensions. However, it was assumed that the lengths in the fabricated models did not vary significantly from the design lengths due to the high accuracy of the 3D printer movement in the XY axes (as opposed to the larger variations in radii due to the resolution, given by the thickness of the layer of deposited material).

The estimated experimental pressure values were calculated in the following manner: First, all the possible 'paths' of pressure drop from inlet to outlet were identified, where these 'paths' are formed by consecutive branches from inlet to outlet, passing through an arterio-venous connection point (i.e. one path is formed by branches: 1, 2, 5, 8, 11 and 16, as shown in Figure 6.8). It was calculated in this manner because, by design, the pressure drop from the inlet to any of the terminal points (connections between arterial and venous tree) is the same, regardless of the path of branches, and being this the case for both trees, the total pressure drop of the network can be calculated by adding up the pressures of any path of branches from inlet to outlet. Having calculated the pressure drops for all the five paths (see Table 6.2), the estimated experimental pressure drop of the models were calculated as the average of the pressure drops in the paths. As it is observed, although in theory the pressure drop in all paths should be the same value (according to the design parameters), there are slight variations possibly due to differing diameters due to fabrication. Thus, the average of the paths was used as the experimental value. The estimated experimental values

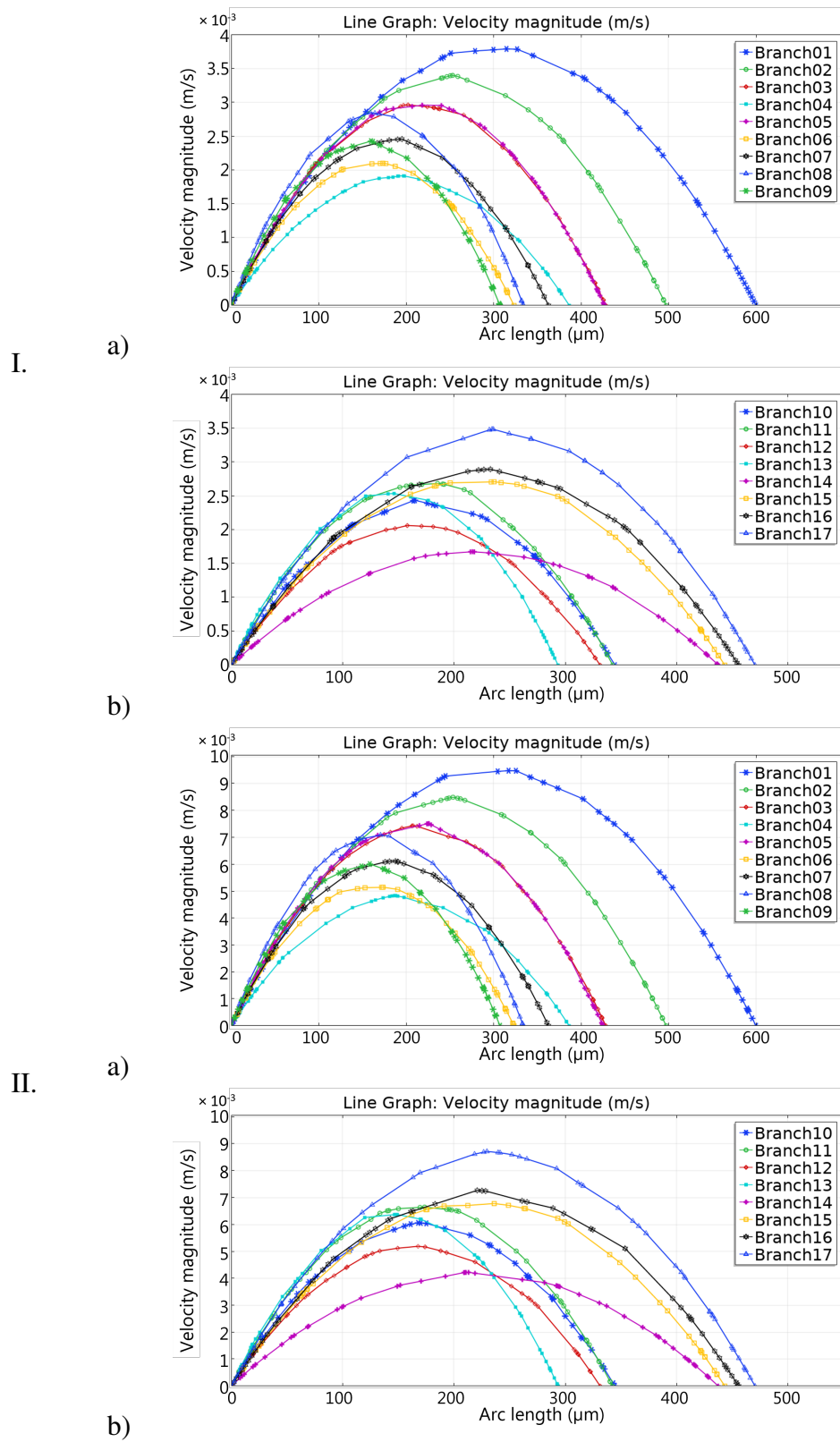


Fig. 6.5 Velocity profiles of each branch in model 01 (at the midplane) for two values of inlet flow rate obtained by CFD analysis. (I.)  $Q_{inlet} = 2 \text{ mL/h}$ . (II.)  $Q_{inlet} = 5 \text{ mL/h}$ . (a) Branches 1-9 (arterial tree). (b) Branches 10-17 (venous tree).

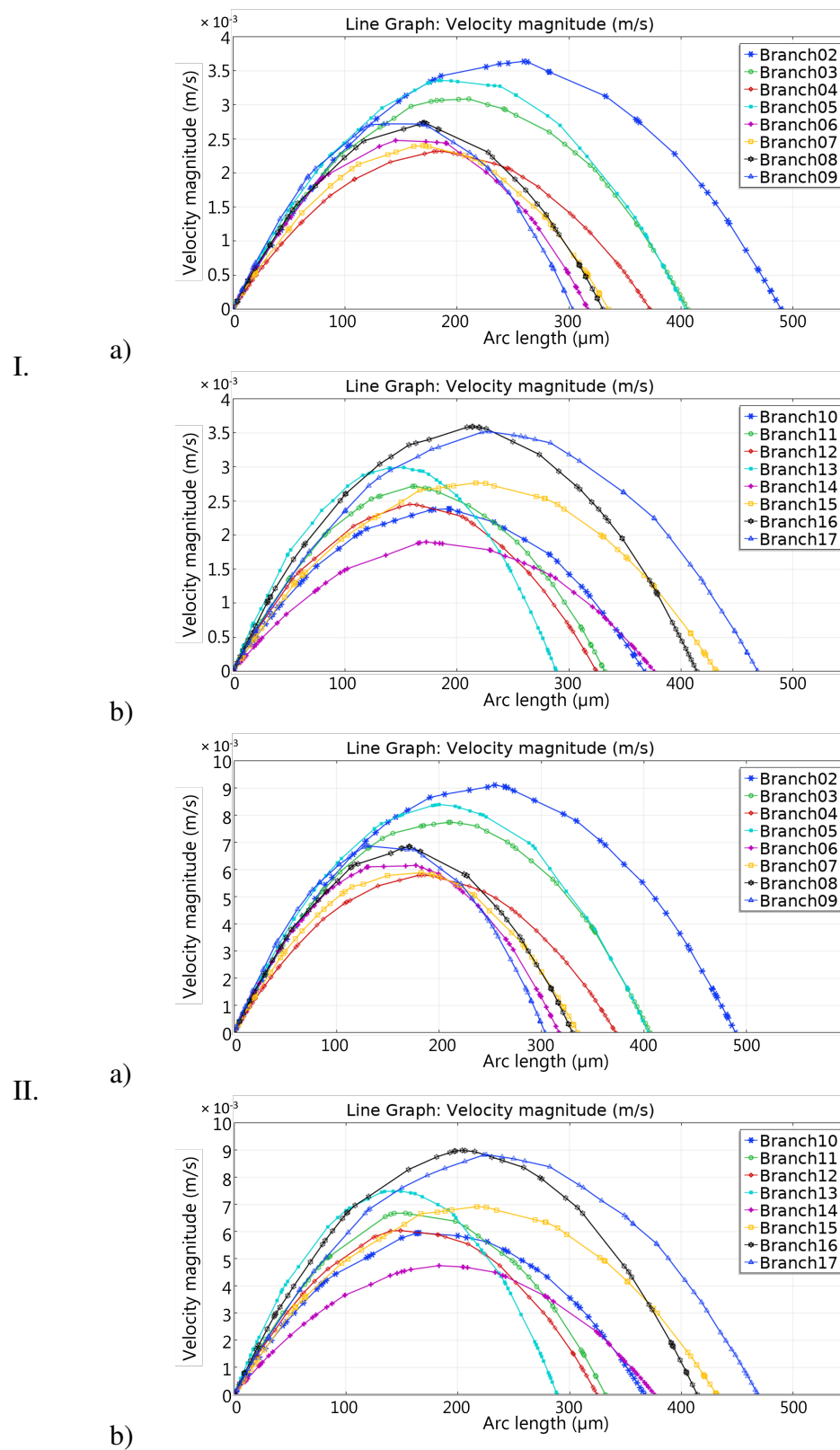


Fig. 6.6 Velocity profiles of each branch in model 02 (at the midplane) for two values of inlet flow rate obtained by CFD analysis. (I.)  $Q_{inlet} = 2$  mL/h. (II.)  $Q_{inlet} = 5$  mL/h. (a) Branches 2-9 (arterial tree). (b) Branches 10-17 (venous tree).

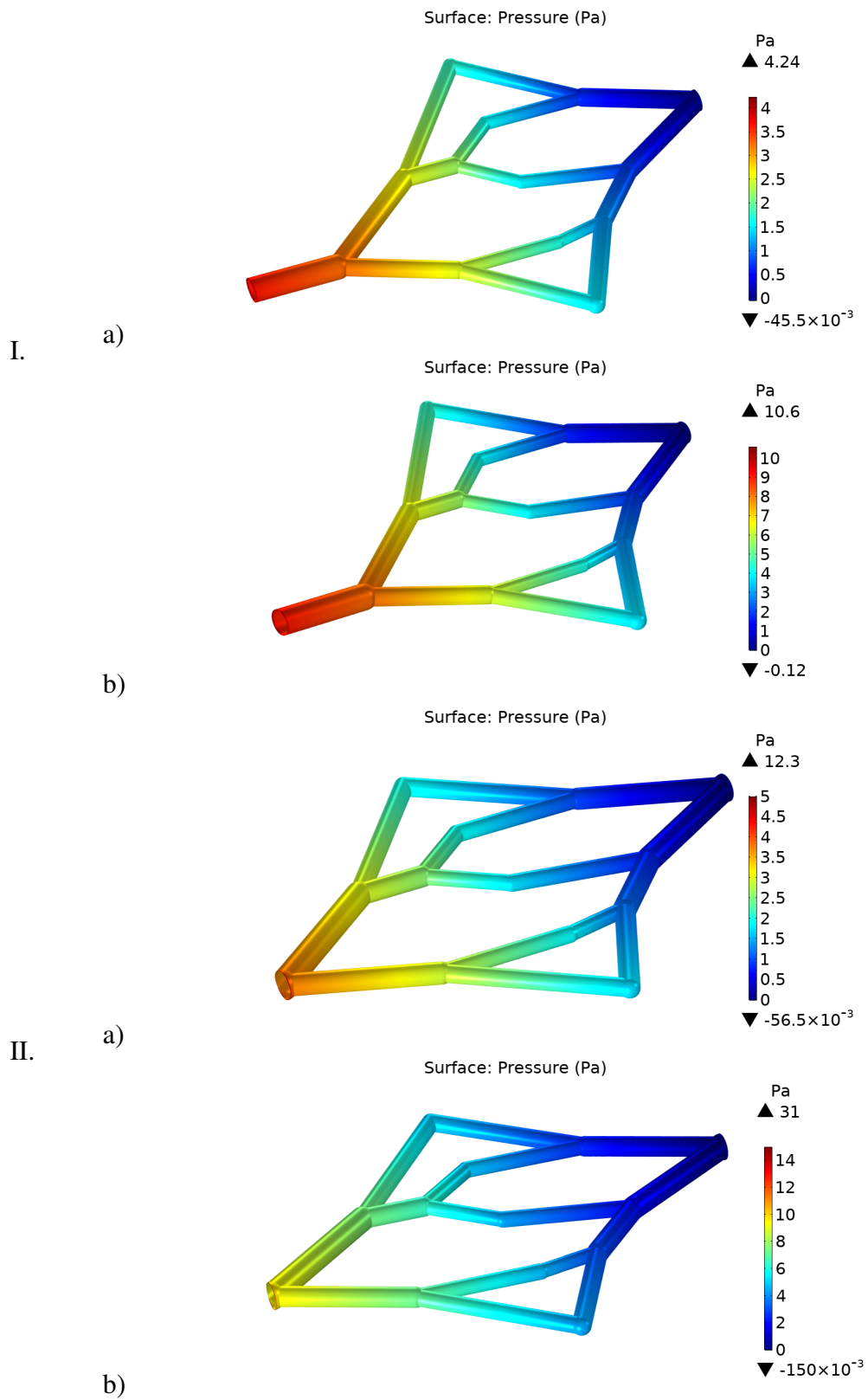


Fig. 6.7 Pressure difference from inlet to outlet ( $\Delta P_{inlet-outlet}$ ) obtained by CFD analysis. Arrows above and below colour legend indicate maximum and minimum computed values in the model, respectively. (I.) Model 1. (II.) Model 2. (a)  $Q_{inlet} = 2$  mL/h. (b)  $Q_{inlet} = 5$  mL/h.

Table 6.2 Estimated values of pressure drop across experimental models in ‘pressure paths’.

|         |                | $\Delta P_{inlet-outlet}$ (Pa) |        |        |        |
|---------|----------------|--------------------------------|--------|--------|--------|
|         |                | M01                            |        | M02    |        |
|         | Branches       | 2 mL/h                         | 5 mL/h | 2 mL/h | 5 mL/h |
| Path 1  | 1-2-4-10-16    | 3.43                           | 7.52   | 2.56   | 5.94   |
| Path 2  | 1-2-5-8-11-16  | 3.54                           | 7.26   | 2.92   | 6.76   |
| Path 3  | 1-2-5-9-12-17  | 3.48                           | 8.05   | 2.71   | 6.82   |
| Path 4  | 1-3-6-13-15-17 | 4.04                           | 8.99   | 2.73   | 7.34   |
| Path 5  | 1-3-7-14-15-17 | 3.58                           | 7.87   | 2.51   | 6.69   |
| Average |                | 3.62                           | 7.94   | 2.69   | 6.71   |

as well as the values obtained from the CFD simulations are shown in Table 6.3. The values from the CFD simulations were obtained by choosing an arbitrary point at the inlet region of the models (where the maximum values are expected) in the pressure plot in COMSOL and recording the measured value at that point.

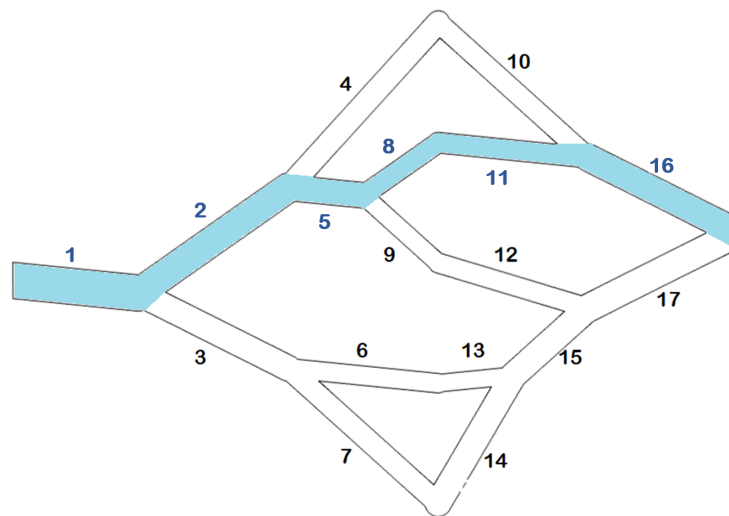


Fig. 6.8 An example of a ‘pressure path’ from inlet to outlet formed by branches 1, 2, 5, 8, 11 and 16. The notation to define a pressure path is from left to right, and from top to bottom. The highlighted path corresponds to pressure path 2.

Above and below the colour legend in the pressure plots (Figure 6.7), the maximum and minimum computed pressure values of the model are indicated next to the arrow heads. The maximum value, however, corresponds to a very small region around the inlet surface (i.e. in Figure 6.7(II).(a), a ‘ring’ of higher pressure is observed). This might be attributed to singularities in the simulation, but this goes beyond the scope of the present work, as only

Table 6.3 Experimental and CFD values of pressure drop across the networks.

|     |                              | Experimental values<br>(Pa) | Approximate values from CFD<br>(Pa) |
|-----|------------------------------|-----------------------------|-------------------------------------|
| M01 | $Q_{inlet} = 2 \text{ mL/h}$ | 3.62                        | 3.7                                 |
|     | $Q_{inlet} = 5 \text{ mL/h}$ | 7.94                        | 9.5                                 |
| M02 | $Q_{inlet} = 2 \text{ mL/h}$ | 2.69                        | 3.9                                 |
|     | $Q_{inlet} = 5 \text{ mL/h}$ | 6.71                        | 10.0                                |

the overall pressure difference of the whole model is considered relevant. Thus, for model 02 the maximum pressure is 3.9 Pa, as measured in the software.

The third value of interest is the shear stress. As mentioned in Chapter 2, some vessel pathologies such as atherosclerosis are directly correlated to haemodynamics, particularly to altered values of shear stress [45]. Here, the shear stress values are expected to be lower than physiological values due to the low inlet flow rates used (2 and 5 mL/h). However, the aim is to observe how close the experimental values are to the CFD simulations.

In COMSOL there are predefined expressions, which define the variables to plot. For example, in order to plot the velocity magnitude, the option ‘spf.u - Velocity magnitude - m/s’ must be selected from the expressions branching menu (Model > Component 1 > Laminar Flow > Velocity and Pressure). For the velocity and pressure presented previously, the expressions to plot were simply selected from the branching menu. However, in the case of the shear stress, it is not available on the list. Therefore, a compound expression is needed to represent it mathematically in terms of the available variables. In a flowing liquid, viscosity can be defined as the proportionality constant between the force applied (shear stress) and the velocity gradient (shear rate) [164], which can be expressed as:

$$\tau = \mu \frac{dv}{dr} \quad (6.1)$$

Shear rate and dynamic viscosity are two predefined variable expressions in COMSOL. Thus, the compound expression for the shear stress plot was obtained by multiplying them (i.e. by writing ‘spf.mu\*spf.sr’ in the expression field, where spf.mu represents the viscosity and spf.sr, the shear rate). Figures 6.9 and 6.10 show the shear stress distribution at the midplane of the model for a better visualisation. It can be observed in the charts that for both CFD models (M01 and M02) branch 13 has the highest wall shear stress from all the branches in their respective trees. Considering that this is the maximum value of shear stress

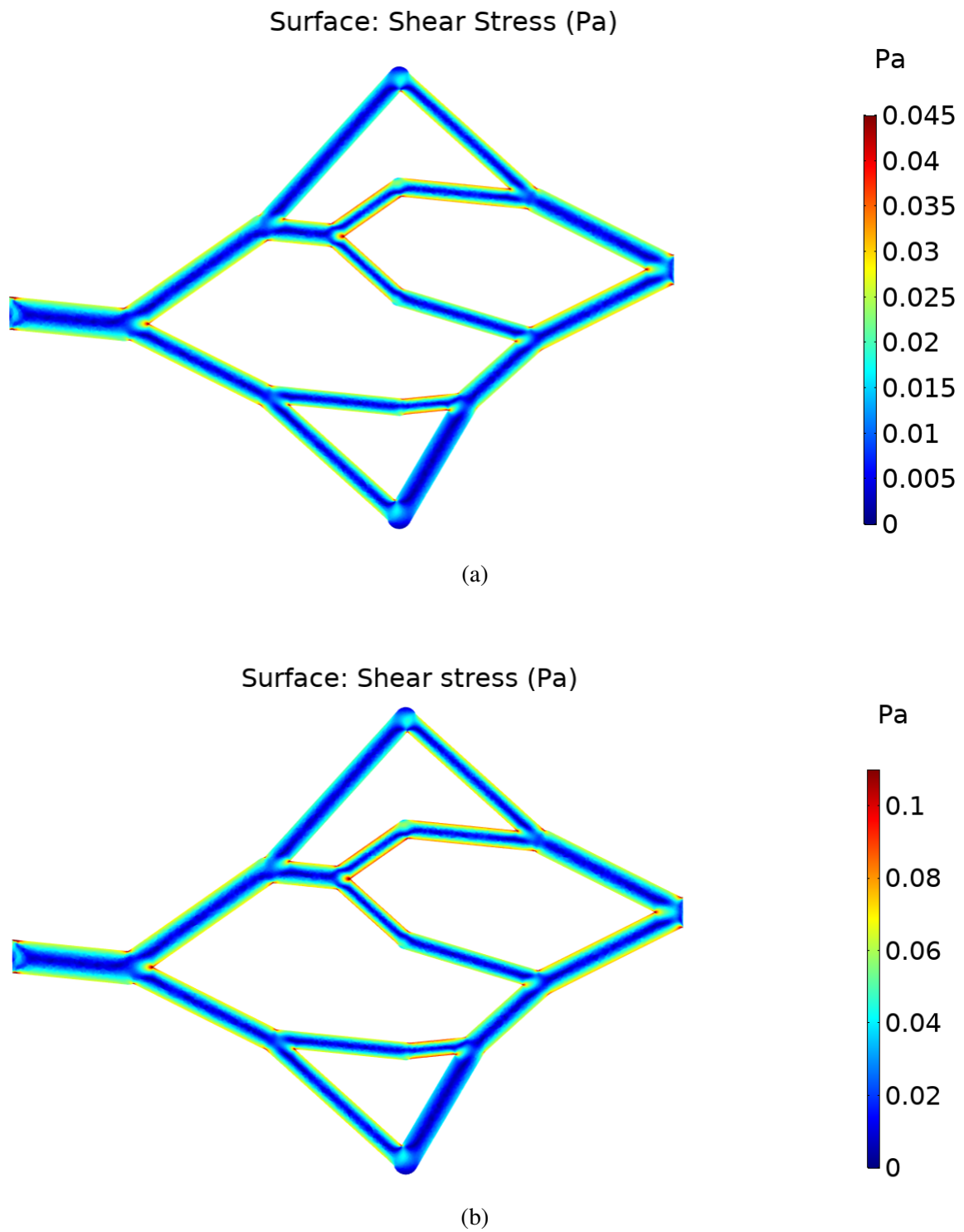


Fig. 6.9 Shear stress in model 01 for two values of inlet flow rate. (a)  $Q_{inlet} = 2$  mL/h. (b)  $Q_{inlet} = 5$  mL/h.

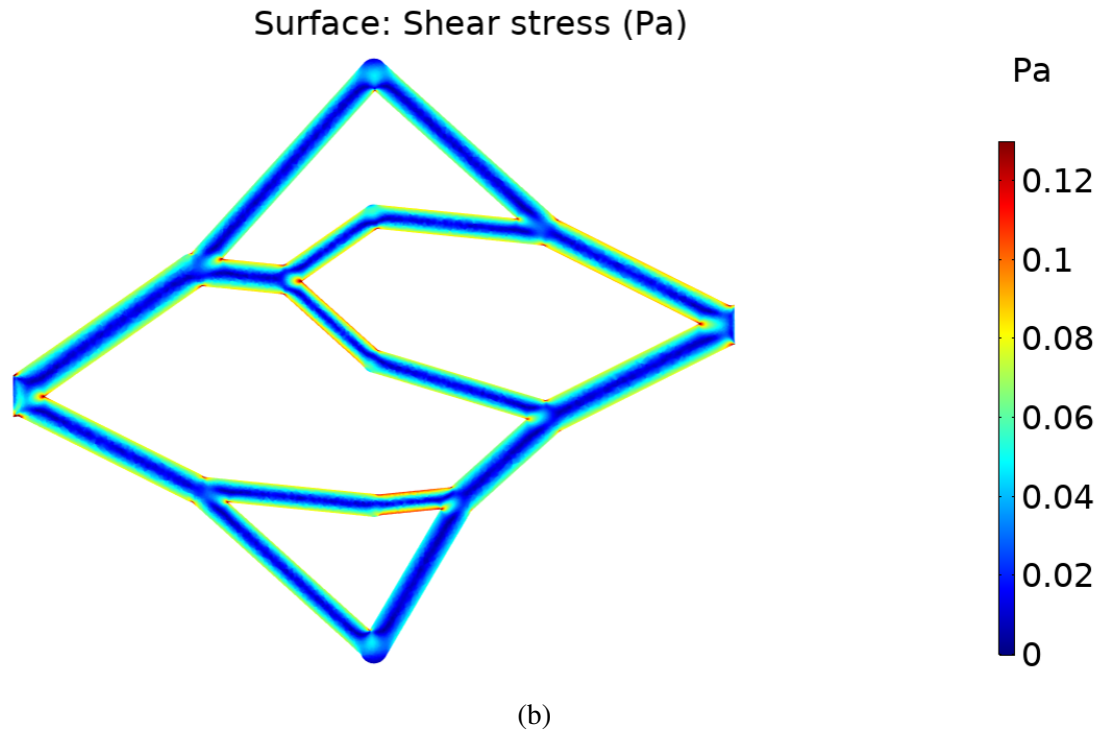
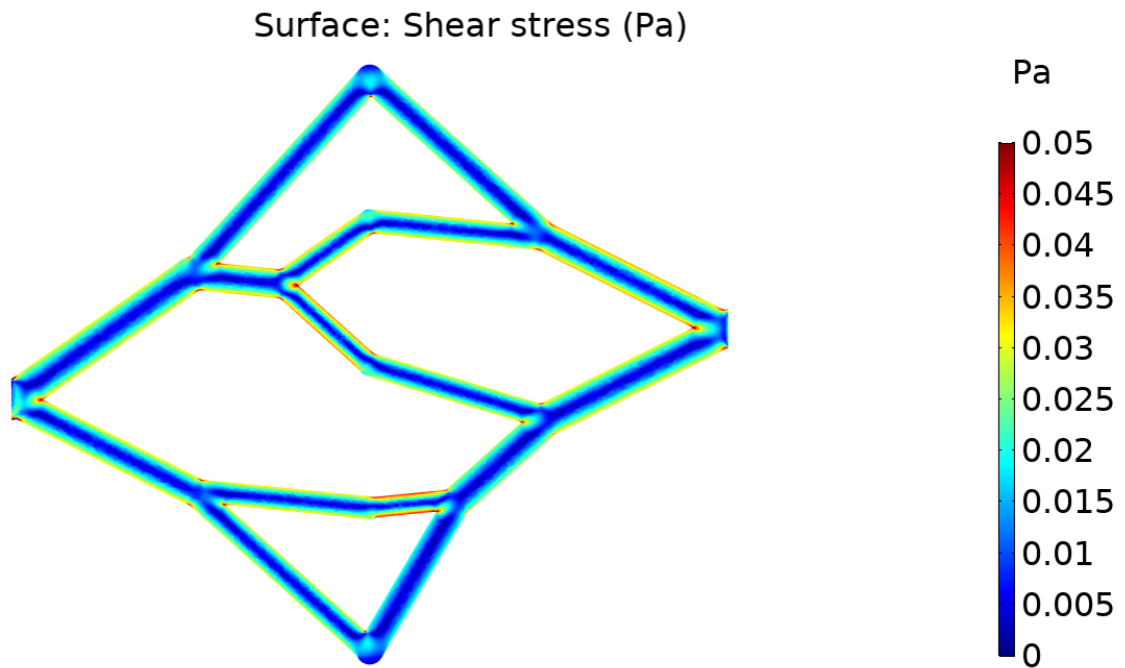


Fig. 6.10 Shear stress in model 02 for two values of inlet flow rate. (a)  $Q_{inlet} = 2$  mL/h. (b)  $Q_{inlet} = 5$  mL/h.

in the simulations, this branch is used for comparison against the experimental value, which is calculated from the experimental velocity measurements. From the Poiseuille equation of flow, the maximum shear stress ( $\tau_w$ ) in a pipe is found at the wall and is given by the following equation:

$$\tau_w = \frac{\mu 2V_{max}}{r} \quad (6.2)$$

where  $\mu$  is the fluid viscosity,  $V_{max}$  is the maximum flow velocity (at the central axis of the pipe) and  $r$  is the pipe radius. Thus, using the experimental value of maximum velocity, experimental measurements of radius and the viscosity of PBS, the experimental wall shear stress of branch 13 is calculated for each case. Table 6.4 shows the calculated experimental values of shear stress and the approximate values obtained from the CFD plot of shear stress at the middle plane.

Table 6.4 Experimental and CFD values of shear stress in branch 13.

|     |                              | Experimental WSS<br>(Pa) | WSS from CFD<br>(Pa) |
|-----|------------------------------|--------------------------|----------------------|
| M01 | $Q_{inlet} = 2 \text{ mL/h}$ | 0.047                    | 0.036                |
|     | $Q_{inlet} = 5 \text{ mL/h}$ | 0.088                    | 0.090                |
| M02 | $Q_{inlet} = 2 \text{ mL/h}$ | 0.033                    | 0.043                |
|     | $Q_{inlet} = 5 \text{ mL/h}$ | 0.088                    | 0.10                 |

Without considering the shear stress at the bifurcations, the average shear stress values from individual branches have a low magnitude. Besides the highest values found in branch 13 for all cases (shown in Table 6.4), in model 01 at a flow rate of 2 mL/h most of the branches have a wall shear stress between 0.015 and 0.025 Pa, while for a flow rate of 5 mL/h, most branches have values between 0.04 and 0.08 Pa. In model 02 for a flow rate of 2 mL/h most branches are between 0.02 and 0.03 Pa, and for 5 mL/h the values are between 0.05 and 0.07 Pa.

It is also evident that the values of shear stress increase locally at the sharp angles of the model, mostly at the bifurcations. Regarding the design of the models, the branches were created using cylinders. At the bifurcations, where three cylinders join, spheres were created (which have the diameter of the largest branch) in order to fill the irregular spaces among the cylinder ends. In the simulations, it appears that the shear stress increases at the edges where the spheres connect to the cylinders, as shown in Figure 6.11. The plot shown belongs

to model 01 at an inlet flow rate of 5 mL/h, and the highest values at the sharp corners are between 0.15 and 0.2 Pa.

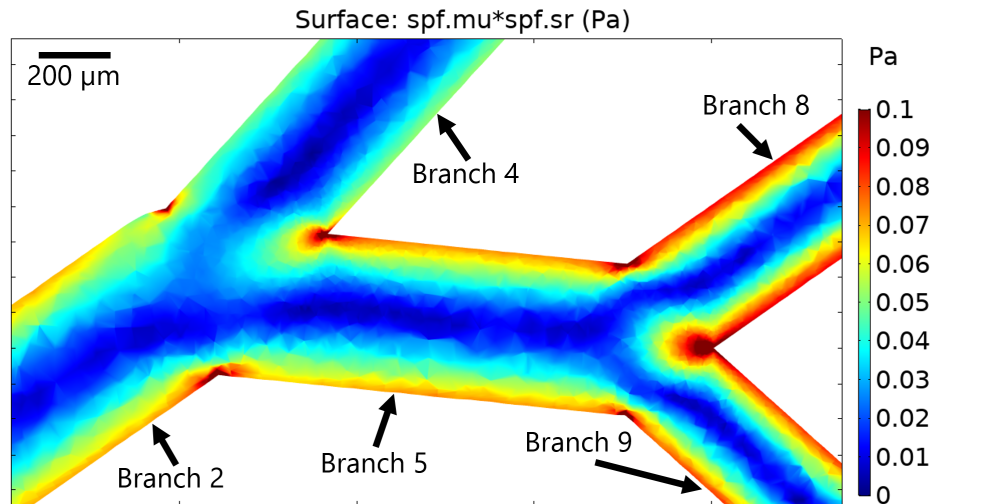


Fig. 6.11 Close-up of shear stress plot of model 01 at 5 mL/h showing points of higher shear stress at sharp edges of the model, including at the spherical joints.

## 6.5 Discussion

The results presented in Section 6.4 show that the CFD simulations are in general accordance with the results obtained experimentally, with slight variations. This section will include discussion on such variations (with focus on the velocity as the main parameter of interest) and includes an additional CFD simulation corresponding to the inlet flow rate value that was originally proposed but not measured experimentally (20 mL/h).

Flow velocity is considered the main parameter of interest, as it was directly measured in the experimental work through particle image analysis. Thus, the validation of the obtained data using CFD analysis is crucial. In the previous section, the charts of velocity magnitude distribution and velocity plots in every branch were presented. In order to determine if the results from experimental and simulated work are in agreement, a direct comparison is presented by combining the experimental and CFD data of model 01 (previously presented in Figures 5.16 and 5.17 for experimental, and in Figure 6.5 for CFD) in a single graph for each branch. This is shown in Figures 6.12 and 6.13. For this comparison, only model 01 was studied while model 02 was omitted given the larger variations due to the challenges of its experimental measurements.

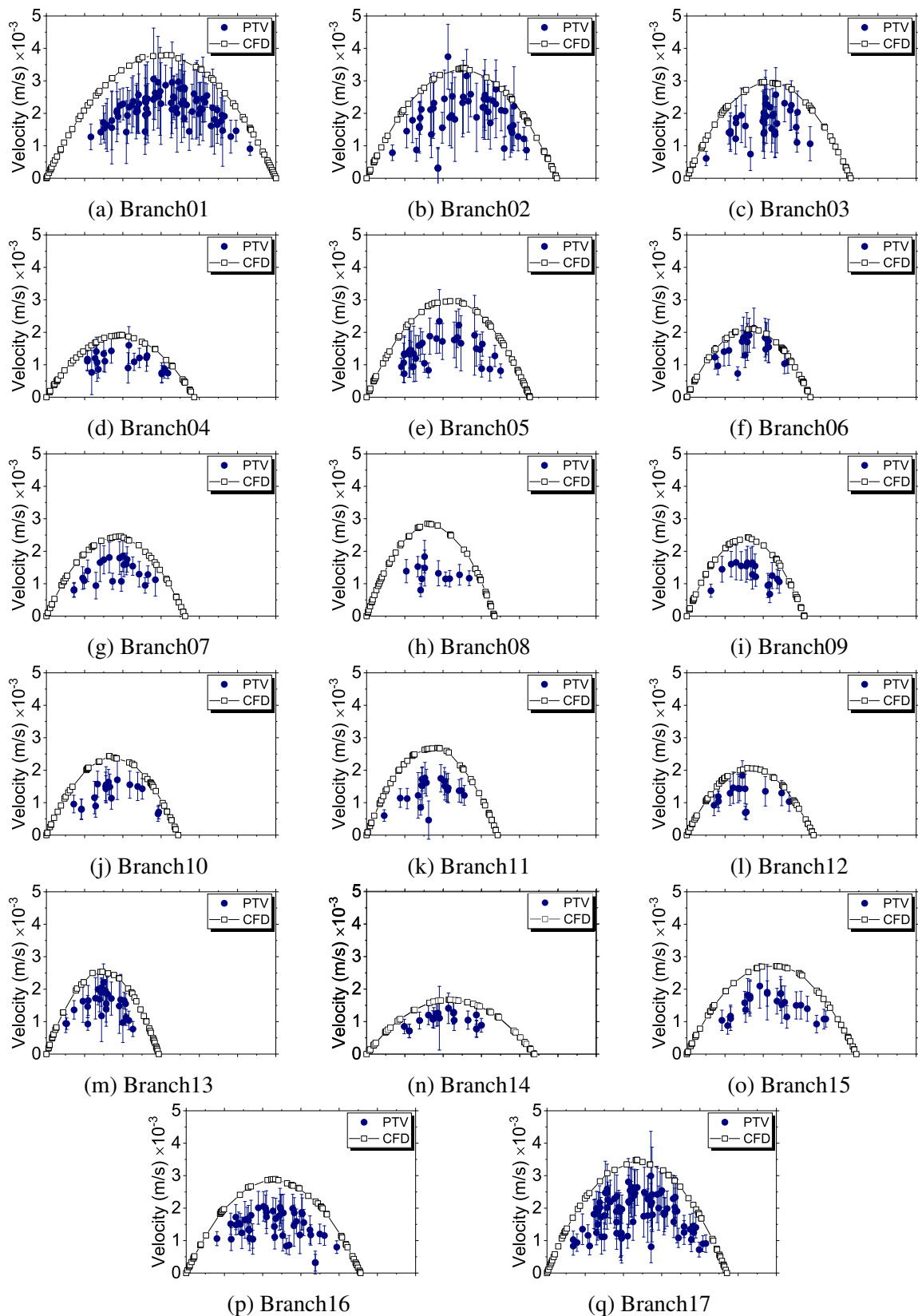


Fig. 6.12 Comparison of CFD and experimentally obtained velocity profiles from model 01 at an inlet flow rate  $Q_{inlet} = 2$  mL/h. Curves with black squared symbols represent CFD data; blue points represent experimental data.

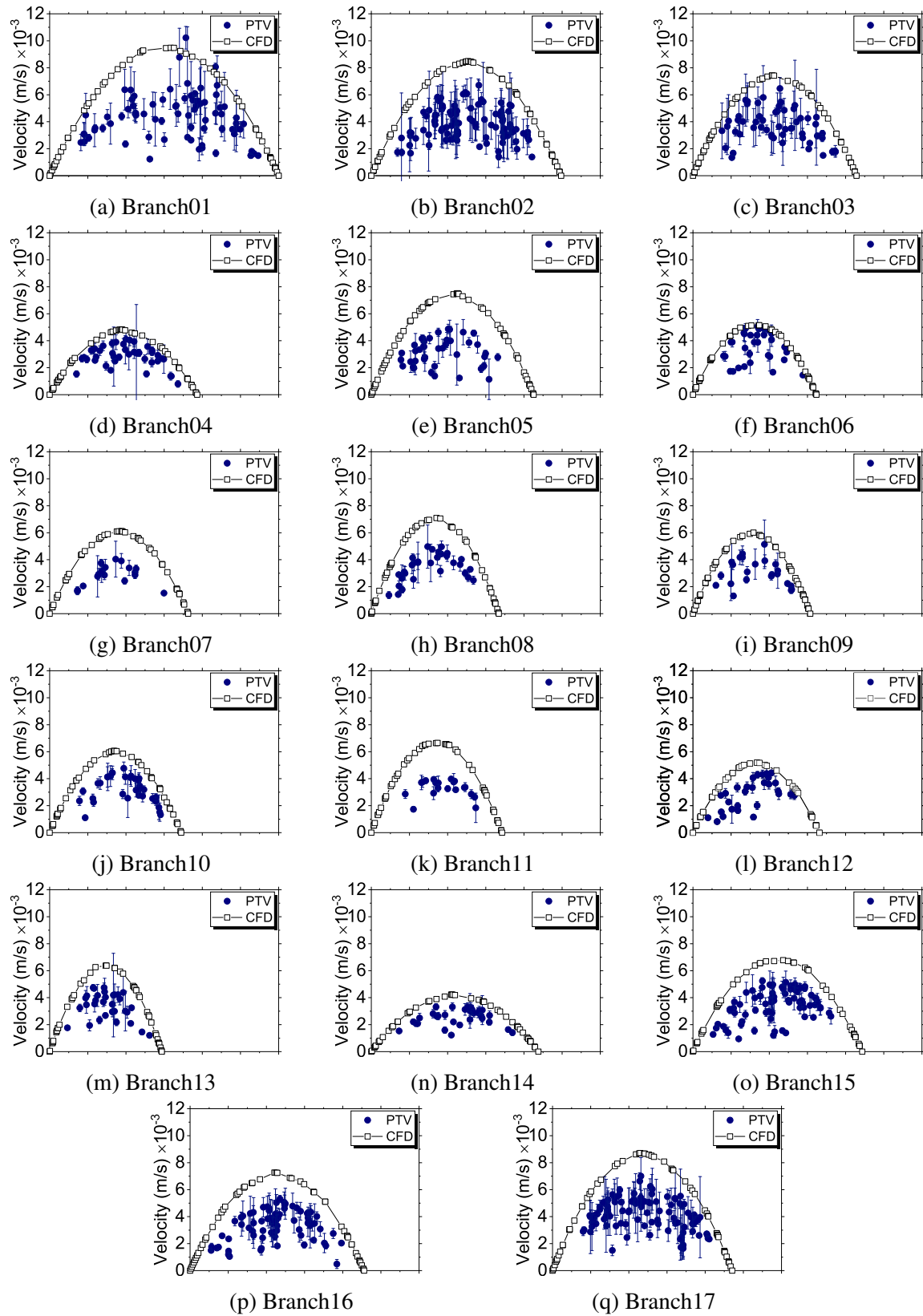


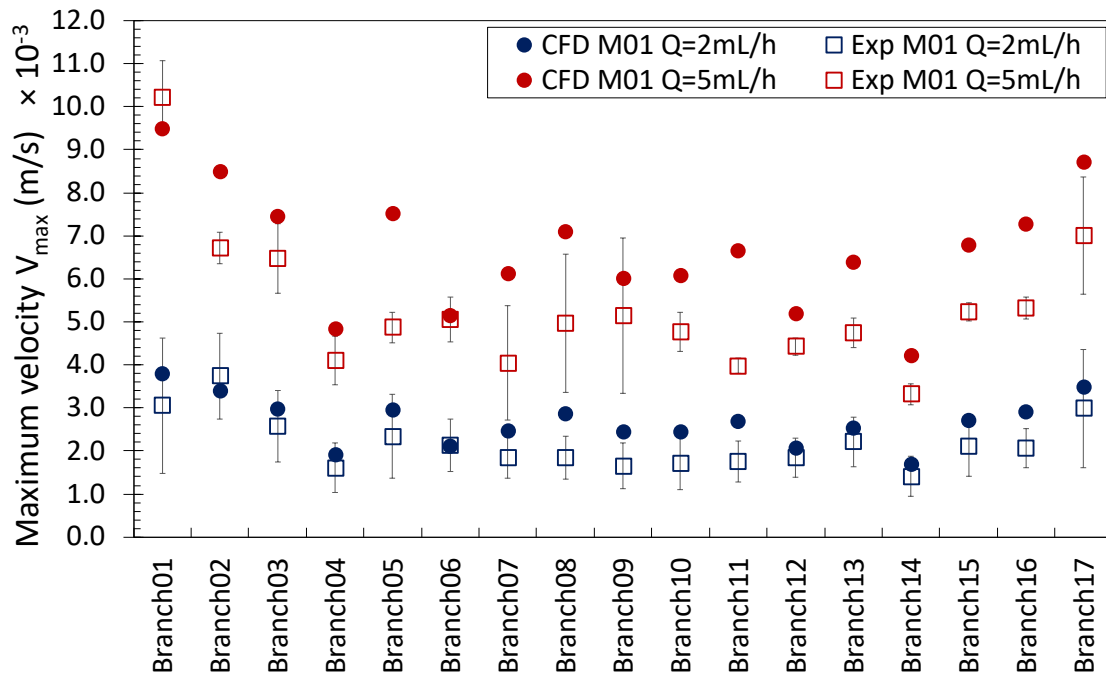
Fig. 6.13 Comparison of CFD and experimentally obtained velocity profiles from model 01 at an inlet flow rate  $Q_{inlet} = 5 \text{ mL/h}$ . Curves with black squared symbols represent CFD data; blue points represent experimental data.

Upon visual inspection, the velocity profiles obtained experimentally match the curves obtained by CFD in shape. Considering that the maximum velocity is the parameter of interest, comparative charts were created including the maximum velocities achieved in each branch in experiments and CFD simulations for both models 01 and 02, using the two values of inlet flow rate of 2 and 5 mL/h. Figure 6.14 shows these charts. As in the previous chapter, the experimental maximum velocity values were obtained using the maximum value from the chart of each branch, and it is presented along with its corresponding standard deviation.

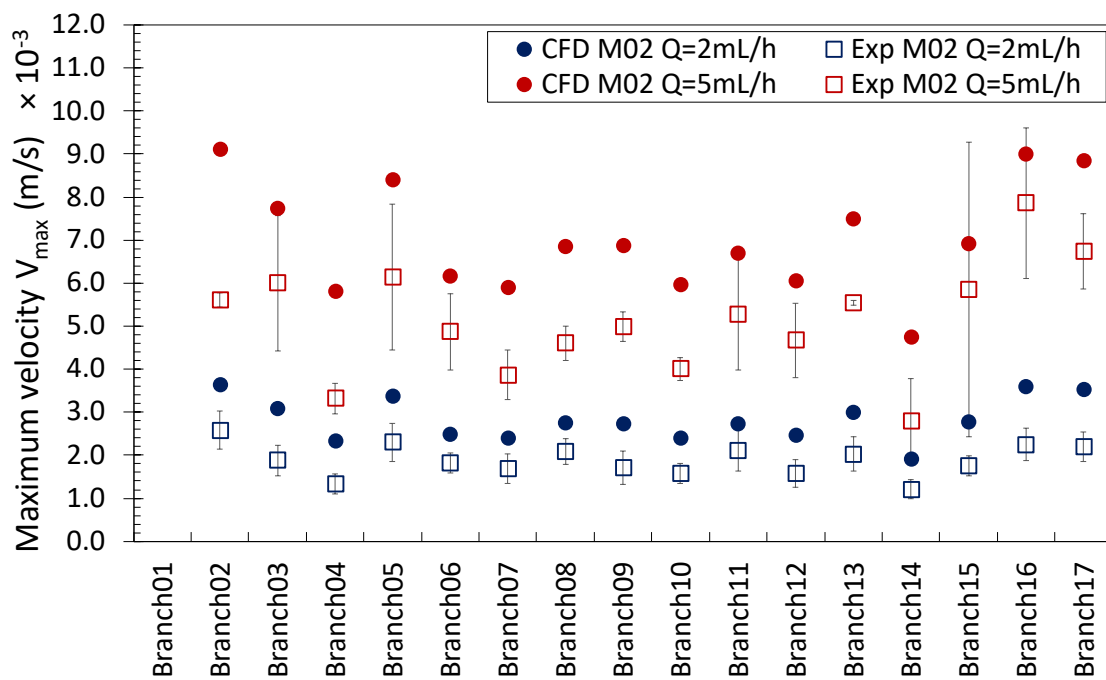
Overall, the velocities obtained experimentally seem to be in accordance with the values obtained by CFD simulations, as they present a similar distribution of data. In general, model 01 (6.14 (a)) shows a smaller difference between experimental and CFD values, while model 02 (6.14 (b)) has experimental data further from the CFD results. This is expected based on the findings from Chapter 5, where model 02 was also deviated from the theoretical values. This is attributed to the tilting of the experimental model 02.

For Model 01, the greatest deviation of the experimental values from the CFD data is found at the highest flow rate (5 mL/h) and in the majority of the branches, the experimental values are smaller than the CFD values. This might be attributed to several factors, including fewer beads detected in the channels with less flow, the highest bead speed not being measured (due to the smaller number of beads), technical limitations of the camera (low fps), and the possibility of having measured within the hydrodynamic entrance region, where the flow is under-developed. These factors have less effect on the lower flow rate (2 mL/h), where the most of the experimental values are closer to the CFD values. It must be noticed that for some branches (e.g from model 01, branch 1 at 5 mL/h) the experimental value is noticeably higher than the CFD value. However, looking back at the charts of velocity profile comparison for this branch (Figure 6.13(a)) it is evident that the maximum experimental value corresponds to a single measurement that exceeds the parabolic shape of the profile and that is likely to be an error from the particle tracking software.

For model 02, all the individual experimental values are smaller than the CFD values, for both flow rates (2 and 5 mL/h). Besides the factors mentioned above, in the particular case of model 02 this is also caused by the fact that the measured velocity of the beads is a projection of the actual velocity due to the severe tilting of the experimental model. Thus, it is logical that all the values are smaller than the CFD and with similar offsets.



(a)



(b)

Fig. 6.14 Comparison between experimental and simulated maximum velocity values. (a) Experimental and CFD model 01. (b) Experimental and CFD model 02. Blue markers represent an inlet flow rate of 2 mL/h and red markers, 5 mL/h. Square markers represent experimental values, and round markers CFD values.

Regarding the pressures, the experimental pressure values were calculated using the experimental values of velocity. However in some branches the velocity measurements are not as close to the CFD values due to the factors discussed before (see branches 10 and 11 in Figure 6.14(a) for the 5 mL/h measurements), therefore the pressure difference measurements of the paths that include those branches might not be accurate, as it is observed that they are smaller than the other paths (see Table 6.2). Thus, the most reliable measurements in the case of the flow rate of 5 mL/h would be the ones from paths 3 and 4, where most of the branches have experimental velocities closer to the CFD values.

In general, model 01 shows a good agreement between the experimental and CFD velocities. Therefore, CFD is regarded as a good alternative to experimental analysis where there are physical limitations. Considering this and the fact that the original experimental inlet flow rate (of 20 mL/h) could not be measured due to technical limitations, a CFD simulation of model 01 using this flow rate was performed using the experimental dimensions. Figure 6.15 shows the velocity distribution at the midplane. Overall, the distribution of velocity is very similar to the models simulated with the lower flow rates, but the magnitude is higher, as expected.

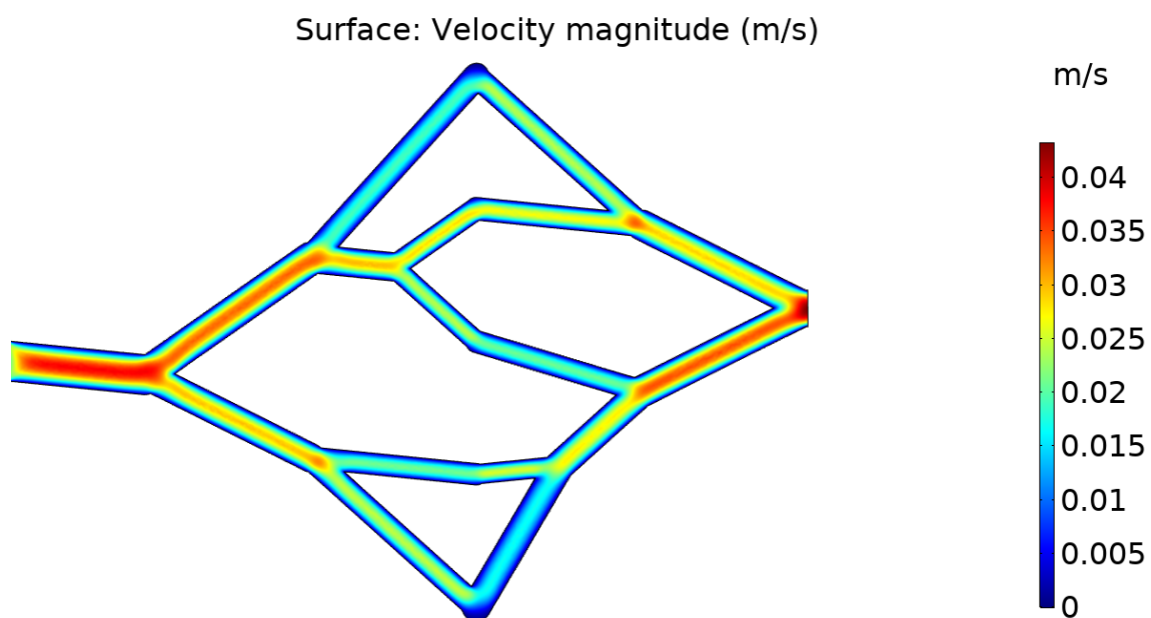


Fig. 6.15 Velocity plot at the midplane, of model 01 with a  $Q_{inlet} = 20$  mL/h.

One important aspect to consider (which was also noted for the lower flow rate models) is that at the upper and lower arterio-venous connection points of the networks the dark blue

regions indicate zero flow. A close-up image of the upper region is shown in Figure 6.16. This presents a design opportunity to improve the shape of the network at these points by rounding the sharp corners. There are reports indicating that eliminating sharp squared corners improves the overall velocity profile in microfluidic channels [159].

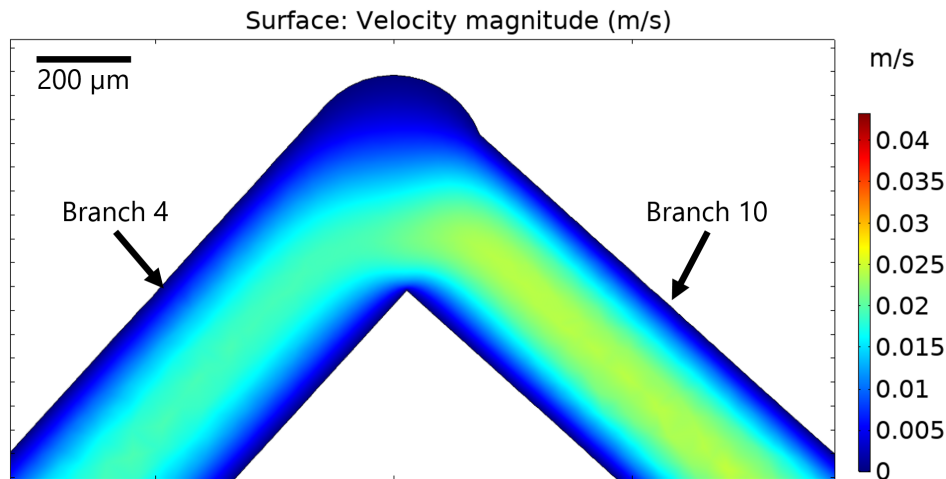


Fig. 6.16 Close-up of upper zero flow region in the velocity plot for model 01 with a  $Q_{inlet} = 20$  mL/h.

The pressure difference across the network is another variable of interest in the model with flow rate of 20 mL/h. Originally, for model 01 the pressure difference used to design the 3D model (using the algorithm) was 1 mm Hg from inlet to terminal points (connections between arterial and venous tree). As there are two trees with the same condition, the total pressure difference across the network was 2 mm Hg. However, there are variations between the original 3D model and the fabricated experimental model. One of such differences are the diameters, which are slightly larger in the experimental model than in the original model. Another difference is the network geometry, as the model lost its original outlet branch (branch 18) and part of its inlet branch (branch 1). In addition, the original 3D model was designed using the viscosity of blood (0.004 kg/m.s) as a design parameter, while the experimental value of viscosity was that of PBS (0.00105 kg/m.s). Thus, given these differences, the expected pressure difference cannot be 2 mm Hg (267 Pa), but a much smaller value. In fact an estimation of the expected pressure difference can be obtained in the same way as it was calculated for the lower flow rate models presented in Section 6.4, by obtaining the pressure difference across the five pressure paths, but using the flow rate value of 20 mL/h. The obtained values are shown in Table 6.5. The pressure difference from the CFD simulation is shown in Figure 6.17.

Table 6.5 Experimental values of pressure drop across the models in all the ‘pressure paths’.

| $\Delta P_{inlet-outlet}$ (Pa) |       |
|--------------------------------|-------|
| M01 - 20 mL/h                  |       |
| Path 1                         | 34.32 |
| Path 2                         | 32.58 |
| Path 3                         | 38.77 |
| Path 4                         | 39.29 |
| Path 5                         | 34.13 |
| Average                        | 35.82 |

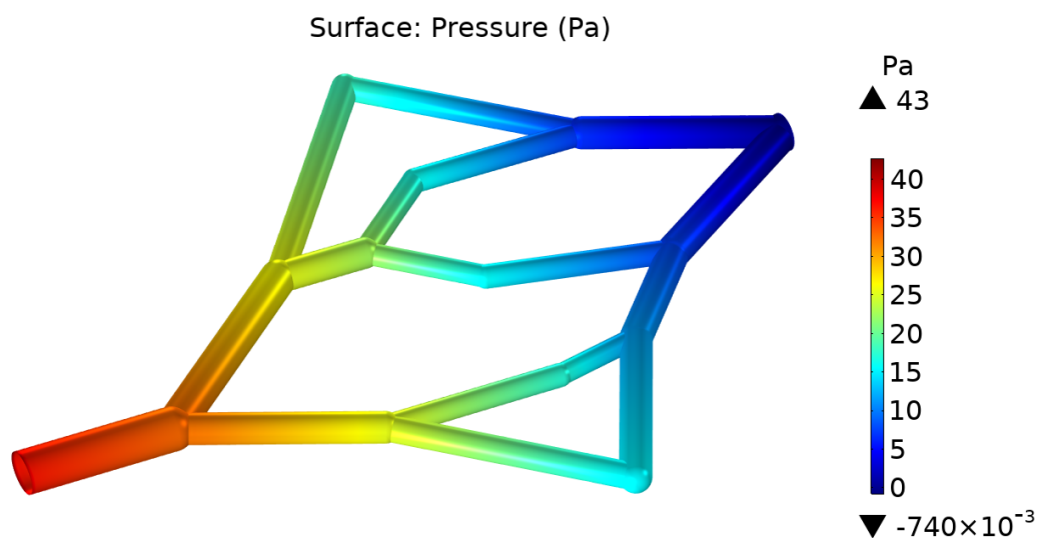


Fig. 6.17 Pressure difference from inlet to outlet ( $\Delta P_{inlet-outlet}$ ) in model 01 at  $Q_{inlet} = 20$  mL/h. Arrows above and below colour legend indicate maximum and minimum computed values in the model, respectively.

Table 6.6 shows the estimated experimental and approximate CFD values of pressure difference across the network (M01) with an inlet flow rate of 20 mL/h. As observed, the CFD value is larger by 3.18 Pa, which is consistent with the previous comparison of pressure difference in the models with lower flow rates, where the experimental values were lower than the CFD values. An explanation for this is that the estimated experimental calculations are based on the theoretical model, which does not consider the effect from the branching angles. The CFD simulation bases its results on the geometry of the model, therefore there could be additional pressure losses at the bifurcations, which the CFD considers but the theoretical model does not.

Table 6.6 Experimental and CFD values of pressure drop across the networks.

|                             | Experimental values<br>(Pa) | Approximate values from CFD<br>(Pa) |
|-----------------------------|-----------------------------|-------------------------------------|
| M01 - $Q_{inlet} = 20$ mL/h | 35.82                       | 39                                  |

In addition to the velocity and pressure difference in the model, the wall shear stress is another important measurement, as inappropriate levels of shear stress can lead to the development of pathological conditions in the circulatory system. In small arteries, physiological shear stress is  $>12$  dynes/cm<sup>2</sup> (1.2 Pa) [165]. Figure 6.18 shows the shear stress distribution in model 01 for the increased inlet flow rate of 20 mL/h. The branches that show the highest shear stress are branch 8 and branch 13 with approximately 0.35 Pa, which is not considered to be in accordance with the physiological values. However, it must be noted that the physiological values involve the flow of blood through the arteries, while in the CFD analysis, PBS is the simulated fluid. Thus, the fluids have different viscosity and consequently cannot be appropriately compared, as blood is considered a non-Newtonian fluid in micro-vessels, in which the viscosity is not constant. Considering this, a second simulation was performed using the viscosity (0.004 kg/m.s) and density (1060 kg/m<sup>3</sup>) of blood, using the same model (01, with experimental diameters), although assuming Newtonian flow for simplicity. The resulting plot is shown in Figure 6.19. The highest shear stress is again found in branches 8 and 13, with a value of approximately 1.35 Pa. If this value is compared against the physiological value previously mentioned for small arteries ( $>1.2$  Pa) from [165], it is in accordance as it is above this value.

In order to fully analyse the physiological blood flow, an additional simulation using in the original network design obtained with the algorithm was performed (i.e. the full model with original diameters and all 18 branches). This CFD simulation includes the properties of blood (density and viscosity), and the corresponding inlet velocity for a flow rate of 20 mL/h. The input algorithm parameters for the original network design were based on physiological values of blood viscosity, pressure difference and flow rate. This simulation allows to compare the simulated pressure against the design pressure, and will allow to observe the real estimated physiological wall shear stress in the model. Figure 6.20 shows the velocity plot obtained by the simulation. The maximum velocity is 0.045 m/s and is found at the inlet and outlet branches. Figure 6.21 shows the plot for the shear stress distribution. The maximum value is 1.68 Pa and is found at the wall of branch 13. This value is smaller than 7 Pa, the physiological limit for healthy wall shear stress found in vivo [41]. However, higher values of shear stress are found at sharp connection zones (including bifurcations), which are

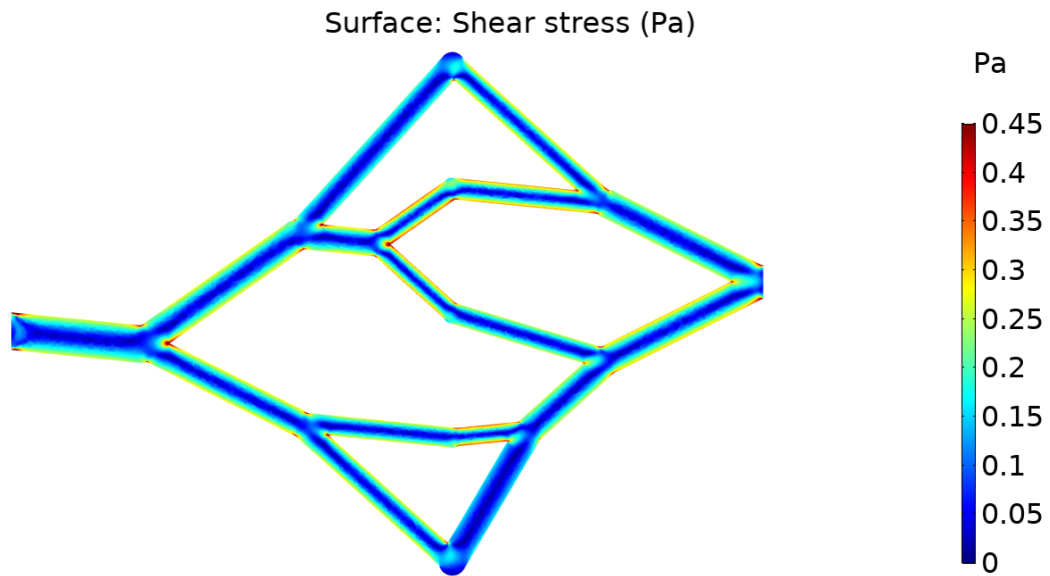


Fig. 6.18 Shear stress distribution in model 01 at  $Q_{inlet} = 20$  mL/h using the properties of the experimental fluid (PBS).

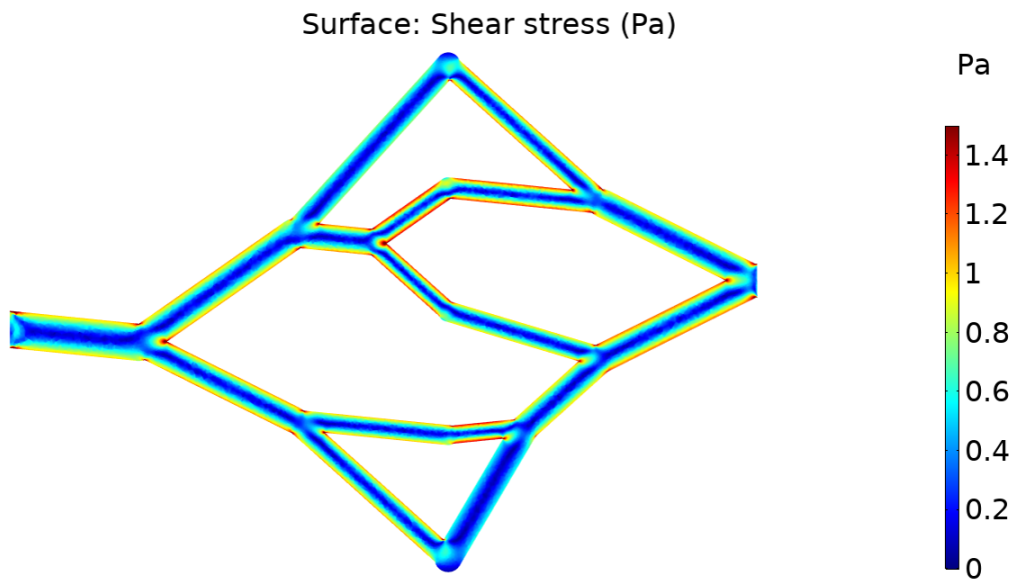


Fig. 6.19 Shear stress distribution in model 01 at  $Q_{inlet} = 20$  mL/h using the properties of blood (viscosity and density).

higher than 2.5 Pa. The maximum value of pressure found at the inlet of the model is 269 Pa, which is only about 1% higher than the pressure difference used in the model construction (2 mm Hg, or 266.67 Pa), which is expected.

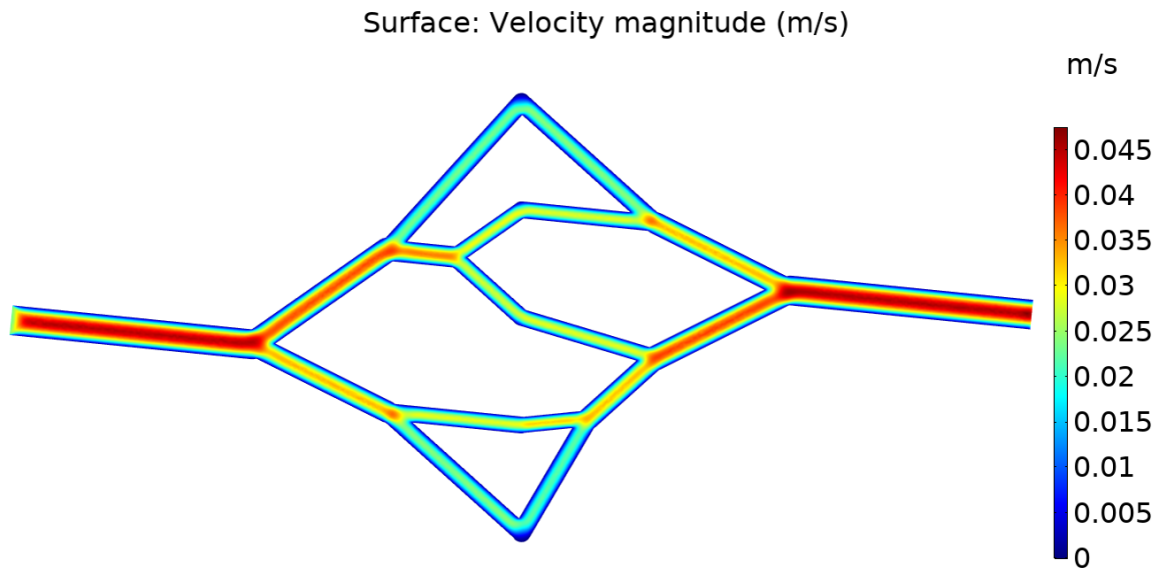


Fig. 6.20 Blood velocity distribution in the original model 01 at  $Q_{inlet} = 20$  mL/h using the properties of blood.

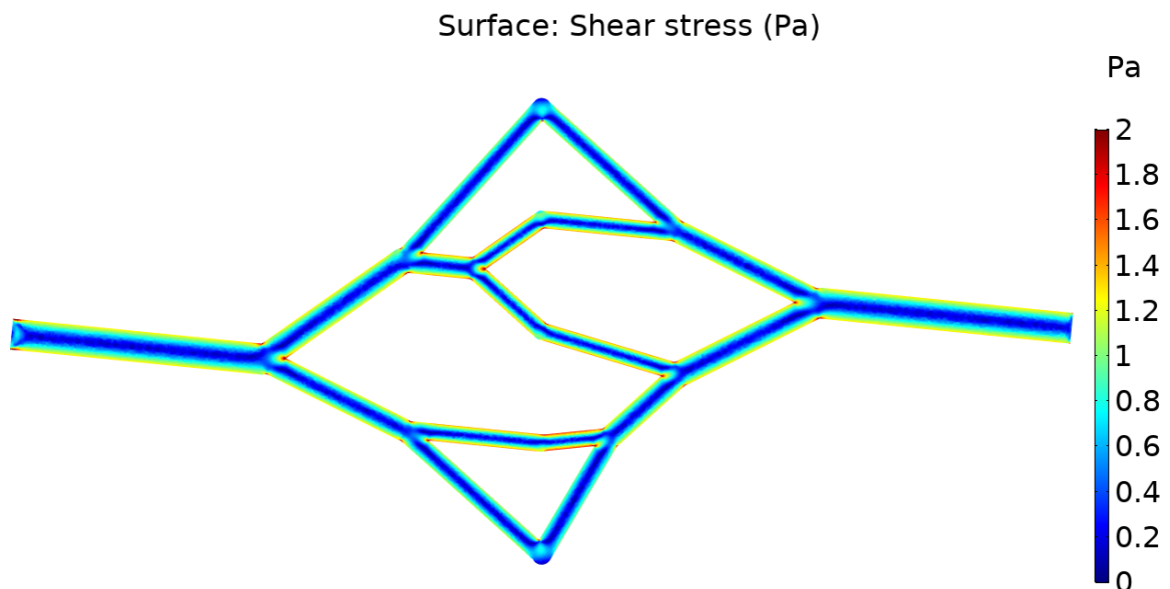


Fig. 6.21 Shear stress distribution in the original model 01 at  $Q_{inlet} = 20$  mL/h using the properties of blood.

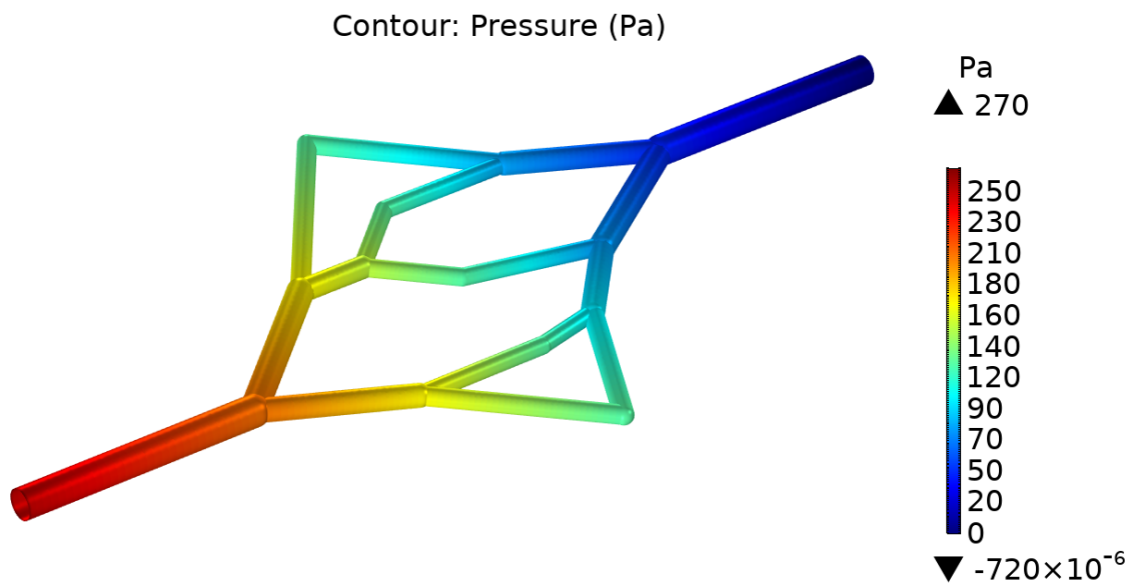


Fig. 6.22 Pressure distribution in the original model 01 at  $Q_{inlet} = 20$  mL/h using the properties of blood. Arrows above and below colour legend indicate maximum and minimum computed values in the model, respectively.

It was also observed that in the shear stress plots for all inlet flow rates (2, 5 and 20 mL/h, shown in Figures 6.9, 6.10 and 6.19), although the average values of each individual branch have a low shear stress, there are zones of higher shear stress, particularly at bifurcations, sharp angles or at the zones where the geometry changes abruptly (i.e. the interfaces between the model's cylinders and spheres). This could be an area of improvement for the algorithm, where additional constraints could be added to ensure smaller bifurcation angles, or a post-processing operation could be implemented to smooth out the sharp edges and discontinuities in the 3D model after the algorithmic construction.

## 6.6 Conclusions

It was demonstrated that the CFD analysis validates the experimental velocities as long as there are no technical fabrication issues with the network design. For model 01 the results were in agreement. However, model 02 was not accurately represented by CFD due to a combination of factors, including the tilting angle with regards to the focal plane, the small number of traceable beads, and low speed of CMOS camera.

As the CFD simulations agree with the experimental particle image analysis, it can be used as an alternative method to measure other parameters in the model, which were not experimentally feasible, such as the shear stress and the pressure difference. Given this, it is safe to assume that CFD analysis can be used instead of the physical experiments.

From the CFD analysis it is evident that in sharp edges and large bifurcation angles, zones of high shear stress are formed. This is because the algorithm for tree formation does not consider the branching angles nor the shear stress. Further improvements to the algorithm could be achieved by considering the branching angles and smoothing out the branch junctions.

The CFD analysis of physiological flow rate (20 mL/h) of the original model 01 shows that the pressure drop is consistent with the value of the algorithmic design and the wall shear stress is within the healthy physiological range. Therefore, this proves that the proposed method can be used to generate 3D vascular network models that could be used in tissue engineering applications where physiological conditions are required.



# Chapter 7

## Conclusions and Future Work

### 7.1 Conclusions

The aim of the present thesis is the development of a method for the generation of physiologically relevant vascular network structures as solid CAD models suitable for additive manufacturing technologies. This was achieved through the integration of three key concepts: i) an algorithm for the automatic generation of vascular trees, ii) design constraints based on human vascular physiology, and iii) the use of a CAD software to produce solid 3D models. While seeking to achieve the main aim, some complementary goals were attained, which include demonstration of the feasibility of the proposed approach by fabricating vascular networks via 3D printing, and the comparison between physical (experimental analysis) and simulated (CFD analysis) flow behaviour in the fabricated networks in order to determine the agreement with the theoretical model used to design the networks.

The main contribution of the present work is the development of a method to produce three-dimensional vascular network models created by algorithmic growth of physiologically constrained vascular trees, which can be fabricated using additive manufacturing techniques. In addition, networks produced by the algorithm were produced by 3D printing, demonstrating feasibility of fabrication. The printed model was further processed by casting PDMS around it inside a chamber, as previously shown in our group [13], with the resulting structure being a hollow, perfusable network embedded in a PDMS block. The network was used to perform flow experiments, which demonstrated that the experimental velocity measurements are in accordance with the theoretical values. Finally, CFD simulations were carried out to further validate the experimental measurements and to observe additional parameters for which experimental work was not feasible. As a general conclusion, the experimental and CFD results have been proved to be similar and in accordance with the theoretical

calculations that were used in the algorithm to produce the networks. Specific conclusions are detailed below for the four main areas of the present work: i) algorithm development; ii) fabrication of model; iii) experimental work; and iv) CFD simulations.

### 7.1.1 Algorithm development and implementation

An algorithm was developed based on the method of CCO, with a space-filling approach. Although the method can be adapted to any pre-defined three-dimensional shape, a cubic-shaped volume was used for simplicity. The optimisation criterion is minimisation of blood volume, using certain physiological constraints and assumptions (Poiseuille's law of flow, Murray's law for bifurcations, flow conservation, Newtonian flow, laminar steady flow). The algorithm creates two independent vascular trees, representing arteries and veins, which are connected at their terminal points. The algorithm was implemented in Visual Basic, which allowed the use of developer tools to execute commands in Autodesk Inventor, as the aim was to obtain 3D solid models of the vascular networks.

The algorithm creates physiologically arranged network structures. The dimensions of the branches in the network are given by a set of initial parameters. Depending on these parameters (e.g. dimensions of 3D volume, number of terminal points, flow rate and pressure difference), the branches of resulting structure can be within the range of tens of micrometers to a few millimetres. Considering that the models are intended for additive manufacturing, it was essential to create a model with suitable dimensions (i.e. equal to or larger than the minimum feature size achievable by the 3D printer, in this case: 250  $\mu\text{m}$ ). For this purpose, the effect of input parameters in the geometry was studied and four main observations were made (from Figures 4.21 to 4.26: i) For an increase in  $Q_{cell}$ , and at a constant branch  $\Delta P$ , the branch radii increase; ii) For an increase in  $\Delta P_{inlet-cell}$  at a constant  $Q$ , the branch radii decrease; iii) For an increase in  $Q_{cell}$ , there is an increase in the radii of the model, and an increase in the  $Q_{inlet}$  at the root branch; and iv) For an increase in  $\Delta P_{inlet-cell}$  there is a decrease in the radii of the model and an overall increase in the  $\Delta P$  of each individual branch in the tree. These increases and/or decreases are not linear, and vary depending on the case, as discussed in Section 4.3.1. By varying these parameters accordingly (within a physiological range of values), a model that fulfilled the 3D printing requirements was achieved. These parameters are also useful for the production of models for other additive manufacturing techniques: as long as the minimum feature size of the equipment is known (resolution), varying the parameters can achieve a model above the fabrication threshold.

### 7.1.2 Inaccuracies in the network fabrication

Following the four observations mentioned above, the parameters were adjusted accordingly and two simplified models were created (with dimensions above the printing threshold) in order to experimentally analyse the behaviour of flow in the channels. Each model consisted of two interconnected trees created on the same plane, where the connection points (terminals for both trees) are located in the middle. The simplified models are considered representative of the range of models that can be created using the algorithm.

The models were 3D printed using a thermoplastic material. PDMS was cast around each printed model inside custom-made PDMS chambers and the printing material was dissolved and flushed out of the network [13]. Given that most of the network fabrication process involves manual labour, it is error-prone. Proof of this is the major tilting that model 02 suffered. In addition, the models lost their inlet and outlet branches, with the exception of a small part of the inlet of model 01, as a result of the PDMS casting and the use of tubing as support (see Figures 5.5 and 5.8).

In addition to the tilting and missing branches, it was also found out that there is a variation between the original design dimensions and those of the fabricated models. In model 01 the variation from the original CAD model was subtle, but in model 02 it represented about 20%. This could have happened due to a variety of factors, such as the accuracy of the 3D printer, a reaction at the inner walls of the PDMS due to the solvent, contraction/expansion of the PDMS due to flow, or simply, error during the manual measurement at the microscope.

### 7.1.3 Experimental analysis of flow in fabricated network

Flow in the fabricated networks was analysed using fluorescent particle tracking. Results from the experimental analysis show that the measured flow velocity profiles in the channels correspond to the parabolic shape of fluids that obey Poiseuille's law. In general, the measured velocity profiles are a result of a combination of factors, such as: the number of particles present in the solution that was inserted into the channels, the speed of the camera for the acquisition of consecutive images, the total number of pictures acquired (the more pictures there are to analyse, the better the probability of obtaining the fastest particle at the central axis), the inlet flow rate, and the focus of the microscope lens at each branch measurement (which was intended to be set at the middle plane of each channel).

From the measurements of maximum velocity, it was observed that at a lower flow rate (2 mL/h) the experimental values were closer to the theoretical values, than at a higher flow rate (5 mL/h). An explanation for this is that at higher flow rates, the tracking of particles becomes more challenging as they travel faster across the channels. Given the limitations of the camera (images acquired with a maximum frame rate of 30 fps), at a high flow rate (5 mL/h) fewer images are obtained of a given particle travelling across a channel, than at a low flow rate (2 mL/h). In this case, the measurements could be improved by using more sophisticated equipment, particularly a high speed camera. In addition to the speed challenge, the vascular networks present a certain degree of tilting (significantly more evident in model 02 than in model 01). As a result, manually focusing the microscope in the middle plane of each channel was challenging, and in some cases the focus is restricted to only a section of the channel. Consequently, model 02 presents higher variability in the comparison of experimental and theoretical data.

Experimental model 01 is considered the most representative model for the present work, as its dimensions are the most accurate compared to the original CAD design. In a similar way, 2 mL/h is considered the most practical flow rate as it provided the best measurement conditions given the equipment limitations. It was observed that in accurate models, as in this case, the experimental data is in agreement with the theoretical calculations of flow velocity.

#### **7.1.4 Computational analysis of flow in fabricated network**

CFD analysis was performed on 3D models of the networks corresponding in diameters and shape to the fabricated PDMS models. It was concluded that the CFD simulations validate the experimental analysis as the values are in agreement. This was concluded from the observations of model 01 at an inlet flow rate of 2 mL/h, which, as stated previously, was the experiment with the best conditions given the technical limitations and therefore, the most precise.

CFD was also used to measure other parameters which were not experimentally feasible, such as pressure difference across the network and shear stress. Given the close agreement shown between CFD and experimental measurements of velocity, it can be assumed that CFD analysis have the potential to replace physical experiments and provide a close approximation of parameters which, otherwise would be technically impossible or impractical to physically measure. Considering this, an additional simulation was performed to observe the flow behaviour using the physiological flow rate value of 20 mL/h (which was used as an original

design parameter for model 01). The results show that the pressure drop corresponds to the value that was defined as an input parameter for the algorithmic design, and also the wall shear stress obtained from the simulation is within the healthy physiological range.

### **7.1.5 Impact of the research in the field of tissue engineering**

Creating physiologically branching networks as CAD 3D models opens up a wide range of possibilities for all tissue engineering techniques that involve additive manufacturing or computer-aided manufacturing processes, as they can benefit from using accurate branching structures (as opposed to the current techniques which use simple CAD designs or lattice-shaped networks). Some of the techniques that could use the 3D models produced here are direct writing, bioprinting, methods using sacrificial templates (created by 3D printing), methods using laser-based material degradation, among others. Having networks in a physiological arrangement may allow the creation of functional and vascularised thick tissue constructs. Pre-vascularised tissue has many advantages such as promoting in vivo integration and a higher cell survival probability. Hence, the impact of being able to create such network models.

The present work shows an overall agreement of the experimental and CFD simulation data with the theoretical data. Therefore, it can be concluded that CFD simulations are a fast and effective method to analyse the flow in vascular networks produced by this method. This is particularly helpful for analysing parameters that cannot be measured experimentally, and to study complex 3D networks which would be impractical to observe under the microscope.

## **7.2 Future Work**

During the course of the present research, different challenges were found at various stages. Most of them were solved, but the remaining represent opportunity areas that could be potentially explored. These have been separated in 3 categories: those related to the algorithm, the experimental analysis and the CFD analysis, and are summarised below.

### 7.2.1 Algorithm

The algorithm described in the present work was programmed using simple functions and operations, so there are aspects of both the algorithm and the code which are either not optimised or have been omitted due to complexity. Examples of this include detection and avoidance of collisions between arterial and venous trees, avoiding sharp edges and large bifurcation angles, and assigning a system to achieve a specific order during tree growth (i.e. setting a probability of selection for the points in the 3D space, as opposed to selecting them all randomly, to make sure that the points closer to the root branch get selected sooner, or alternatively, setting a staged growth by defining temporary growth boundaries within the 3D space).

As a continuation of the work here presented, a new algorithm and code have been developed in the research group by Guy et al. [101]. This algorithm includes solutions to the problems of collisions and sharp angles, allows the construction of more than 2 interconnected trees, and presents an optimised code which reduced the computing time to seconds or a few minutes (for networks that would take a few hours with the original code).

Further improvements could be considered to achieve a model that resembles healthy physiological vasculature. Studies show that at larger artery bifurcation angles, the values of shear stress become lower (abnormal), which can lead to development of pathologies such as atherosclerosis [152]. Therefore, an improvement to the algorithm could be to include a design constraint to limit the bifurcation angles to a certain value and adding a curvature to the branches involved, as depicted in Figure 7.1.

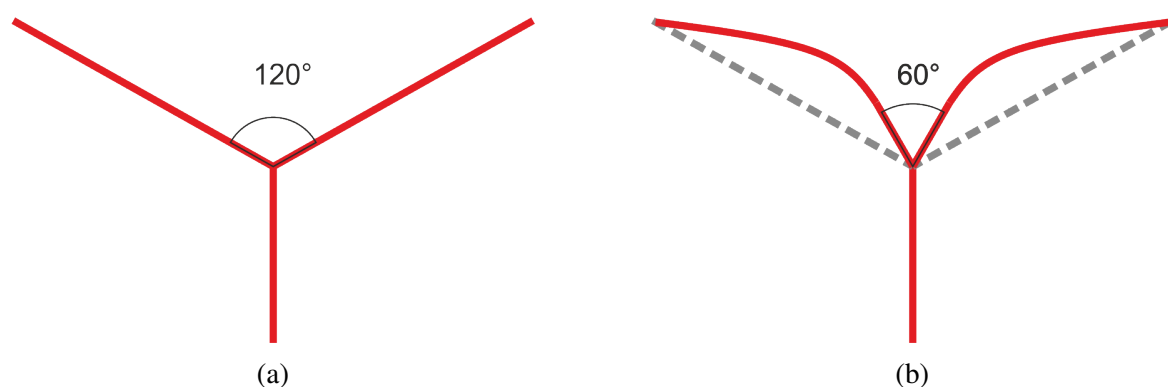


Fig. 7.1 Depiction of reduced branching angle with curved branches. (a) Branching angles produced by the original algorithm. (b) Alternative branching angles approach by limiting the angle and adding optimal curvatures to the branches.

### 7.2.2 Experimental analysis

The experimental analysis presented various challenges at different stages. Some of these could potentially be solved by changing the original approach. The first challenge was due to the fact that the hollow network fabrication relies on manual PDMS casting around the 3D printed model. During the step of subjecting the cast PDMS to vacuum to eliminate bubbles, the 3D printed model can rotate around its axis within the PDMS, which can result in the network being tilted from the original position (parallel to the surface). One potential idea to solve this would be to try a slower incremental vacuum process, where the vacuum is slowly increased at controlled intervals to try to avoid abrupt disruption in the PDMS chamber. Another idea would be to skip the processes of degassing and baking, and let the model polymerise at room temperature for 4-5 days. Alternatively, different fabrication techniques could be explored.

The biggest challenge in the experimental phase was that the intended value of inlet flow rate in the models (20 mL/h) was not feasible, as particle tracking could not be achieved at velocities higher than 5 mL/h using the available equipment. The microscope camera acquires images at a maximum rate of 30 fps. Performing the measurements using a high speed camera could be an option to allow analysis of higher flow rates.

Another factor that may improve the accuracy of the experimental measurements is increasing the number of fluorescent beads, particularly at higher velocities. It was observed that there were a smaller number of traced particles in the experiments with a flow rate of 5 mL/h, than for 2 mL/h. As the particles travel faster, less of them become accurately detected in the particle tracking software.

Experimental pressure measurement was originally intended but could not be achieved. The sensors with which the measurements were attempted have a measuring range of 0 to 1 psi (0 to 51.7 mm Hg). The expected measurements given the theoretical calculations for pressure difference between inlet and outlet for model 01 were of 2 mm Hg, which represents 3.87% of the sensor range. Low sensitivity of the sensor in this range might explain the large variations in measurements. A sensor with a smaller range might improve the measurements.

Finally, given that the ultimate purpose of the networks is to be used in biological applications, there are two relevant additional tasks that would be interesting to explore. The first one is the attachment of cells into the vascular networks to allow a study of the flow behaviour closer to natural physiological conditions. Endothelialisation of PDMS channels

(the application of a mono or multi layer of endothelial cells inside the channels) is a viable technique (see [166]), as PDMS is a biocompatible material. The second relevant task is to fabricate a network that covers a defined 3D volume (as opposed to the planar network here presented), and to test the functionality of the network embedded within a cell-laden hydrogel, similarly to the work presented by Justin et al. [13].

### **7.2.3 CFD analysis**

CFD simulations helped validate the experimental work and it was observed that it is in accordance with the theoretical calculations. There are two tasks that could be carried out to take advantage of the great potential of the CFD simulation package. The first task is to simulate more complex network structures built in 3D volumes. It would be interesting to observe the flow behaviour in models with more than 2 interconnected trees, with multiple inlets or outlets. The second task would be to simulate additional physics in the models, which have been omitted for simplicity in the present work. Example of this could be simulating pulsatility of flow in the vessels, oxygen diffusion from the fluid into the bulk material where the network is embedded, the Newtonian behaviour of blood flow, and the presence of red blood cells.

# References

- [1] Sebastian Giwa, Jedediah K Lewis, Luis Alvarez, Robert Langer, Alvin E Roth, et al. The promise of organ and tissue preservation to transform medicine. *Nature biotechnology*, 35(6):530–542, June 2017.
- [2] Organ Donation Statistics, April 2018. Last Modified: 2020-06-16.
- [3] OPTN: Organ Procurement and Transplantation Network - OPTN.
- [4] Annual Activity Report 2018/19 - Organ Donation and Transplantation - NHS Blood and Transplant. Technical report, 2019.
- [5] Anthony Holmes, Robert Brown, and Kevin Shakesheff. Engineering tissue alternatives to animals: applying tissue engineering to basic research and safety testing. *Regenerative Medicine*, 4(4):579–592, July 2009.
- [6] Jordan S. Miller, Kelly R. Stevens, Michael T. Yang, Brendon M. Baker, Duc-Huy T. Nguyen, et al. Rapid casting of patterned vascular networks for perfusable engineered three-dimensional tissues. *Nature Materials*, 11(9):768–774, September 2012.
- [7] Jiankang He, Feng Xu, Yaxiong Liu, Zhongmin Jin, and Dichen Li. Advanced tissue engineering strategies for vascularized parenchymal constructs. *Journal of Mechanics in Medicine and Biology*, 14(01):1430001, August 2013.
- [8] Sangil Min, In Kap Ko, and James J. Yoo. State-of-the-Art Strategies for the Vascularization of Three-Dimensional Engineered Organs. *Vascular Specialist International*, 35(2):77–89, June 2019.
- [9] Esther C. Novosel, Claudia Kleinhans, and Petra J. Kluger. Vascularization is the key challenge in tissue engineering. *Advanced Drug Delivery Reviews*, 63(4-5):300–311, April 2011.
- [10] Daniel Sazer and Jordan Miller. Vascular Networks Within 3d Printed and Engineered Tissues. In *3D Printing and Biofabrication*, Reference Series in Biomedical Engineering, pages 1–27. Springer, Cham, 2017.
- [11] David B. Kolesky, Kimberly A. Homan, Mark A. Skylar-Scott, and Jennifer A. Lewis. Three-dimensional bioprinting of thick vascularized tissues. *Proceedings of the National Academy of Sciences*, 113(12):3179–3184, March 2016.
- [12] Willie Wu, Adam DeConinck, and Jennifer A. Lewis. Omnidirectional Printing of 3d Microvascular Networks. *Advanced Materials*, 23(24):H178–H183, June 2011.

- [13] Alexander W. Justin, Roger A. Brooks, and Athina E. Markaki. Multi-casting approach for vascular networks in cellularized hydrogels. *Journal of the Royal Society, Interface*, 13(125), 2016.
- [14] Min Lee and Benjamin M. Wu. Recent Advances in 3d Printing of Tissue Engineering Scaffolds. In Michael A.K. Liebschner, editor, *Computer-Aided Tissue Engineering, Methods in Molecular Biology*, pages 257–267. Humana Press, Totowa, NJ, 2012.
- [15] Samantha Paulsen and Jordan Miller. Tissue Vascularization Through 3d Printing: Will Technology Bring Us Flow? *Developmental Dynamics*, 244, January 2015.
- [16] William Lafayette Mondy, Don Cameron, Jean-Pierre Timmermans, Nora De Clerck, Alexander Sasov, et al. Computer-aided design of microvasculature systems for use in vascular scaffold production. *Biofabrication*, 1(3):035002, 2009.
- [17] William Lafayette Mondy, Don Cameron, Jean-Pierre Timmermans, Nora De Clerck, Alexander Sasov, et al. Micro-CT of Corrosion Casts for Use in the Computer-Aided Design of Microvasculature. *Tissue Engineering Part C: Methods*, 15(4):729–738, March 2009.
- [18] Bert Vandeghinste, Bram Trachet, Marjolijn Renard, Christophe Casteleyn, Steven Staelens, et al. Replacing Vascular Corrosion Casting by In Vivo Micro-CT Imaging for Building 3d Cardiovascular Models in Mice. *Molecular Imaging and Biology*, 13(1):78–86, February 2011.
- [19] Christoph Schürmann, Felix Gremse, Hanjoong Jo, Fabian Kiessling, and Ralf P. Brandes. Micro-CT Technique Is Well Suited for Documentation of Remodeling Processes in Murine Carotid Arteries. *PLoS ONE*, 10(6), June 2015.
- [20] Keely A. Heintz, Michael E. Bregenzer, Jennifer L. Mantle, Kelvin H. Lee, Jennifer L. West, and John H. Slater. Fabrication of Three-Dimensional Biomimetic Microfluidic Networks in Hydrogels. *Advanced healthcare materials*, 5(17):2153–2160, September 2016.
- [21] John P. Morgan, Peter F. Delnero, Ying Zheng, Scott S. Verbridge, Junmei Chen, et al. Formation of microvascular networks *in vitro*. *Nature Protocols*, 8(9):1820–1836, September 2013.
- [22] Thomas J. Hinton, Quentin Jallerat, Rachelle N. Palchesko, Joon Hyung Park, Martin S. Grodzicki, et al. Three-dimensional printing of complex biological structures by freeform reversible embedding of suspended hydrogels. *Science Advances*, 1(9), October 2015.
- [23] Walter F. Boron and Emile L. Boulpaep. *Medical Physiology*. Elsevier, 2017.
- [24] Richard E Klabunde. *Cardiovascular physiology concepts*. 2nd ed. edition, 2011.
- [25] V. V. Gafiychuk and I. A. Lubashevsky. On the Principles of the Vascular Network Branching. *Journal of Theoretical Biology*, 212(1):1–9, September 2001.

- [26] D. Guidolin, B. Nico, G. Mazzocchi, A. Vacca, G. G. Nussdorfer, and D. Ribatti. Order and disorder in the vascular network. *Leukemia*, 18(11):1745–1750, November 2004.
- [27] Jeroen Rouwkema, Nicolas C. Rivron, and Clemens A. van Blitterswijk. Vascularization in tissue engineering. *Trends in Biotechnology*, 26(8):434–441, August 2008.
- [28] Christophe Bureau, Jean-Marie Pron, Jean-Pierre Vinel, Yoshiya Ito, Robert S. McCuskey, et al. Hepatic Circulation. In Juan Rods, Jean-Pierre Benhamou, Andres T. Blei, Jrg Reichen, and Mario Rizzetto, editors, *Textbook of Hepatology*, pages 73–88. Blackwell Publishing Ltd, Oxford, UK, June 2007.
- [29] Hellmut G. Augustin and Gou Young Koh. Organotypic vasculature: From descriptive heterogeneity to functional pathophysiology. *Science*, 357(6353), August 2017.
- [30] Richard Bibb, Nadine Nottrodt, and Arnold Gillner. Artificial vascularized scaffolds for 3d-tissue regeneration — a report of the ArtiVasc 3d Project. *International Journal of Bioprinting*, 2(1):93–102, January 2016.
- [31] Jean Leonard Poiseuille. *Recherches experimentales sur le mouvement des liquides dans les tubes de tres-petits diametres*. Imprimerie Royale, 1844.
- [32] G. Hagen. Ueber die Bewegung des Wassers in engen cylindrischen Röhren. *Annalen der Physik*, 122(3):423–442, 1839.
- [33] E Hagenbach. Uber die bestimmung der zahigkeit einer fliissigkeit durch den ausflub aus rohren. *Ann. Phys. Chem*, 10:385–425, 1860.
- [34] S P Sutera and R Skalak. The History of Poiseuille’s Law. *Annual Review of Fluid Mechanics*, 25(1):1–20, 1993.
- [35] Y. C. Fung. *Biomechanics: Circulation*. Springer Science & Business Media, November 1996.
- [36] Charalambos Vlachopoulos, Michael O’Rourke, and Wilmer W. Nichols. *McDonald’s Blood Flow in Arteries: Theoretical, Experimental and Clinical Principles*. CRC Press, July 2011.
- [37] David N. Ku. Blood Flow in Arteries. *Annual Review of Fluid Mechanics*, 29(1):399–434, 1997.
- [38] T. J. . Pedley. *The Fluid Mechanics of Large Blood Vessels T. J. Pedley*. Cambridge Monographs on Mechanics. University Press, Cambridge, 1980.
- [39] Huan Lei, Dmitry A. Fedosov, Bruce Caswell, and George Em Karniadakis. Blood flow in small tubes: quantifying the transition to the non-continuum regime. *Journal of fluid mechanics*, 722, May 2013.
- [40] Prosenjit Bagchi. Mesoscale simulation of blood flow in small vessels. *Biophysical Journal*, 92(6):1858–1877, March 2007.

- [41] Theodoros G. Papaioannou and Christodoulos Stefanadis. Vascular wall shear stress: basic principles and methods. *Hellenic journal of cardiology: HJC = Hellenike kardiologike epitheorese*, 46(1):9–15, February 2005.
- [42] Robin Få hræus and Torsten Lindqvist. The viscosity of the blood in narrow capillary tubes. *American Journal of Physiology-Legacy Content*, 96(3):562–568, March 1931. Publisher: American Physiological Society.
- [43] Jacek J. Paszkowiak and Alan Dardik. Arterial Wall Shear Stress: Observations from the Bench to the Bedside. *Vascular and Endovascular Surgery*, 37(1):47–57, January 2003.
- [44] Joji Ando and Kimiko Yamamoto. Vascular Mechanobiology - Endothelial Cell Responses to Fluid Shear Stress. *Circulation Journal*, 73(11):1983–1992, 2009.
- [45] F. J. H. Gijzen. *Modeling of wall shear stress in large arteries*. Technische Universiteit Eindhoven, Eindhoven, 1998.
- [46] Nicolaas Westerhof, Nikolaos Stergiopoulos, and Mark I. M. Noble. Chapter 2. Law of Poiseuille. In *Snapshots of Hemodynamics: An Aid for Clinical Research and Graduate Education*. Springer US, 2 edition, 2010.
- [47] Shuping Ge, Liping Bu, Honghai Zhang, Erik Schelbert, Michelle Disterhoft, et al. A real-time 3-dimensional digital Doppler method for measurement of flow rate and volume through mitral valve in children: A validation study compared with magnetic resonance imaging. *Journal of the American Society of Echocardiography*, 18(1):1–7, January 2005.
- [48] J Weinreb, S Kumari, G Phillips, and R Pochaczewsky. Portal vein measurements by real-time sonography. *American Journal of Roentgenology*, 139(3):497–499, September 1982.
- [49] Raffaele Ponzini, Christian Vergara, Giovanna Rizzo, Alessandro Veneziani, Alberto Roghi, et al. Womersley Number-Based Estimates of Blood Flow Rate in Doppler Analysis: In Vivo Validation by Means of Phase-Contrast MRI. *IEEE Transactions on Biomedical Engineering*, 57(7):1807–1815, July 2010.
- [50] C. D. Murray. The Physiological Principle of Minimum Work: II. Oxygen Exchange in Capillaries. *Proceedings of the National Academy of Sciences of the United States of America*, 12(5):299–304, May 1926.
- [51] C. D. Murray. The Physiological Principle of Minimum Work: I. The Vascular System and the Cost of Blood Volume. *Proceedings of the National Academy of Sciences of the United States of America*, 12(3):207–214, March 1926.
- [52] Cecil D. Murray. The Physiological Principle of Minimum Work Applied to the Angle of Branching of Arteries. *The Journal of General Physiology*, 9(6):835–841, July 1926.
- [53] Rossitti S and Löfgren J. Vascular dimensions of the cerebral arteries follow the principle of minimum work. *Stroke*, 24(3):371–377, March 1993.

- [54] Jung Yeop Lee and Sang Joon Lee. Murray's law and the bifurcation angle in the arterial micro-circulation system and their application to the design of microfluidics. *Microfluidics and Nanofluidics*, 8(1):85, May 2009.
- [55] T. F. Sherman. On connecting large vessels to small. The meaning of Murray's law. *The Journal of General Physiology*, 78(4):431–453, October 1981.
- [56] Katherine A. McCulloh, John S. Sperry, and Frederick R. Adler. Water transport in plants obeys Murray's law. *Nature*, 421(6926):939–942, February 2003.
- [57] David R. Emerson, Krzysztof Cieřlicki, Xiaojun Gu, and Robert W. Barber. Biomimetic design of microfluidic manifolds based on a generalised Murray's law. *Lab on a Chip*, 6(3):447–454, 2006.
- [58] David Stephenson, Alexander Patronis, David M. Holland, and Duncan A. Lockerby. Generalizing Murray's law: An optimization principle for fluidic networks of arbitrary shape and scale. *Journal of Applied Physics*, 118(17):174302, November 2015.
- [59] David Stephenson and Duncan A. Lockerby. A generalized optimization principle for asymmetric branching in fluidic networks. *Proceedings of the Royal Society A: Mathematical, Physical and Engineering Sciences*, 472(2191):20160451, July 2016.
- [60] Yifang Zhou, Ghassan S. Kassab, and Sabee Molloy. On the design of the coronary arterial tree: a generalization of Murray's law. *Physics in Medicine and Biology*, 44(12):2929–2945, November 1999.
- [61] Ghassan S. Kassab. Scaling laws of vascular trees: of form and function. *American Journal of Physiology-Heart and Circulatory Physiology*, 290(2):H894–H903, February 2006.
- [62] Tomás Alarcón, Helen M. Byrne, and Philip K. Maini. A design principle for vascular beds: the effects of complex blood rheology. *Microvascular Research*, 69(3):156–172, May 2005.
- [63] M. Zamir. Optimality principles in arterial branching. *Journal of Theoretical Biology*, 62(1):227–251, October 1976.
- [64] Akira Kamiya and Tatsuo Togawa. Optimal branching structure of the vascular tree. *The bulletin of mathematical biophysics*, 34(4):431–438, December 1972.
- [65] M. Zamir and N. Brown. Arterial branching in various parts of the cardiovascular system. *American Journal of Anatomy*, 163(4):295–307, April 1982.
- [66] M. Zamir. Shear forces and blood vessel radii in the cardiovascular system. *The Journal of General Physiology*, 69(4):449–461, April 1977.
- [67] M. Zamir. Nonsymmetrical bifurcations in arterial branching. *The Journal of General Physiology*, 72(6):837–845, December 1978.
- [68] M. Zamir. Local geometry of arterial branching. *Bulletin of Mathematical Biology*, 44(5):597–607, September 1982.

- [69] M. Zamir. Distributing and delivering vessels of the human heart. *The Journal of General Physiology*, 91(5):725–735, May 1988.
- [70] Veronika S. Kopylova, Stanislav E. Boronovskiy, and Yaroslav R. Nartsissov. Fundamental principles of vascular network topology. *Biochemical Society Transactions*, 45(3):839–844, June 2017.
- [71] John A. Adam. Blood Vessel Branching: Beyond the Standard Calculus Problem. *Mathematics Magazine*, 84(3):196–207, June 2011.
- [72] Mohammad Sayed Razavi and Ebrahim Shirani. Development of a general method for designing microvascular networks using distribution of wall shear stress. *Journal of Biomechanics*, 46(13):2303–2309, September 2013.
- [73] Jamel Khamassi, Claas Bierwisch, and Peter Pelz. Geometry optimization of branchings in vascular networks. *Physical Review E*, 93(6):062408, June 2016.
- [74] Xiang-Qi Wang, Arun S. Mujumdar, and Christopher Yap. Effect of bifurcation angle in tree-shaped microchannel networks. *Journal of Applied Physics*, 102(7):073530, October 2007.
- [75] Vinicius R. Pepe, Luiz A. O. Rocha, and Antonio F. Miguel. Optimal Branching Structure of Fluidic Networks with Permeable Walls, May 2017.
- [76] Antonio F. Miguel. A general model for optimal branching of fluidic networks. *Physica A: Statistical Mechanics and its Applications*, 512:665–674, December 2018.
- [77] W. Wayne Lutt. *Overview*. Morgan & Claypool Life Sciences. Publication Title: Hepatic Circulation: Physiology and Pathophysiology.
- [78] David M. Hoganson, Howard I. Pryor, Ira D. Spool, Owen H. Burns, J. Randall Gilmore, and Joseph P. Vacanti. Principles of Biomimetic Vascular Network Design Applied to a Tissue-Engineered Liver Scaffold. *Tissue Engineering. Part A*, 16(5):1469–1477, May 2010.
- [79] Rudolf Karch, Friederike Neumann, Martin Neumann, and Wolfgang Schreiner. Staged Growth of Optimized Arterial Model Trees. *Annals of Biomedical Engineering*, 28(5):495–511, May 2000.
- [80] J. Bezy-Wendling and A. Bruno. A 3d dynamic model of vascular trees. *Journal of Biological Systems*, 07(01):11–31, March 1999.
- [81] Marek Kretowski, Yan Rolland, Johanne Bézy-Wendling, and Jean-Louis Coatrieux. Fast algorithm for 3-D vascular tree modeling. *Computer Methods and Programs in Biomedicine*, 70(2):129–136, February 2003.
- [82] Ghassan Hamarneh and Preet Jassi. VasuSynth: Simulating vascular trees for generating volumetric image data with ground-truth segmentation and tree analysis. *Computerized Medical Imaging and Graphics*, 34(8):605–616, December 2010.
- [83] Preet Jassi and Ghassan Hamarneh. VasuSynth: Vascular Tree Synthesis Software, April 2011.

- [84] Lars Ole Schwen and Tobias Preusser. Analysis and Algorithmic Generation of Hepatic Vascular Systems, 2012.
- [85] A. A. Linninger, I. G. Gould, T. Marinnan, C.-Y. Hsu, M. Chojecki, and A. Alaraj. Cerebral Microcirculation and Oxygen Tension in the Human Secondary Cortex. *Annals of Biomedical Engineering*, 41(11):2264–2284, November 2013.
- [86] W. Schreiner. Computer generation of complex arterial tree models. *Journal of Biomedical Engineering*, 15(2):148–150, March 1993.
- [87] W. Schreiner and P. F. Buxbaum. Computer-optimization of vascular trees. *IEEE transactions on bio-medical engineering*, 40(5):482–491, May 1993.
- [88] Rudolf Karch, Friederike Neumann, Martin Neumann, and Wolfgang Schreiner. A three-dimensional model for arterial tree representation, generated by constrained constructive optimization. *Computers in Biology and Medicine*, 29(1):19–38, January 1999.
- [89] M. Kretowski, Y. Rolland, Johanne Bezy-Wendling, and J. L. Coatrieux. Physiologically based modeling of 3-D vascular networks and CT scan angiography. *IEEE Transactions on Medical Imaging*, 22(2):248–257, February 2003.
- [90] M. Krękowski and J. Bézy-Wendling. Computer modelling of vascular systems. *TASK Quarterly : scientific bulletin of Academic Computer Centre in Gdansk*, Vol. 8, No 2:223–229, 2004.
- [91] Dominik Szczerba and Gábor Székely. Macroscopic Modeling of Vascular Systems. In *Medical Image Computing and Computer-Assisted Intervention — MICCAI 2002*, Lecture Notes in Computer Science, pages 284–292. Springer, Berlin, Heidelberg, September 2002.
- [92] Manfred Georg, Tobias Preusser, and Horst K Hahn. Global Constructive Optimization of Vascular Systems. January 2004.
- [93] Jie Li, William C. Regli, and Wei Sun. An approach to integrating shape and biomedical attributes in vascular models. *Computer-Aided Design*, 39(7):598–609, July 2007.
- [94] Jie Li, William C. Regli, and Wei Sun. Mathematical Representation of the Vascular Structure and Applications. In *Proceedings of the 2007 ACM Symposium on Solid and Physical Modeling*, SPM '07, pages 373–378, New York, NY, USA, 2007. ACM.
- [95] X. Liu, H. Liu, A. Hao, and Q. Zhao. Simulation of Blood Vessels for Surgery Simulators. In *2010 International Conference on Machine Vision and Human-machine Interface*, pages 377–380, April 2010.
- [96] Matthias Schneider, Sven Hirsch, Bruno Weber, and Gábor Székely. Physiologically Based Construction of Optimized 3-D Arterial Tree Models. In *Medical Image Computing and Computer-Assisted Intervention – MICCAI 2011*, Lecture Notes in Computer Science, pages 404–411. Springer, Berlin, Heidelberg, September 2011.

- [97] Matthias Schneider, Johannes Reichold, Bruno Weber, Gábor Székely, and Sven Hirsch. Tissue metabolism driven arterial tree generation. *Medical Image Analysis*, 16(7):1397–1414, October 2012.
- [98] Marek Kociński, Artur Klepaczko, Andrzej Materka, Martha Chekenya, and Arvid Lundervold. 3d image texture analysis of simulated and real-world vascular trees. *Computer Methods and Programs in Biomedicine*, 107(2):140–154, August 2012.
- [99] Lars Ole Schwen, Weiwei Wei, Felix Gremse, Josef Ehling, Lei Wang, et al. Algorithmically generated rodent hepatic vascular trees in arbitrary detail. *Journal of Theoretical Biology*, 365:289–300, January 2015.
- [100] Miguel A. Galarreta-Valverde, Maysa M. G. Macedo, Choukri Mekkaoui, and Marcel P. Jackowski. Three-dimensional synthetic blood vessel generation using stochastic L-systems. volume 8669, page 86691I. International Society for Optics and Photonics, March 2013.
- [101] Andrew A Guy, Alexander W Justin, Dulce M Aguilar-Garza, and Athina E Markaki. 3d printable vascular networks generated by accelerated constrained constructive optimization for tissue engineering. *IEEE Transactions on Biomedical Engineering*, pages 1–1, 2019.
- [102] Y. Rolland, J. Bézy-Wendling, R. Duvauferrier, and A. Bruno. Modeling of the Parenchymous Vascularization and Perfusion. *Investigative Radiology*, 34(3):171, March 1999.
- [103] Aristid Lindenmayer. Mathematical models for cellular interactions in development I. Filaments with one-sided inputs. *Journal of Theoretical Biology*, 18(3):280–299, March 1968.
- [104] Ibrahim T. Ozbolat, Kazim K. Moncal, and Hemanth Gudapati. Evaluation of bio-printer technologies. *Additive Manufacturing*, 13:179–200, January 2017.
- [105] Jesse K. Placone and Adam J. Engler. Recent Advances in Extrusion-Based 3d Printing for Biomedical Applications. *Advanced Healthcare Materials*, 7(8):1701161, 2018.
- [106] Pallab Datta, Bugra Ayan, and Ibrahim T. Ozbolat. Bioprinting for vascular and vascularized tissue biofabrication. *Acta Biomaterialia*, 51:1–20, March 2017.
- [107] Anwarul Hasan, Arghya Paul, Nihal E. Vrana, Xin Zhao, Adnan Memic, et al. Microfluidic techniques for development of 3d vascularized tissue. *Biomaterials*, 35(26):7308–7325, August 2014.
- [108] Ian S. Kinstlinger and Jordan S. Miller. 3d-printed fluidic networks as vasculature for engineered tissue. *Lab on a Chip*, 16(11):2025–2043, May 2016.
- [109] David B. Kolesky, Ryan L. Truby, A. Sydney Gladman, Travis A. Busbee, Kimberly A. Homan, and Jennifer A. Lewis. 3d Bioprinting of Vascularized, Heterogeneous Cell-Laden Tissue Constructs. *Advanced Materials*, 26(19):3124–3130, May 2014.

- [110] Jen-Huang Huang, Jeongyun Kim, Nitin Agrawal, Arjun P. Sudarsan, Joseph E. Maxim, et al. Rapid Fabrication of Bio-inspired 3d Microfluidic Vascular Networks. *Advanced Materials*, 21(35):3567–3571, September 2009.
- [111] Luiz E. Bertassoni, Martina Cecconi, Vijayan Manoharan, Mehdi Nikkhah, Jesper Hjortnaes, et al. Hydrogel Bioprinted Microchannel Networks for Vascularization of Tissue Engineering Constructs. *Lab on a chip*, 14(13):2202–2211, July 2014.
- [112] Xue-Ying Wang, Zi-He Jin, Bo-Wen Gan, Song-Wei Lv, Min Xie, and Wei-Hua Huang. Engineering interconnected 3d vascular networks in hydrogels using molded sodium alginate lattice as the sacrificial template. *Lab on a Chip*, 14(15):2709–2716, July 2014.
- [113] T. J. Hinton, Andrew Lee, and Adam W. Feinberg. 3d bioprinting from the micrometer to millimeter length scales: Size does matter. *Current Opinion in Biomedical Engineering*, 1:31–37, March 2017.
- [114] Xiaoxiao Han, Richard Bibb, and Russell Harris. Design of bifurcation junctions in artificial vascular vessels additively manufactured for skin tissue engineering. *Journal of Visual Languages & Computing*, 28:238–249, June 2015.
- [115] Sarwat F. Khattak, Surita R. Bhatia, and Susan C. Roberts. Pluronic F127 as a Cell Encapsulation Material: Utilization of Membrane-Stabilizing Agents. *Tissue Engineering*, 11(5-6):974–983, May 2005.
- [116] OpenStax. Structure and Function of Blood Vessels - Anatomy and Physiology - OpenStax CNX, March 2013.
- [117] Paul Bourke. Point, Line, Plane, October 1998.
- [118] Thomas Ludewig. Function LineLineIntersect in VBA.
- [119] Rui Lima, Takuji Ishikawa, Yohsuke Imai, and Takami Yamaguchi. Blood Flow Behavior in Microchannels: Past, Current and Future Trends. In *Single and Two-Phase Flows on Chemical and Biomedical Engineering*. 2012.
- [120] Andrea Pfreundt, Karsten Brandt Andersen, Maria Dimaki, and Winnie E. Svendsen. An easy-to-use microfluidic interconnection system to create quick and reversibly interfaced simple microfluidic devices. *Journal of Micromechanics and Microengineering*, 25(11):115010, September 2015.
- [121] Azeem Zulfiqar, Andrea Pfreundt, Winnie Edith Svendsen, and Maria Dimaki. Fabrication of polyimide based microfluidic channels for biosensor devices. *Journal of Micromechanics and Microengineering*, 25(3):035022, February 2015.
- [122] Ludwig Prandtl. Entstehung von Wirbeln bei Wasserströmungen - 2. Anwendungenauf die Strömung durch Krümmer, Hohlräume und Verzweigungsstücke. *Institut für Wissenschaftlichen Film (IWF), Göttingen*, 1936.
- [123] Ludwig Prandtl. Entstehung von Wirbeln bei Wasserströmungen - 1. Entstehung von Wirbeln und künstliche Beeinflussung der Wirbelbildung. *Institut für Wissenschaftlichen Film (IWF), Göttingen*, 1936.

- [124] Seok Hwan Lee, Joohyun Lee, Sejong Chun, and Woong Kang. In situ measurement of micro flow rate using near infrared absorption method. *Optics Express*, 26(13):17078–17091, June 2018.
- [125] Yang Jun Kang. Microfluidic-Based Technique for Measuring RBC Aggregation and Blood Viscosity in a Continuous and Simultaneous Fashion. *Micromachines*, 9(9), September 2018.
- [126] Wi-Han Kim, Chan Il Kim, Sang-Won Lee, SooHee Lim, Cheol-woo Park, et al. Particle Image Velocimetry of the Blood Flow in a Micro-channel Using the Confocal Laser Scanning Microscope. *Journal of the Optical Society of Korea*, 14(1):42–48, March 2010.
- [127] N. T Nguyen. Micromachined flow sensors—a review. *Flow Measurement and Instrumentation*, 8(1):7–16, March 1997.
- [128] Jonathan T. W. Kuo, Lawrence Yu, and Ellis Meng. Micromachined Thermal Flow Sensors - A Review. *Micromachines*, 3:550–573, 2012.
- [129] M. Richter, P. Woias, and D. Weiß. Microchannels for applications in liquid dosing and flow-rate measurement. *Sensors and Actuators A: Physical*, 62(1):480–483, July 1997.
- [130] Jorge Alvarado, José Mireles, and Guillermo Soriano. Development and characterization of a capacitance-based microscale flowmeter. *Flow Measurement and Instrumentation*, 20(2):81–84, April 2009.
- [131] Nima Arjmandi, Chengxun Liu, Willem Van Roy, Liesbet Lagae, and Gustaaf Borghs. Method for Flow Measurement in Microfluidic Channels Based on Electrical Impedance Spectroscopy. *Microfluidics and Nanofluidics*, 12(1-4):17–23, January 2012.
- [132] Daniel C. Leslie, Brett A. Melnikoff, Daniel J. Marchiarullo, Devin R. Cash, Jerome P. Ferrance, and James P. Landers. A simple method for the evaluation of microfluidic architecture using flow quantitation via a multiplexed fluidic resistance measurement. *Lab on a Chip*, 10(15):1960–1966, August 2010.
- [133] Lucie Campagnolo, Milan Nikolic, Julien Perchoux, Yah Leng Lim, Karl Bertling, et al. Flow profile measurement in microchannel using the optical feedback interferometry sensing technique. *Microfluidics and Nanofluidics*, pages 1613–4982, July 2012.
- [134] Thierry Bosch, Caroline Bès, Lorenzo Scalise, and Guy Plantier. Optical feedback interferometry. In C. A. Grimes, E.C. Dickey, and M.V. Pishko, editors, *Encyclopedia of Sensors*, volume X, pages 1–20. American Scientific Publishers, 2006.
- [135] Liron Stern, Avraham Bakal, Mor Tzur, Maya Veinguer, Noa Mazurski, et al. Doppler-Based Flow Rate Sensing in Microfluidic Channels. *Sensors (Basel, Switzerland)*, 14(9):16799–16807, September 2014.

- [136] P. C. Sousa, F. T. Pinho, M. A. Alves, and Monica Oliveira. Flow of a blood analogue solution through microchannels with bifurcations. In *Proceedings of the Japan-Portugal Nano-Biomedical Engineering (BME) Symposium 2011*, volume 1, p25. Portugal, June 2011.
- [137] Katie L. Pitts and Marianne Fenech. Micro-particle Image Velocimetry for Velocity Profile Measurements of Micro Blood Flows. *Journal of Visualized Experiments : JoVE*, (74), April 2013.
- [138] Guillaume Boutin, Min Wei, Yilin Fan, and Lingai Luo. Experimental measurement of flow distribution in a parallel mini-channel fluidic network using PIV technique. *Asia-Pacific Journal of Chemical Engineering*, 11(4):630–641, July 2016.
- [139] Bastian E. Rapp. Chapter 29 - Computational Fluid Dynamics. In Bastian E. Rapp, editor, *Microfluidics: Modelling, Mechanics and Mathematics*, Micro and Nano Technologies, pages 609–622. Elsevier, Oxford, January 2017.
- [140] Joaquim Peiró and Spencer Sherwin. Finite Difference, Finite Element and Finite Volume Methods for Partial Differential Equations. In Sidney Yip, editor, *Handbook of Materials Modeling: Methods*, pages 2415–2446. Springer Netherlands, Dordrecht, 2005.
- [141] Gregory Nicholas de Boer, Adam Johns, Nicolas Delbosc, Daniel Burdett, Morgan Tatchell-Evans, et al. Three computational methods for analysing thermal airflow distributions in the cooling of data centres. *International Journal of Numerical Methods for Heat and Fluid Flow*, 28(2):271–288, February 2018.
- [142] Bastian E. Rapp. Chapter 32 - Finite Element Method. In Bastian E. Rapp, editor, *Microfluidics: Modelling, Mechanics and Mathematics*, Micro and Nano Technologies, pages 655–678. Elsevier, Oxford, January 2017.
- [143] Romain Noël, Fei Ge, Yue Zhang, Laurent Navarro, and Guy Courbebaisse. Lattice Boltzmann method for modelling of biological phenomena. In *2017 25th European Signal Processing Conference (EUSIPCO)*, pages 2654–2658, August 2017. ISSN: 2076-1465.
- [144] Alexandre Joel chorin. Numerical Solution of Boltzmann’s Equation. In *Computational Fluid Mechanics*, pages 49–64. Academic Press, January 1989.
- [145] A. M. Artoli, D. Kandhai, H. C. J. Hoefsloot, A. G. Hoekstra, and P. M. A. Slood. Lattice Boltzmann, a Robust and Accurate Solver for Interactive Computational Hemodynamics. In *Computational Science — ICCS 2003*, Lecture Notes in Computer Science, pages 1034–1043, Berlin, Heidelberg, 2003. Springer.
- [146] Joseph O’Connor, Philip Day, Parthasarathi Mandal, and Alistair Revell. Computational fluid dynamics in the microcirculation and microfluidics: what role can the lattice Boltzmann method play? *Integrative Biology*, 8(5):589–602, May 2016.
- [147] Valero-Lara Pedro. *Analysis and Applications of Lattice Boltzmann Simulations*. IGI Global, May 2018.

- [148] Owen Ball, Bao-Ngoc B. Nguyen, Jesse K. Placone, and John P. Fisher. 3d Printed Vascular Networks Enhance Viability in High-Volume Perfusion Bioreactor. *Annals of Biomedical Engineering*, 44(12):3435–3445, December 2016.
- [149] Xiaoxiao Han, Richard Bibb, and Russell Harris. Artificial Vascular Bifurcations – Design and Modelling. *Procedia CIRP*, 49:14–18, January 2016.
- [150] Xiao Liu, Yubo Fan, Xiaoyan Deng, and Fan Zhan. Effect of non-Newtonian and pulsatile blood flow on mass transport in the human aorta. *Journal of Biomechanics*, 44(6):1123–1131, April 2011.
- [151] Jiho Yang, Y. Eugene Pak, and Tae-Rin Lee. Predicting bifurcation angle effect on blood flow in the microvasculature. *Microvascular Research*, 108:22–28, November 2016.
- [152] Thanapong Chaichana, Zhonghua Sun, and James Jewkes. Computation of hemodynamics in the left coronary artery with variable angulations. *Journal of Biomechanics*, 44(10):1869–1878, July 2011.
- [153] Krzysztof Jurczuk, Marek Kretowski, Pierre-Antoine Eliat, Herve Saint-Jalmes, and Johanne Bezy-Wendling. In Silico Modeling of Magnetic Resonance Flow Imaging in Complex Vascular Networks. *IEEE Transactions on Medical Imaging*, 33(11):2191–2209, November 2014.
- [154] L. Grinberg, T. Anor, J. R. Madsen, A. Yakhov, and G. E. Karniadakis. Large-Scale Simulation of the Human Arterial Tree. *Clinical and Experimental Pharmacology and Physiology*, 36(2):194–205, February 2009.
- [155] Uwe Köhler, Ian Marshall, Malcolm B. Robertson, Quan Long, X. Yun Xu, and Peter R. Hoskins. MRI measurement of wall shear stress vectors in bifurcation models and comparison with CFD predictions. *Journal of Magnetic Resonance Imaging*, 14(5):563–573, 2001.
- [156] Ian Marshall, Shunzhi Zhao, Panorea Papathanasopoulou, Peter Hoskins, and X Yun Xu. MRI and CFD studies of pulsatile flow in healthy and stenosed carotid bifurcation models. *Journal of Biomechanics*, 37(5):679–687, May 2004.
- [157] Ian Marshall. Computational simulations and experimental studies of 3d phase-contrast imaging of fluid flow in carotid bifurcation geometries. *Journal of Magnetic Resonance Imaging*, 31(4):928–934, 2010.
- [158] C. Simoncini, Y. Rolland, V. Morgenthaler, K. Jurczuk, H. Saint-Jalmes, et al. Blood Flow Simulation in Patient-Specific Segmented Hepatic Arterial Tree. *IRBM*, 38(3):120–126, June 2017.
- [159] Wan Shi Low, Nahrizul Adib Kadri, and Wan Abu Bakar bin Wan Abas. Computational Fluid Dynamics Modelling of Microfluidic Channel for Dielectrophoretic BioMEMS Application. *The Scientific World Journal*, 2014:1–11, 2014.
- [160] Xiaoxiao Han, Richard Bibb, and Russell Harris. Engineering design of artificial vascular junctions for 3d printing. *Biofabrication*, 8(2):025018, 2016.

- [161] Pierre J. Carreau. Rheological Equations from Molecular Network Theories. *Transactions of the Society of Rheology*, 16(1):99–127, March 1972.
- [162] Pranali Choudhari and M. S. Panse. Finite Element Modeling and Simulation of Arteries in the Human Arm to Study the Aortic Pulse Wave Propagation. *Procedia Computer Science*, 93:721–727, January 2016.
- [163] Yucheng Liu and Gary Glass. Effects of Mesh Density on Finite Element Analysis. SAE Technical Paper 2013-01-1375, SAE International, Warrendale, PA, April 2013. ISSN: 0148-7191, 2688-3627.
- [164] Donald A. McDonald. *Blood flow in arteries*. E. Arnold, 1960.
- [165] Denise C. Fernandes, Thaís L. S. Araujo, Francisco R. M. Laurindo, and Leonardo Y. Tanaka. Chapter 7 - Hemodynamic Forces in the Endothelium: From Mechanotransduction to Implications on Development of Atherosclerosis. In Protásio L. Da Luz, Peter Libby, Antonio C. P. Chagas, and Francisco R. M. Laurindo, editors, *Endothelium and Cardiovascular Diseases*, pages 85–95. Academic Press, January 2018.
- [166] Robert G. Mannino, Navaneeth KR Pandian, Abhishek Jain, and Wilbur A. Lam. Engineering “Endothelialized” Microfluidics for Investigating Vascular and Hematologic Processes Using Non-Traditional Fabrication Techniques. *Current opinion in biomedical engineering*, 5:13–20, March 2018.



## **Appendix A**

**Calculations for theoretical values of maximum velocity with original CAD model diameters and experimental diameters**







## **Appendix B**

**Tables for estimation of pressure difference paths (inlet to outlet) based on experimental data (radius and flow rate)**

## B.1 Model 01 - 2mL/h

| path 1 Model 01 at 2mL/h (Experimental Dimensions) |          |          |                   |         |          |
|--|----------|----------|-------------------|---------|----------|
| 1 > 2 > 4 > 10 > 16                                |          |          |                   |         |          |
| branch   | r        | l        | Q                 | visc    | DeltaP   |
| 1  | 0.000301 | 0.002    | 5.63267E-10       | 0.00105 | 0.36695  |
| 2  | 0.000249 | 0.002903 | 2.86235E-10       | 0.00105 | 0.577965 |
| 4  | 0.000194 | 0.003558 | 1.03297E-10       | 0.00105 | 0.700968 |
| 10   | 0.000173 | 0.003215 | 1.07981E-10       | 0.00105 | 1.048339 |
| 16   | 0.000229 | 0.00261  | 2.90689E-10       | 0.00105 | 0.737662 |
|  | m        | m        | m <sup>3</sup> /s | kg/m.s  | Pa       |
| inlet-out  |          |          |                   |         | 3.431884 |

| path 2 Model 01 at 2mL/h (Experimental Dimensions) |          |          |                   |         |          |
|--|----------|----------|-------------------|---------|----------|
| 1 > 2 > 5 > 8 > 11 > 16                            |          |          |                   |         |          |
| branch   | r        | l        | Q                 | visc    | DeltaP   |
| 1  | 0.000301 | 0.002    | 5.63267E-10       | 0.00105 | 0.36695  |
| 2  | 0.000249 | 0.002903 | 2.86235E-10       | 0.00105 | 0.577965 |
| 5  | 0.000214 | 0.001132 | 1.80048E-10       | 0.00105 | 0.259842 |
| 8  | 0.000168 | 0.00138  | 1.11131E-10       | 0.00105 | 0.520938 |
| 11   | 0.000172 | 0.00238  | 1.46711E-10       | 0.00105 | 1.07923  |
| 16   | 0.000229 | 0.00261  | 2.90689E-10       | 0.00105 | 0.737662 |
|  | m        | m        | m <sup>3</sup> /s | kg/m.s  | Pa       |
| inlet-out  |          |          |                   |         | 3.542587 |

| path 3 Model 01 at 2mL/h (Experimental Dimensions) |          |        |                   |         |          |
|--|----------|--------|-------------------|---------|----------|
| 1 > 2 > 5 > 9 > 12 > 17                            |          |        |                   |         |          |
| branch   | r        | l      | Q                 | visc    | DeltaP   |
| 1  | 0.000301 | 0.0020 | 5.63267E-10       | 0.00105 | 0.36695  |
| 2  | 0.000249 | 0.0029 | 2.86235E-10       | 0.00105 | 0.577965 |
| 5  | 0.000214 | 0.0011 | 1.80048E-10       | 0.00105 | 0.259842 |
| 9  | 0.000154 | 0.0016 | 7.93087E-11       | 0.00105 | 0.589663 |
| 12   | 0.000166 | 0.0024 | 1.03681E-10       | 0.00105 | 0.879132 |
| 17   | 0.000237 | 0.0026 | 3.57903E-10       | 0.00105 | 0.809089 |
|  | m        | m      | m <sup>3</sup> /s | kg/m.s  | Pa       |
| inlet-out  |          |        |                   |         | 3.482642 |

| path 4 Model 01 at 2mL/h (Experimental dimensions) |          |          |                   |         |          |
|--|----------|----------|-------------------|---------|----------|
| 1 > 3 > 6 > 13 > 15 > 17                           |          |          |                   |         |          |
| branch   | r        | l        | Q                 | visc    | DeltaP   |
| 1  | 0.000301 | 0.002    | 5.63267E-10       | 0.00105 | 0.36695  |
| 3  | 0.000215 | 0.002609 | 2.24283E-10       | 0.00105 | 0.73908  |
| 6  | 0.000162 | 0.002381 | 1.09585E-10       | 0.00105 | 1.012932 |
| 13   | 0.000148 | 0.001066 | 1.16641E-10       | 0.00105 | 0.702378 |
| 15   | 0.000222 | 0.001575 | 2.3849E-10        | 0.00105 | 0.413493 |
| 17   | 0.000237 | 0.002645 | 3.57903E-10       | 0.00105 | 0.809089 |
|  | m        | m        | m <sup>3</sup> /s | kg/m.s  | Pa       |
| inlet-out  |          |          |                   |         | 4.043923 |

| path 5 Model 01 at 2mL/h (Experimental dimensions) |          |          |                   |         |          |
|--|----------|----------|-------------------|---------|----------|
| 1 > 3 > 7 > 14 > 15 > 17                           |          |          |                   |         |          |
| branch   | r        | l        | Q                 | visc    | DeltaP   |
| 1  | 0.000301 | 0.002    | 5.63267E-10       | 0.00105 | 0.36695  |
| 3  | 0.000215 | 0.002609 | 2.24283E-10       | 0.00105 | 0.73908  |
| 7  | 0.000182 | 0.003196 | 1.10955E-10       | 0.00105 | 0.873728 |
| 14   | 0.000219 | 0.002359 | 1.39045E-10       | 0.00105 | 0.381274 |
| 15   | 0.000222 | 0.001575 | 2.3849E-10        | 0.00105 | 0.413493 |
| 17   | 0.000237 | 0.002645 | 3.57903E-10       | 0.00105 | 0.809089 |
|  | m        | m        | m <sup>3</sup> /s | kg/m.s  | Pa       |
| inlet-out  |          |          |                   |         | 3.583614 |

## B.2 Model 01 - 5mL/h

| path 1 Model 01 at 5mL/h (Experimental Dimensions) |          |          |                   |         |                    |
|--|----------|----------|-------------------|---------|--------------------|
| 1 > 2 > 4 > 10 > 16                                |          |          |                   |         |                    |
| branch   | r        | l        | Q                 | visc    | DeltaP             |
| 1  | 0.000301 | 0.002    | 1.33726E-09       | 0.00105 | 0.871183           |
| 2  | 0.000249 | 0.002903 | 7.52714E-10       | 0.00105 | 1.519879           |
| 4  | 0.000194 | 0.003558 | 2.46732E-10       | 0.00105 | 1.674314           |
| 10   | 0.000173 | 0.003215 | 2.07629E-10       | 0.00105 | 2.015778           |
| 16   | 0.000229 | 0.00261  | 5.68895E-10       | 0.00105 | 1.443643           |
|  | m        | m        | m <sup>3</sup> /s | kg/m.s  | Pa                 |
|  |          |          |                   |         | inlet-out 7.524798 |

| path 2 Model 01 at 5mL/h (Experimental Dimensions) |          |          |                   |         |                   |
|--|----------|----------|-------------------|---------|-------------------|
| 1 > 2 > 5 > 8 > 11 > 16                            |          |          |                   |         |                   |
| branch   | r        | l        | Q                 | visc    | DeltaP            |
| 1  | 0.000301 | 0.002    | 1.33726E-09       | 0.00105 | 0.871183          |
| 2  | 0.000249 | 0.002903 | 7.52714E-10       | 0.00105 | 1.519879          |
| 5  | 0.000214 | 0.001132 | 5.22205E-10       | 0.00105 | 0.753637          |
| 8  | 0.000168 | 0.00138  | 2.40613E-10       | 0.00105 | 1.127892          |
| 11   | 0.000172 | 0.00238  | 2.101E-10         | 0.00105 | 1.545526          |
| 16   | 0.000229 | 0.00261  | 5.68895E-10       | 0.00105 | 1.443643          |
|  | m        | m        | m <sup>3</sup> /s | kg/m.s  | Pa                |
|  |          |          |                   |         | inlet-out 7.26176 |

| path 3 Model 01 at 5mL/h (Experimental Dimensions) |          |        |                   |         |                    |
|--|----------|--------|-------------------|---------|--------------------|
| 1 > 2 > 5 > 9 > 12 > 17                            |          |        |                   |         |                    |
| branch   | r        | l      | Q                 | visc    | DeltaP             |
| 1  | 0.000301 | 0.0020 | 1.33726E-09       | 0.00105 | 0.871183           |
| 2  | 0.000249 | 0.0029 | 7.52714E-10       | 0.00105 | 1.519879           |
| 5  | 0.000214 | 0.0011 | 5.22205E-10       | 0.00105 | 0.753637           |
| 9  | 0.000154 | 0.0016 | 2.01838E-10       | 0.00105 | 1.500675           |
| 12   | 0.000166 | 0.0024 | 2.1731E-10        | 0.00105 | 1.842607           |
| 17   | 0.000237 | 0.0026 | 6.90877E-10       | 0.00105 | 1.56182            |
|  | m        | m      | m <sup>3</sup> /s | kg/m.s  | Pa                 |
|  |          |        |                   |         | inlet-out 8.049802 |

| path 4 Model 01 at 5mL/h (Experimental dimensions) |          |          |                   |         |                    |
|--|----------|----------|-------------------|---------|--------------------|
| 1 > 3 > 6 > 13 > 15 > 17                           |          |          |                   |         |                    |
| branch   | r        | l        | Q                 | visc    | DeltaP             |
| 1  | 0.000301 | 0.002    | 1.33726E-09       | 0.00105 | 0.871183           |
| 3  | 0.000215 | 0.002609 | 5.88116E-10       | 0.00105 | 1.938016           |
| 6  | 0.000162 | 0.002381 | 2.58025E-10       | 0.00105 | 2.385011           |
| 13   | 0.000148 | 0.001066 | 2.32522E-10       | 0.00105 | 1.400173           |
| 15   | 0.000222 | 0.001575 | 4.82376E-10       | 0.00105 | 0.836342           |
| 17   | 0.000237 | 0.002645 | 6.90877E-10       | 0.00105 | 1.56182            |
|  | m        | m        | m <sup>3</sup> /s | kg/m.s  | Pa                 |
|  |          |          |                   |         | inlet-out 8.992546 |

| path 5 Model 01 at 5mL/h (Experimental dimensions) |          |          |                   |         |                    |
|--|----------|----------|-------------------|---------|--------------------|
| 1 > 3 > 7 > 14 > 15 > 17                           |          |          |                   |         |                    |
| branch   | r        | l        | Q                 | visc    | DeltaP             |
| 1  | 0.000301 | 0.002    | 1.33726E-09       | 0.00105 | 0.871183           |
| 3  | 0.000215 | 0.002609 | 5.88116E-10       | 0.00105 | 1.938016           |
| 7  | 0.000182 | 0.003196 | 2.37684E-10       | 0.00105 | 1.871671           |
| 14   | 0.000219 | 0.002359 | 2.8811E-10        | 0.00105 | 0.790022           |
| 15   | 0.000222 | 0.001575 | 4.82376E-10       | 0.00105 | 0.836342           |
| 17   | 0.000237 | 0.002645 | 6.90877E-10       | 0.00105 | 1.56182            |
|  | m        | m        | m <sup>3</sup> /s | kg/m.s  | Pa                 |
|  |          |          |                   |         | inlet-out 7.869055 |

### B.3 Model 02 - 2mL/h

| path 1 Model 02 at 2mL/h (Experimental Dimensions) |          |          |                   |         |          |
|--|----------|----------|-------------------|---------|----------|
| 1 > 2 > 4 > 10 > 16                                |          |          |                   |         |          |
| branch   | r        | l        | Q                 | visc    | DeltaP   |
| 2  | 0.000246 | 0.002903 | 2.62945E-10       | 0.00105 | 0.557315 |
| 4  | 0.000187 | 0.003558 | 9.07869E-11       | 0.00105 | 0.706305 |
| 10   | 0.000185 | 0.003215 | 9.26033E-11       | 0.00105 | 0.686992 |
| 16   | 0.000209 | 0.00261  | 1.66196E-10       | 0.00105 | 0.613714 |
|  | m        | m        | m <sup>3</sup> /s | kg/m.s  | Pa       |
| inlet-out  |          |          |                   |         | 2.564325 |

| path 2 Model 02 at 2mL/h (Experimental Dimensions) |          |          |                   |         |          |
|--|----------|----------|-------------------|---------|----------|
| 1 > 2 > 5 > 8 > 11 > 16                            |          |          |                   |         |          |
| branch   | r        | l        | Q                 | visc    | DeltaP   |
| 2  | 0.000246 | 0.002903 | 2.62945E-10       | 0.00105 | 0.557315 |
| 5  | 0.000203 | 0.001132 | 1.76442E-10       | 0.00105 | 0.31448  |
| 8  | 0.000166 | 0.00138  | 9.68979E-11       | 0.00105 | 0.476574 |
| 11   | 0.000167 | 0.00238  | 1.15647E-10       | 0.00105 | 0.957596 |
| 16   | 0.000209 | 0.00261  | 1.66196E-10       | 0.00105 | 0.613714 |
|  | m        | m        | m <sup>3</sup> /s | kg/m.s  | Pa       |
| inlet-out  |          |          |                   |         | 2.919679 |

| path 3 Model 02 at 2mL/h (Experimental Dimensions) |          |        |                   |         |          |
|--|----------|--------|-------------------|---------|----------|
| 1 > 2 > 5 > 9 > 12 > 17                            |          |        |                   |         |          |
| branch   | r        | l      | Q                 | visc    | DeltaP   |
| 2  | 0.000246 | 0.0029 | 2.62945E-10       | 0.00105 | 0.557315 |
| 5  | 0.000203 | 0.0011 | 1.76442E-10       | 0.00105 | 0.31448  |
| 9  | 0.000152 | 0.0016 | 8.22003E-11       | 0.00105 | 0.64397  |
| 12   | 0.000163 | 0.0024 | 8.62698E-11       | 0.00105 | 0.796583 |
| 17   | 0.000236 | 0.0026 | 1.74316E-10       | 0.00105 | 0.400801 |
|  | m        | m      | m <sup>3</sup> /s | kg/m.s  | Pa       |
| inlet-out  |          |        |                   |         | 2.713149 |

| path 4 Model 02 at 2mL/h (Experimental dimensions) |          |          |                   |         |          |
|--|----------|----------|-------------------|---------|----------|
| 1 > 3 > 6 > 13 > 15 > 17                           |          |          |                   |         |          |
| branch   | r        | l        | Q                 | visc    | DeltaP   |
| 3  | 0.000205 | 0.002609 | 1.64177E-10       | 0.00105 | 0.654851 |
| 6  | 0.000159 | 0.002381 | 8.2676E-11        | 0.00105 | 0.82353  |
| 13   | 0.000145 | 0.001066 | 8.79693E-11       | 0.00105 | 0.567213 |
| 15   | 0.000218 | 0.001575 | 1.51546E-10       | 0.00105 | 0.285179 |
| 17   | 0.000236 | 0.002645 | 1.74316E-10       | 0.00105 | 0.400801 |
|  | m        | m        | m <sup>3</sup> /s | kg/m.s  | Pa       |
| inlet-out  |          |          |                   |         | 2.731574 |

| path 5 Model 02 at 2mL/h (Experimental dimensions) |          |          |                   |         |          |
|--|----------|----------|-------------------|---------|----------|
| 1 > 3 > 7 > 14 > 15 > 17                           |          |          |                   |         |          |
| branch   | r        | l        | Q                 | visc    | DeltaP   |
| 3  | 0.000205 | 0.002609 | 1.64177E-10       | 0.00105 | 0.654851 |
| 7  | 0.000168 | 0.003196 | 7.3536E-11        | 0.00105 | 0.788858 |
| 14   | 0.000189 | 0.002359 | 7.61784E-11       | 0.00105 | 0.376567 |
| 15   | 0.000218 | 0.001575 | 1.51546E-10       | 0.00105 | 0.285179 |
| 17   | 0.000236 | 0.002645 | 1.74316E-10       | 0.00105 | 0.400801 |
|  | m        | m        | m <sup>3</sup> /s | kg/m.s  | Pa       |
| inlet-out  |          |          |                   |         | 2.506256 |

## B.4 Model 02 - 5mL/h

| path 1 Model 02 at 5mL/h (Experimental Dimensions) |          |          |             |           |          |
|--|----------|----------|-------------|-----------|----------|
| 1 > 2 > 4 > 10 > 16                                |          |          |             |           |          |
| branch   | r        | l        | Q           | visc      | DeltaP   |
| 2  | 0.000246 | 0.002903 | 5.3328E-10  | 0.00105   | 1.130294 |
| 4  | 0.000187 | 0.003558 | 2.07416E-10 | 0.00105   | 1.61366  |
| 10   | 0.000185 | 0.003215 | 2.34313E-10 | 0.00105   | 1.738289 |
| 16   | 0.000209 | 0.00261  | 3.93598E-10 | 0.00105   | 1.453445 |
|  | m        | m        | m3/s        | kg/m.s    | Pa       |
|  |          |          |             | inlet-out | 5.935688 |

| path 2 Model 02 at 5mL/h (Experimental Dimensions) |          |          |             |           |          |
|--|----------|----------|-------------|-----------|----------|
| 1 > 2 > 5 > 8 > 11 > 16                            |          |          |             |           |          |
| branch   | r        | l        | Q           | visc      | DeltaP   |
| 2  | 0.000246 | 0.002903 | 5.3328E-10  | 0.00105   | 1.130294 |
| 5  | 0.000203 | 0.001132 | 3.43931E-10 | 0.00105   | 0.613003 |
| 8  | 0.000166 | 0.00138  | 2.44891E-10 | 0.00105   | 1.204453 |
| 11   | 0.000167 | 0.00238  | 2.84452E-10 | 0.00105   | 2.355367 |
| 16   | 0.000209 | 0.00261  | 3.93598E-10 | 0.00105   | 1.453445 |
|  | m        | m        | m3/s        | kg/m.s    | Pa       |
|  |          |          |             | inlet-out | 6.756562 |

| path 3 Model 02 at 5mL/h (Experimental Dimensions) |          |        |             |           |          |
|--|----------|--------|-------------|-----------|----------|
| 1 > 2 > 5 > 9 > 12 > 17                            |          |        |             |           |          |
| branch   | r        | l      | Q           | visc      | DeltaP   |
| 2  | 0.000246 | 0.0029 | 5.3328E-10  | 0.00105   | 1.130294 |
| 5  | 0.000203 | 0.0011 | 3.43931E-10 | 0.00105   | 0.613003 |
| 9  | 0.000152 | 0.0016 | 2.16048E-10 | 0.00105   | 1.692548 |
| 12   | 0.000163 | 0.0024 | 2.12061E-10 | 0.00105   | 1.95809  |
| 17   | 0.000236 | 0.0026 | 6.19707E-10 | 0.00105   | 1.42488  |
|  | m        | m      | m3/s        | kg/m.s    | Pa       |
|  |          |        |             | inlet-out | 6.818815 |

| path 4 Model 02 at 5mL/h (Experimental dimensions) |          |          |             |           |          |
|--|----------|----------|-------------|-----------|----------|
| 1 > 3 > 6 > 13 > 15 > 17                           |          |          |             |           |          |
| branch   | r        | l        | Q           | visc      | DeltaP   |
| 3  | 0.000205 | 0.002609 | 4.24175E-10 | 0.00105   | 1.691902 |
| 6  | 0.000159 | 0.002381 | 2.00426E-10 | 0.00105   | 1.996433 |
| 13   | 0.000145 | 0.001066 | 2.35997E-10 | 0.00105   | 1.521675 |
| 15   | 0.000218 | 0.001575 | 3.7375E-10  | 0.00105   | 0.703322 |
| 17   | 0.000236 | 0.002645 | 6.19707E-10 | 0.00105   | 1.42488  |
|  | m        | m        | m3/s        | kg/m.s    | Pa       |
|  |          |          |             | inlet-out | 7.338213 |

| path 5 Model 02 at 5mL/h (Experimental dimensions) |          |          |             |           |          |
|--|----------|----------|-------------|-----------|----------|
| 1 > 3 > 7 > 14 > 15 > 17                           |          |          |             |           |          |
| branch   | r        | l        | Q           | visc      | DeltaP   |
| 3  | 0.000205 | 0.002609 | 4.24175E-10 | 0.00105   | 1.691902 |
| 7  | 0.000168 | 0.003196 | 1.87505E-10 | 0.00105   | 2.011462 |
| 14   | 0.000189 | 0.002359 | 1.72981E-10 | 0.00105   | 0.855082 |
| 15   | 0.000218 | 0.001575 | 3.7375E-10  | 0.00105   | 0.703322 |
| 17   | 0.000236 | 0.002645 | 6.19707E-10 | 0.00105   | 1.42488  |
|  | m        | m        | m3/s        | kg/m.s    | Pa       |
|  |          |          |             | inlet-out | 6.686648 |

